

2007

Effects of molecular motion on deuteron magic angle spinning NMR spectra

Yuanyuan Huang
College of William & Mary - Arts & Sciences

Follow this and additional works at: <https://scholarworks.wm.edu/etd>



Part of the [Atomic, Molecular and Optical Physics Commons](#), and the [Biophysics Commons](#)

Recommended Citation

Huang, Yuanyuan, "Effects of molecular motion on deuteron magic angle spinning NMR spectra" (2007).
Dissertations, Theses, and Masters Projects. Paper 1539623519.
<https://dx.doi.org/doi:10.21220/s2-zhn6-e445>

This Dissertation is brought to you for free and open access by the Theses, Dissertations, & Master Projects at W&M ScholarWorks. It has been accepted for inclusion in Dissertations, Theses, and Masters Projects by an authorized administrator of W&M ScholarWorks. For more information, please contact scholarworks@wm.edu.

Effects of Molecular Motion on Deuteron Magic Angle Spinning NMR Spectra

Yuanyuan Huang

Williamsburg, Virginia

Master of Science, the College of William and Mary, 2002
Bachelor of Science, Wuhan University, 2001

A Dissertation presented to the Graduate Faculty
of the College of William and Mary in Candidacy for the Degree of
Doctor of Philosophy

Department of Physics

The College of William and Mary
August, 2007

APPROVAL PAGE

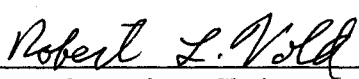
This dissertation is submitted in partial fulfillment of
the requirements for the degree of

Doctor of Philosophy

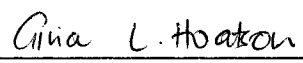


Yuanyuan Huang

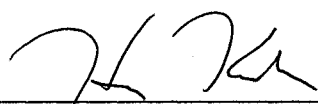
Approved by the Committee, May, 2007



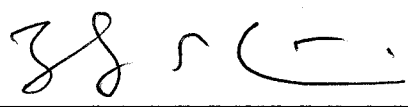
Committee Chair
Professor Robert L. Vold, Applied Science
College of William and Mary



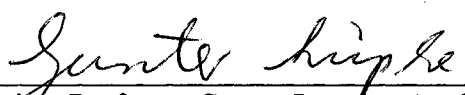
Professor Gina L. Hoatson, Physics
College of William and Mary



Professor Henry Krakauer, Physics
College of William and Mary



Associate Professor Shiwei Zhang, Physics
College of William and Mary



Associate Professor Gunter Luepke, Applied Science
College of William and Mary

To my parents and sister for their unending support

Table of Contents

	Page
Acknowledgements	viii
List of Tables	ix
List of Figures	x
Abstract	xiv
Chapter 1. Theory of Solid State Deuteron NMR	2
1.1 Introduction	2
1.2 General spin interactions	3
1.2.1 Zeeman interaction	3
1.2.2 Chemical shift anisotropy	7
1.2.3 Quadrupole coupling interaction	12
1.2.4 Spin-spin coupling interaction	17
1.3 Spherical tensors and operator	19
1.3.1 Cartesian tensors and operators	19
1.3.2 Spherical tensors for quadrupole coupling	23
1.4 NMR spectrometer	25
1.5 Essential techniques in deuteron NMR	30
1.5.1 Quadrupole echo	30
1.5.2 On/Off magic angle spinning	33
Chapter 2. On/Off Magic Angle Spinning	35
2.1 Theory	35
2.1.1 Powder pattern in solid state NMR	35

2.1.2	Semi-classical calculation of MAS spectra	41
2.1.3	Deuteron MAS in molecular motion studies	44
2.2	Deuteron On/Off MAS experiment	46
2.2.1	Rotation echoes	46
2.2.2	Angle adjustment	48
2.3	Data collection and processing	54
2.3.1	Quadrature detection	54
2.3.2	CYCLOPS phase cycling	56
2.3.3	Fourier transformation	58
2.3.4	Phase correction	60
	Chapter 3. Simulation of Deuteron Spectra with Molecular Motion	65
3.1	Introduction	65
3.2	Theory of molecular motion	66
3.2.1	Motion effects	66
3.2.2	Multi-axis molecular motion	71
3.2.3	Stochastic Liouville equation	75
3.3	Simulation of static spectra	78
3.3.1	Theory of static simulation	78
3.3.2	Representative quadrupole echo line shape simulations	84
3.4	Simulation of deuteron On/Off MAS	86
3.4.1	Periodic Hamiltonians	86
3.4.2	Direct integration	90
3.4.3	Floquet method	92

3.4.4 Chemical shift effects	99
3.5 Conclusion	105
Chapter 4. Dynamics of Urea and its Inclusion Compound	106
4.1 Introduction	106
4.2 Structure and dynamics of urea and its inclusion compound	107
4.2.1 Structure of urea and UIC	107
4.2.2 Guest molecular motion	110
4.3 Host molecular motion	111
4.3.1 CO and CN motions	111
4.3.2 Experiment procedures	112
4.3.3 Results	114
4.4 Simulation and motion rates	120
4.4.1 Simulation of UIC spectra.	120
4.4.2 CO and CN motion rates	127
4.5 Discussion	133
4.5.1 Arrhenius energy of CO and CN motions	133
4.5.2 Advantages of OMAS	135
Chapter 5. Dynamics in Phenylalanine	136
5.1 Introduction	136
5.2 Experiments and simulations of L-phenylalanine-d ₈	138
5.2.1 Quadrupole echo and MAS experiments	138
5.2.2 T _{1Z} relaxation study	146
5.2.3 Simulation of phenylalanine MAS spectra	152

5.3 NAPME/ β -cyclodextrin inclusion compound	158
5.3.1 MAS Experiments	158
5.3.2 Simulation and discussion	162
5.4 Conclusion	166
Appendix Wigner Rotation Matrices	167
Bibliography	168
Vita	176

Acknowledgements

First of all, I appreciate the supports and encouragements from my parents and sister. They inspire and push me to travel so far and accomplish so much. Their advices and inspirations will benefit me forever. Thanks my advisor, Prof. Robert L. Vold for guiding and encouraging me. I thank Prof. Gina L. Hoatson for her help and contributions to this work. I also appreciate the kindness and helps from people in my group: William Brouwer, Donghua Zhou, Murugesan Vijayakumar, Jacob Godwin-Jones, Peter de Castro and other members of our group. At the end, I thank the professors and support staffs (Paula, Sylvia and Carolyn) for their help and kindness

List of Tables

1.1 Spin interaction from various sources	20
1.2 Isotropic, antisymmetric, and symmetric tensors	20
2.1 Console setup for angle adjustment using KBr	49
2.2 CYCLOPS phase cycling	56
3.1. Methods for generating sets of powder angles α and β .	84
4.1 Hydrogen Bond Parameters for pure urea and hexadecane-UIC	109
4.2 Two frame representation of urea jump motions in C ₈ A-UIC	122
4.3 One-frame representation of urea jump motions in urea/C ₈ A inclusion	122
4.4 Temperature dependent jump rates of UIC-C ₈ A	130
4.5. UIC activation parameters	134
5.1 Best fit parameters from the MAS spectrum in figure 5.4	144
5.2 The Euler angles of phenyl ring deuteron	154

List of Figures

1.1	Nuclear spins in the magnetic field	4
1.2	Relative magnitudes of various spin interactions	7
1.3	Numerical simulation of a CSA power pattern	11
1.4	The first order quadrupole coupling perturbation	15
1.5	Simulation of deuteron quadrupole echo	16
1.6	Multiple-frame transformation	24
1.7	Schematic representation of the NMR magnet	26
1.8.	Transmitter section of NMR spectrometer	27
1.9	Schematic representation of the NMR MAS probe	28
1.10	Schematic representation of NMR receiver	29
1.11	Quadrupole echo pulse sequence.	30
1.12	The magic angle spinning experiment	33
2.1	Chemical shift powder pattern of $\text{Pb}(\text{NO}_3)_2$	37
2.2	The MAS rotor.	39
2.3	The moving path of nuclear spins in MAS experiments	47
2.4	Experimental MAS FID	48
2.5	The structure of MAS angle adjustment module	50
2.6	Urea-MAS spectrum after fine angle tuning	52
2.7	On/Off MAS urea- d_4 line shape with different offset angles	53
2.8	CYCLOPS	57
2.9	The relationship between real and imaginary FID	59
2.10	The linear phase distorted line shape.	61

2.11 Truncation effects	62
2.12 Decreasing exponential apodization	64
3.1 Quadrupole echo spectra with different motional rates	68
3.2 Variable temperature ^2H -OMAS of urea inclusion compounds	70
3.3 The defocusing and refocusing of quadrupole-induced free precession	80
3.4 Flow chart for simulation of QE powder pattern	83
3.5 Motion rates and QE powder pattern	85
3.6 τ_1 and quadrupole echo line shape	86
3.7 Flow chart for simulation of On/Off MAS powder pattern	88
3.8 Spin flow in the rotor-fixed frame	93
3.9 Line shape and L_F matrix size	99
3.10 Simulations of MAS spectra under the effects from co-axis CSA.	103
3.11 Simulations of the effects of coaxial CSA interaction with different motion rates	104
3.12 Simulations of the effects of co-axis and non co-axis CSA	105
4.1 Structure of urea	108
4.2 One unit cell for octanoic acid / urea inclusion compound ($\text{C}_8\text{A-UIC}$)	110
4.3 Molecular motions in urea	112
4.4 The sensitivity of urea spectra to the offset angle	115
4.5 Deuteron OMAS spectra ($\nu_R = 20$ kHz) of $\text{C}_8\text{A-UIC}$ at 46.05 MHz	116
4.6 Expanded view of the third (a) and the second (b) side bands, $\nu_R = 20$ kHz	117
4.7 Deuteron OMAS spectra of $\text{C}_8\text{A-UIC}$ at 46.05 MHz	118

4.8. Expanded view of (a) the third and (b) the second sidebands, $\nu_R = 25$ kHz	119
4.9 Temperature dependence of the second sideband in MAS and OMAS	121
4.10. OMAS simulations showing the effects of changing k_{CO}	125
4.11 OMAS simulation showing the effects of changing k_{CN} .	126
4.12 The effects of the difference site-dependent quadrupole coupling constants	127
4.13 Contour maps of $z = e^{-x^2}$ for 46.05MHz OMAS spectra of C_8A-UIC	129
4.14 Temperature-dependent experimental (a) and simulated (b) OMAS spectra	131
4.15 The second sideband: (a) experimental spectra (b) simulated spectra	132
4.16 Simulated (dash) and experimental (solid) OMAS spectra of C_8A-UIC	133
4.17. The Arrhenius plot for rotation about the CO bond	135
4.18 The Arrhenius plot for rotation about the CN bond	135
5.1 Structure of L-phenylalanine	138
5.2 the motion of phenylalanine	139
5.3 Quadrupole echo spectra of L-phen- d_8	142
5.4 17.6T MAS Spectrum of L-Phenylalanine- d_8 at 253 K	143
5.5 5 Temperature dependent MAS side band line shapes of L-phe- d_8 .	147
5.6 Phenylalanine T_{1Z} relaxation experiments	149
5.7 The center and the left first sideband of the relaxation spectra	150
5.8 Points chosen to measure site-selective relaxation times	151
5.9 T_{1Z} measurements of the intensity profile	152
5.10 The calculated MAS spectra	155
5.11 The center band of calculated MAS	155

5.12 Simulations of flip, immobile and para-deuteron	156
5.13 The simulation of phenylalanine MAS spectrum	157
5.14 Comparison between simulation and experiment	158
5.15 Amplitude profiles of L-phen-d ₈	159
5.16 The MAS Spectrum of NAPME/ β -CD inclusion compound at 340 K	162
5.17 VT-MAS Spectra of NAPME/ α -CD inclusion compound	162
5.18 19-Site system	164
5.19 Multi-site Simulation of diffusion in a 15° cone	165
5.20 Multi-site Simulation of diffusion in a 60° cone.	166
5.21 Simulation at 15kHz with 60° cone-angle	167

Abstract

Solid state deuteron NMR experiments, especially magic angle spinning (MAS) and off-magic angle spinning (OMAS), are developed to explore dynamical systems. A theoretical discussion of interactions relevant for spin-1 nuclei is presented. Practical aspects of MAS/OMAS experiments are described in detail. The dominant quadrupolar coupling interaction in deuteron NMR has been simulated and the effects of multiple-frame molecular motions on MAS/OMAS spectra are taken into account in this calculation. Effects of chemical shift anisotropy are also simulated, and shown to be small under conditions of rapid sample spinning.

Two numerical methods, direct integration and an efficient simulation routine based on Floquet theory, are discussed. Improvements in computational efficiency of the Floquet method in computing solid state deuteron MAS/OMAS spectrum makes the quantitative analysis of molecular motion possible: complex multiple frame molecular motions, deuteron quadrupolar interactions and chemical shift anisotropy are now included in a single simulation routine and the effects of the multiple-frame molecular motions can be analyzed by comparing the line shapes of simulations with those of experiments.

The enhanced motional sensitivity of deuteron NMR MAS/OMAS makes it possible to detect temperature-dependent motion rates of urea molecules in octanoic acid/urea inclusion compounds. Temperature-dependent deuteron OMAS line shapes have been recorded and fitted through least-square procedures, to provide rates of rotation about both CN and CO bonds. Activation energies have been calculated for these motions. The power and utility of OMAS is demonstrated by this investigation.

The phenyl ring motions in appropriately labeled L-phenylalanine and *N*-acetyl-L-phenylalanine methyl ester/ cyclodextrin inclusion compound have also been studied through high field deuteron MAS experiments. Phenylalanine MAS spectra with ultra-fast ring-flip motion have been simulated and the range of phenyl ring flip rates is obtained by comparing the simulated and experimental spectra. In the studies of phenylalanine/ cyclodextrin inclusion compound, an approach to a physically reasonable diffusion model has also been made by increasing the number of jump sites per unit solid angle included in the calculation. These simulations involve repeated diagonalization of very large matrices and demonstrate the capability of the approach to handle complex dynamical systems.

Effects of Molecular Motion on Deuteron Magic Angle Spinning NMR Spectra

Chapter 1

Theory of Solid State Deuteron NMR

1.1 Introduction

Solid state deuteron NMR is particularly suited to the study of molecular motion. It has long been known that line shapes of deuteron NMR spectra are sensitive to motion over the range of rates $10^3 \sim 10^6 \text{ s}^{-1}$, so that matching temperature changes with corresponding simulations can be used to determine rates in this range¹⁻³. The interaction of the deuteron quadrupole moment with the electric field gradient at the site of the nucleus is by far the dominant perturbation: generally, the strength of this interaction is between 150~250 kHz, while chemical shift anisotropy is less than 1kHz even at 17.4T, and homonuclear, magnetic dipole-dipole interactions are also smaller than hundreds Hz. The dominant quadrupolar interaction simplifies the simulation of deuteron powder patterns and makes deuteron NMR an important method for gaining information about the dynamics of systems as diverse as crystals, liquid crystals, polymers, lipids, glasses⁴⁻⁶.

With the recent advent of commercially available high spinning speed Magic Angle Spinning (MAS) probes, fast sample rotation (above 25 kHz) becomes increasingly attractive as an alternative to traditional quadrupole echo experiments^{7, 8}. High-speed deuteron MAS spectra have much greater signal/noise ratio than static quadrupolar echo experiments, and the frequency resolution is also greatly improved. In Off-angle MAS

(OMAS) experiments, a small, controllable fraction of the quadrupolar interaction is reintroduced by a tiny adjustment away from exact magic angle conditions. This reintroduced quadrupolar interaction defines a new dynamical window for slow motion and enables determination of slow motional rates. This thesis is focused on theoretical and experimental development of On/Off-MAS as a useful tool in the study of dynamical systems that exhibit complex motions occurring on several different time scales.

1.2 General Spin Interactions

1.2.1 Zeeman interaction

In most NMR experiments, the sample is put in a static uniform magnetic field, B_0 , and a series of radio frequency pulses is applied, and subsequent signals from the excited spins are recorded. After data processing, these signals can be used to determine the magnitude of various nuclear spin interactions. By means of appropriate theories and models, the structure of molecules, their arrangement and degree of order with respect to the crystalline lattice, and their dynamic behavior on multiple time scales can be determined. From the classical viewpoint⁹⁻¹¹, randomly distributed individual nuclear magnetic moments are aligned preferentially with the applied field direction (Z-direction), and a net magnetization arises (fig. 1.1). The magnetization μ_i from the i^{th} nucleus with a spin angular momentum I_i and the precession of the net magnetization M in the magnetic field can be calculated:

$$\begin{aligned}\mu_i &= \gamma \cdot I_i \\ M &= \sum_i \mu_i\end{aligned}\tag{1.1}$$

$$\frac{dM}{dt} = \gamma \cdot M \times B_0 \quad (1.2)$$

Where the constant γ is the magnetogyric ratio. The net magnetization precesses about B_0 at a constant rate called the Larmor frequency, which is $\omega_0 = -\gamma B_0$.

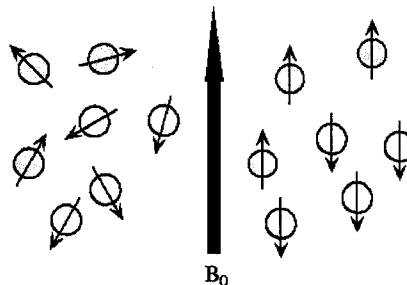


FIG. 1.1 Nuclear spins in the magnetic field

Randomly distributed individual nuclear magnetic moments are aligned preferentially with the applied field and a net magnetization arises. Nuclei with positive magnetogyric ratio align along the $-Z$ direction and nuclei with negative magnetogyric ratio align along $+Z$ direction. Their precession frequency is called the Larmor frequency ($\omega_0 = -\gamma B_0$).

From the quantum mechanical viewpoint, the nuclear spin system is polarized along the applied field, and the state of an individual spin is an incoherent superposition of Zeeman eigenstates¹², which depend on the nature of the nuclear angular momentum I . The proportion of the spin system in each eigenstate is given by the Boltzmann distribution for a thermal equilibrium sample¹³⁻¹⁵. For an isolated nuclear spin, the Hamiltonian is given by

$$\hat{H}_Z = -\gamma \cdot \hbar \hat{I}_Z B_0 \quad (1.3)$$

and for the state $|I, m\rangle$, the energy $E_{I, m}$ is

$$\begin{aligned} E_{I, m} &= \langle I, m | \hat{H} | I, m \rangle = -\gamma \cdot \hbar B_0 \langle I, m | \hat{I}_Z | I, m \rangle \\ &= -m\gamma \cdot \hbar B_0 \end{aligned} \quad (1.4)$$

Here the integer m can take $2I+1$ different values between $-I$ and $+I$. At thermal equilibrium, an ensemble of nuclear spins distributes over these Zeeman states and the population of the state $|I, m\rangle$ at temperature T is written as:

$$P_{I,m} = \frac{\exp\left(-\frac{E_{I,m}}{kT}\right)}{\sum_{m'=-I}^I \exp\left(-\frac{E_{I,m'}}{kT}\right)} \quad (1.5)$$

The expectation value of the net magnetization $\langle \hat{\mu} \rangle$ for the sample is the sum of contribution from each possible eigenstates. For isolated nuclei with $I = 1/2$, the expectation value of the net magnetization is the population difference.

$$\langle \hat{\mu} \rangle = \gamma \cdot \hbar (p_{1/2,1/2} - p_{1/2,-1/2}) \quad (1.6)$$

If a many-spin ensemble contains N identical nuclear spins with $I = 1/2$, 2^N superposition states are needed to define the state of every spin completely. Calculations based on the superposition are impractical because N is generally very large, at least 10^{12} .

The alternative is to use density matrix formalism^{9, 14, 16, 17} to describe a many-spin ensemble¹⁸. The elements of the spin density matrix, ρ_{mn} , are defined as:

$$\rho_{mn} = \overline{|I, m\rangle \langle I, n|} \quad (1.7)$$

where the $|I, m\rangle$ refers to states of a single spin and the bar denotes an average over all spins in the ensemble. Diagonal elements of the spin density matrix represent populations of the basic Zeeman eigenstates, and the off-diagonal elements are called coherences. It can be shown¹³ that the expectation value of an observable quantity represented by operator A is given by

$$\langle A \rangle = \text{Tr}(A\rho) = \sum_{i=-I}^I \sum_{j=-I}^I A_{ij} \rho_{ji} \quad (1.8)$$

Where $\text{Tr}(A\rho)$ is the trace of the product of operator A and the density matrix.

For nuclei in a constant, uniform magnetic field B_0 at temperature T under equilibrium conditions, the density matrix is

$$\rho_{eq} = \frac{\exp\left(-\frac{\hat{H}_z}{kT}\right)}{Z} \quad (1.9)$$

here Z is the trace of $\exp\left(-\frac{\hat{H}_z}{kT}\right)$, and \hat{H}_z is the time independent Zeeman Hamiltonian.

Time dependent spin interactions, which are described by $\hat{H}(t)$, change the density matrix $\rho(t)$ via the propagator, $\exp\left(-i \cdot \int_0^t \hat{H}(t') dt'\right)$:

$$\frac{d\rho(t)}{dt} = -i[\hat{H}(t), \rho(t)] \quad (1.10)$$

↓

$$\rho(t) = \hat{T} \cdot \exp\left(-i \int_0^t \hat{H}(t') dt'\right) \cdot \rho(0) \cdot \exp\left(i \int_0^t \hat{H}(t') dt'\right) \quad (1.11)$$

where \hat{T} is Dyson time-ordering operator^{19, 20}. If the spin interaction, \hat{H} , is independent of time, the Dyson time-ordering operator may be neglected and the density matrix evolves in time according to:

$$\rho(t) = \exp(-i\hat{H}t) \cdot \rho(0) \cdot \exp(i\hat{H}t) \quad (1.12)$$

Since the Zeeman interaction usually dominates the behavior of the spin system, the spins precess at Larmor Frequency (10~900 MHz). In general, weaker interactions can be decomposed into two parts: only one that commutes with the Zeeman term and the other that does not; the former shows significant effects on the nuclear spin system. For the purposes of this thesis, the most important weaker interactions include chemical shifts,

quadrupole coupling, and spin-spin coupling. For nuclei of spin $\frac{1}{2}$, where quadrupole coupling is absent, magnetic dipole-dipole coupling cannot be ignored, however for deuterons ($I = 1$), the dominant interaction is quadrupole coupling. The relative strengths of these interactions are shown schematically in fig.1.2

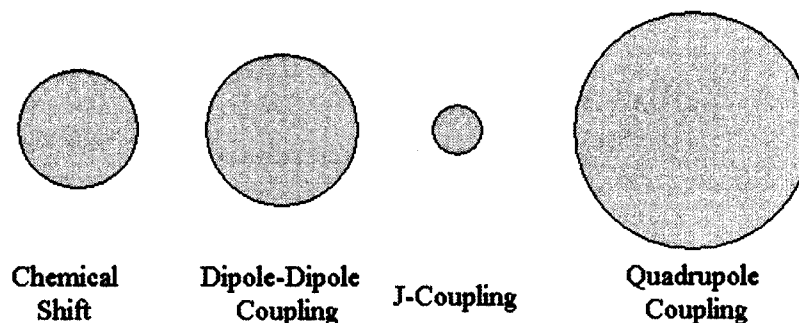


FIG.1.2 Relative magnitudes of various spin interactions
 Quadrupole coupling vanishes for $I = 1/2$. The figure proximately shows the relative strength of each spin interactions.⁹

1.2.2 Chemical shift anisotropy

Chemical shift interactions occur when the electrons surrounding a nucleus interact with the applied magnetic field. The motion of the electrons in B_0 produces a secondary magnetic field that adds to the applied uniform magnetic field, causing a shift of the precession frequency relative to the Larmor frequency of a bare nucleus. The magnitude of the chemical shift is linearly proportional to B_0 and depends on the electron distribution. The Hamiltonian for this interaction is

$$\hat{H}_{CS} = \gamma \hat{I} \cdot \sigma \cdot B_0 \quad (1.13)$$

Here, σ is the chemical shielding tensor. The chemical shielding tensor is always decomposable into symmetric σ_S and anti-symmetric components, σ_{AS} .

$$\sigma = \sigma_S + \sigma_{AS}$$

or

$$\begin{pmatrix} \sigma_{XX} & \sigma_{XY} & \sigma_{XZ} \\ \sigma_{YX} & \sigma_{YY} & \sigma_{YZ} \\ \sigma_{ZX} & \sigma_{ZY} & \sigma_{ZZ} \end{pmatrix} = \begin{pmatrix} \sigma_{XX} & \frac{1}{2}(\sigma_{XY} + \sigma_{YX}) & \frac{1}{2}(\sigma_{XZ} + \sigma_{ZX}) \\ \frac{1}{2}(\sigma_{XY} + \sigma_{YX}) & \sigma_{YY} & \frac{1}{2}(\sigma_{YZ} + \sigma_{ZY}) \\ \frac{1}{2}(\sigma_{XZ} + \sigma_{ZX}) & \frac{1}{2}(\sigma_{YZ} + \sigma_{ZY}) & \sigma_{ZZ} \end{pmatrix} \quad (1.14)$$

$$+ \begin{pmatrix} 0 & \frac{1}{2}(\sigma_{XX} - \sigma_{YY}) & \frac{1}{2}(\sigma_{XZ} - \sigma_{ZX}) \\ \frac{1}{2}(\sigma_{YX} - \sigma_{XY}) & 0 & \frac{1}{2}(\sigma_{YZ} - \sigma_{ZY}) \\ \frac{1}{2}(\sigma_{ZX} - \sigma_{XZ}) & \frac{1}{2}(\sigma_{ZY} - \sigma_{YZ}) & 0 \end{pmatrix}$$

When the Zeeman interaction is significantly stronger than any other interactions, only σ_S commutes with H_Z and shows shielding effects. σ_S can be further decomposed into an isotropic part, σ_{ISO} , and an anisotropic part, σ_{CSA} . In the molecule-fixed principal axis frame (PAS), where the tensor σ_S is diagonal, σ_{ISO} , σ_{CSA} , and the asymmetry parameter η are defined as:

$$\sigma_{ISO} = \frac{1}{3}(\sigma_{XX}^{PAS} + \sigma_{YY}^{PAS} + \sigma_{ZZ}^{PAS}) \quad (1.15.a)$$

$$\sigma_{CSA} = \sigma_{ZZ}^{PAS} - \sigma_{ISO} \quad (1.15.b)$$

$$\eta_{CS} = \frac{\sigma_{XX}^{PAS} - \sigma_{YY}^{PAS}}{\sigma_{CSA}} \quad (1.15.c)$$

The Hamiltonian of the spin system is the sum of the dominant Zeeman interaction \hat{H}_0 and the symmetric component of chemical shift interaction \hat{H}_{CS} .

$$\hat{H} = \hat{H}_0 + \hat{H}_{CS} \quad (1.16)$$

After transforming the chemical shift tensor from PAS to the LAB frame, which is rotating around the B_0 direction at the Larmor frequency, the Hamiltonian in this rotating reference frame \hat{H}^{LAB} is

$$\hat{H}^{LAB}(t) = \hat{R}_Z^{-1}(\omega_0 t) \hat{H}_0 \hat{R}_Z(\omega_0 t) + \hat{R}_Z^{-1}(\omega_0 t) \hat{H}_{CS} \hat{R}_Z(\omega_0 t) - \omega_0 \hat{I}_Z \quad (1.17)$$

And since the Zeeman interaction is not affected by the rotation, the first term of $\hat{H}^{LAB}(t)$ cancels the third term, and only the chemical shift interaction is left.

$$\begin{aligned}\hat{H}_{CS}^{LAB}(t) &= \hat{R}_Z^{-1}(\omega_0 t) \hat{H}_{CS} \hat{R}_Z(\omega_0 t) \\ &= \gamma \begin{pmatrix} \hat{I}_X \cos(\omega_0 t) + \hat{I}_Y \sin(\omega_0 t) \\ \hat{I}_Y \cos(\omega_0 t) - \hat{I}_X \sin(\omega_0 t) \\ \hat{I}_Z \end{pmatrix} \cdot \sigma \cdot B_0\end{aligned}\quad (1.18)$$

This is a periodically time-dependent Hamiltonian. The first-order Hamiltonian is obtained by averaging over one Larmor precession period, t_p :

$$\begin{aligned}\bar{H}_{CS}^{(0)} &= \frac{1}{t_p} \int_0^{t_p} \hat{H}_{CS}^{LAB}(t) dt \\ &= \gamma \cdot \hat{I}_Z \sigma_{ZZ}^{LAB} B_0\end{aligned}\quad (1.19)$$

It is clear that only the σ_{ZZ} component of the chemical shift tensor in LAB frame contributes to the first order average chemical shift interaction. Note that this procedure is entirely equivalent to dropping that part of \hat{H}_{CS} that does not commute with \hat{H}_0 .

In order to calculate σ_{ZZ} in the LAB frame, considering a spin with direction defined by Euler angles $(\alpha \beta \gamma)$, which rotate the chemical shift from PAS to LAB frame^{21, 22}.

The tensor under the rotation becomes:

$$\sigma^{LAB} = R^{-1}(\alpha, \beta, \gamma) \cdot \sigma^{PAS} \cdot R(\alpha, \beta, \gamma) \quad (1.20)$$

$$\sigma_{ZZ}^{LAB} = \sigma_{ISO} + \frac{1}{2} \sigma_{CSA} \cdot [3 \cos^2 \beta - 1 + \eta_{CS} \sin^2 \beta \cdot \cos 2\alpha] \quad (1.21)$$

Thus, the precession frequency is independent of Euler angle γ , and for spins the orientation dependence is given by

$$\begin{aligned}
 \omega_{CS} &= \gamma \cdot \hat{I}_z \sigma_{ZZ}^{LAB} B_0 \\
 &= -\omega_0 \sigma_{ZZ}^{LAB} \\
 &= -\omega_0 \sigma_{ISO} - \frac{1}{2} \omega_0 \sigma_{CSA} \left[3 \cos^2 \beta - 1 + \eta_{CS} \sin^2 \beta \cdot \cos 2\alpha \right]
 \end{aligned} \tag{1.22}$$

In a liquid sample, rapid random reorientational molecular motion averages the orientation dependent second term in Eq. 1.22 to zero, and the NMR spectrum shows a single narrow peak at $\omega_0 - \omega_{ISO}$.

In a solid powder sample, all molecular orientations are present and the contribution from the anisotropic component depends on the fraction of crystallites that have orientation specified by Euler angles (α, β) . Each combination of angles (α, β) defines a point on the unit sphere. For a randomly oriented set of crystallites, there will be equal numbers of molecules in a volume specified by patches on the sphere with equal solid angle and the single peak becomes a powder pattern (fig 1.3).

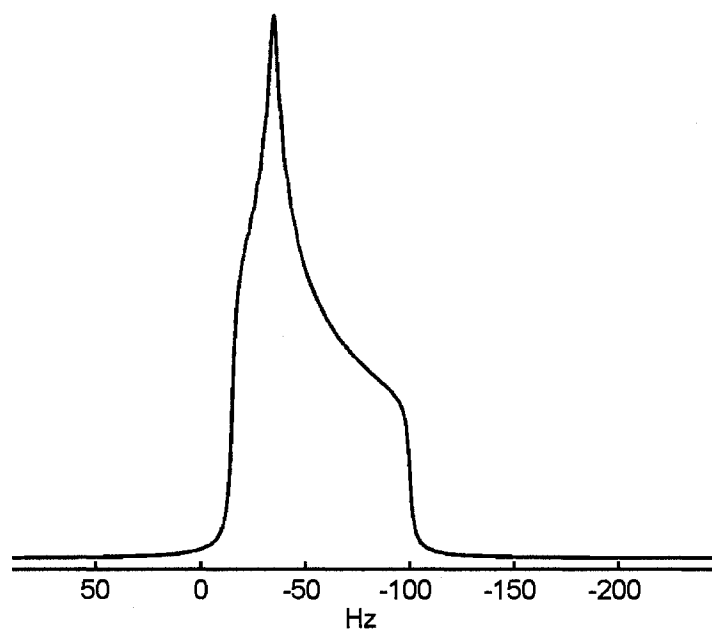


FIG 1.3 Numerical simulation of a CSA power pattern

The parameters are $\omega_0 = 46.7 \times 10^6$ Hz, $\sigma_{ISO} = 46.7$ Hz, $\sigma_{CSA} = 46.7$ Hz, $\eta_{CS} = 0.4$. The spectrum is drawn from a powder average that includes 5000 random powder orientations.

The barycenter ("center of gravity") of the powder pattern occurs at σ_{ISO} and the characteristic line shape permits determination of σ_{CSA} and the asymmetry parameter η_{CS} .

In most NMR experiments, absolute resonance frequencies are not reported. Instead, offset frequencies, which define peak positions relative to the isotropic resonance frequency of a standard reference sample, σ_{ref} , are reported in units of parts per million (ppm) of the applied field. This universal practice permits easy comparison of results that are obtained in different laboratories with different magnets. The offset frequency in ppm is defined as:

$$\delta_{ISO} = \frac{\sigma_{ref} - \sigma_{ISO}}{\sigma_{ref}} \quad (1.23)$$

The value of the chemical shift in ppm is a constant that only depends on the electron distribution near the nuclear spin and can be used without considering the strength of the applied magnetic field. Analysis of chemical shifts study can be used to gain information about electronic wave functions and molecular structure.²³⁻²⁵

1.2.3 Quadrupole coupling interaction

All nuclei with spin greater than $\frac{1}{2}$ possess electric quadrupole moments, which interacts not only with the applied magnetic field but also with the electric field gradient at the site of the nucleus^{1,26}. This interaction changes the nuclear spin Zeeman energy levels and affects the NMR spectrum. The strength of the quadrupole interaction depends on the magnitude of the nuclear quadrupole moment, and the magnitude and orientation of the electric field gradient tensor. The magnitude of the nuclear quadrupole moment, Q , is constant for a given nucleus and generally independent of the chemical environment. For deuterons, this is very small ($Q = 2.8 \times 10^{-31} \text{ m}^2$) and the contribution of quadrupole coupling to the NMR spectrum is between 150 kHz and 200 kHz. Depending on external field strength, the Zeeman interaction (Larmor frequency) is typically between 45 MHz and 750MHz. Hence, the quantization direction of the nuclear spin is still along B_0 while the electric field gradient tensor remains fixed in the molecule. Thus, the quadrupole coupling interaction has an orientational dependence with respect to the applied magnetic field even though it is not a strictly magnetic interaction like chemical shift or dipole-dipole coupling. An exact mathematical treatment of quadrupole coupling based on multipole expansions of nuclear and electronic charge distributions and the use of the Wigner-Eckart theorem¹² supports this qualitative description.

It can be shown that the Hamiltonian operator for coupling between the nuclear quadrupole moment and the electronic electric field gradient (EFG) tensor, V , is given by

$$\hat{H}_Q = \frac{eQ}{2I(2I-1)\hbar} \cdot \hat{I} \cdot V \cdot \hat{I} \quad (1.24)$$

In the EFG principal axis system (PAS), the elements of the electric field gradient tensor are written as

$$V_{ZZ}^{PAS} = eq_{ZZ} \quad (1.25.a)$$

$$\eta_Q = \frac{V_{XX}^{PAS} - V_{YY}^{PAS}}{V_{ZZ}^{PAS}} \quad (1.25.b)$$

η_Q is the quadrupole asymmetry parameter. The principal axes are labeled by convention such that V_{ZZ} is the largest component of the EFG tensor. For deuterons in organic molecules, Z-direction is typically oriented along the C-D or N-D bonds, and the near cylindrical symmetry of the bonding orbital implies that the asymmetry parameter is small^{27,28}. The quadrupole Hamiltonian in the PAS is

$$\hat{H}_Q^{PAS} = \frac{e^2 q_{ZZ} Q}{4I(2I-1)\hbar} \cdot \left[3\hat{I}_{Z,PAS}^2 - \hat{I}^2 + \frac{1}{2}\eta_Q (\hat{I}_{X,PAS}^2 - \hat{I}_{Y,PAS}^2) \right] \quad (1.26)$$

and $C_Q = e^2 q_{ZZ} Q / \hbar$ is called the quadrupole coupling constant.

If the PAS is rotated into LAB by Euler angles $(\alpha \beta \gamma)$, the Hamiltonian after averaging over a Larmor period may be written as the sum of the first, second and higher order terms.

$$\hat{H}_Q^{LAB} = \hat{H}_Q^{(1)} + \hat{H}_Q^{(2)} + O^{(\geq 3)} \dots \quad (1.27)$$

And in Eq. 1.27:

$$\hat{H}_Q^{(1)} = \frac{e2qQ}{4I(2I-1)\hbar} \cdot \frac{1}{2} (3\cos^2\beta - 1 + \eta_Q \cos 2\alpha \cdot \sin^2\beta) \cdot (3\hat{I}_Z^2 - \hat{I}^2) \quad (1.28)$$

$$\begin{aligned} \hat{H}_Q^{(2)} = & \frac{e2qQ}{4I(2I-1)\hbar} \left\{ \frac{3}{2} \sin\beta \cos\alpha \cdot [\hat{I}_Z(\hat{I}_+ + \hat{I}_-) + (\hat{I}_+ + \hat{I}_-)\hat{I}_Z] + \frac{3}{4} \sin^2\beta \cdot (\hat{I}_+^2 + \hat{I}_-^2) \right. \\ & + \eta_Q (\cos^2\beta + 1) \cdot (\hat{I}_+^2 + \hat{I}_-^2) \\ & + \eta_Q \frac{1}{2} \sin\beta [(\cos\beta \cos 2\alpha - i \sin 2\alpha) \cdot (\hat{I}_+ \hat{I}_Z + \hat{I}_Z \hat{I}_+) + (\cos\beta \cos 2\alpha + i \sin 2\alpha) \cdot (\hat{I}_- \hat{I}_Z + \hat{I}_Z \hat{I}_-)] \\ & \left. + \eta_Q \frac{i}{4} \sin 2\alpha \cos\beta \cdot (\hat{I}_+^2 - \hat{I}_-^2) \right\} \quad (1.29) \end{aligned}$$

In general, the second order terms for deuterons are entirely negligible because C_Q , which is between 150~250 kHz, is small compared to the Larmor frequency, which is 46.7 MHz in a 7.6 T magnetic field. Thus, the total Hamiltonian is adequately represented by the first order quadrupolar perturbation:

$$\hat{H} = \hat{H}_0 + \hat{H}_{CS} + \hat{H}_Q^{(1)} \quad (1.30)$$

The Hamiltonian matrix has large diagonal elements if the Zeeman interaction is the dominant term, and the off diagonal elements are, for deuterons, negligibly small. The resulting energy levels are illustrated in fig. 1.4.

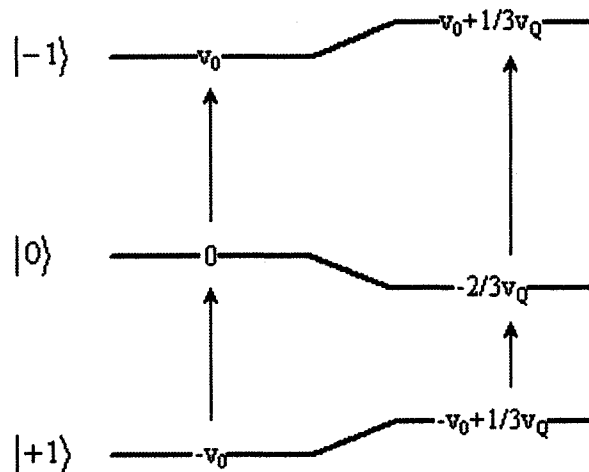


FIG 1.4. The first order quadrupole coupling perturbation

The Zeeman energy levels are modified by the first order quadrupole interaction. The allowed transitions give a two-line spectrum, symmetric about ν_0 , with separation of $2\nu_Q$. The PAS orientation is defined by Euler angle (α, β) that specify the orientation of the magnetic field vector, in the principal axis system of the field gradient.

The first and second order quadrupole coupling interaction corrections to the Zeeman energies levels for spin state $|I, m\rangle$ are

$$E_m^{(1)} = \frac{e^2 q Q}{4I(2I-1)} (3m^2 - I(I+1)) \cdot \frac{1}{2} [3 \cos^2 \beta - 1 + \eta_Q \cos 2\alpha \sin^2 \beta] \quad (1.31.a)$$

$$E_m^{(2)} = -\frac{e^2 q Q}{4I(2I-1)} \frac{m}{\omega_0} \left\{ -\frac{1}{5} (I(I+1) - 3m^2) \cdot (3 + \eta_Q^2) \right. \\ + \frac{1}{28} (8I(I+1) - 12m^2 - 3) \cdot [(\eta_Q^2 - 3) \cdot (3 \cos^2 \beta - 1) + 6\eta_Q \sin^2 \beta \cos 2\alpha] \\ + \frac{1}{8} (18I(I+1) - 34m^2 - 5) \cdot \left[\frac{1}{140} (18 + \eta_Q^2) \cdot (35 \cos^4 \beta - 30 \cos^2 \beta + 3) \right. \\ \left. \left. + \frac{3}{7} \eta_Q \sin^2 \beta \cos 2\alpha \cdot (7 \cos^2 \beta - 1) + \frac{1}{4} \eta_Q^2 \sin^4 \beta \cos 4\alpha \right] \right\} \quad (1.31.b)$$

The first order correction has the same orientation dependence as the chemical shift interaction, but its magnitudes are opposite in sign for the allowed $|-1\rangle \leftrightarrow |0\rangle$ and $|0\rangle \leftrightarrow |1\rangle$ transitions:

$$\begin{aligned} \Delta E_{0,1}^{(1)} &= E_1^{(1)} - E_0^{(1)} \\ &= \frac{3 \cdot e^2 q Q}{4} \cdot \frac{1}{2} [3 \cos^2 \beta - 1 + \eta_Q \cos 2\alpha \sin^2 \beta] \end{aligned} \quad (1.32.a)$$

and

$$\begin{aligned} \Delta E_{-1,0}^{(1)} &= E_0^{(1)} - E_{-1}^{(1)} \\ &= -\frac{3 \cdot e^2 q Q}{4} \cdot \frac{1}{2} [3 \cos^2 \beta - 1 + \eta_Q \cos 2\alpha \sin^2 \beta] = -\Delta E_{0,1}^{(1)} \end{aligned} \quad (1.32.b)$$

Therefore the quadrupole powder pattern line shape looks like two mirror image chemical shift line shapes.

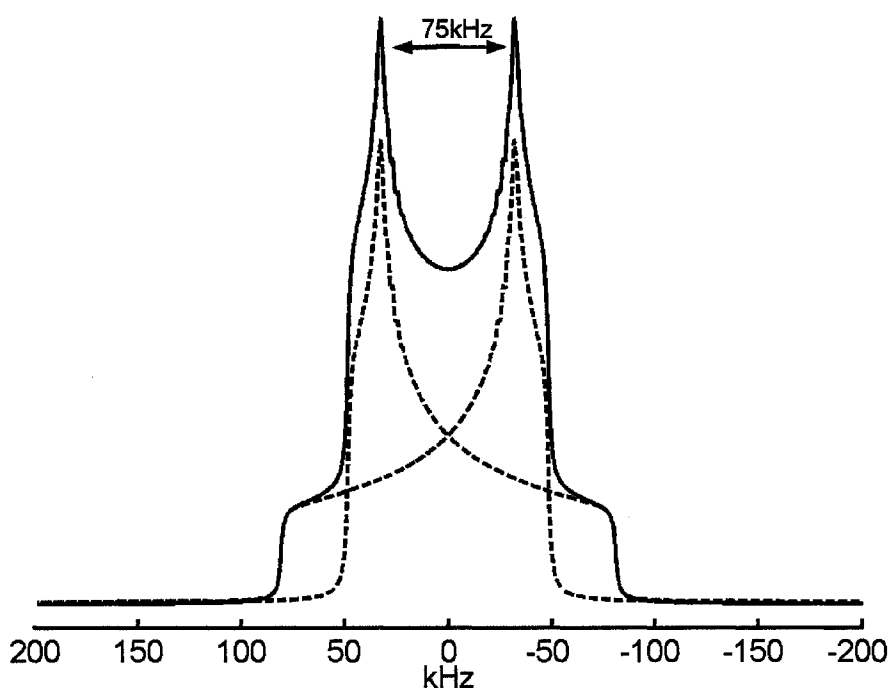


FIG. 1.5 Simulation of deuteron powder line shape

The simulation assumed that deuteron parameters are $C_Q=100$ kHz and $\eta_Q=0.2$. The dashed lines are the transitions: $m = +1$ to $m = 0$ and $m = 0$ to $m = -1$. For asymmetry parameter $\eta_Q = 0$, the two "horns" are separated by $\frac{3}{4} C_Q$, and for any η_Q , the two "shoulders" are separated by $\frac{3}{2} C_Q$.

1.2.4 Spin-spin coupling interaction

Interactions between pairs of spins in a magnetic field can occur directly (dipole-dipole coupling), or indirectly through polarization of electrons that are around each nucleus (J-coupling) ²⁹. Dipole-dipole coupling is described by a traceless tensor, but the trace of the indirect J-coupling tensor does not vanish. Hence, in liquid samples where rapid, isotropic molecular tumbling averages the spin-spin coupling interactions, only the indirect coupling survives. This interaction is also present in solids, but for deuterons it is too small to be observed. On the other hand, deuteron dipole-dipole coupling is often responsible for line widths.

The strength of the dipolar coupling is proportional to $1/r^3$ where r is the internuclear distance between interacting spins. Since the internuclear vector is fixed in the molecule, and the local field produced at one spin depends on the orientation of this vector as well as its length, the dipolar coupling is also orientation dependent. Dipolar coupling can occur between nuclei with the homo or hetero magnetogyric ratio. Although these homonuclear and heteronuclear couplings have slightly different corrections to the Zeeman energy levels, the dipole Hamiltonian between two spins S and I can always be written as

$$\begin{aligned}\hat{H}_{dd} &= -\left(\frac{\mu_0}{4\pi}\right) \cdot \gamma_I \gamma_S \hbar \cdot \left(\frac{\hat{I} \cdot \hat{S}}{r^3} - \frac{(\hat{I} \cdot \vec{r})(\hat{S} \cdot \vec{r})}{r^5} \right) \\ &= -2\hat{I} \cdot D \cdot \hat{S}\end{aligned}\tag{1.33}$$

Where D is the dipolar coupling tensor. In PAS (with Z_{PAS} along the internuclear vector) the dipolar coupling tensor is

$$D = \begin{pmatrix} -\frac{d}{2} & 0 & 0 \\ 0 & -\frac{d}{2} & 0 \\ 0 & 0 & +d \end{pmatrix} \quad (1.34)$$

$$d = \hbar \frac{\mu_0 \gamma_I \gamma_S}{4\pi \cdot r^3}$$

For homo and heteronuclear dipolar coupling with orientation $(\alpha \beta \gamma)$, the first order average Hamiltonian is

$$\bar{H}_{I,S}^{(0)} = -\frac{1}{2} d (3 \cos^2 \beta - 1) \cdot [3 \hat{I}_Z \hat{S}_Z - \hat{I} \cdot \hat{S}] \quad (1.35)$$

In a many-spin system, the degeneracy of Zeeman levels is lifted by the second term of $\bar{H}_{I,S}^{(0)}$, resulting many possible transition frequencies. The many-body nature of this interaction prevents an exact treatment, but qualitatively the line shape is broadened to an approximately Gaussian shape with width on the order of D , computed for the closest pair of spins¹³.

For heteronuclear dipolar coupling, the periodic time dependent terms in Eq 1.35 are truncated further since the spin system is observed in the LAB frame, which rotates around Z-axis at the Larmor frequency of spin I or S . Thus only the $\hat{I}_Z \cdot \hat{S}_Z$ term survives in Eq 1.35 and the first order average Hamiltonian for heteronuclear dipolar coupling is

$$\bar{H}_{I,S}^{(0)} = -d (3 \cos^2 \beta - 1) \cdot \hat{I}_Z \hat{S}_Z \quad (1.36)$$

Since this Hamiltonian has the same orientation dependence as the chemical shift and there are two mirror transitions, the spectrum is similar to the spectrum for quadrupole coupling, consisting of "horns" separated by the dipolar coupling constant d . In practice,

such spectra are rarely observed: the multiplicity of dipolar couplings for spin pairs with different distances and orientations washes out any fine structure and the result is a featureless, often approximately Gaussian line. Moreover, the width of this line covers only a tiny fraction of the peak separation produced by quadrupole coupling. Deuteron dipole coupling will therefore be ignored in the remainder of this thesis.

1.3 Spherical tensors and operators

1.3.1 Cartesian tensor and operators

For all the spin interactions, the contribution to the NMR spectrum is observed in the laboratory (LAB) frame. It can be shown that signals acquired by demodulating with respect to two quadrature reference signals at the pulse carrier frequency is equivalent to detecting transverse magnetization in a frame rotating about the laboratory Z-axis. However, the operators describing the relevant spin interactions are time independent only in crystal or molecule fixed principal axis (PAS) frames. Multiple-frame transformations are required in order to rotate relevant spin tensors from their PAS into a common, crystal fixed frame and then to the LAB (or rotating) frame. Detailed discussion can be found in reference ¹³ and ³⁰.

The interaction Hamiltonian for a spin I can be represented heuristically as a coupling of the spin angular momentum to a local magnetic field, B_{loc} :

$$\hat{H} = -\gamma \cdot \hat{I} \cdot B_{loc} \quad (1.37)$$

Different interactions lead to a local magnetic field in the form of a product of a tensor A that depends on the type of the spin interaction, and a Cartesian vector operator \hat{J} that relates to the source of interaction, as shown in table 1.1.

$$B_{loc} = A \cdot \hat{J} \quad (1.38)$$

Table 1.1. Spin interaction²²

Source	A	\hat{J}	\hat{H}
Chemical Shift	σ	B_0	$-\gamma \cdot \hat{I} \cdot \sigma \cdot B_0$
Quadrupole Coupling	V	\hat{I}	$-\gamma \cdot \hat{I} \cdot V \cdot \hat{I}$
Dipole Coupling	D	\hat{S}	$-\gamma \cdot \hat{I} \cdot D \cdot \hat{S}$

The tensor A is a second rank Cartesian tensor and its elements depend on the orientation and strength of the spin interaction. In general, the spin Hamiltonian can be rewritten as a linear sum of its elements.

$$\begin{aligned} \hat{H} &= \sum_{m,n=X,Y,Z} A_{m,n} \hat{I}_m \hat{J}_n \\ &= \sum_{m,n=X,Y,Z} A_{m,n} \hat{R}_{m,n} \end{aligned} \quad (1.39)$$

And the nine components of \hat{R} can be classified in three groups shown in table 1.2

Table 1.2. Isotropic, antisymmetric, and symmetric tensors

Isotropic, $\hat{R}^{(0)}$	$\frac{1}{3} \sum_{m=X,Y,Z} \hat{R}_{m,m}$
Antisymmetric tensor, $\hat{R}^{(1)}$	$\frac{1}{2} (\hat{R}_{m,n} - \hat{R}_{n,m})$
Symmetric tensor, $\hat{R}^{(2)}$	$\frac{1}{2} (\hat{R}_{m,n} + \hat{R}_{n,m}) - \delta_{m,n} \cdot \frac{1}{3} \hat{R}_{k,k}$

A spherical irreducible tensor, $\hat{T}_{p,q}$, is an entity that transforms under rotation into a linear combination of tensor components with the same rank:

$$\begin{aligned}
R(\alpha, \beta, \lambda) \hat{T}_{p,q} R'(\alpha, \beta, \gamma) &= \sum_k T_{p,k} D_{k,q}^{(r)}(\alpha, \beta, \lambda) \\
R(\alpha, \beta, \lambda) A_{p,q} R'(\alpha, \beta, \gamma) &= \sum_k A_{p,k} D_{k,q}^{(r)}(\alpha, \beta, \lambda)
\end{aligned} \tag{1.40}$$

where $D_{m,n}^{(r)}(\alpha, \beta, \lambda)$ are the elements of Wigner rotation matrices^{16, 22}.

$$D_{m,n}^{(r)}(\alpha, \beta, \gamma) = \exp(-ima) d_{m,n}^{(r)}(\beta) \exp(-in\gamma) \tag{1.41}$$

For the second rank Wigner rotation matrix, $m, n = -2, -1, 0, +1, +2$, and $d_{m,n}^{(2)}$ are

$$\begin{aligned}
d_{2,2}^2 &= \left(\frac{1 + \cos \beta}{2} \right)^2 \\
d_{2,1}^2 &= -\frac{1 + \cos \beta}{2} \cdot \sin \beta \\
d_{2,0}^2 &= \frac{\sqrt{6}}{4} \sin^2 \beta \\
d_{2,-1}^2 &= -\frac{1 - \cos \beta}{2} \cdot \sin \beta \\
d_{2,-2}^2 &= \left(\frac{1 - \cos \beta}{2} \right)^2
\end{aligned} \tag{1.42}$$

And other elements of $d^{(2)}$ can be calculated by the relationship

$$d_{m,n}^{(j)} = (-1)^{n-m} d_{n,m}^{(j)} = d_{-n,-m}^{(j)} \tag{1.43}$$

\hat{R} can be rewritten in a form of corresponding irreducible tensors $\hat{T}_{m,n}$, which are defined as

$$\begin{aligned}
\hat{T}_{0,0} &= -\sqrt{\frac{1}{3}} \sum_{m=X,Y,Z} R_{m,m} \\
\hat{T}_{1,0} &= i\sqrt{\frac{1}{2}}(R_{XY} - R_{YX}) \\
\hat{T}_{1,\pm 1} &= \mp i\frac{1}{2}[R_{YZ} - R_{ZY} \pm i(R_{ZX} - R_{XZ})] \\
\hat{T}_{2,0} &= \sqrt{\frac{1}{6}}(2R_{ZZ} - R_{XX} - R_{YY}) \\
\hat{T}_{2,\pm 1} &= \mp\frac{1}{2}[R_{XZ} + R_{ZX} \pm i(R_{YZ} + R_{ZY})] \\
\hat{T}_{2,\pm 2} &= \mp\frac{1}{2}[R_{XX} - R_{YY} \pm i(R_{XY} + R_{YX})]
\end{aligned} \tag{1.44}$$

$\hat{T}_{0,0}$ is a scalar and is invariant under frame rotation. $\hat{T}_{1,m}$ and $\hat{T}_{2,m}$ are two vectors and their elements are just transform among themselves under rotation: a component of $\hat{T}_{1,m}$ or $\hat{T}_{2,m}$ transforms into a linear combination of the other components in $\hat{T}_{1,m}$ or in $\hat{T}_{2,m}$. The three-component $\hat{T}_{1,m}$ transform under rotation like an ordinary Cartesian vector, while the five-component $\hat{T}_{2,m}$ transform like second rank spherical tensors. When both the spin operators and interaction tensor elements are re-written in spherical tensor notation, the interaction Hamiltonian takes the form of a scalar contraction of irreducible tensors.

$$\hat{H} = \sum_{k=0}^2 \sum_{q=-k}^{+k} (-1)^q \Lambda_{k,-q} \hat{T}_{k,q} \tag{1.45}$$

This is important because the algebra of irreducible tensor operators has been extensively investigated and many useful theorems are available to facilitate deriving Hamiltonian matrix elements.

1.3.2 Spherical tensors for quadrupole coupling

Based on the discussion in section 1.3.1, the quadrupole coupling Hamiltonian can be written as

$$\begin{aligned}\hat{H}_Q &= \frac{eQ}{2I(2I-1)\hbar} \cdot \hat{I} \cdot V \cdot \hat{I} \\ &= \sum_{k=0}^2 \sum_{q=-k}^{+k} (-1)^q \Lambda_{k,-q}^Q \hat{T}_{k,q}^Q\end{aligned}\quad (1.46)$$

Since the electric field gradient (EFG) tensor, V , is traceless and symmetric, only its second rank components differ from zero^{1, 30}. Thus, the Hamiltonian of quadrupolar interaction is the sum of five-second rank components:

$$\hat{H}_Q = \sum_{q=-2}^{+2} (-1)^q \Lambda_{2,-q}^Q \hat{T}_{2,q}^Q \quad (1.47)$$

Where the spin spherical tensor operators $\hat{T}_{2,q}^Q$ are

$$\begin{aligned}\hat{T}_{2,0}^Q &= \sqrt{\frac{1}{6}} \cdot (3\hat{I}_Z^2 - \hat{I} \cdot \hat{I}) \\ \hat{T}_{2,\pm 1}^Q &= \mp (\hat{I}_\pm \hat{I}_Z + \hat{I}_Z \hat{I}_\pm) \\ \hat{T}_{2,\pm 2}^Q &= \frac{1}{2} \hat{I}_\pm^2\end{aligned}\quad (1.48)$$

and the EFG tensor components in the PAS are:

$$\begin{aligned}\Lambda_{2,0}^{PAS} &= \sqrt{6} \cdot \frac{e^2 q_{ZZ} Q}{4I(2I-1)} \\ \Lambda_{2,\pm 1}^{PAS} &= 0 \\ \Lambda_{2,\pm 2}^{PAS} &= \frac{e^2 q_{ZZ} Q}{4I(2I-1)} \cdot \eta_Q\end{aligned}\quad (1.49)$$

Here η_Q is defined in Eq. 1.25.

For the LAB frame Hamiltonian, the first order average interaction is

$$\begin{aligned}\hat{H}^{(0)} &= \frac{\omega_0}{2\pi} \sum_{q=-2}^{+2} (-1)^q \hat{T}_{2,q}^Q \Lambda_{2,-q}^Q \int_0^{2\pi/\omega_0} \exp(i\omega_0 t q) dt \\ &= \hat{T}_{2,0}^Q \Lambda_{2,0}^Q\end{aligned}\quad (1.50)$$

In many of the experiments to be described, it will be necessary to transform the relevant operators from the PAS to LAB coordinates in several steps (fig. 1.6); for example, from PAS to crystal fixed axes and then from crystal fixed axes to the LAB frame. The final spectrum can then be calculated by summing over orientations described explicitly by the latter transformation.

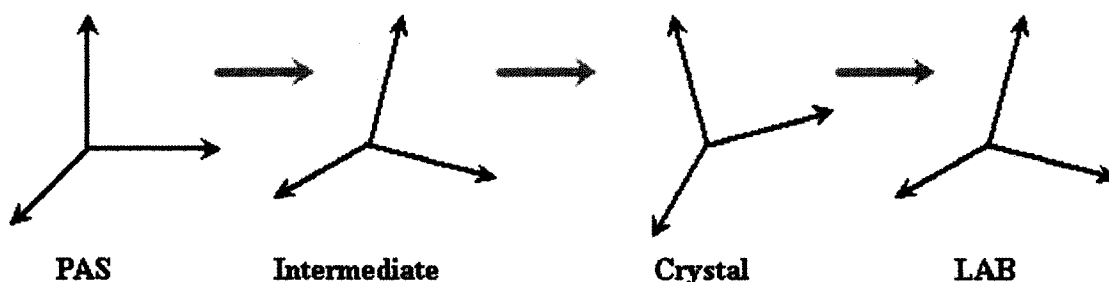


FIG. 1.6. Multiple-frame transformation

The rotation begins from PAS frame to the first of several intermediate frames chosen to model particular experimental situations, followed by a final rotation from crystal-fixed axes into the LAB frame. For non-rotating samples, the powder average is carried out over the last rotation (Crystal \rightarrow LAB).

If the interaction tensor is rotated from frame A to frame B, the relationship between the components of the tensor in the two frames is

$$\begin{aligned}\hat{\Lambda}^B &= \hat{\Lambda}^A \cdot D_{A \rightarrow B} \\ \Downarrow \\ \Lambda_{2,m}^B &= \sum_{n=-2}^{n=+2} \Lambda_{2,n}^A \cdot D_{n,m}^2(\alpha, \beta, \gamma)\end{aligned}\quad (1.51)$$

Here D is the second rank Wigner rotation matrix that rotates frame A into frame B via Euler angles (α, β, γ) . Thus, if the multiple-frame transformation from the PAS frame to

the LAB frame occurs through several rotations based on a series of Euler transformations, the relationship between spin interactions in the LAB and PAS frames is

$$\hat{\Lambda}^{LAB} = \hat{\Lambda}^{PAS} \cdot D_{PAS \rightarrow Int} \cdot D_{Int \rightarrow Cry} \cdot D_{Cry \rightarrow LAB} \quad (1.52)$$

For example, the first-order Hamiltonian for average quadrupole coupling interaction in the lab frame is

$$\begin{aligned} \hat{H}^{(0)} &= \hat{T}_{2,0}^Q \Lambda_{2,0}^Q \\ &= \hat{T}_{2,0}^Q \cdot \left[\hat{\Lambda}^{PAS} \cdot D_1(\Omega_1) \cdot D_2(\Omega_2) \cdots D(\Omega_N) \right]_{2,0} \end{aligned} \quad (1.53)$$

Where $\hat{\Lambda}^{PAS} \cdot D_1(\Omega_1) \cdot D_2(\Omega_2) \cdots D(\Omega_N)_{2,0}$ is the center element of $\hat{\Lambda}^{LAB}$.

The use of spherical tensors to describe the quadrupole Hamiltonian makes calculations that involve multiple-frame rotations much easier. Examples of this formalism will be presented in Chapter 3.

1.4 NMR spectrometer

For a typical solid state NMR spectrometer, the sample is contained in a cylindrical tube that holds 5-50 mg of polycrystalline powder, containing about 10^{21} spins. The individual nuclear magnetic moments are very small and the net magnetization comes from the tiny difference between equilibrium spin populations. The voltage induced in a coil around the sample is rarely larger than a few micro-volts^{12, 31}. NMR experiments therefore require extremely low noise amplifiers that must also recover quickly from overloads produced by the kilovolt pulses used to stimulate the spins.

In order to obtain useful NMR signals, a stable, perfectly uniform and homogeneous magnetic field is necessary. Furthermore, resolution improves with field strength because chemical shifts scale proportional to field strength while line widths typically remain field independent. In modern NMR spectrometers, the need for high fields is met by superconducting magnets.

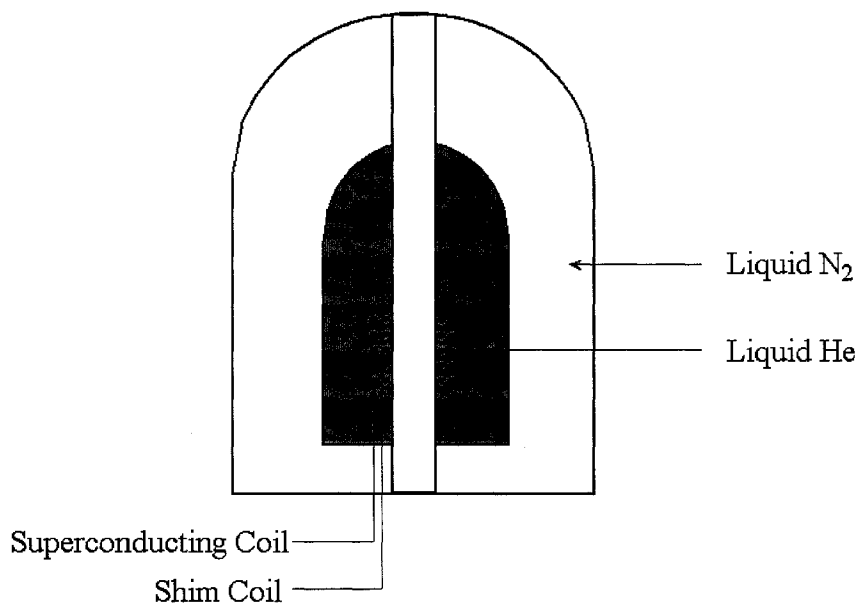


FIG 1.7 Schematic representation of the NMR magnet

The heart of the NMR magnet, a superconducting solenoid coil, is cooled to 4 K or below by immersion in a bath of liquid He. The inner, liquid helium is surrounded by a large reservoir of liquid N₂. The reservoirs are separated from each other by a vacuum to reduce thermal leakage. In addition to the superconducting coil, groups of superconducting shim coils and removable room temperature shim coils are used to reduce residual inhomogeneity of the magnetic field to less than 0.01 ppm over an active sample volume of about 1 cm³.

In order to excite the spins, radio frequency current pulses are applied to a solenoid wrapped around the sample and tuned to the desired carrier frequency. A single-channel instrument is shown schematically in fig. 1.8

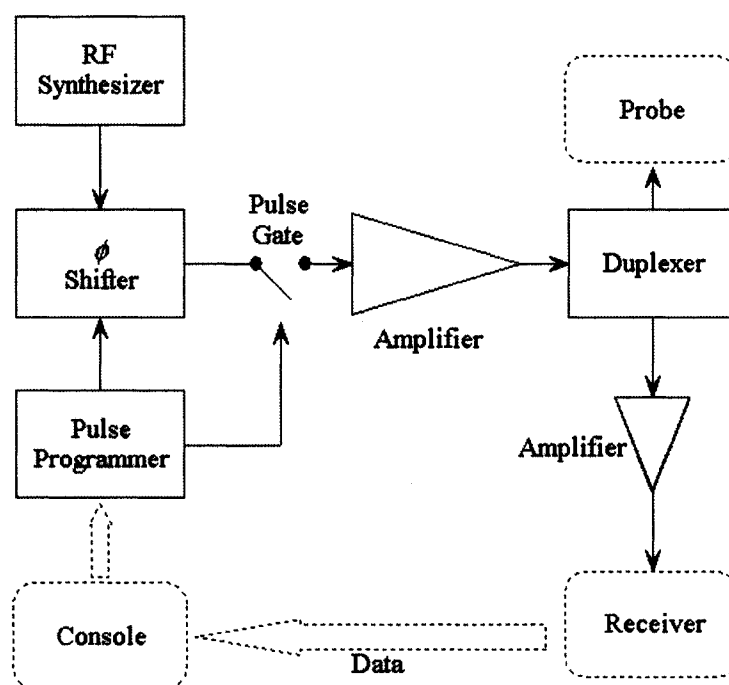


FIG 1.8. Transmitter section of NMR spectrometer

A typical pulse generator is shown here. In experiments, Bruker AVANCE® electronics are used to program pulse durations, amplitudes, separations, and phases. Phase coherence from one pulse to the next is maintained by gating a continuous voltage rather than switching an oscillator on and off. The duplexer serves dual roles, sending rf pulses into the probe and collecting subsequent NMR signals.

The radio frequency synthesizer produces a continuous oscillating signal, whose phase can be shifted while the frequency is digitally selectable to 0.1 Hz for frequencies between about 30 and 750 MHz. Filtered by the discontinuous pulse gate control, which can be programmed for different experiments, the continuous oscillating signal becomes a series of radio frequency pulses that are sent into the NMR probe by the duplexer. Not shown in this schematic diagram is the circuitry used to demodulate the detected signal prior to digitizing it and accumulating multiple scans for signal averaging.

The probe keeps the sample in the central, most uniform region of the magnetic field. In magic angle spinning experiments (see section 1.5.2), the probe is able to spin the rotor stably at close to supersonic speeds, by means of two high-pressure N₂-airflows. In addition, the sample temperature is controlled by a third airflow. Different types of probes are used for different purposes, but the basic design of each probe is similar.

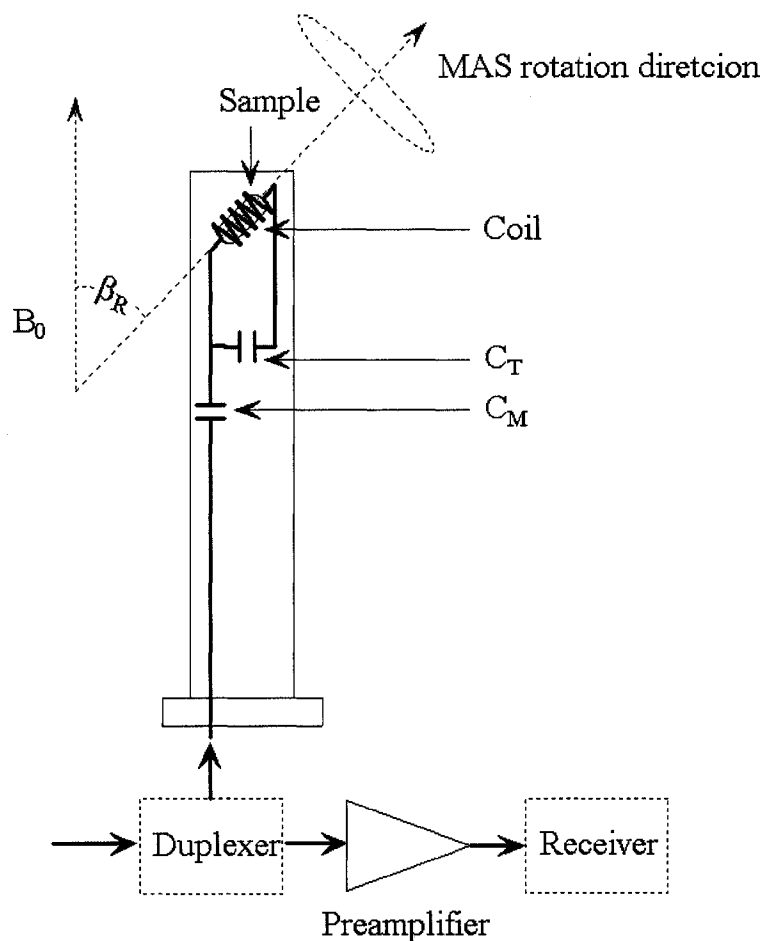


FIG 1.9. Schematic representation of the NMR MAS probe

There are two groups of capacitors and inductors, denoted here generically by C_M and C_T. C_M couples the external signals into the probe circuit with maximum efficiency and C_T is wired in parallel with the coil enclosing the sample. The resonant frequency of the probe is $\omega_{OSC} = (L \cdot C_T)^{-1/2}$. Solid samples are contained in a cylindrical tube that can be spun rapidly about its long axis.

There are two groups of capacitors and inductors, which serve to tune the coil to the desired Larmor frequency and match its resonant impedance to the output impedance of the transmitter amplifier (see fig. 1.9). It is necessary to adjust the values of matching and tuning capacitors whenever the sample is changed. Furthermore, the probe temperature also affects the electrical properties and minor tuning adjustments are necessary during variable temperature experiments that may last several hours.

The coil same employed to excite the nuclear spins is used to observe the signal (fig. 1.10). The NMR signal generated by the nuclear spins goes through the receiver circuit to the computer. Further analysis of the signal depends on the detection method and a typical procedure will be discussed in Ch. 2.^{13, 32, 33}

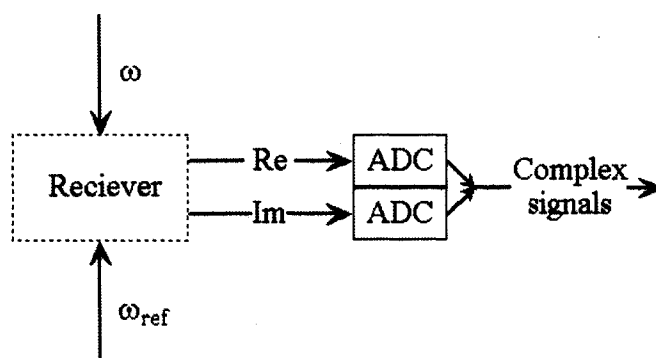


FIG 1.10. Schematic representation of NMR receiver

The incoming signal is divided into two equal parts, and demodulating each with respect to the CW carrier frequency at phase zero in channel A (termed “Re”) and a 90° d phase shifted carrier frequency in channel B (termed “Im”).

1.5 Essential techniques in deutron NMR

1.5.1 Quadrupole echo

The nature of solid state NMR powder patterns, in which the signals are distributed over a wide range of frequencies, necessitates the use of very short, high-power RF pulses. For example, in deutron quadrupole echo experiments, the radio frequency pulses last only 1~10 μ s. Thus the probe ring-down and electronic dead-time problems are severe and necessitate the use of echo techniques, rather than simple pulse-acquire experiments^{1,34}. In quadrupole echo experiments, the magnetization refocuses at a time after the pulse ring-down and undistorted signal beginning at the peak of the echo is recorded^{7,8}.

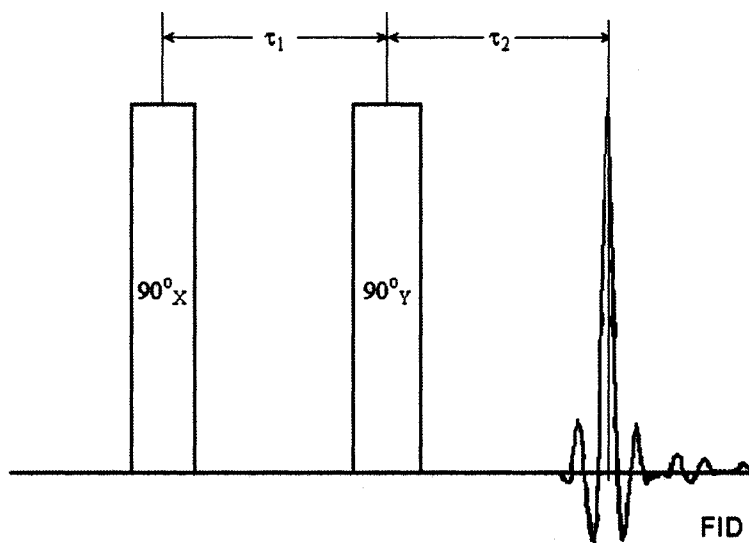


FIG. 1.11 Quadrupole echo pulse sequence

There are two pulses with a 90° phase shift between them. The echo appears after the refocussing period τ_2 , whose value is close to the defocusing period τ_1 .

The quadrupole echo pulse sequence consists of two 90° pulses with a 90° phase shift, as shown in Fig. 1.11. The pulses are separated by interval τ_1 and the echo appears at time τ_2 , whose value is close to τ_1 .

The density matrix after an ideal θ° -pulse with X -phase is

$$\rho(0^+) = \exp(-i\theta \cdot I_X) I_Z \exp(i\theta \cdot I_X) = I_Z \cos\theta - I_Y \sin\theta \quad (1.54)$$

Thus, after the first pulse, the magnetization has been rotated to the $-Y$ direction. If no relaxation occurs during τ_1 , the density matrix evolves under the quadrupolar Hamiltonian in the lab frame with precession frequency ω_Q . Prior to the second pulse, the density matrix is

$$\rho(\tau_1^-) = -\cos\omega_Q\tau_1 \cdot I_Y + i\sin\omega_Q\tau_1 \cdot I_X \quad (1.55)$$

After the second pulse with a 90° phase shift respect to the first pulse, the rf field in the rotating frame is aligned along Y , and the density matrix becomes

$$\rho(\tau_1^+) = -\cos\omega_Q\tau_1 \cdot I_Y - i\sin\omega_Q\tau_1 \cdot I_X \quad (1.56)$$

After the refocusing period τ_2 , the density matrix is

$$\begin{aligned} \rho(\tau_1 + \tau_2) = & -\cos\omega_Q\tau_1 \cdot [\cos\omega_Q\tau_2 \cdot I_Y - i\sin\omega_Q\tau_2 \cdot I_X] \\ & -i\sin\omega_Q\tau_1 \cdot [\cos\omega_Q\tau_2 \cdot I_X - i\sin\omega_Q\tau_2 \cdot I_Y] \end{aligned} \quad (1.57)$$

if τ_1 and τ_2 are equal, the density matrix is the same for all values of ω_Q , and now the magnetization for every powder increment has the same phase as it had at $t = 0$, just after

the first pulse. A more realistic treatment that accounts for precession during pulses of finite width t_W , shows that $\tau_2 = \tau_1 + t_W/2$ is a more exact condition for echo formation^{8,30}:

$$\rho(2\tau) = \rho(0^+) = -I_y \quad (1.58)$$

Now, Free Induction Decays signals (FID) can be acquired without distortion simply by making τ long enough. In practice, it is useful to ensure that a point is digitized exactly at the top of the echo. This can be accomplished by starting acquisition well before the echo maximum and discarding the initial several points.

When the chemical shifts are neglected, deuteron powder patterns are symmetric about their isotropic chemical shifts since the $+1 \Leftrightarrow 0$ and $-1 \Leftrightarrow 0$ spin transitions are mirror images. If there are observable chemical shifts, then one or the other powder pattern will show phase distortions. They can be removed to some extent by additional pulses, designed to refocus the first order interactions without compromising the quadrupole echo.^{35,36} The intensity profile of quadrupole echo spectra can be analyzed to determine the quadrupole coupling constant, which provides information about the electronic and molecular structure. Moreover, by changing the pulse interval τ_1 , quadrupole echo experiments can also be used to measure the transverse relaxation time. Dynamic processes on time scales that roughly match the pulse spacing (typically 10-200 μ s) produce large effects because they interfere with echo formation. The quadrupole echo pulse pair is also the basic detection sequence in a variety of more complex deuteron NMR experiments, such as inversion recovery for measuring orientation-dependent spin lattice relaxation, and indirect determination of double quantum precession frequencies and line shapes³⁷⁻³⁹.

1.5.2 On/Off magic angle spinning

Quadrupole echo experiments are widely employed to generate solid state deuteron spectra, but the broad, static powder patterns have poor resolution and relatively lower sensitivity than the magic angle spinning (MAS)^{13, 16}. In magic angle spinning, the powder sample is rotated rapidly and coherently in the cylindrical rotor around an axis that orientates at the magic angle ($\beta_R = 54.74^\circ$) with respect to the applied magnetic field, as shown in fig.1.12.

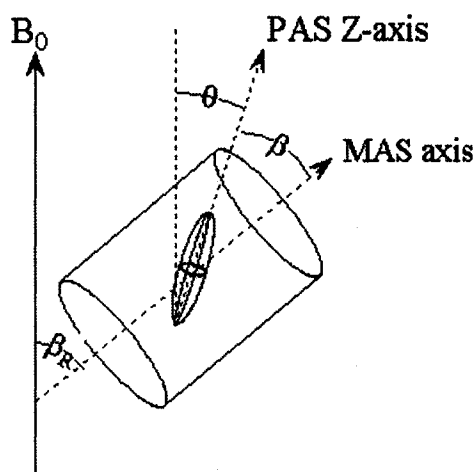


FIG. 1.12 The magic angle spinning experiment

The sample is spun rapidly about a spinning axis oriented at the magic angle ($\beta_R = 54.74^\circ$) with respect to the applied magnetic field. MAS removes the effects of chemical shift anisotropy and heteronuclear dipolar coupling, and concentrates the quadrupole powder pattern into a series of narrow "spinning side bands" at multiples of the spin rate.

At physically attainable spinning speeds, the MAS spectrum consists of a center band and a manifold of narrow sidebands located at integer multiples of the spinning frequency. The resolution and sensitivity are significantly improved compared to the static quadrupole echo spectrum, for which the same integrated intensity is distributed continuously over a wide frequency range. In the (usually unattainable) limit of spin rate much larger than the quadrupole coupling constant, the sidebands would have zero

intensity and the overall gain in signal would be roughly equal to the ratio of static quadrupole broadening to residual center band line width: easily a factor of 100 or more. In practice, intensity gains of 20-30 are not uncommon. Intensity profiles of the MAS sidebands can be analyzed in much the same manner as quadrupole echo line shapes to determine the dynamical properties although the calculations are more difficult and time consuming. Simultaneously, slower motional processes broaden individual spinning sidebands. Detailed analysis and discussions of On/Off MAS will be presented in Chapter 2 and 3.

In ordinary MAS, the angle is adjusted exactly to the magic angle and all interactions that are described by second-rank Cartesian tensors are averaged as described above. The central and side bands in MAS spectra consist of single narrow peaks, whose intensities vary in a predictable manner with the side band order, the strength of the spin interactions, and the rates of molecular motion. In Off-angle Magic Angle Spinning (OMAS), the angle is purposely adjusted away from the exact magic angle by a small amount (0.01° - 0.2°). This has the effect of adding an experimentally controllable amount of first order quadrupole coupling back into the spin Hamiltonian. Consequently, the spinning sidebands split into small powder patterns, whose characteristic line shapes and intensities are determined by the strength of the reintroduced spin interaction, and by molecular motion on a time scale fixed by the reduced quadrupole coupling. Thus, OMAS sideband line shapes show higher sensitivity to slow dynamic processes than ordinary MAS sidebands. Deuteron OMAS is a useful technique in molecular motion studies.

Chapter 2

On/Off Magic Angle Spinning

2.1 Theory

2.1.1 Powder pattern in solid state NMR

Calculations of powder patterns due to any single-particle second rank tensor interaction, such as chemical shift anisotropy or quadrupolar coupling, require very similar sets of coordinate transformations. For example, the chemical shift tensor observed in the lab frame is given by:

$$\sigma^{LAB}(\alpha \ \beta \ \gamma) = R^{-1}(\alpha \ \beta \ \gamma) \cdot \sigma^{cs} \cdot R(\alpha \ \beta \ \gamma) \quad (2.1)$$

Here $R(\alpha \ \beta \ \gamma)$ is the rotation matrix that rotates the chemical shift tensor from the molecular frame into the lab frame via Euler angles $(\alpha \ \beta \ \gamma)$.

$$\begin{aligned} R(\alpha \ \beta \ \gamma) &= \begin{pmatrix} \cos\alpha & -\sin\alpha & 0 \\ \sin\alpha & \cos\alpha & 0 \\ 0 & 0 & 1 \end{pmatrix} \cdot \begin{pmatrix} \cos\beta & 0 & \sin\beta \\ 0 & 1 & 0 \\ -\sin\beta & 0 & \cos\beta \end{pmatrix} \cdot \begin{pmatrix} \cos\gamma & -\sin\gamma & 0 \\ \sin\gamma & \cos\gamma & 0 \\ 0 & 0 & 1 \end{pmatrix} \\ &= \begin{pmatrix} \cos\alpha \cos\beta \cos\gamma - \sin\alpha \sin\gamma & -\cos\alpha \cos\beta \sin\gamma - \sin\alpha \cos\gamma & \cos\alpha \sin\beta \\ \sin\alpha \cos\beta \cos\gamma + \cos\alpha \sin\gamma & -\sin\alpha \cos\beta \sin\gamma + \cos\alpha \cos\gamma & \sin\alpha \sin\beta \\ -\sin\beta \cos\gamma & \sin\beta \sin\gamma & \cos\beta \end{pmatrix} \end{aligned} \quad (2.2)$$

And generally, σ^{CS} is

$$\sigma^{CS} = \begin{pmatrix} \sigma_{XX} & \sigma_{XY} & \sigma_{XZ} \\ \sigma_{YX} & \sigma_{YY} & \sigma_{YZ} \\ \sigma_{ZX} & \sigma_{ZY} & \sigma_{ZZ} \end{pmatrix} \quad (2.3)$$

In an isotropic solution, motional averaging of the chemical shift tensor is equivalent to averaging over all possible molecular orientations with the probability $P = \sin(\beta)$, which accounts for equal numbers of molecules per unit solid angle⁹. The average over all possible orientations in isotropic solution is thus

$$\begin{aligned} \overline{\sigma^{LAB}} &= \frac{1}{8\pi^2} \int_0^{2\pi} d\alpha \cdot \int_0^\pi \sin\beta \cdot d\beta \cdot \int_0^{2\pi} d\gamma \cdot \sigma^{LAB} \cdot P(\alpha \ \beta \ \gamma) \\ &= 1 \cdot \begin{pmatrix} 0 & 0 & 0 \\ 0 & 0 & 0 \\ 0 & 0 & \sigma_{ISO} \end{pmatrix} \end{aligned} \quad (2.4)$$

After explicit integration, the only non-zero element of the averaged chemical shift tensor in the LAB frame is the ISO component:

$$\sigma_{ISO} = \left(\overline{\sigma^{LAB}} \right)_{ZZ} = \frac{1}{3} \left(\sigma^{PAS}_{XX} + \sigma^{PAS}_{YY} + \sigma^{PAS}_{ZZ} \right) \quad (2.5)$$

This is expected: the trace of a tensor is invariant to the rotation. When this analysis is applied to the quadrupole interaction, the result is precisely zero since that is the trace of the EFG tensor. In isotropic solution, the chemical shift interaction gives a single, extremely sharp resonance, whose frequency measures the trace of the shielding tensor. All information about chemical shift anisotropy is lost, so that many fine details of the chemical environment of the nucleus are veiled⁴⁰.

In contrast with liquid samples, a solid powder sample consists of numerous small crystallites with spin interactions that are defined by their fixed, random orientations with

respect to the static magnetic field. The dominant nuclear spin interactions are *not* averaged to zero because large amplitude rotational motion, if present at all, is generally not isotropic. Thus, crystallites with different orientations $\Omega(\alpha \beta \gamma)$ give rise to different frequencies in the spectrum. The superposition of these peaks, once again weighted by $\sin(\beta)$, produces the characteristic "powder pattern" line shape^{13, 41, 42}. For example, a ^{207}Pb spectrum of solid lead nitrate, taken at 17.6T, is shown in figure 2.1.

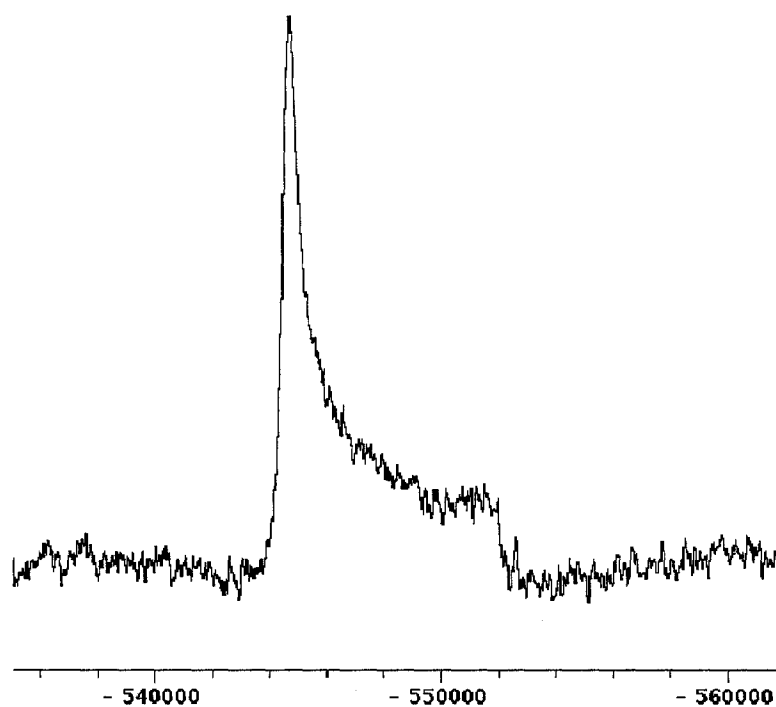


FIG. 2.1. Chemical shift powder pattern of $\text{Pb}(\text{NO}_3)_2$

The experiment consists of 128 scans after $4 \mu\text{s}$ 90° pulses, carried out at 320K in 17.6 T magnetic field. A 4mm sample rotor was used. The spectrum shows a chemical shift powder pattern in the $-540 \text{ kHz} \sim -560 \text{ kHz}$ frequency window relative to Pb's Larmor frequency, slightly distorted by a pulse ring down signal since echo detection was not used.

If the random powder average angles are (α, β, θ) , the contribution to NMR spectrum by chemical shift anisotropy is:

$$\begin{aligned}
\omega_{CS} &= \gamma \cdot \hat{I}_Z \sigma_{ZZ}^{LAB} B_0 \\
&= -\omega_0 \sigma_{ZZ}^{LAB} \\
&= -\omega_0 \sigma_{ISO} - \frac{1}{2} \omega_0 \sigma_{CSA} [3 \cos^2 \beta - 1 + \eta_{CS} \sin^2 \beta \cdot \cos 2\alpha]
\end{aligned} \tag{2.6}$$

Generally, chemical shift powder patterns show three singularities that occur in the spectrum corresponding to specific orientations:

$$(\alpha = 0, \beta = 0) \quad \omega_{CS} = -\omega_0 \cdot (\sigma_{ISO} + \sigma_{CSA}) \tag{2.7.a}$$

$$(\alpha = 0, \beta = 90) \quad \omega_{CS} = -\omega_0 \cdot \left[\sigma_{ISO} - \frac{1}{2} \sigma_{CSA} \cdot (1 - \eta_{CS}) \right] \tag{2.7.b}$$

$$(\alpha = 90, \beta = 90) \quad \omega_{CS} = -\omega_0 \cdot \left[\sigma_{ISO} - \frac{1}{2} \sigma_{CSA} \cdot (1 + \eta_{CS}) \right] \tag{2.7.c}$$

and if η_{CS} is zero, only two singularities are evident as fig. 2.1 shows. Chemical shift powder patterns of simple molecules can readily be analyzed to obtain the principal components of the chemical shift tensors. However, this type of simulation becomes unreliable when the spectrum consists of several of overlapping powder patterns. In addition, the signal/noise ratio of the powder pattern is relatively low because the spectral intensity spreads over a wide frequency range.

It was realized long ago^{43,44} that rotating the sample tends to average the effects of local fields perpendicular to the rotation axis. When this idea is applied to second rank tensor interactions, which have the symmetry of second rank rather than first rank spherical harmonics, it can be shown that rotating the sample about an axis inclined at the magic angle ($\beta_R = 54.74^\circ$) with respect to the applied field will achieve the same effect as rapid isotropic tumbling. This technique, Magic angle spinning (MAS), has been widely used in solid state NMR because it provides a convenient means to obtain a high-resolution spectrum of an arbitrary powder sample. Specifically, the average of the

orientation dependence of the secular part of all first order second rank tensor spin interactions can be shown to be of the form:

$$\langle 3 \cos^2 \beta - 1 \rangle = \frac{1}{2} (3 \cos^2 \beta_R - 1) \cdot \langle 3 \cos^2 \beta' - 1 \rangle \quad (2.8)$$

where β_R is the angle between the rotor axis and the static field, and β' is the angle between the rotor axis and a typical crystallite as shown in fig 2.2. If β_R is set to $\cos^{-1}(\sqrt{1/3})=54.74^\circ$, it is clear that $\langle 3 \cos^2 \beta - 1 \rangle$ is zero. Thus, if the spinning rate is fast enough, the interaction averages to zero. When the spinning rate is comparable to the width of the static powder pattern (5~30 kHz), the time dependent nonsecular parts of the Hamiltonian produce modulation of the observed free induction decay signal at multiples of the spinning frequency^{13, 14, 45}.

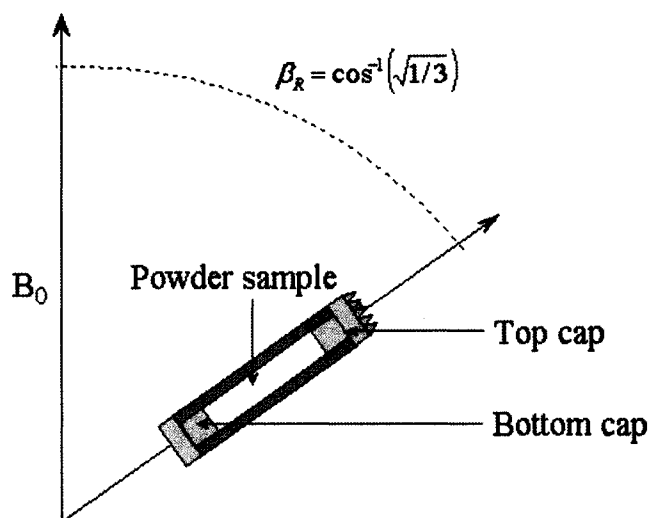


FIG. 2.2 The MAS rotor

Two high pressure N_2 -flows are used to spin the rotor. The drive gas acts on the top cap, while the bearing gas serves to keep the rotor from crashing into the NMR receiver coil. MAS rotors used in this thesis are made of zirconia (ZrO_2), precision machined to very close tolerance (better than 0.001"). The maximum rotation speed depends on the size of the rotor. A 2.5mm rotor can be spun as fast as 35 kHz, but centrifugal forces limit 4mm rotors to spin no faster than 12 kHz.

In MAS, the static spectrum is replaced by a center band flanked by a manifold of spinning side bands. Compared to the static spectrum, where NMR signal is continuously distributed over the whole frequency range, the MAS spectrum has a higher signal/noise ratio because the same integrated intensity is now concentrated in a small number of narrow peaks, whose widths are between 50~2000 Hz. In low magnetic fields (2 ~5 T), where the experimentally achievable spinning speed can far exceed the breadth of the static chemical shift anisotropy powder pattern (3~20 kHz) and completely average the chemical shift anisotropy, the MAS spectrum contains only the sharp center band, whose offset frequency measures the trace of the shielding tensor⁴⁵. This may not be exactly the same as the value found from a liquid-state spectrum because of differences in molecular conformation, bulk magnetic susceptibility, and solvent effects. In practice, a slow spinning speed that is comparable to the width of the static powder pattern is often used so that the MAS spectrum contains at least a few sidebands as well as the center band. It is then possible to recover the chemical shift anisotropy parameters from the intensities of the side bands^{45,46}. MAS is also used to suppress broadening due to heteronuclear and homonuclear dipolar coupling. However, removal of proton dipolar coupling simply by magic angle spinning is typically not feasible because the required spinning speed is too fast (> 50 kHz) due to the strong coupling interaction of proton. Fortunately, the elaborate and elegant pulse methods⁴⁷⁻⁴⁹ used for this purpose are not needed in deuterium NMR studies presented in this thesis, because most of the protons were replaced by deuterons.

2.1.2 Semi-classical calculation of MAS spectra

As described in former sections, sidebands appear in the spectrum at integer multiples of the spinning speed, ν_R . Generally, the appearance of sidebands in a complex spectrum leads to problems assigning the transitions, and may degrade the resolution and sensitivity. Some multiple pulse experiments, such as chemical shift scaling, can reduce the effective size of chemical shift anisotropy and thereby reduce MAS sidebands. These techniques, such as 2D-PASS⁵⁰, are designed to eliminate sidebands altogether at the expense of introducing line shape distortions due to pulse artifacts. These techniques are not very effective for deuteron quadrupole powder patterns, since they typically require application of several pulses during each rotor period and for high speed MAS ($\nu_R > 20$ kHz), the rotor period may not be long enough.

In most cases, analysis of chemical shift anisotropy or quadrupole interaction is an important aim of NMR experiments, and the rotational sideband intensities provide the necessary information to recover the spin interaction parameters. Furthermore, as will be shown in later sections, the width of individual side bands and the envelope of sideband intensities change with temperature, thus providing a remarkably wide kinetic window for motion rates measurement of molecular motion. So the calculation of sidebands intensity is important for these reasons.

The classical approach can be used to calculate sideband intensities in absence of effects of molecular motion. When the sample is spinning at angle β_R with speed ω_R , the time-dependent precession frequency for a crystallite defined by a fixed orientation $\Omega(\alpha, \beta, \gamma)$, with respect to a rotor-fixed frame, is given by

$$\omega(\Omega; t) = -\omega_0 b_0^R(t) \sigma^R b_0^R(t) \quad (2.9)$$

Where ω_0 is Larmor frequency and $b_0^R(t)$ is the orientation of B_0 in the rotor frame and σ^R is the interaction tensor in the rotor frame.

$$b_0^R = \begin{pmatrix} \sin \beta_R \cos \omega_R t & \sin \beta_R \sin \omega_R t & \cos \beta_R \end{pmatrix} \quad (2.10)$$

$$\begin{aligned} \sigma^R &= R^{-1} \cdot \sigma^{PAS} \cdot R \\ &= R^{-1} \begin{pmatrix} \alpha & \beta & \gamma \end{pmatrix} \cdot \begin{pmatrix} \sigma_{xx}^{PAS} & 0 & 0 \\ 0 & \sigma_{yy}^{PAS} & 0 \\ 0 & 0 & \sigma_{zz}^{PAS} \end{pmatrix} \cdot R \begin{pmatrix} \alpha & \beta & \gamma \end{pmatrix} \end{aligned} \quad (2.11)$$

Here $R(\alpha \ \beta \ \gamma)$ is the rotation matrix that rotates the interaction tensor σ^{PAS} from PAS into the rotor frame. When $\beta_R = 54.74^\circ$, the contribution frequency $\omega(\Omega; t)$ becomes:

$$\begin{aligned} \omega(\alpha \ \beta \ \gamma; \ t) &= -\omega_0 \left\{ \sigma_{iso} + [A_1 \cos(\omega_R t + \gamma) + B_1 \sin(\omega_R t + \gamma)] \right. \\ &\quad \left. + [A_2 \cos(2\omega_R t + 2\gamma) + B_2 (2\omega_R t + 2\gamma)] \right\} \end{aligned} \quad (2.12)$$

Where:

$$A_1 = \frac{2}{3} \sqrt{2} \cdot \sin \beta \cdot \cos \beta \cdot [\cos^2(\sigma_{xx}^{PAS} - \sigma_{zz}^{PAS}) + \sin^2(\sigma_{yy}^{PAS} - \sigma_{zz}^{PAS})] \quad (2.13.a)$$

$$B_1 = \frac{2}{3} \sqrt{2} \cdot \sin \alpha \cdot \cos \alpha \cdot \sin \beta \cdot (\sigma_{xx}^{PAS} - \sigma_{yy}^{PAS}) \quad (2.13.b)$$

$$\begin{aligned} A_2 &= \frac{1}{3} \left[(\cos^2 \beta \cdot \cos^2 \alpha - \sin^2 \alpha) \cdot (\sigma_{xx}^{PAS} - \sigma_{zz}^{PAS}) \right. \\ &\quad \left. + (\cos^2 \beta \cdot \sin^2 \alpha - \cos^2 \alpha) \cdot (\sigma_{yy}^{PAS} - \sigma_{zz}^{PAS}) \right] \end{aligned} \quad (2.14.a)$$

$$B_2 = -\frac{2}{3} \cdot \sin \alpha \cdot \cos \alpha \cdot \cos \beta \cdot (\sigma_{xx}^{PAS} - \sigma_{yy}^{PAS}) \quad (2.14.b)$$

Now, the free induction decay signal, $s(t)$, of the observed magnetization is given by integral over all possible powder orientations and all possible rotor phase angle γ

$$s(t) = \frac{1}{8\pi^2} \int_0^{2\pi} \int_0^{2\pi} \int_0^{2\pi} \exp \left[i \cdot \int_0^t \omega(\alpha \ \beta \ \gamma; \ t') dt' \right] \cdot \sin \beta \cdot d\alpha \ d\beta \ d\gamma \quad (2.15)$$

Once the decay signal is calculated numerically, we can obtain the frequency spectrum by Fourier transformation. In addition, if the property of the Bessel functions of the first kind is employed:

$$\exp(iz \sin \phi) = \sum_{k=-\infty}^{+\infty} \exp(ik\phi) \cdot J_k(z) \quad (2.16)$$

Then Eq. 2.17 gives the FID.

$$\begin{aligned} & \exp\left(i \cdot \int_0^t \omega(\alpha \ \beta \ \gamma; \ t') dt'\right) \\ &= \sum_{j=-\infty}^{+\infty} J_j(\bar{A}_2) \sum_{j'=-\infty}^{+\infty} J_{j'}(\bar{A}_2) \sum_{k=-\infty}^{+\infty} J_k(\bar{B}_2) \sum_{k'=-\infty}^{+\infty} J_{k'}(\bar{B}_2) \sum_{l=-\infty}^{+\infty} J_l(\bar{A}_1) \sum_{l'=-\infty}^{+\infty} J_{l'}(\bar{A}_1) \sum_{m=-\infty}^{+\infty} J_m(\bar{B}_1) \sum_{m'=-\infty}^{+\infty} J_{m'}(\bar{B}_1) \\ & \times \exp\left\{i(-\omega_0 \sigma_{ISO} t + \omega_R t \cdot (2j + 2k + l + m))\right\} \\ & \times \exp\left\{\gamma \cdot [2(j - j') + 2(k - k') + (l - l') + (m - m')]\right\} \\ & \times \exp\left(-\frac{\pi}{2} [(k - k') + (m - m')]\right) \end{aligned} \quad (2.17)$$

where

$$\begin{aligned} \bar{A}_1 &= -\frac{2\sqrt{2}}{3} \frac{\omega_0}{\omega_R} \cdot A_1 \\ \bar{B}_1 &= -\frac{2\sqrt{2}}{3} \frac{\omega_0}{\omega_R} \cdot B_1 \\ \bar{A}_2 &= -\frac{2}{3} \frac{\omega_0}{\omega_R} \cdot A_2 \\ \bar{B}_2 &= -\frac{2\sqrt{2}}{3} \frac{\omega_0}{\omega_R} \cdot B_2 \end{aligned} \quad (2.18)$$

Thus, the Fourier transform of the FID consists of a central peak at $-\omega_0 \sigma_{ISO}$ and side bands at the integer multiple of ω_R . The contribution from site (α, β, γ) to MAS side band at a frequency $f = \omega_0 \sigma_{ISO} + n\omega_R$ can be calculated by Eq. 2.17 when $n = 2j + 2k + l + m$.

In addition to the static powder average over angles α and β , an extra angular average over the initial rotor phase angle γ is necessary since this appears in Eq. 2.17.⁴⁵
⁵¹ ⁵². Other interactions, such as heteronuclear dipolar and quadrupolar coupling, can be calculated in the same way as chemical shifts by substituting the relevant interaction

tensors. The information of chemical shift anisotropy and asymmetry, the heteronuclear dipolar and the quadrupolar coupling can be obtained by comparing experiments and simulations. However, this analytical calculation is unable to simulate a dynamical system, where nuclear spins can change their orientation angles ($\alpha \beta \gamma$). In practice, two numerical methods, direct integration and Floquet methods, can be used to simulate dynamical MAS spectra. A detailed discussion of these two methods can be found in Chapter 3.

2.1.3 Deuteron MAS in molecular motion studies

In organic molecules, the dominant (quadrupole) interaction is ideally suited for following rotational dynamics over an extremely wide kinetic window¹⁶. Interesting molecular segments can be easily labeled and isolated if necessary from dipolar interactions with nearby protons by heteronuclear decoupling. Deuteron spectra are relative uncomplicated, consisting of simple powder patterns for each crystallographically distinguishable spin. Furthermore, the approximate uniaxiality of the electron density around deuterons in organic molecules leads to negligible asymmetry parameter η_Q and to near coincidence of the electric field tensor principal Z-axis with C-D bond axes ($<3^\circ$). This provides a powerful tool to track rotational dynamics of individual C-D bonds in flexible molecules. Deuteron NMR spectroscopy has been used to investigate dynamics in a diverse range of materials: single crystals⁵³, polycrystalline powders⁵⁴, amorphous materials^{55,56}, surface immobilized systems⁵⁷, liquid crystals⁵⁸, and lipid membranes⁵⁹.

Different deuteron experiments are used for various purposes. For example, two-dimensional experiments can be used to separate quadrupolar and paramagnetic shift interactions in paramagnetic molecules. In molecular motion studies, quadrupole echoes and 2-D exchange are the most widely used techniques at present. However, the low resolution of these static methods limits their applications to simple systems or those that can be obtained by selective labeling. In comparison, deuteron MAS (especially in magnetic fields above 10 T) yields much better resolution and greatly improved signal/noise ratio^{17, 60, 61}. Typical deuteron quadrupole coupling constants are between 100kHz and 200kHz, which is much larger than the available sample rotation speed (35 kHz with our equipment). Therefore, a series of sidebands always shows in deuteron spectra, whose widths and intensity profiles are affected by molecular structure and dynamics and contain the information about molecular motions.

Simulation of the static deuteron line shape is straightforward and efficient, but simulation of the MAS line shape involves an inherently time dependent Hamiltonian and requires longer computation time^{49, 52, 60, 62}. Two methods can deal with the important complication that the Hamiltonian, $H(t)$, does not commute with itself at different times: direct integration of the relevant equations⁴², and Floquet theory^{60, 63, 64}. Direct integration is similar to the static simulation, except that the evolution is computed over a large number of tiny time steps during which the Hamiltonian can be treated as effectively time independent. The Floquet method takes the advantage of the periodic nature of the time dependent Hamiltonian and replaces $H(t)$ with an effective, time independent Hamiltonian defined with respect to an infinite basis set of periodically time

dependent states. A detailed discussion of simulation via these two methods can be found in Chapter 3.

2.2 Deuteron On/Off MAS experiment

2.2.1 Rotational echoes

In NMR experiments, initial spin states are prepared by one or more short pulses, and the evolution of spin magnetization is recorded as an observable free induction decay signal (FID) after the final detecting pulse. For non-spinning powder samples, the Hamiltonian is independent of time and the FID signal is simply the sum of different signals from all possible crystallite orientations. In MAS, because the applied magnetic field periodically changes its direction with respect to the principal axis frame that is fixed with respect to the rotor, the Hamiltonian for a single crystallite changes with time during FID period. For a component of magnetization arising from a particular orientation $\Omega(\alpha \beta \gamma)$, the moving path of the projection of its orientation for different β is shown in fig. 2.3.a. From another point of view, since there are so many nuclear spins ($>10^{12}$ - 10^{16}) in a powder sample, there are always a macroscopic number of spins whose interaction tensor orientations share the same moving path as the interaction tensor with the orientation $\Omega(\alpha \beta \gamma)$ with different initial phase angles as shown in fig. 2.3.b. In effect, each possible path, which is defined by a fixed value of β , gives a FID signal that comes from all the spins with that value of β but with different initial phase angles with respect to the rotor.

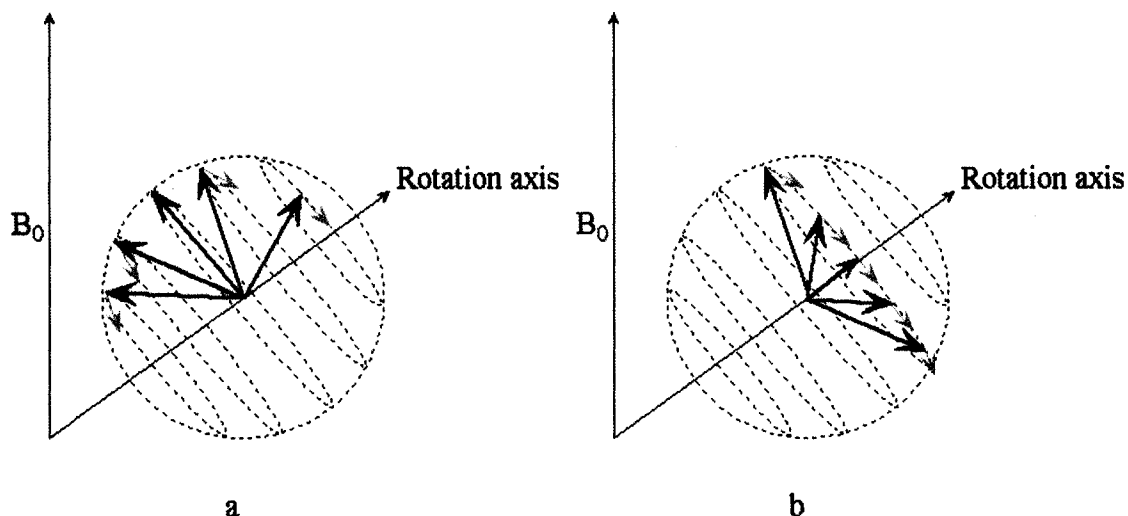


FIG. 2.3. The moving path of nuclear spins in MAS experiments

(a) Spin tensors whose PAS orient with respect to the rotation axis at different Euler angles β follow different rotation paths. (b) Spin tensors whose PAS orient with the same β angle share the same path, but their phase angles are different. The sub-ensemble spins that share the same β angle refocus to their initial states once per rotor period, leading to formation of a train of rotational echoes.

From this viewpoint, the spin sub-ensemble that corresponds to a given orientation-moving path acts like a single spin in static NMR experiments. The observable FID is the result of summation over all possible orientation-moving paths. At the beginning of each rotor period, the magnetizations from all spin sub-ensembles have different initial phase angles, and they dephase at different rates. However, at the end of each rotor period each ensemble is restored to its initial status. Thus, the overall FID consists of a sequence of repeated rotational echoes, as shown in Figure 2.4.

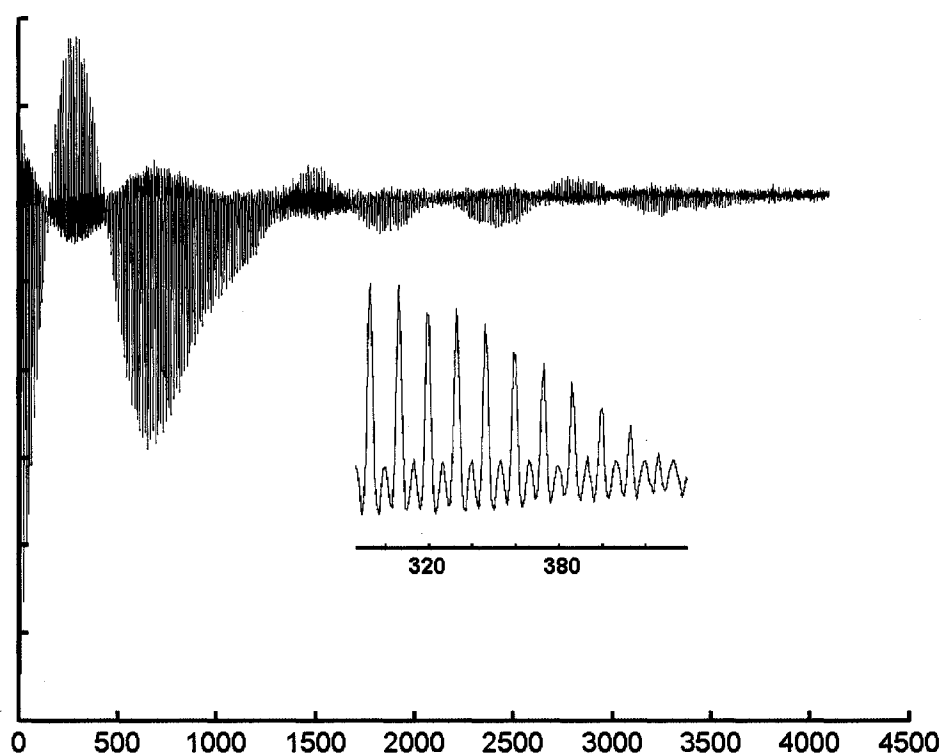


FIG. 2.4 Experimental MAS FID

The real (in phase) component of a FID signal from phenylalanine- d_8 in 17.6T magnetic field is shown here. The spin rate is 20 kHz and the temperature is 303 K. The signal consists of hundreds of rotational echoes as the inset shows. The time interval between two successive echoes is the rotor period, $1/20 \text{ kHz} = 50 \mu\text{s}$. The dwell time is $2.5 \mu\text{s}$ and 20 data points are recorded during each rotor period.

2.2.2 Angle adjustment

As discussed in section 2.1, the average of the orientation dependence of the nuclear spin interaction can be written as Eq. 2.8. In On-MAS experiments, the magic angle β_R is adjusted as close to $\cos^{-1}(\sqrt{1/3}) \approx 54.74^\circ$ as possible in order to obtain the best suppression of anisotropic interactions. In Off-MAS experiments, although a tiny offset angle ($0.01^\circ \sim 0.2^\circ$) is introduced on purpose, it is still necessary to know the exact MAS condition for reference purposes.

An ideal sample for adjustment of the rotor angle should not require any form of decoupling to achieve a sharp spectrum. The most common standard sample is KBr^{13,31,46}, looking at the ⁷⁹Br ($I = 3/2$) signal. Since the signal from ⁷⁹Br is very strong and the spin-lattice relaxation time is short, magic angle adjustment experiments can be finished in a short time period. The satellite transitions for this $I = 3/2$ nucleus split into side bands, whose intensities and widths are used to determine the optimum angle. Generally, a 2.5mm rotor filled with 10 mg fine-grounded KBr powder can be spun at 20~35 kHz. Only 10~20 scans have to be accumulated to get a FID signal that is sensitive enough for the angle adjustment. Other parameters for the acquisition are shown in table 2.1:

Table 2.1. Console setup for angle adjustment using KBr

Parameter	Name of Variable*	Value
Pulse Program	PULPROG	ZG (single pulse)
Spectra window width	SWH	125 kHz
The size of FID	TD	2048
Scan delay	D1	30 ms
Pulse length	P1	2 μ s
Pulse power	PL1	3 db

* These names are used in Bruker XWINNMR® and TOPSPIN® software.

After the spin rate has been stabilized for several minutes, the angle setting procedure can be performed either on the FID itself or on the Fourier transformed spectrum. When the FID signal is used, the real part FID is observed directly in the acquire (ACQU in XWINNMR®) window. If the angle is close to the magic angle, rotational echoes will appear on top of an exponential decay that arises from the center band. When the rotor angle is adjusted closer to the magic angle, via a ten-turn dial located at the bottom of the probe, more rotational echoes will appear in the FID and will persist for longer times.

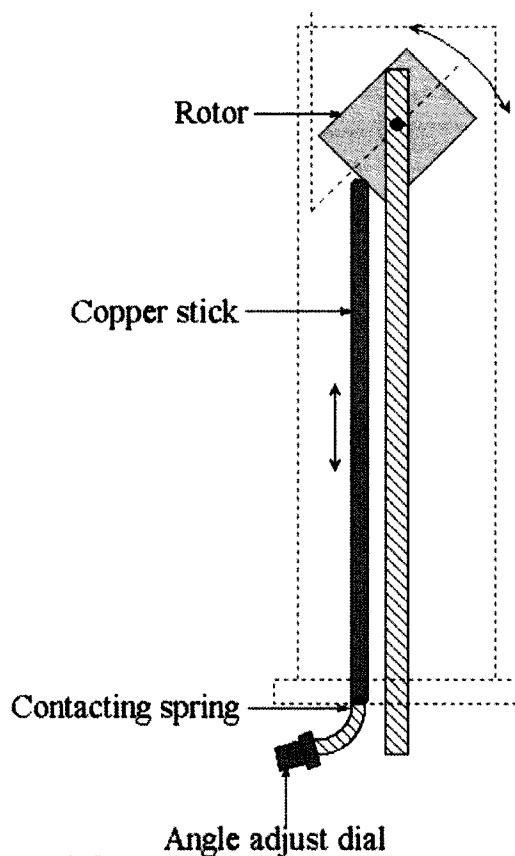


FIG. 2.5 The structure of MAS angle adjustment module

The angle adjust dial is at the bottom of the MAS probe and contacts the rotor through a spring and a long copper stick. If the angle is far way from exact magic angle conditions, the copper stick can lose contact with the rotor. It is then necessary to remove the cover of the MAS probe and make coarse adjustments visually outside the magnet.

If the rotor angle is adjusted away from the magic angle, rotational echoes towards the end of the FID will disappear. Alternatively, when the spectrum is used to adjust rotor angle, the sidebands and center band become sharper and additional sidebands become visible towards the edges of the spectrum. The rotor angle needs to be adjusted until the maximum number of rotational echoes or the narrowest side/center-bands are found. At the room temperature, the narrowest ^{79}Br side band line width is about 150 Hz when the

spinning speed is 20 kHz in 17.6 T magnetic field. It is possible when the rotor is too far away from the magic angle, the long control stick loses its contact with the rotor assembly, and the dial fails to change the angle. In this case, we must remove the cover of the MAS probe and rotate the dial until the control stick contacts the rotor again. The rotor angle drifts slightly over a period of weeks. The angle also changes slightly with temperature since the relevant probe components have different coefficients of thermal expansion. In variable temperature experiments, not only the circuit tuning but also rotor angle re-adjustment is required at each temperature.

In order to achieve additional precision of magic angle adjustment in critical experiments, such as ST-MAS or Off-MAS, an extra-fine angle tuning via a urea-d₄ powder sample can be used after coarse adjustment with KBr⁶⁰. Fig 2.6 shows a urea-d₄ MAS spectrum (dash line) that was acquired right after KBr angle tuning. In comparison, in fig. 2.6, the extra-fine angle tuning via urea-d₄ MAS spectrum (solid line) is also shown under the same conditions (spin speed, temperature, etc.). However, the tuning with urea-d₄ is time consuming if the angle is far away from magic angle. Therefore, when an extremely precise spinning angle is required, it is recommended to use both samples. within this manner it is possible to obtain urea-d₄ sidebands as narrow as 80 Hz; the angle can be adjusted with accuracy approaching $\pm 0.01^\circ$.

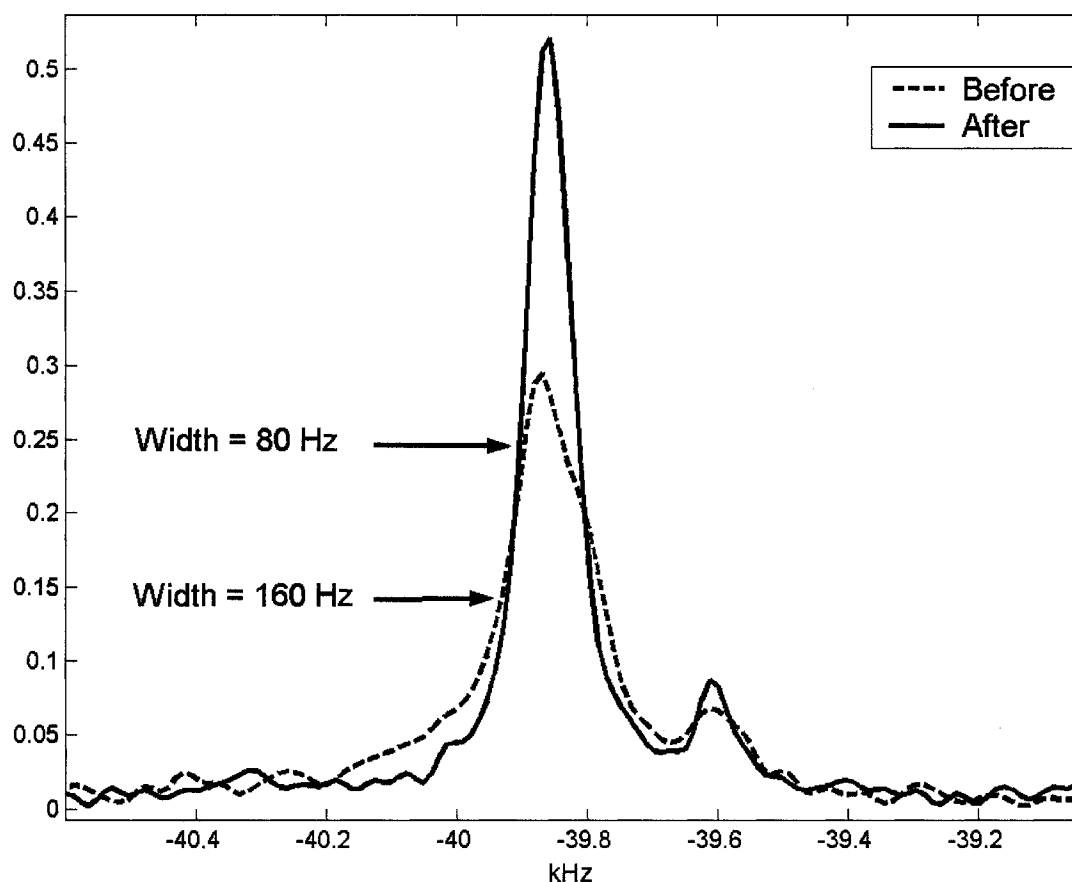


Fig.2.6 Urea- d_4 MAS spectrum after careful angle adjustment

The dashed line is one MAS sideband right after KBr angle adjustment, and the solid line is the same spectrum after a tiny angle adjustment. Even when the side band line width of KBr is minimized, the line width of urea- d_4 can be further narrowed by additional angle tuning. Approximately, urea- d_4 MAS spectrum depends on the offset angle as fig. 2.7. shows. When using urea- d_4 angle tuning, the angle can be set within $\beta_R \pm 0.01^\circ$. The spectra are acquired with 20 kHz spinning speed and the temperature is 303 K. A single 90° pulse (1.6 μs , 1.2 dB) is used for urea and dwell time is 2.5 μs . For each urea spectrum, 64 scans are acquired and the scan delay is two seconds.

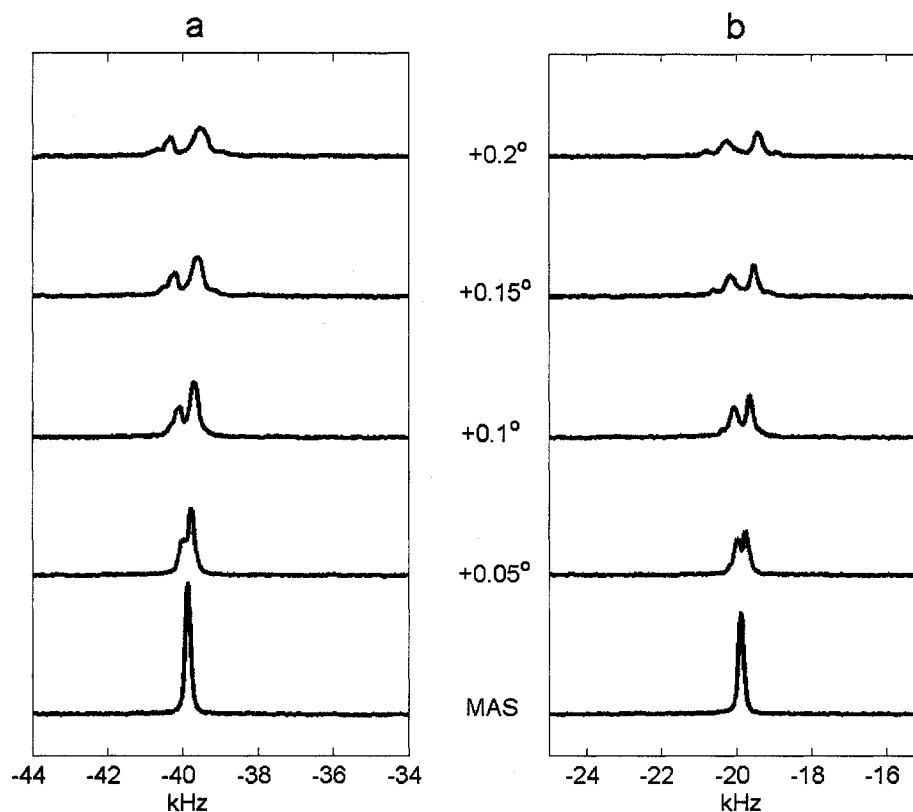


FIG. 2.7 On/Off MAS urea- d_4 line shape with different offset angles

The spectra were acquired with 20 kHz spinning speed and the temperature was 303 K. After single 90° pulse ($1.6 \mu\text{s}$), 128 scans are taken and FFT is done to obtain the MAS spectrum. The dwell time is $2.5 \mu\text{s}$ and the recycle delay is two seconds.

The basic angle adjustment for Off-MAS experiments is similar to the On-MAS procedure. However, since the offset angle cannot be directly measured, its value can be only known indirectly by simulating the reintroduced quadrupole coupling interaction. In deuteron OMAS experiments, a scaled quadrupole coupling interaction on the order of $\frac{1}{2}C_Q |3\cos^2(\beta-\Delta)-1|=100-2000 \text{ Hz}$ is reintroduced⁶⁰, so that the offset angle can be determined approximately by measuring the distance between the OMAS doublet of each rotational side band.

2.3 Data collection and processing

2.3.1 Quadrature detection

Since magnetization is rotating around the applied magnetic field at the Larmor frequency and RF pulses are applied near the same frequency, demodulated FID signals are sampled over frequencies within the audio range. For a single spin species, if the offset from the carrier frequency is ω , the FID is:

$$\begin{aligned} S(t) &= S \cdot \exp(i \cdot \omega \cdot t) \\ &= S \cos(\omega \cdot t) + i \cdot S \sin(\omega \cdot t) \\ &= \text{Re}(S) + i \text{Im}(S) \end{aligned} \quad (2.19)$$

The detection of only the real component, $\text{Re}(S)$, with one analog/digital converter (ADC), would yield after Fourier transformation a complex-valued spectrum whose real part would be symmetric about the frequency origin. Thus, single-phase detection cannot distinguish the difference between true signals with positive and negative offsets from the carrier. In early instruments, this problem was addressed by a technique called time-proportional-phase-increment (TPPI). During TPPI, the receiver reference phase is cycled repeatedly through 0° , 90° , 180° and 270° at successive data points. In all modern spectrometers, this procedure has been superseded by simultaneous digitization of two demodulated signals, using two ADCs and two demodulators with a 90° phase shift relative to the carrier frequency, to detect both $\text{Re}(S)$ and $\text{Im}(S)$. The signal/noise ratio is improved over single phase detection by a factor $\sqrt{2}$, and the resulting Fourier transform spectrum distinguishes positive from negative carrier offset frequencies. During the acquisition period, a (complex-valued) data point is recorded at every dwell time t_{dw} . The useful spectral width (frequency window) is defined as:

$$f_{sw} = \frac{1}{t_{dw}} \quad \text{Quadrature} \quad (2.20)$$

By convention, the frequency window is defined over the range $-f_{sw}/2$ to (almost) $f_{sw}/2$ rather than zero to f_{sw} ³³.

The space between frequencies of the Discrete Fourier Transform (DFT) is given by

$$\Delta f = \frac{1}{t_{acqu}} = \frac{f_{sw}}{N} \quad (2.21.a)$$

$$t_{acqu} = N \cdot t_{dw} \quad (2.21.b)$$

where N is the number of sampled FID points, t_{dw} is the spacing between them, and t_{acqu} is the total acquisition time per scan. In practice, one chooses f_{sw} to span the expected range of signals and t_{dw} to achieve adequate digital resolution. This fixes the length of the FID to be sampled, which of course must be short enough that the signal just decays into noise by the end of the acquisition (after signal averaging!).

Discrete sampling introduces the problem of *aliasing*: signals that differ by multiples of f_{sw} are indistinguishable. Thus, the signals that have true frequencies outside the spectral window will be folded back into the observed range unless the signal is passed through an analog filter prior to digitization, in which case, such signals are lost.. In order to avoid this phenomenon, It is necessary to sample fast enough so that aliasing does not occur. In fast MAS experiments, where the rotor spins at speeds >25 kHz, the dwell time can be as short as $2 \mu\text{s}$ ($f_{sw} = 500$ kHz) and digital resolution is limited by the duration of the rotational echo train. Detailed discussions about DFT and NMR signal detection methods can be found in the literature^{32, 33, 65, 66}.

2.3.2 CYCLOPS phase cycling

Phase cycling is an essential practical feature of pulsed NMR experiments that suppresses a variety of experimental artifacts. This technique is used to discriminate against unwanted signals on the basis of their phase properties. Such unwanted signals can arise from coherent noise, amplitude imbalance in the receiver channels, and a variety of artifacts generated by multiple pulses^{13,33}. For a single pulse MAS experiment, the most common phase cycle is especially easy and contains only four steps: X, Y, -X, -Y (cyclically ordered phase sequence, CYCLOPS). The major unwanted signal in this experiment comes from imbalance in the spectrometer hardware: different offset levels and signal-gain imbalance in real (RE) and imaginary (IM) channels.

When the CYCLOPS phase cycling method is used, two signals with 90° phase shift are sampled. For one phase cycle, the phase status of both channels is shown in table 2.2.

Table 2.2 CYCLOPS phase cycling

Scan	Pulse	Receiver	RE-channel	IM-channel
1	+X	+X	+Y	+X
2	+Y	+Y	-X	+Y
3	-X	-X	-Y	-X
4	-Y	-Y	+X	-Y

As the pulse phase is incremented with successive scans, the initial magnetization is placed periodically along the +Y, -X, -Y, -X directions in the rotating frame. Then the data streams from the two channels are routed to the computer as shown in Table 2.2. Figure 2.8 shows how this procedure removes artifacts associated with DC offsets and amplitude imbalance. More complex phase cycles are needed to fully suppress unwanted artifacts from more complex pulse sequences⁹.

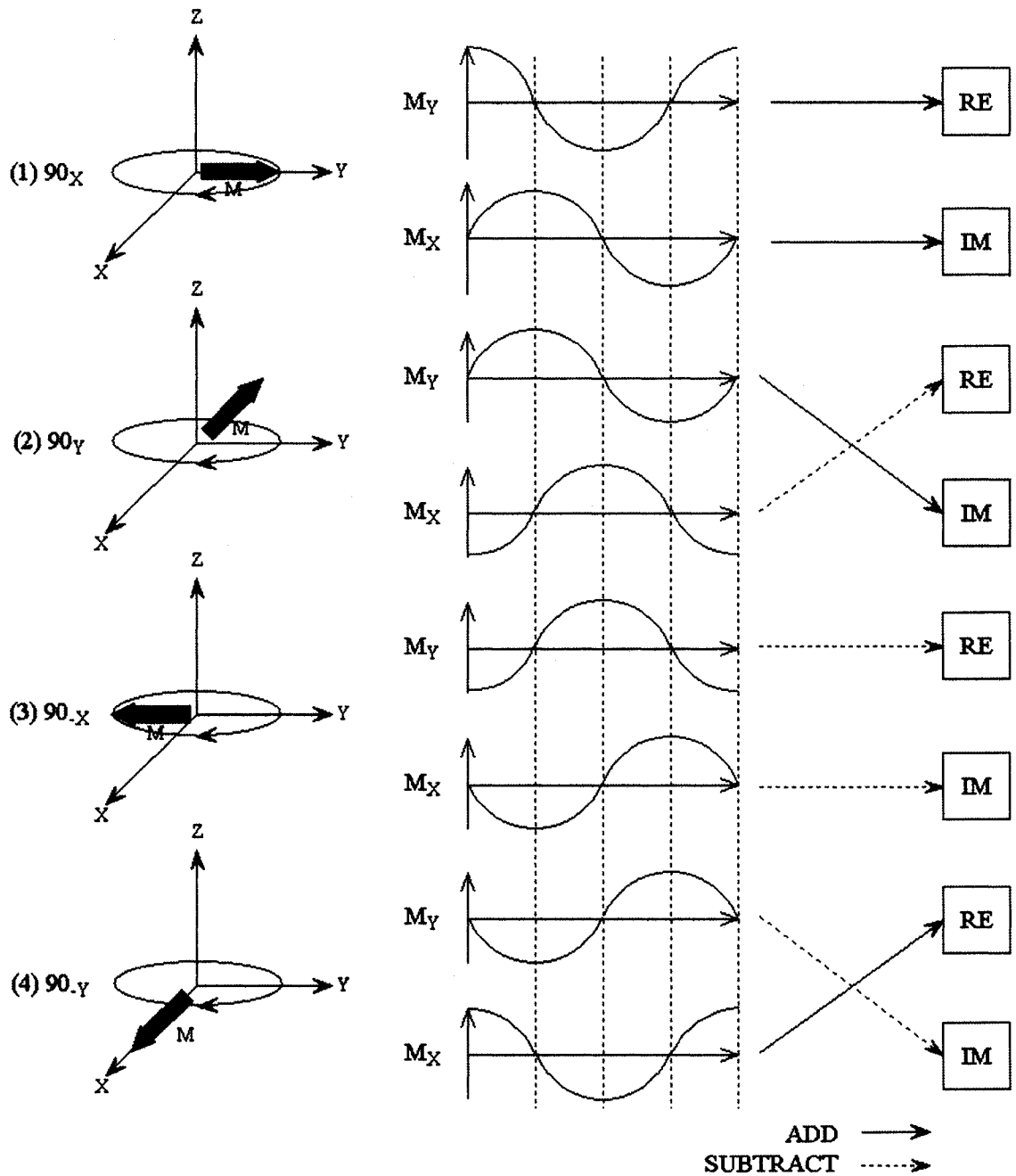


FIG. 2.8 CYCLOPS

In CYCLOPS, as the pulse phase increase step by step, the initial magnetization is placed periodically along +Y, -X, -Y, -X directions and the RE and IM data streams alternatively add/subtract the signals from RE and IM channels. DC offset and signal-gain imbalances are eliminated by this four step phase cycle.

2.3.3 Fourier transformation

After the digitization and summation of many acquisitions to improve signal/noise, the time domain FID data is converted into a frequency spectrum by discrete Fourier transformation (DFT). Compared with continuous-wave spectroscopy where sequential measurements of the responses for various frequencies are required, Fourier transformation NMR has overwhelming multiplex advantages^{14, 67}. The mathematical definition of the Fourier transformation and its discrete counterpart is as follows:

$$S(\Omega) = \int_0^{\infty} S(t) \cdot \exp(-i \cdot \Omega t) dt \quad \text{For continuous signal } S(t) \quad (2.22.a)$$

$$F(k) = \sum_{n=0}^{N-1} F(n) \cdot \exp\left(-i \cdot \frac{kn}{N}\right) \quad \text{For discrete signal } F(n), \text{ DFT} \quad (2.22.b)$$

The experimental, digitized FID signal contains real and imaginary components and the DFT of this signal also has real (absorption) and imaginary (dispersion) components (fig. 2.9).

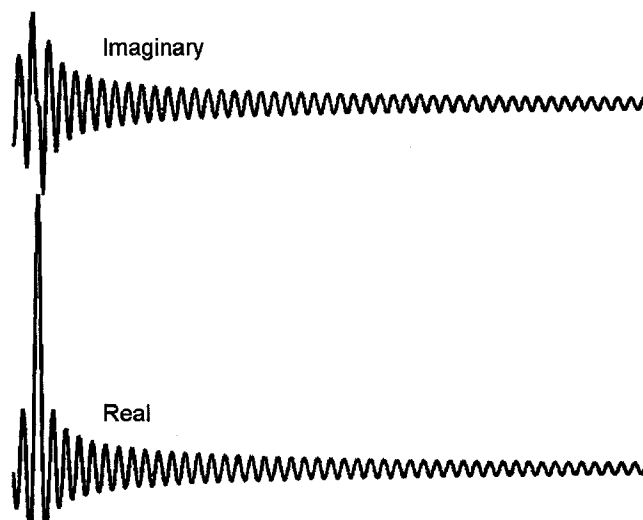
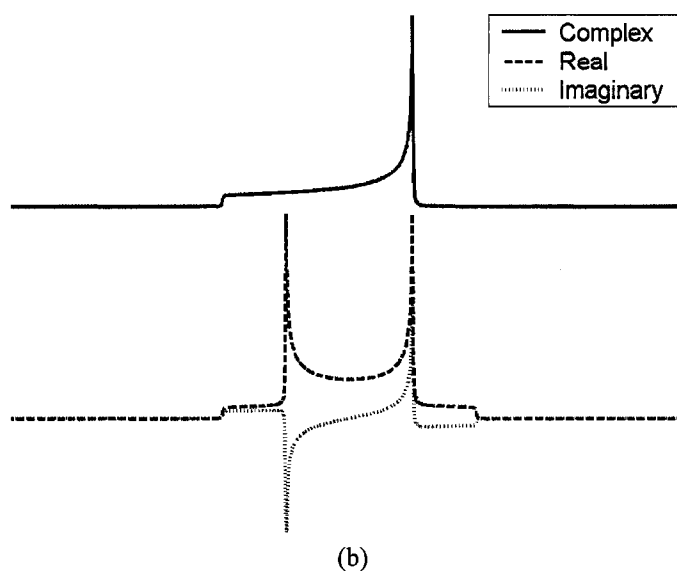


FIG. 2.9.a



(b)
 FIG. 2.9 The relationship between real and imaginary FID components
 (a): FID in the time domain. (b): the spectrum in the frequency domain. When the FID has zero imaginary part, the real part of the spectrum is symmetric and the imaginary part is antisymmetric.

The most important Fourier pair for visualizing NMR experiments is the exponential-Lorentzian pair:

$$L(\nu) = \int_0^{\infty} \exp\left(-\frac{t}{\tau}\right) \cdot \exp(-i \cdot 2\pi\nu \cdot t) dt = \frac{1}{i \cdot 2\pi\nu + 1/\tau} \quad (2.23)$$

The full width of $L(\nu)$ at half-maximum intensity is $1/(\pi\tau)$ Hz. In the remainder of this section, the FID will be modeled simply as a decaying exponential function. In order to obtain fully absorptive and artifact-free spectra, effects on the DFT of phase errors, bandwidths, spectrometer dead time and residual DC offset, have to be taken into account and eliminated.

2.3.4 Phase correction

In modern NMR spectrometers, the phase shift between real and imaginary reference signals is exactly equal 90° , but little attention is paid to the exact phase relation between the transmitter carrier frequency and the receiver reference phase. Depending on circuit details, appreciable phase difference between these two signals can arise. Moreover, signal delays introduced by analog filters in the transmitter and receiver lines results in arbitrary phase shifts. A simple, post-acquisition phase shift (zeroth-order phase correction) is employed to compensate for these differences:

$$\begin{aligned} \operatorname{Re}(F_{new}(\omega)) &= \operatorname{Re}\{ (\cos\psi + i\sin\psi) \cdot F_{old} \} \\ &= \cos\psi \operatorname{Re}(F_{old}(\omega - \omega_0)) - \sin\psi \operatorname{Im}(F_{old}(\omega - \omega_0)) \end{aligned} \quad (2.24)$$

The value of zeroth-order phase correction, ψ , is chosen to make the new "real" channel in the time domain exactly into a cosine function, and the new "imaginary" channel into a sine function. This correction can be done either in the time domain, by timing the complex FID with $\exp(-i\psi)$ or in the frequency domain as Eq. 2.24 shows.

FID data points are recorded after a short idle time period (dead time, $5\sim 10 t_{dw}$) in order to avoid the distortion from the RF pulse ring-down signal. However, loss of the initial data points selectively suppresses rapidly decaying signals and causes unacceptable distortions of broad powder patterns. In quadrupole echo or Hahn echo experiments, a spin echo occurs at an approximate time τ_1 ($30\sim 100 t_{dw}$) after the last pulse, and the useful FID begins at the top of this echo, thereby eliminating most ring-down effects and linear phase distortions. In On/Off MAS experiments, the useful FID begins as the top of the first rotational echo, which occurs at $20\sim 40 t_{dw}$ and this fully eliminates the ring-down effects. However, if acquisition is not started exactly at the top of the first echo, where

signals have the same phase regardless of their precession frequency, then signals in the frequency domain will exhibit a phase distortion proportional to their offset from the carrier frequency.

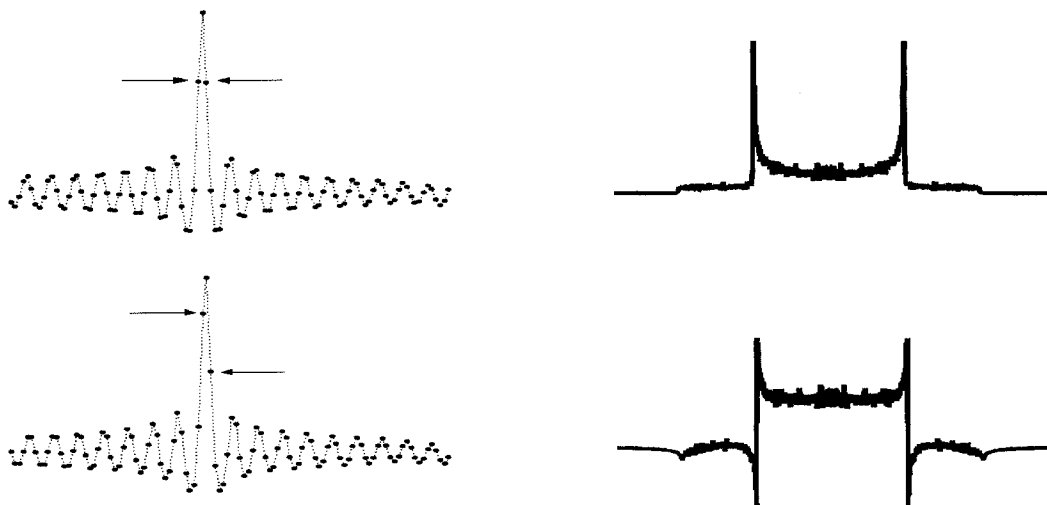


FIG. 2.10 The line shape with linear phase distortion

Here the simulation of two Quadrupole echo experiments is shown. The top FID records a data point almost right at the top of the echo, therefore its line shape has no large linear phase distortion: a time domain left-shift operation, which moves the first point of FID to the top of echo near $\tau_1 = 60 \mu\text{s}$, is sufficient to obtain an undistorted line shape. The FID at the bottom is obtained with the same parameters, but a slightly different τ_1 value ($60.75 \mu\text{s}$). Other simulation parameters are $C_Q = 180 \text{ kHz}$, dwell time = $2.5 \mu\text{s}$, $\eta_Q = 0$, and both FID signals contain 2048 points. As the two arrows point out, the top of this FID falls between two sampling points, and introduces a strong linear phase distortion into the line shape. This can be removed, post acquisition, by reconstructing a new spectrum, $\cos(\phi_i) \text{Re}((F_{old}(\nu_i)) + \sin(\phi_i) \text{Im}((F_{old}(\nu_i)))$, where the correction phase ϕ_i used for each point is linearly proportional to offset from the carrier frequency.

In MAS, since the first rotational echo occurs at approximately one rotor period ($10 \sim 30 t_{dw}$) after the rf pulse, the phase distortions are usually removed by a combination of discrete left shifts and a small linear phase correction, described by Eq. 2.25.

$$F_n^{new} = \exp\left(i\psi_0 + i\frac{n}{N}\psi_1\right) \cdot F_n^{old} \quad (2.25)$$

Here ψ_0 is the zeroth-order (constant) and ψ_1 is the first-order (linear) phase correction, and N is the number of data points in the FID. The linear phase correction can be avoided, if desired, by making the rotor period an exact multiple of the dwell time.

At the end of acquisition, a truncation effect occurs if the NMR signal is cut off before it has had time to decay to zero. This may be hard to avoid, if data have to be accumulated for several hours before sufficient time domain signal is obtained. The final spectrum can be viewed as the product of the FID and the box function of width t_{acq} in the time domain. The truncation effect convolutes each peak with a sinc function, $\sin(\nu-\nu_\tau)/(\nu-\nu_\tau)$ where $\nu_\tau = 1/t_{acq}$. Negative lobes from closely spaced peaks overlap and small signals are veiled.

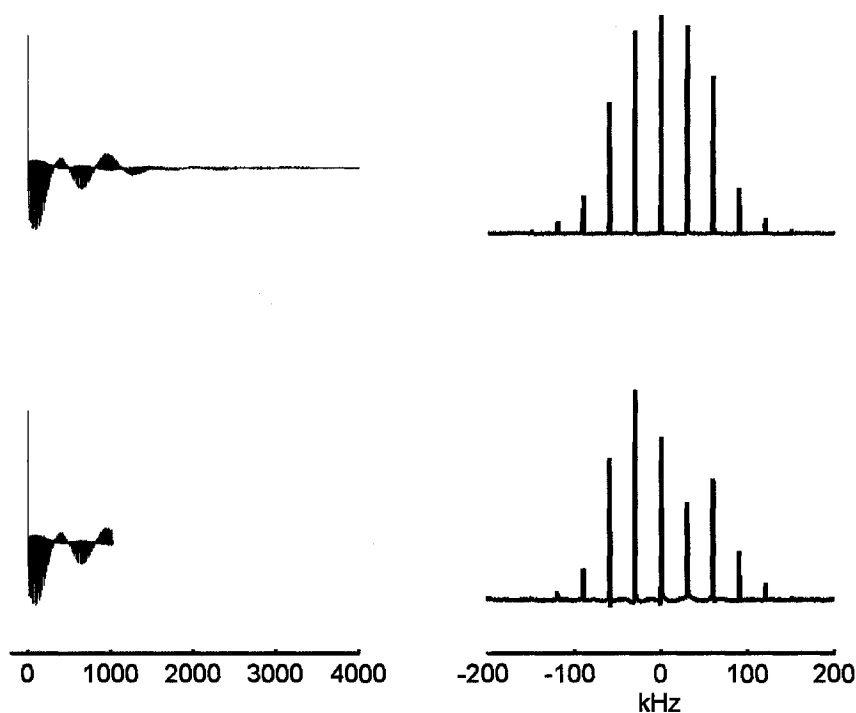


FIG 2.11 Truncation effects

MAS spectra of pure phenylalanine- d_8 are shown here with 30 kHz spinning speed. The full FID (top) contains 4096 data points and its DFT does not show any truncation effect. But the truncated FID (bottom) contains only 1024 data points, and its spectrum shows strong truncation effect. In order to eliminate such effects, the FID needs to continue until it drops to no more than 5% of its maximum amplitude.

When the FID decays quickly to less than 5% of its maximum value, extra zeroes can be "padded" added at the end of the FID in the time domain (zero-filling) in order to obtain smooth spectra. Zero-filling is equivalent to trigonometric interpolation of the frequency domain spectrum.

Apodization can also be used in NMR data processing to ameliorate truncation artifacts. In most spectra shown in this thesis, decreasing exponential apodization is used to reduce noise with some sacrifice of resolution. Generally, a 50 ~ 200 Hz exponential apodization is applied to the MAS FID before DFT. The relationship between the FID before apodization and after apodization can be described by Eq. 2.26.

$$FID_k^{new} = FID_k^{old} \cdot \exp(-\psi \cdot k \cdot t_{dwell})$$

$$\psi = \pi \cdot W$$
(2.26)

Figure 2.12 shows how the DFT spectrum changes with W . It is also possible to use *negative* line broadening to improve resolution somewhat at the expense of signal to noise ratio and introduction of truncation artifacts.

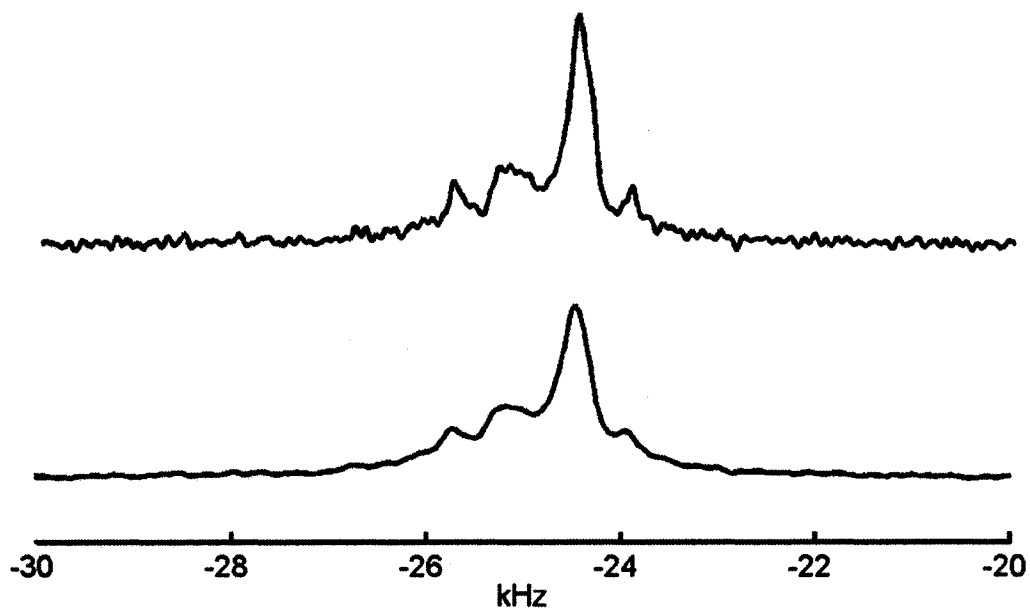


FIG. 2.12 Exponential apodization trades resolution for signal to noise ratio.

The second sideband of an OMAS spectrum of octanoic acid/urea- d_4 inclusion compound are shown here. The temperature was 273 K and the spinning speed was 25 kHz. A single 90° pulse ($1.6\mu\text{s}$) was used and 512 scans were acquired to obtain the FID. The top spectrum was obtained by DFT without apodization and contains lots of noise. With 25 Hz apodization, the bottom spectrum is smoother and the precision of spectrum fitting is improved.

Chapter 3

Simulation of Deuteron Spectra with Molecular Motion

3.1 Introduction

Molecular motion plays an important role in determining diverse bulk physical properties, such as heat capacity associated with rapid internal rotations of molecular groups and impact resistance of polymers^{3, 16, 56}. A quantitative measure of random, large amplitude molecular motion in a solid is provided by defining an appropriate autocorrelation function, $G(\tau)$:

$$G(\tau) = \overline{f(t)f(t')} = \overline{f(t)f(t+\tau)} \quad (3.1)$$

where $f(t)$ is a time-dependent function that describes molecular orientation at time t . It is assumed to be a random function of time. $G(t)$ is the ensemble average of the product of f -values measured at two different times t and $t+\tau$. Stationary random processes are characterized by correlation functions that depend only on the time difference, $\tau = t'-t$, and not on the individual measurement times t and t' . It is convenient to assume that in what follows, $f(t)$ is defined such that its time average, $\overline{f(t)} = \overline{f(t')}$, is zero. If it is assumed that averages over time are equivalent to averages over orientations (Ergodic hypothesis), $G(\tau)$ is given quite generally by

$$G(\tau) = \int_{\Omega_0} f(\Omega_0)P(\Omega_0)d\Omega_0 \int_{\Omega} f(\Omega(t))p(\Omega_0, \Omega)d\Omega \quad (3.2)$$

Where $P(\Omega_0)$ is the probability of having orientation Ω_0 at $t = 0$, and $p(\Omega_0, \Omega, t)$ is the conditional probability that the orientation is Ω at a later time t . The most common motional model used to simulate NMR line shapes assumes that motion proceeds by random, sudden jumps among a small number of discrete, orientational "sites", defined by particular values $\Omega_0, \Omega_1, \Omega_2 \dots$ etc. If the mean lifetime in a given site is defined by $1/2k^{-1}$, it can be shown that the relevant correlation function is exponential⁶⁸:

$$G(\tau) = G(0) \exp(-k \cdot \tau) \quad (3.3)$$

where the parameter k , whose unit is sec^{-1} , is a quantitative measure of the motional rate, and $G(0) = \overline{f(\Omega_0)f(\Omega_0)}$ is a constant that depends on the specific orientational function $f(\Omega)$ under consideration. In this chapter it will be shown how these correlation functions are used to develop explicit expressions for NMR line shapes that depend on the motional rate.

3.2 Effects of molecular motion on deuteron line shapes

3.2.1 Theory of molecular motion

Deuteron NMR spectroscopy is an attractive technique for studies of molecular motion for several reasons. As mentioned previously, the dominant spin interaction of the deuteron is nuclear quadrupole interaction, so that complications arising from many-body dipolar coupling can be ignored. Thus, the relevant Hamiltonian can be described by a single-spin tensor. This greatly simplifies the description of reorientational dynamics of individual sites. Moreover, in most organic molecules, the principal axis of the deuteron electric-field gradient tensor is parallel to the chemical bond direction and therefore electric-field gradient monitors bond reorientation in a very direct manner. Finally, it is

possible by means of selective isotopic labeling to monitor reorientational motion of individual functional groups in complex molecules^{69,70}.

Motion affects deuteron spectra in different ways depending on the motion rate. Ultrafast motions, such as librations and vibrations, have rates that are normally greater than the Larmor frequency. They lead to averaging of the quadrupole tensor over a restricted range of orientations and produce orientation-dependent spin lattice relaxation (T_1). Ultrafast motion rates often show an Arrhenius temperature dependence and the measurement of deuteron T_1 temperature dependence can be used to track the motion⁷¹. Slower motional regimes include the "fast" regime ($10^6 < k < 10^9 \text{ s}^{-1}$), the "intermediate" regime ($10^3 < k < 10^6 \text{ s}^{-1}$) and the "slow" regime ($k < 10^3 \text{ s}^{-1}$). Motions in these regimes frequently occur in solid materials including simple crystals and inclusion compounds^{37, 58} and also in complex polymers and proteins⁷². Deuteron NMR line shapes are strongly affected by motion in the fast and intermediate regime, while magnetization transfer and two-dimensional exchange experiments^{53, 73} probe slow motion. An important new result of the work presented in this thesis is that deuteron MAS and OMAS experiments extend the range of rates accessible via line shape simulation well into the slow regime⁶⁰.

Fast and intermediate molecular motion ($10^3 < k < 10^8 \text{ s}^{-1}$) can be investigated by quadrupole echo line shape experiments^{30, 37, 74}. For example, fig. 3.1 shows line shapes simulated for motion, which consists of random jumps among three orientations of an EFG tensor that could mimic rotational motion of a methyl group about its pseudo-threefold axis.

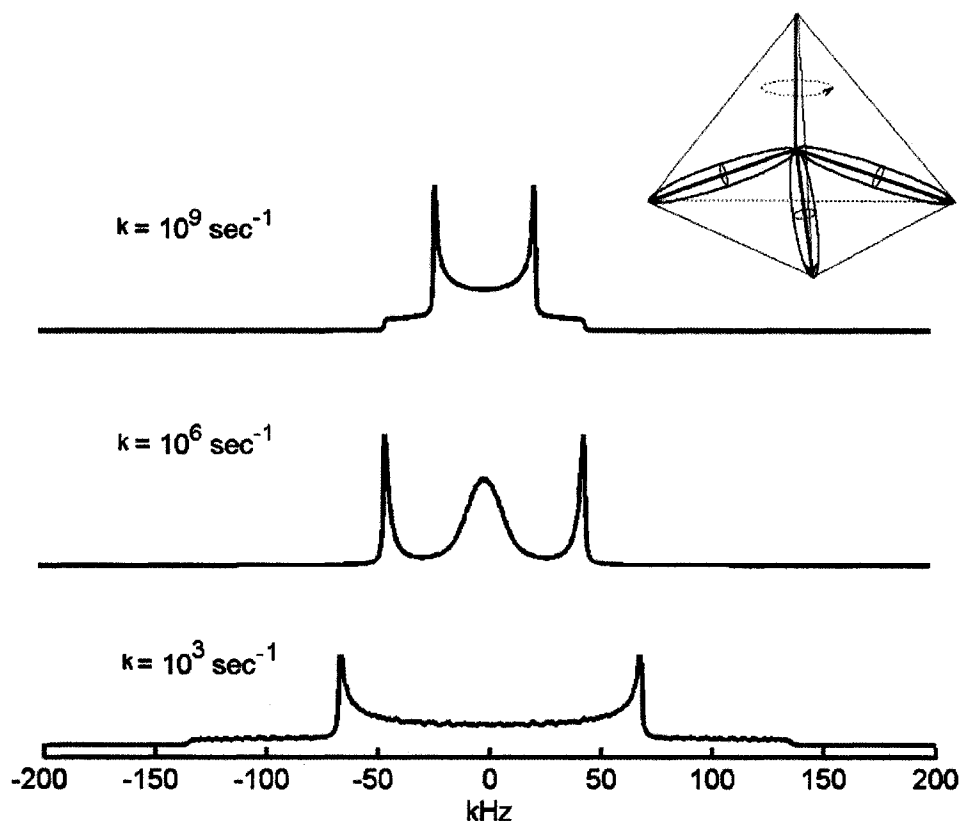


FIG. 3.1 Quadrupole echo spectra with different motional rates

Simulation parameters: $C_Q = 180$ kHz, $\eta_Q = 0$ and $\tau_1 = 30$ μ s, dwell time is 2.5 μ s (Spectral window = ± 200 kHz). The motion consist of random jumps at rate k , between three sites that have Euler orientation angles: $(0\ 109^\circ\ 0)$, $(0\ 109^\circ\ 120^\circ)$ and $(0\ 109^\circ\ 240^\circ)$, the principal Z-axis of the EFG tensor points approximately at three vertices of a tetrahedron.

Deuteron powder patterns are insensitive to motion in the slow regime ($k < 10^3$ s $^{-1}$) because the uncertainty principle broadening is less than the underlying homogeneous line width. Selective inversion (magnetization transfer) and its two-dimensional analog^{53, 73} have been used to investigate this motional regime, although both techniques suffer from intrinsically low signal/noise ratio.

Deuteron On/Off MAS is a very attractive alternative to selective inversion and 2D exchange experiments. The advantages of deuteron MAS experiments include improved signal/noise ratio and enhanced sensitivity to molecular motion over a much wider

dynamic range. Because of the averaging effects of rapid sample rotation, the residual homogeneous line width arising from unresolved dipolar coupling is reduced by at least an order of magnitude, so that the line widths of individual rotational sidebands are sensitive to k -values as small as $10\text{-}50\text{ sec}^{-1}$. Simultaneously, the intensity profile of the sideband manifold remains sensitive to motion from the slow to intermediate time scales. In Off-MAS experiments, it is possible to controllably reintroduce a fraction of the quadrupole coupling interaction by setting a tiny offset angle, Δ , from the magic angle β_R . The narrow sidebands observed in MAS experiments reveal fine structure with line shapes that are very sensitive to motions on the time scale of the reintroduced quadrupole coupling interaction. This reintroduced interaction is experimentally adjustable, and is typically on the order $\frac{1}{2}C_Q|3\cos^2(\beta_R - \Delta) - 1| = 100 \sim 2000\text{ Hz}$. Representative Off-MAS spectra simulated under different temperatures are shown in fig. 3.2.

Although On/Off MAS experiments show a high sensitivity to molecular motion, they pose computational challenges to quantitative analysis and simulation. Since the powder sample mechanically spins with the rotor, the spin Hamiltonian depends on both orientation and time. Traditional numerical methods that are used to simulate static powder patterns with time-independent Hamiltonians are no longer applicable. Numerically efficient extensions of existing theory that are required to account for coherent sample rotation will be discussed later in this chapter.

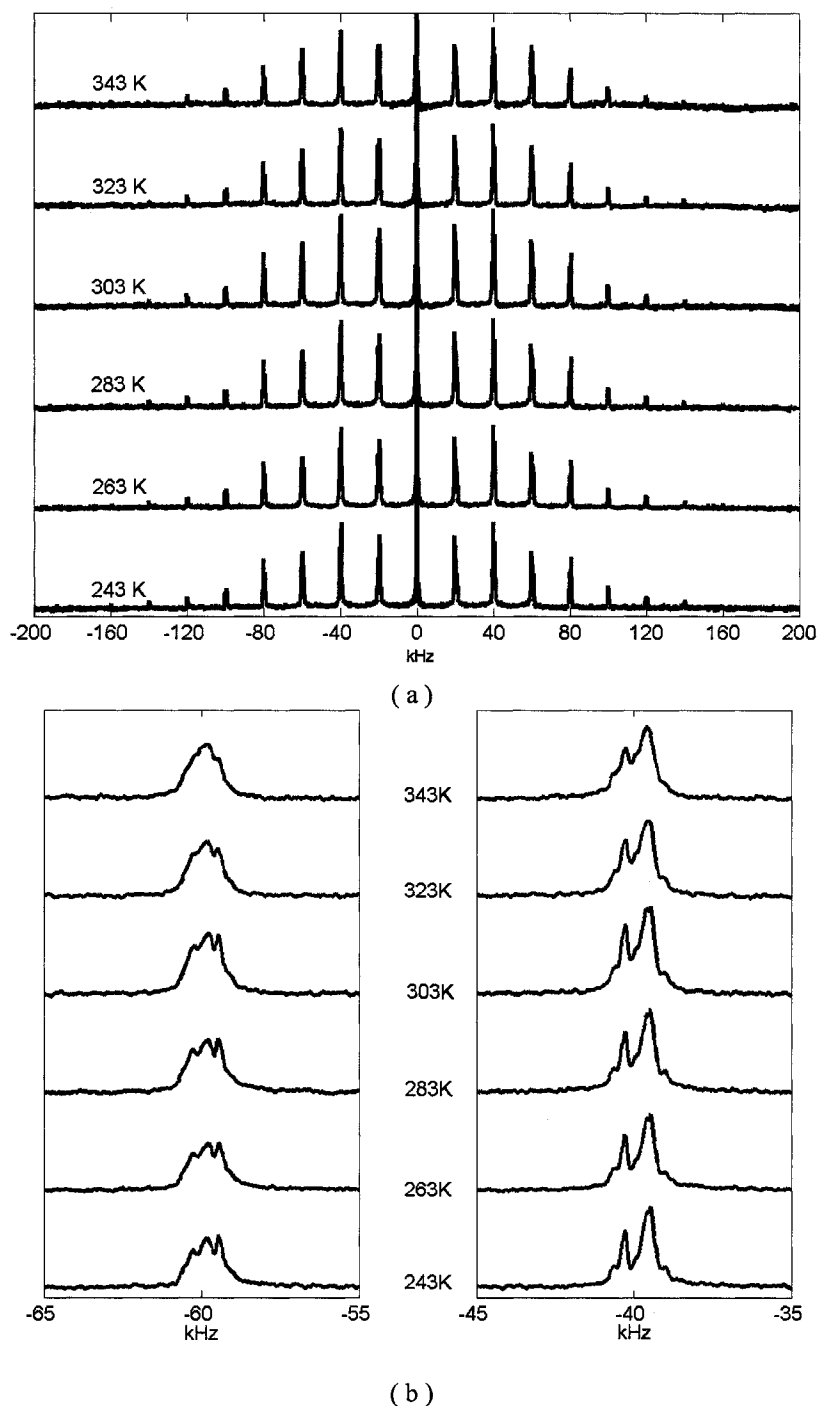


Figure 3.2 Variable Temperature Deuteron OMAS Spectra of Urea inclusion compounds (a): The simulated OMAS line shapes are shown in the full spectra window and (b): The first and second sidebands are shown on expanded scale. The shapes of their sub peaks change with temperature. These sub peaks appear when the magic angle is purposely misadjusted. Detailed discussions of urea OMAS simulations can be found in Chapter 4.

3.2.2 Multi-axis Molecular Motion

In order to describe molecular jump motion among multiple sites in a complex dynamical system, an exchange matrix K can be incorporated in sets of Bloch equations⁷⁵⁻⁷⁷ or more generally (see section 3.2.3) into the stochastic Liouville equation for the spin density matrix. For a single type of spin in the magnetic field, the time evolution of complex transverse magnetization $M = M_X + iM_Y$ viewed in the rotating frame can be described by the Bloch equation.^{12, 78}

$$\frac{dM}{dt} = -i\omega M - \frac{1}{T_2} M \quad (3.4.a)$$

$$M = M_X + iM_Y \quad (3.4.b)$$

where ω is the offset between the resonant frequency and the carrier frequency used to pulse the spins and to detect the resulting free precession, and T_2 is the spin-spin relaxation time. This equation is valid only in absence of time dependent rf fields; more general equations are described in standard textbooks^{12, 13}. In a spin system for which the spins can jump suddenly at an average motion rate k between equally populated sites A and B, with respective precession frequencies ω_A and ω_B , the coupled Bloch equations are:

$$\frac{dM_A}{dt} = i\omega_A M_A - \frac{1}{T_2} M_A - kM_A + kM_B \quad (3.5.a)$$

$$\frac{dM_B}{dt} = i\omega_B M_B - \frac{1}{T_2} M_B - kM_B + kM_A \quad (3.5.b)$$

Coupled Bloch equations can easily be rewritten in vector-matrix form for any number of sites:

$$\frac{d\bar{M}}{dt} = (i\Omega + R + K)\bar{M} \quad (3.6)$$

$$\bar{M} = \begin{pmatrix} M_1 \\ M_2 \\ \vdots \\ M_N \end{pmatrix} \quad (3.7)$$

where Ω is the diagonal matrix of precession frequencies, and individual sites are now labeled by numbers 1,2,3...:

$$\Omega = \begin{pmatrix} \omega_1 & 0 & 0 & 0 \\ 0 & \omega_2 & 0 & 0 \\ 0 & 0 & \ddots & 0 \\ 0 & 0 & 0 & \omega_N \end{pmatrix} \quad (3.8)$$

and R is a diagonal matrix of site-specific, phenomenological transverse relaxation rates in absence of the jump motion is:

$$R = \begin{pmatrix} 1/T_{21} & 0 & 0 & 0 \\ 0 & 1/T_{22} & 0 & 0 \\ 0 & 0 & \ddots & 0 \\ 0 & 0 & 0 & 1/T_{2N} \end{pmatrix} \quad (3.9)$$

The elements of the rate matrix, K , describe the molecular motion. If k_{ij} is the jump rate from site i to site j , then the K matrix is given by

$$K = \begin{pmatrix} k_1 & k_{12} & & k_{1N} \\ k_{21} & k_2 & & k_{2N} \\ & & \ddots & \\ k_{N1} & k_{N2} & & k_N \end{pmatrix} \quad (3.10)$$

Commonly used motional models include nearest neighbor jumps among sites defined along an arc or around a closed ring, and equally probable jumps among all sites (strong collisions). The corresponding four site K matrices for arc, ring and strong collision are:

$$K_{\text{linear}} = \begin{pmatrix} k_1 & k_{12} & 0 & 0 \\ k_{21} & k_2 & k_{23} & 0 \\ 0 & k_{32} & k_3 & k_{34} \\ 0 & 0 & k_{42} & k_4 \end{pmatrix} \quad (3.11.a)$$

$$K_{\text{ring}} = \begin{pmatrix} k_1 & k_{12} & 0 & k_{14} \\ k_{21} & k_2 & k_{23} & 0 \\ 0 & k_{32} & k_3 & k_{34} \\ k_{41} & 0 & k_{42} & k_4 \end{pmatrix} \quad (3.11.b)$$

$$K_{\text{all-sites}} = \begin{pmatrix} k_1 & k_{12} & k_{13} & k_{14} \\ k_{21} & k_2 & k_{23} & k_{24} \\ k_{31} & k_{32} & k_3 & k_{34} \\ k_{41} & k_{42} & k_{43} & k_4 \end{pmatrix} \quad (3.11.c)$$

For equally populated sites, K is a symmetric matrix. More generally, k_{ij} and k_{ji} are related by the principle of detailed balance (microscopic reversibility): if k_{ij} refers to the flow of magnetization from site j to site i , then $p_i k_{ij} = p_j k_{ji}$. Moreover, the diagonal elements of K are just the negative of the sum of off-diagonal elements in the same row.

$$k_i = - \sum_{j=1, j \neq i}^N k_{i,j} \quad (3.12)$$

The structure of the rate matrix becomes complicated when molecular motion occurs at different rates by rotation around several axes.

A common example of such multi-axis motion is provided by a rotating methyl group, whose spins are rotating respect to the methyl symmetric axis and at the same time the orientation of the axis is jumping between two directions. The rate matrix, K_I , for the rotation can be modeled by jumps among three sites equally spaced around a ring:

$$K_1 = \begin{pmatrix} -2k_1 & k_1 & k_1 \\ k_1 & -2k_1 & k_1 \\ k_1 & k_1 & -2k_1 \end{pmatrix} \quad (3.13)$$

while the rate matrix, K_2 , for the motion of the symmetric axis is

$$K_2 = \begin{pmatrix} -k_2 & k_2 \\ k_2 & -k_2 \end{pmatrix} \quad (3.14)$$

Since there are six possible sites for each spin, the final K matrix is 6 by 6 and is partitioned as shown below:

$$K = \begin{pmatrix} k_{local} - k_2 \cdot I & k_2 \cdot I \\ k_2 \cdot I & k_{local} - k_2 \cdot I \end{pmatrix} = \begin{pmatrix} -2k_1 - k_2 & k_1 & k_1 & k_2 & 0 & 0 \\ k_1 & -2k_1 - k_2 & k_1 & 0 & k_2 & 0 \\ k_1 & k_1 & -2k_1 - k_2 & 0 & 0 & k_2 \\ k_2 & 0 & 0 & -2k_1 - k_2 & k_1 & k_1 \\ 0 & k_2 & 0 & k_1 & -2k_1 - k_2 & k_1 \\ 0 & 0 & k_2 & k_1 & k_1 & -2k_1 - k_2 \end{pmatrix} \quad (3.15)$$

In general, for a set of N sites that arise from all possible combinations of multi-axis motions, it is possible to define the site orientations in terms of Euler angles for composite rotations from each possible orientation of the principal axis frame of the deuteron EFG tensor to a single reference frame, fixed with respect to crystal-fixed axes. It is necessary to insure that the site labeling used in the composite rate matrix is consistent with that used to construct the equivalent one-frame rotations.

3.2.3 Stochastic Liouville equation

The complete density matrix equations of motion for a spin system that can jump among N sites are far more complex than the Bloch equations presented in the previous section. The Liouville-von Neumann equation for the spin at site j is

$$\begin{aligned} \frac{d}{dt} \rho^{(j)} &= -i \cdot [\rho^{(j)}(t), H(t)] \\ &= (i\Omega + R) \cdot [\rho^{(j)}(t) - \rho^{(j)}(\infty)] \end{aligned} \quad (3.16)$$

where $\rho^{(j)}(\infty)$ is the equilibrium spin density matrix. The superoperator Ω is determined from the commutation properties of $\rho^{(j)}(t)$ with $H(t)$, and R is the relaxation superoperator. In this representation, $\rho^{(j)}$ is a column vector of density matrix elements. For a single deuteron ($I = 1$), the ordinary density matrix is 3×3 , so $\rho^{(j)}$ has nine elements.

Each site-specific density matrix has its own Liouville equation of the same form as that for site j , and the density matrix for the multi-site ensemble is built as the direct sum

$$\rho = \rho^{(1)} \oplus \rho^{(2)} \oplus \dots \oplus \rho^{(N)} \quad (3.17)$$

The result is a giant matrix if many sites are included: For N sites, the dimension is $9N^2$. For example, the two-coupled Bloch equations for jumps between sites A and B are replaced in this formalism by no less than 36 coupled equations! Fortunately, considerable simplification is possible⁷¹.

The nine elements of the density matrix for each site can be classified into three groups according to their coherence number as Eq. 3.18 shows.

$$\rho = \begin{bmatrix} \rho_Z \\ M_+ \\ M_- \end{bmatrix} \quad (3.18)$$

where

$$\rho_Z = \begin{bmatrix} \rho_{11} \\ \rho_{22} \\ \rho_{33} \end{bmatrix} \quad M_+ = \begin{bmatrix} \rho_{12} \\ \rho_{23} \\ \rho_{13} \end{bmatrix} \quad M_- = \begin{bmatrix} \rho_{21} \\ \rho_{32} \\ \rho_{31} \end{bmatrix} \quad (3.19)$$

According to the secular approximation⁷⁹, off-diagonal elements of the relaxation super-operator that describes the jump motion are negligible, resulting the following differential equation:

$$\frac{d}{dt} \begin{bmatrix} \rho^{(1)} \\ \rho^{(2)} \\ \vdots \\ \rho^{(N)} \end{bmatrix} = \begin{bmatrix} L_1 + K_1 & K_{12} & \cdots & K_{1n} \\ K_{21} & L_2 + K_2 & \cdots & K_{N2} \\ \vdots & \vdots & \ddots & K \\ K_{N1} & K_{N2} & \cdots & L_N + K_N \end{bmatrix} \begin{bmatrix} \rho^{(1)} \\ \rho^{(2)} \\ \vdots \\ \rho^{(N)} \end{bmatrix} \quad (3.20)$$

where L_j is the Liouvillian superoperator of the j^{th} site. For the quadrupole Hamiltonian, L_j can be simply written as

$$L_j = \begin{bmatrix} R_Z^{(j)} & 0 & 0 \\ 0 & i\omega^{(j)} + R_2 & 0 \\ 0 & 0 & -i\omega^{(j)} + R_2 \end{bmatrix} \quad (3.21)$$

$R_Z^{(j)}$ is the transition probability matrix produced, for example, by rapid small angle libration, for spin-lattice relaxation within site j . R_2 is a diagonal subset of relaxation super-operator matrix elements that describe site-specific transverse relaxation (dephasing) of single and multiple quantum coherences, and $\omega^{(j)}$ are the corresponding diagonal matrices of precession frequencies matrix for site j . the jump rate k_{ij} connects site i with j by the Markov jump process whose rate is k_{ij} :

$$K_{ij} = k_{ij} \cdot I \quad (3.22)$$

where I is the 9×9 identity matrix. Since the density matrix is Hermitian, the equations for M_+ do not couple with those for M_- . Moreover, it can be shown that in absence of the rf fields the equations for ρ_Z do not couple with those for M_{\pm} . Finally, since the spins do not change state during the jumps, coupling between individual density matrix elements $\rho_{12}^{(j)}$, $\rho_{23}^{(j)}$, and $\rho_{13}^{(j)}$ is non-secular and therefore negligible. As a result, the Stochastic Liouville equation needed for each of the three observable coherences reduces to exactly the same form as the N-site Bloch equation (Eq. 3.6) presented in section 3.3.2.

$$\frac{d}{dt} \vec{M} = (i\Omega + R + K) \cdot \vec{M} \quad (3.23)$$

Here, the diagonal precession matrix is

$$\Omega = \begin{bmatrix} \omega_1 & 0 & \cdots & 0 \\ 0 & \omega_2 & \cdots & 0 \\ \vdots & \vdots & & \vdots \\ 0 & 0 & \cdots & \omega_N \end{bmatrix} \quad (3.24)$$

Where ω_j is the precessional frequency of j^{th} site.

For multi-axis motion, the PAS of the deuteron at site j can be rotated into the LAB frame via a series of Euler rotations $(\alpha_i, \beta_i, \gamma_i)$, and the resulting precession frequency for coherence $\rho_{12}^{(j)}$ is given by

$$\omega^{(1)}_j = \frac{3e^2qQ}{4} \cdot W_{2,0}^Q \quad (3.25)$$

where $W_{2,0}^Q$ is given by

$$W_{2,0}^Q = [\bar{T} \cdot D_1(\alpha_1\beta_1\gamma_1) \cdot D_2(\alpha_2\beta_2\gamma_2) \cdots]_{2,0} \quad (3.26)$$

$$\begin{aligned} \bar{T} &= [T_{2,2} \quad T_{2,1} \quad T_{2,0} \quad T_{2,-1} \quad T_{2,-2}] \\ &= \begin{bmatrix} \sqrt{\frac{1}{6}}\eta_Q & 0 & 1 & 0 & \sqrt{\frac{1}{6}}\eta_Q \end{bmatrix} \end{aligned} \quad (3.27)$$

and D is the second rank Wigner rotation matrix.

It is worth noting that $W_{2,0}^Q$ for $\rho_{23}^{(j)}$ is simply opposite in sign to that for $\rho_{12}^{(j)}$. Thus, when chemical shifts are ignored, the signal arising from $\rho_{23}^{(j)}$ is just the complex conjugate of that from $\rho_{12}^{(j)}$ and need not be computed separately. In this case, the dauntingly large set of equations arising from the Stochastic Liouville equation reduces exactly to the result of the semi-classical Bloch equations. One new result that arises from this density matrix formalism is that when chemical shifts can *not* be ignored, it is sufficient to solve two independent sets of N first order coupled differential equations. Numerical methods for solving these equations are discussed in the following sections.

3.3 Simulation of static spectra

3.3.1 Theory of static simulation

The most common pulse sequence for solid state deuteron NMR motion studies is the quadrupole echo sequence. In this experiment, which works best when site specific chemical shifts are negligible, the carrier frequency is adjusted to exact resonance and two 90° pulses that differ in phase by 90° are applied to the sample. The spacing between the two pulses is τ_1 , and signal is recorded starting at time τ_2 after the second pulse. Based on the discussion in sections 3.2.2 and 3.2.3, the time evolution of transverse magnetization for either of the two transitions between pulses can be written as

$$\frac{d}{dt}M_{\pm} = (i\Omega_{\pm} + K)M_{\pm} = A_{\pm} \cdot M_{\pm} \quad (3.28)$$

When chemical shifts are ignored, $A_{+} = A_{-}$ and the \pm subscript can be ignored. We note in passing that the existence of site-specific chemical shifts implies that exact resonance

cannot be achieved for all spins, and the result is a differential phase shift in the resulting echo signal for each site. For a non-rotating sample, A is independent of time, and in this case the time evolution of M is simply given by the matrix exponential, $M(t) = e^{(At)}M(0)$. In simple quadrupole echo experiments, the first $\pi/2$ -pulse creates single quantum coherence. If equal site populations and uniform spectral coverage by the pulse are assumed, this corresponds to the initial condition

$$\bar{M}(0) = \frac{1}{N} \cdot \begin{pmatrix} 1 \\ 1 \\ \vdots \\ 1 \end{pmatrix} \quad (3.29)$$

In more complicated experiments, for example, those designed to monitor orientation dependent spin-lattice relaxation, different initial conditions can be set up via arbitrarily complex sequences of preparation pulses.

At time $\tau_1 = t$ later, just before the second pulse, the spin magnetization is

$$\bar{M}(t_-) = \exp(A \cdot \tau_1) \cdot \bar{M}(0) \quad (3.30)$$

If the second pulse is so strong that quadrupole-induced precession during the pulse is negligible, it can be shown that the $\pi/2$ pulse simply rotates M by 180° ⁸⁰ so that $\bar{M}(t_+)$ after the pulse is just $\bar{M}^*(\tau_1)$. It follows that at time t_2 later,

$$\bar{M}(\tau_2, \tau_1) = \exp(A \cdot \tau_2) \cdot \exp(A^* \cdot \tau_1) \cdot \bar{M}(0) \quad (3.31)$$

In effect, the second pulse reverses the precession direction of the magnetization and a spin echo appears at time $\tau_2 = \tau_1$, as shown in fig. 3.3. It should be noted that because the quadrupole Hamiltonian transforms as a second rank tensor while the Zeeman

Hamiltonian is a first rank interaction, single quantum quadrupole coherence is rotated 180° by a 90° pulse.

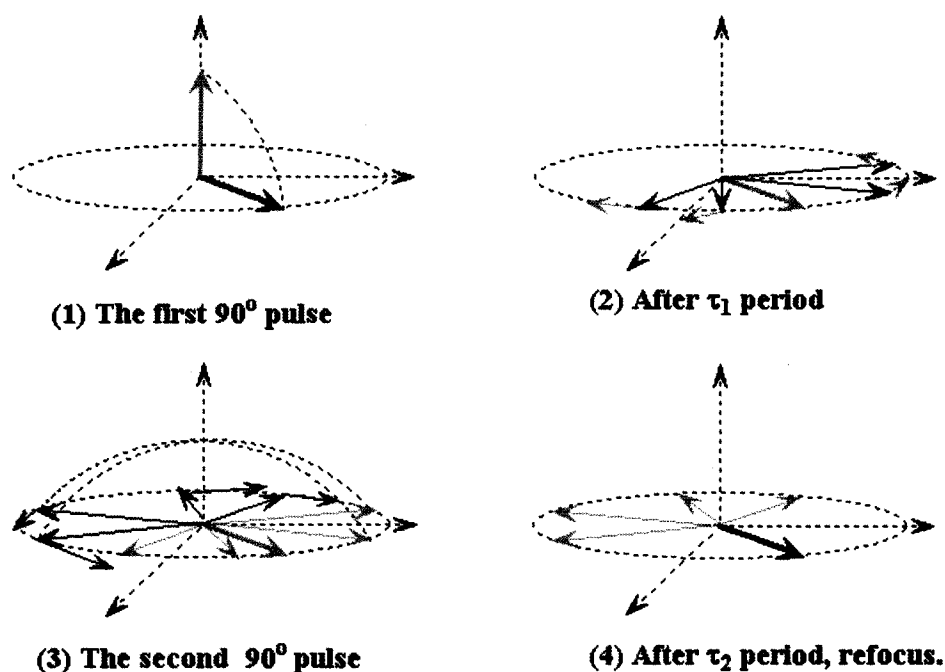


FIG. 3.3 The defocusing and refocusing of quadrupole-induced free precession. After the first pulse, the initial spin magnetizations (isochromats) dephase for time τ_1 . Because of the 90° -phase shift, the second pulse reverses sign of the accumulated phase of each isochromat. Therefore, the spin magnetizations refocus after τ_2 .

$M(t, \tau_1, \tau_2)$ during the acquisition period is given by

$$\begin{aligned}\vec{M}(t, \tau_2, \tau_1) &= \exp(A \cdot t) \cdot \vec{M}(\tau_2, \tau_1) \\ &= \exp(A \cdot t) \exp(A \cdot \tau_2) \exp(A^* \cdot \tau_1) \cdot \vec{M}(0)\end{aligned}\quad (3.32)$$

The observed FID signal is the sum of individual sites:

$$F(t, \tau_2, \tau_1) = 1 \cdot \vec{M}(t, \tau_2, \tau_1) \quad (3.33)$$

After Fourier transformation, the resulting line shape is

$$S(\omega) = -\text{Re}\left(1 \cdot (A - i\omega \cdot I)^{-1} \cdot \vec{M}(\tau_2, \tau_1)\right) \quad (3.34)$$

It is easy to see that calculating $F(t, \tau_1, \tau_2)$ in the time domain avoids the computationally intensive task of a different matrix inversion for each point in the frequency spectrum. Furthermore, corrections for finite pulse power and apodization are easier to perform in the time domain than in the frequency domain³³.

The most computationally intensive step in computing the N-site quadrupole echo line shape is the diagonalization of the $N \times N$ matrix A , which must be done for each of several thousands crystallite orientations in a powder sample. In general, the required time for finding all the eigenvalues and eigenvectors of an $N \times N$ matrix scales as N^3 , but in practice, special properties of the A -matrix defined in Eq. 3.28 make the scaling somewhat weaker, and dependent on the specific motional model and the relative magnitude of motion rates and precession frequencies. For example, A is tri-diagonal in the simple case of nearest-neighbor jumps along an arc, a reasonable model for restricted libration. In this case, test calculations reveal that the computation time appears to scale roughly as the 1.5 power of the number of sites regardless of whether the motion is in the slow, intermediate or fast regime. However, for the "all-sites" motional model, K is a full matrix, and the scaling increases roughly from $N^{0.8}$ in the slow regime, where A is diagonally dominant, to $N^{2.3}$ in the fast regime³⁰, where the equations become relatively stiff. With the present generation of desktop workstations, a complete calculation of the quadrupole echo line shape for N-site jumps can be carried out in 20-30 seconds for N as large as 100.

The complex eigenvector matrix S is given by

$$S^{-1}AS = \Lambda \quad (3.35)$$

where Λ is the diagonal eigenvalue matrix. $M(t, \tau_1, \tau_2)$ is then given by

$$\begin{aligned}\bar{M}(t, \tau_2, \tau_1) &= \exp(A \cdot t) \cdot \bar{M}(\tau_2, \tau_1) \\ &= S^{-1} \exp(\Lambda \cdot t) S \cdot \bar{M}(\tau_2, \tau_1)\end{aligned}\quad (3.36)$$

and by defining:

$$\sigma(t) = S \cdot \bar{M}(t, \tau_1, \tau_2) \quad (3.37)$$

one can obtain the very efficient equation

$$\sigma(t) = \exp(\Lambda t) \cdot \sigma(0) \quad (3.38)$$

One drawback of this approach is that because A is non-hermitian, S^l is not simply the adjoint of S but must be computed explicitly. There are other ways to compute the exponential of a matrix that avoid this complication, but test calculations using MATLAB reveal that they are not much more efficient, at least for matrices of the type considered in this thesis.

In order to complete the line shape computation, a small time Δt increment is chosen according to the required spectral window. N_p data points of the FID signal are computed from the recursion relation step by step. In practice, this recursion becomes numerically unstable for N_p greater than ~ 256 unless a small negative quantity is added to the real part of each eigenvalue. This also serves the important function of slightly broadening the spectral lines computed for each powder increment, so that fewer need be computed to insure convergence to a smooth line shape.

$$\sigma_{N_p} = \exp(\Lambda \cdot \Delta t) \cdot \sigma_{N_p-1} \quad (3.39)$$

$$F_{N_p} = 1 \cdot S^{-1} \cdot \sigma_{N_p} \quad (3.40)$$

A flow chart for the complete calculation is given in fig. 3.4:

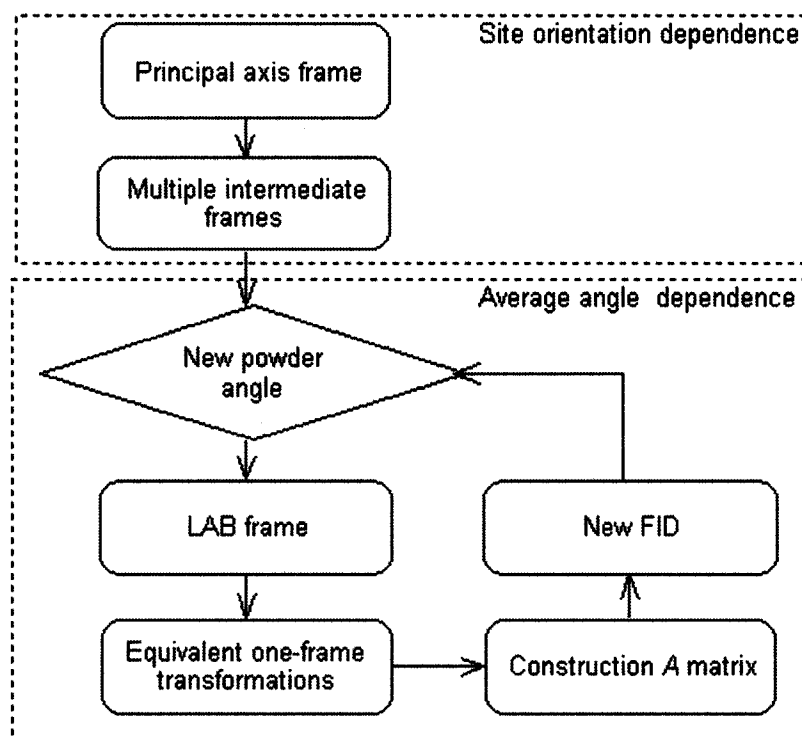


FIG. 3.4 Flow chart for simulation of QE powder pattern

In QE powder pattern simulations, site dependent frame transformations are pre-calculated outside the loop over crystallite orientations. Once a new powder angle is given, equivalent one-frame (PAS to LAB) Euler angles are obtained for each site, and the elements of the A matrix can be calculated. The resulting FIDs for different powder angles are accumulated and the final spectrum is obtained by DFT of the final FID.

In order to account for all randomly oriented crystallites, it is necessary to integrate numerically over only two Euler angles α and β . For a set of angles $\Omega=(\alpha,\beta)$, the powder average FID signal is given by

$$\bar{F}_N(t) = \frac{\sum_{j=0}^N w_j(\Omega_j) \cdot F_N(t, \Omega_j) \cdot p(\Omega_j)}{\sum_{j=0}^N w_j(\Omega_j)} \quad (3.41)$$

where $w_j(\Omega_j)$ is the integration weight, the probability of finding the crystallite with the orientation Ω , and for an isotropic distribution of crystallite orientations, the probability distribution equation $p(\Omega_j)$ is a constant and can be ignored. It is highly desirable to optimize the choice of powder angles to achieve line shape convergence for the minimum

possible number of orientations. Numerous schemes have been proposed, as summarized in table 3.1

Table 3.1. Methods for generating sets of powder angles α and β

	α	β_j	w_j
Planar grid ⁺	$2\pi k/N_\alpha$	$\pi(j+0.5)/N_\beta$	$\sin(\beta_j)$
Spherical grid ⁺	$2\pi k/N_\alpha$	$\cos^{-1}\left(1-2j+1/N_\beta\right)$	1
Planar ZCW*	$2\pi(jM \bmod N)/N$	$\pi(j+0.5)/N$	$\sin(\beta_j)$
Spherical ZCW*	$2\pi(jM \bmod N)/N$	$\cos^{-1}\left(1-2j+1/N\right)$	1

⁺ N_α and N_β are the numbers of integration steps. α and β are independent to each other, $k = 0, 1, 2, \dots, N_\alpha$ and for each α_k , β_j loops over $j = 0, 1, 2, \dots, N_\beta$.

* N and M are chosen such that $M=F(m)$ and $N = F(m+1)$, where $F(m)$ is the m^{th} Fibonacci number, $j=0, 1, 2, \dots, N-1$ ⁴².

3.3.2 Representative quadrupole echo line shape simulations

The following figure shows how the powder pattern changes as the motion rate increases from $1 \times 10^3 \text{ s}^{-1}$ to $1 \times 10^9 \text{ s}^{-1}$ and how the spectra intensity changes with τ_1 . The effects from motion rates are shown in fig. 3.5. It is obvious that at the fast limitation, the line shapes are similar to static quadrupole echo line shapes, but with much smaller equivalent motion-averaged C_Q . In fig. 3.6, the time between two pulses, τ_1 , is changed. And these simulations can be used in relaxation studies^{53, 70}.

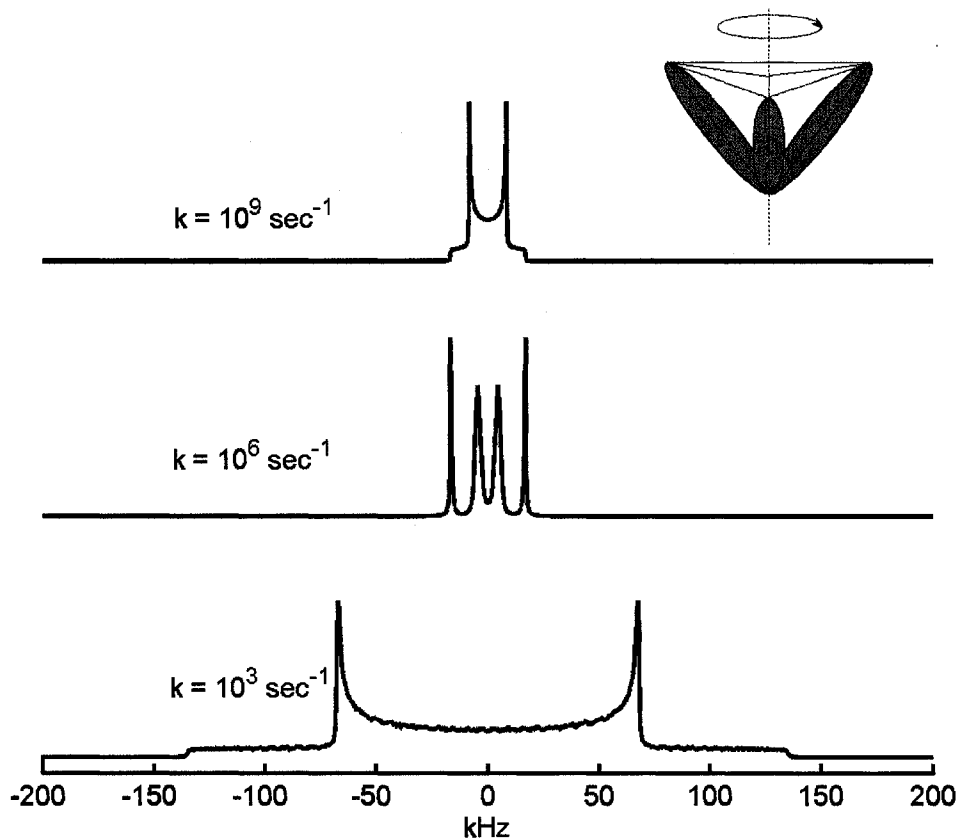


FIG 3.5 Motion rates and QE powder pattern

As the motion rate increases from 10^3 to 10^9 s^{-1} , the line shape of quadrupole echo spectrum changes. The three sites point to $(0, 30^\circ, 0)$, $(0, 30^\circ, 120^\circ)$ and $(0, 30^\circ, 240^\circ)$. When the motion is slow, the dynamical effect can be ignored. But as the motion becomes fast, the line shape changes and at the fast limit ($k = 10^9$ s^{-1}), the QE line shape is similar to the slow line shapes only with a smaller equivalent C_Q : the fast rotation averages most part of C_Q and only the terms in EFG that are parallel to the rotation axis survive. The simulation parameters are: $C_Q = 180$ kHz, $\eta_Q = 0$, and dwell time = 2.5 μs (spectrum window is ± 200 kHz). 500 Hz exponential broadening was applied and τ_1 is 25 μs .

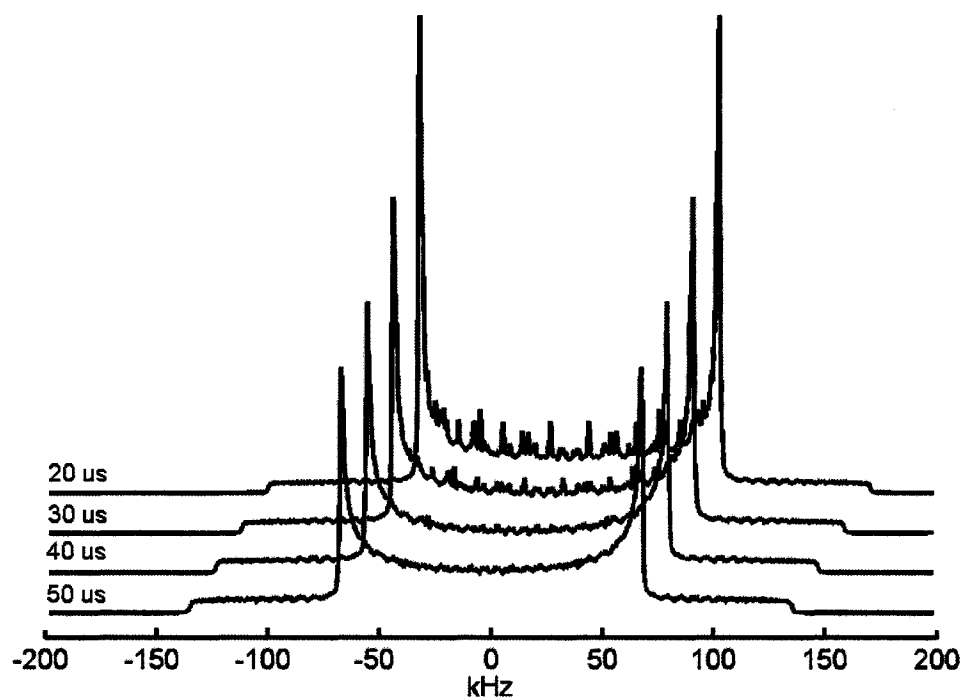


FIG 3.6. τ_1 and quadrupole echo line shape

As τ_1 increase from 20 μs to 50 μs , the intensity of quadrupole echo spectrum changes. The simulation used the same parameters as fig. 3.5, the motion rate is 10^3 s^{-1} . Since the motion is slow, the relaxation effect can be observed via the change of τ_1 .

3.4 Simulation of deuteron On/Off MAS

3.4.1 Periodic Hamiltonians

Magic angle spinning is an important recent addition to the arsenal of NMR techniques used to investigate molecular motion⁶⁰. In deuteron On/Off MAS experiments, mechanical rotation of a polycrystalline sample at rate ν_R about a fixed axis periodically changes the direction of the applied static magnetic field relative to a reference frame fixed in a given crystallite. This results in a periodically time-dependent Hamiltonian, which can be incorporated in the Stochastic Liouville equation in the usual

way^{61, 81, 82}. However, since this Hamiltonian no longer commutes with itself at different instants of time, solving the resulting differential equations poses a formidable computational problem.

If the spin system Hamiltonian is known and the initial density matrix is given, the evolution of the density matrix in absence of relaxation is governed by a Stochastic Liouville equation

$$\frac{d\sigma(t)}{dt} = -i[H(t), \sigma(t)] \quad (3.42)$$

and the solution is given formally by

$$\sigma(t) = U(t,0) \cdot \sigma(0) \cdot U^*(t,0) \quad (3.43)$$

$$U(t,0) = T \exp\left(-i \int_0^t H(t') dt'\right) \quad (3.44)$$

where T is the Dyson time ordering operator^{19, 20, 83}, which is necessary to define the meaning of the integral inside the exponential. Thus, the solution of the Liouville von-Neuman density matrix equation for rotating samples is significantly more complicated than that for static samples.

A second important complication is presented by the powder average procedure, illustrated in fig. 3.7.

below in section 3.4.3. The first order quadrupole coupling interaction gives the precession frequency for a site with powder orientation (ϕ, θ, ψ) and initial rotor phase angle γ as

$$\omega^{(1)}(t) = \frac{3e^2qQ}{4} \cdot W_{2,0}^Q(t) \quad (3.45)$$

And

$$W_{2,0}^Q(t) = \left[\bar{T} \cdot \overbrace{D_1(\alpha_1\beta_1\gamma_1)D_2(\alpha_2\beta_2\gamma_2)\dots}^{\text{intermediate rotation}} \cdot \overbrace{D(\phi,\theta,\psi)}^{\text{Powder Average}} \cdot \overbrace{D(0,\beta_R,2\pi\nu_R t + \gamma)}^{\text{RotorPhase}} \right]_{2,0} \quad (3.46)$$

$$\begin{aligned} \bar{T} &= [T_{2,2} \quad T_{2,1} \quad T_{2,0} \quad T_{2,-1} \quad T_{2,-2}] \\ &= \begin{bmatrix} \sqrt{\frac{1}{6}}\eta_Q & 0 & 1 & 0 & \sqrt{\frac{1}{6}}\eta_Q \end{bmatrix} \end{aligned} \quad (3.47)$$

where ν_R is the rotation speed in Hz and β_R is the magic angle in MAS experiments.

There are two fundamentally different approaches to solving the time dependent Stochastic Liouville equation that describes random jump motion combined with coherent sample rotation. A straightforward method is direct numerical integration⁸⁴. The other more elegant procedure is based on Floquet formalism^{52, 60, 62, 63, 85}. These two methods have comparable computational efficiency, and both are subject to the same stiffness considerations that apply to equations for non-rotating samples. It will be shown below that direct integration is more efficient when the rotor spins slowly, while Floquet formalism is better for fast sample rotation.

3.4.2 Direct Integration

The time dependence of the Hamiltonian due to coherent sample rotation implies that the propagators must be re-calculated each step of the numerical integration. One natural approach is to create a series of propagators for each point of the FID period.

$$\bar{M}_N = \exp(A_N)\bar{M}_{N-1} \quad (3.48)$$

where M_N, A_N are

$$M_N = M_+(N \cdot \Delta t) \quad (3.49)$$

$$A_N = i\Omega(N \cdot \Delta t) + K \quad (3.50)$$

The rate matrix K is independent of time, but the time step Δt must be made small so that $\Omega(t)$ won't vary appreciably for $0 < t < \Delta t$. Because the Hamiltonian is periodic, it is more efficient to construct an average Hamiltonian, which describes the evolution over one rotor period, τ_R .

Except for the first rotation period, the propagators for the n^{th} rotor cycle are given by

$$\exp(A(n\tau_R + t)) = \exp(A(t)) \cdot \exp^n(A_R) \quad t \in [0, \tau_R) \quad (3.51)$$

or

$$U_{n+N} = U_N \cdot U_R^n \quad N = 0, 1, 2, \dots, n-1 \quad (3.52)$$

Where

$$U_R = \exp(A_{N-1}) \cdot \exp(A_{N-2}) \cdots \exp(A_0) \quad (3.53)$$

Here, n is the number of complete rotor cycles and U_R is the propagator for one rotor cycle. Thus, only the propagators for the first rotation period need to be assembled as the product of a relatively large number of exponential matrices. Moreover, once U_R has been determined, propagators that share the same rotor phase angle can be obtained by n^{th} rotor

cycle shift U_R^n . The density matrix, $\sigma_N = \sigma(N\Delta t)$, in the first rotor cycle is calculated in the same way as for a static simulation.

$$\sigma_N = U_N \sigma_{N-1} \quad (3.54)$$

the following density matrix, $\sigma_{n+N} = \sigma(n\tau_R + N\Delta t)$ of n^{th} rotor cycle is

$$\sigma_{n+N} = U_N \cdot U_R^n \cdot \sigma_{n+N-1} \quad (3.55)$$

Then FID signal is the sum of individual site magnetizations.

$$F_{n+N} = \mathbf{1} \cdot \sigma_{n+N} = \mathbf{1} \cdot U_N \cdot U_R^n \cdot \sigma_{n+N-1} \quad (3.56)$$

The time step Δt is usually chosen to be an integer fraction of the rotor period, $\Delta t = \tau_R/N$, and it is highly advisable to make the rotor period equal to an integer multiple of the dwell time t_{DW} used to acquire the signal, $\tau_R = M t_{DW}$. This guarantees that each point of the experimental data sampled during the first rotor period, F_k , can be computed from a subset of products of $U_R(k)$. Only this sub-set of propagators need be retained to compute corresponding points of subsequent rotor periods.

If Δt is too large or the rotor is spinning very fast, the approximation that the Hamiltonian remains constant during the time step breaks down, while if it is too small the computation can become extremely slow. Moreover, a long enough string of rotational echoes must be simulated to cover the entire observed FID. For fast sample rotation, with rotor periods on the order of a few tens of microseconds, hundreds of rotational echoes occur and this consumes significant computation time.

3.4.3 Floquet method

Floquet formalism provides a complementary and conceptually attractive alternative to the direct integration method. In this approach, the finite-dimensional time-independent basis set is replaced by an infinite-dimensional time-dependent basis set, obtained by Fourier expansion of the relevant operators in an infinite series of harmonic functions $\exp(2\pi\nu_R t)$ of the rotor phase. The coefficients of the differential equations obtained by expansion in the Floquet basis and then time *independent*. In practice, the infinite Floquet basis set must be truncated and the number of basis functions included in the calculation greatly affects the total computing time. The basis set must be large enough to ensure the convergence for all observable rotational sidebands, and this requires at least three or four times as many basis functions as the number of observable sidebands. For a full width deuteron line shape spanning about 200 kHz, the number of observable sidebands is on the order of $n = 200 / \nu_R$. Thus for a 10 kHz spin rate, $n = 20$, each jump site would be described by a Floquet basis of 120 –160 functions, and numerical computations for mere than two or three jump sites would be impossibly slow. However, the number of observable sidebands decreases at least linearly with spin rate, and the time required for matrix diagonalization increases with the cube of the matrix size. The time required for Floquet computation of the line-shape therefore scales approximately as $1/\nu_R^3$. Moreover, at fast jump rates, motional narrowing leads to even fewer side bands and hence much smaller matrices. Thus, as higher spin rates become more widely available, the Floquet approach becomes increasingly attractive⁶⁰.

Floquet theory for systems with intermediate time scale jump dynamics has been described by several authors.^{64, 82} An equivalent description is discussed here, based on the semi-classical model of Sethi and co-workers^{52, 85} who view the spins in a stationary frame

corresponding to a reference subset of crystallites that have fixed orientation relative to laboratory fixed coordinates:

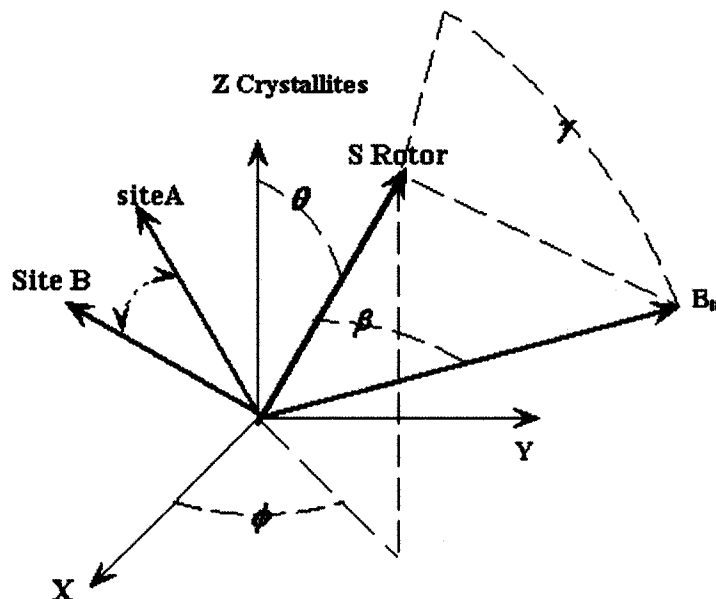


FIG 3.8 Spin flow in the rotor-fixed frame.

Two groups of Euler angles are used in order to describe the PAS directions of site A and B. The nucleus on these sites can exchange with each other while the crystallite is rotating around the rotor axis. Here, ϕ and θ describe the orientation of the reference subset z-axis with respect to the rotor, and the rotor phase angle γ is time independent for this subset. β is the fixed angle between the rotor axis and the magnetic field direction. Another two groups of Euler angles, which are used to define the principal axis system of particular tensor interactions, are not shown. Spins are flowing in and out of subsets A and B as the rotor spins around the magic angle.

In fig. 3.8, ϕ and θ describe the orientation of the reference subset Z axis with respect to the rotor, and the rotor phase angle γ is now time *independent*. β_R is the fixed angle between the rotor axis and the magnetic-field direction. Also shown are two principal Z-axis for two different equilibrium orientations of two deuteron EFG tensors. The Euler angles (α_{PAS} , β_{PAS} , γ_{PAS}) that define the rotations R_A and R_B connecting the principal-axis systems to the reference frame of two sites A and B are omitted for clarity. Using the stochastic Liouville equation, it can be shown that the time evolution of complex transverse magnetization $M_+ = M_x + iM_y$ of spins in the reference subset is determined by the differential equation with an extra term that describes nuclear spins flow.

$$\frac{\partial M_+(\phi, \theta, \beta_R, \gamma, t)}{\partial t} = i \cdot \omega(\phi, \theta, \beta_R, \gamma) \cdot M_+(\phi, \theta, \beta_R, \gamma, t) + \omega_R \cdot \frac{\partial M_+(\phi, \theta, \beta_R, \gamma, t)}{\partial \gamma} \quad (3.57)$$

The spin precession frequency, $\omega(\phi, \theta, \beta_R, \gamma)$, is time independent in this representation, since the subset has been defined to include all crystallites with the same fixed rotor phase angle γ . The second term in Eq. 3.57 represents the spins flow, which goes into and comes out of the chosen subset as the rotor turns. According to Floquet theory, both the complex transverse magnetization and the spin precession frequency may be expanded as infinite series of complex exponential functions of γ :

$$M_+(\theta, \phi, \beta_R, \gamma, t) = \sum_{j=-\infty}^{+\infty} C_j(\theta, \phi, \beta_R, t) \cdot \exp(ij\gamma) \quad (3.58)$$

$$\omega(\theta, \phi, \beta_R, \gamma) = \sum_{m=-P}^{+P} W_m(\theta, \phi, \beta_R) \cdot \exp(im\gamma) \quad (3.59)$$

Eq. 3.57 is thus decomposed into an infinite set of coupled differential equations for the time dependent coefficients C_j , which are connected by the spin precession frequency terms W_m :

$$\frac{\partial C_j(\theta, \phi, \beta_R, t)}{\partial t} = i \sum_{m=-P}^{+P} W_m(\theta, \phi, \beta_R) \cdot C_{j-m}(\theta, \phi, \beta_R, t) + i\omega_R \cdot jC_j(\theta, \phi, \beta_R, t) \quad (3.60)$$

If a reorientation process connects two sites as shown in Fig. 3.8, the reference subset now has two possible orientations, A and B.

Assuming that the reorientation process consists of jumps with rate k_{AB} from A to B and k_{BA} from B to A, the equation of motion for magnetization of the subset is now given by:

$$\frac{\partial}{\partial t} \begin{bmatrix} M_A \\ M_B \end{bmatrix} = i \begin{bmatrix} \omega_A + ik_{AB} & -ik_{AB} \\ -ik_{AB} & \omega_B + ik_{AB} \end{bmatrix} \cdot \begin{bmatrix} M_A \\ M_B \end{bmatrix} + \omega_R \frac{\partial}{\partial \gamma} \begin{bmatrix} M_A \\ M_B \end{bmatrix} \quad (3.61)$$

Analogous Floquet expansions yield the results (Eq. 3.62)

$$\begin{cases} \frac{\partial C_j^A}{\partial t} = i \sum_{m=-P}^{+P} W_m^A(\alpha_A, \beta_A, \gamma_A, \beta_R, \theta, \phi) \cdot C_{j-m}^A + i\omega_R C_j^A - k_{AB} C_j^A + k_{BA} C_j^B \\ \frac{\partial C_j^B}{\partial t} = i \sum_{m=-P}^{+P} W_m^B(\alpha_B, \beta_B, \gamma_B, \beta_R, \theta, \phi) \cdot C_{j-m}^B + i\omega_R C_j^B - k_{BA} C_j^B + k_{AB} C_j^A \end{cases} \quad (3.62)$$

or

$$\frac{\partial \bar{C}}{\partial t} = iL_F \cdot \bar{C}$$

where

$$\bar{C} = \begin{bmatrix} C_j^A \\ C_j^B \end{bmatrix} \quad (3.63.a)$$

$$L_F = \begin{bmatrix} H_F^A + ik_{AB} \cdot I & -ik_{BA} \cdot I \\ -ik_{AB} \cdot I & H_F^B + ik_{BA} \cdot I \end{bmatrix} \quad (3.63.b)$$

Thus the superoperator L_F includes both spin-precession terms (H_F) and motional rates

(k):

$$L_F = \begin{bmatrix} \ddots & W_{-1}^A & W_{-2}^A & 0 & 0 & -ik_{AB} & 0 & 0 & 0 & 0 \\ W_1^A & W_0^A - \omega_R + ik_{AB} & W_{-1}^A & W_{-2}^A & 0 & 0 & -ik_{AB} & 0 & 0 & 0 \\ W_2^A & W_1^A & W_0^A + ik_{AB} & W_{-1}^A & W_{-2}^A & 0 & 0 & -ik_{AB} & 0 & 0 \\ 0 & W_2^A & W_1^A & W_0^A + \omega_R + ik_{AB} & W_{-1}^A & 0 & 0 & 0 & -ik_{AB} & 0 \\ 0 & 0 & W_2^A & W_1^A & \ddots & 0 & 0 & 0 & 0 & -ik_{AB} \\ -ik_{BA} & 0 & 0 & 0 & 0 & \ddots & W_{-1}^B & W_{-2}^B & 0 & 0 \\ 0 & -ik_{BA} & 0 & 0 & 0 & W_1^B & W_0^B - \omega_R + ik_{BA} & W_{-1}^B & W_{-2}^B & 0 \\ 0 & 0 & -ik_{BA} & 0 & 0 & W_2^B & W_1^B & W_0^B + ik_{BA} & W_{-1}^B & W_2^B \\ 0 & 0 & 0 & -ik_{BA} & 0 & 0 & W_2^B & W_1^B & W_0^B + \omega_R - ik_{BA} & W_{-1}^B \\ 0 & 0 & 0 & 0 & -ik_{BA} & 0 & 0 & W_2^B & W_1^B & \ddots \end{bmatrix} \quad (3.64)$$

The extension of this formalism to jumps among N sites is obvious.

For fast MAS ($\nu_R = 20 \sim 50\text{kHz}$), no more than twenty sidebands (six pairs) are left with significant intensity in deuteron MAS spectrum. It is therefore permissible to

truncate the Floquet matrix for each site to size $\sim 60 \times 60$ or less. The minimum required size can be determined empirically by monitoring convergence of the line shape for the highest order observable sidebands. Now the free induction decay period is divided into N intervals, whose duration, Δt , is equal to the experimental sampling interval. The coefficients of each site in the reference subset are then obtained by straightforward matrix diagonalization. For site A and B, the differential equation of the coefficients is:

$$\begin{pmatrix} C_A(N\Delta t) \\ C_B(N\Delta t) \end{pmatrix} = \exp(iL_F \cdot \Delta t) \cdot \begin{pmatrix} C_A((N-1)\Delta t) \\ C_B((N-1)\Delta t) \end{pmatrix} \quad (3.65)$$

Although the L_F matrix can be very large (up to $\sim 60N$, where N is the number of jump sites), it only has to be diagonalized once for each crystallite orientation since none of the terms in Eq. 3.65 depend on time.

The powder average is performed by integrating over the rotor phase angle γ as well as the reference subset angles ϕ and θ . The average over γ can be performed in closed form, and this eliminates all but the zero order C-coefficients:

$$\begin{aligned} \overline{M_+(\theta, \phi, N\Delta t, \beta_R)} &= \overline{\sum_{i \in \text{all sites}} M_i(\theta, \phi, N\Delta t, \beta_R)} \\ \overline{M_i(\theta, \phi, N\Delta t, \beta_R)} &= \frac{1}{2\pi} \int_0^{2\pi} M_i(\theta, \phi, N\Delta t, \beta_R, \gamma) d\gamma \\ &= \frac{1}{2\pi} \sum_{j=-\infty}^{+\infty} \int_0^{2\pi} C_j^i(\theta, \phi, N\Delta t, \beta_R) \exp(ij\alpha) d\gamma \\ &= \sum_{j=-\infty}^{+\infty} C_j^i(\theta, \phi, N\Delta t, \beta_R) \cdot \delta(j) = C_0^i(\theta, \phi, N\Delta t, \beta_R) \end{aligned} \quad (3.66)$$

where the bar over $M_+(\theta, \phi, N\Delta t)$ denotes the phase angle average over all sites, whose phase angle distributes uniformly over $[0, 2\pi]$. The FID signal is obtained by further averaging $C_0^i(\phi, \theta, N \cdot \Delta t)$ over an isotropic distribution of (ϕ, θ) .

The precession terms W_m , $m = \pm 2, \pm 1, 0$ in L_F are given by:

$$W_m(\beta_R) = d_{m0}^{(2)}(\beta_R) \cdot \sum_{r,q} \lambda_r^{(2)} D_{r,q}^{(2)}(\alpha, \beta, \gamma) D_{q,m}^{(2)}(\phi, \theta, 0) \quad (3.67)$$

where m for first order quadrupole interactions varies from -2 to $+2$ and D_{ij} is the element of the second rank Wigner rotation matrix. Wigner rotation matrix $D(\alpha, \beta, \gamma)$ rotates the EFG tensor from its principal axis system to the reference subset frame, and $D(\phi, \theta, 0)$ rotates the reference subset axes into alignment with the rotor fixed frame, about whose z-axis the rotor spins. The irreducible spherical tensor components $\lambda_r^{(2)}$ of the ^2H quadrupole interaction are defined in the principal axis system of the EFG tensor:

$$\begin{aligned} \lambda_0^{(2)} &= \sqrt{3/8} \cdot \frac{e^2 q_{zz} Q}{\hbar} \\ \lambda_{\pm 1}^{(2)} &= 0 \\ \lambda_{\pm 2}^{(0)} &= \eta_Q / 4 \cdot \frac{e^2 q_{zz} Q}{\hbar} \\ \eta_Q &= \frac{q_{xx} - q_{yy}}{q_{zz}} \end{aligned} \quad (3.68)$$

Therefore, $C_Q = \frac{e^2 q_{zz} Q}{\hbar}$ is the quadrupole coupling constant and η_Q is the asymmetry parameter. In general, η_Q are site dependent, but the site label has been suppressed in Eq. 3.68 to simplify the notation. For multiple frame rotations, the precession terms W_m , and $m = \pm 2, \pm 1, 0$ could be written as

$$W_m(\beta_R) = d_{m0}^{(2)}(\beta_R) \cdot \frac{3e^2 q_{zz} Q}{4} \left[\bar{B} \cdot \overbrace{D(\alpha_1 \beta_1 \gamma_1) D(\alpha_2 \beta_2 \gamma_2) \cdots D(\phi, \theta, 0)}^{\text{multiple frame rotation}} \right]_{m,0} \quad (3.69)$$

$$\bar{B} = \left[\sqrt{\frac{1}{6}} \eta_Q \quad 0 \quad 1 \quad 0 \quad \sqrt{\frac{1}{6}} \eta_Q \right] \quad (3.70)$$

Since the calculation of multiple frame rotations is independent of the powder angles ϕ and θ , it can be done out of the powder average loop in order to improve

computational efficiency. The number of powder increments needed to achieve convergence can be as small as 100, depending on the motional regime. However, it is necessary to examine the effect of basis size on the computed sideband intensities. A typical convergence testing calculation is shown in fig 3.9, demonstrating that the number of side bands included in calculation needs to be at least the twice of the number of experimentally observed side bands in order to avoid truncation error. In practice, this renders Floquet simulations for slow sample rotation unacceptably time consuming for all but the simplest dynamical systems.

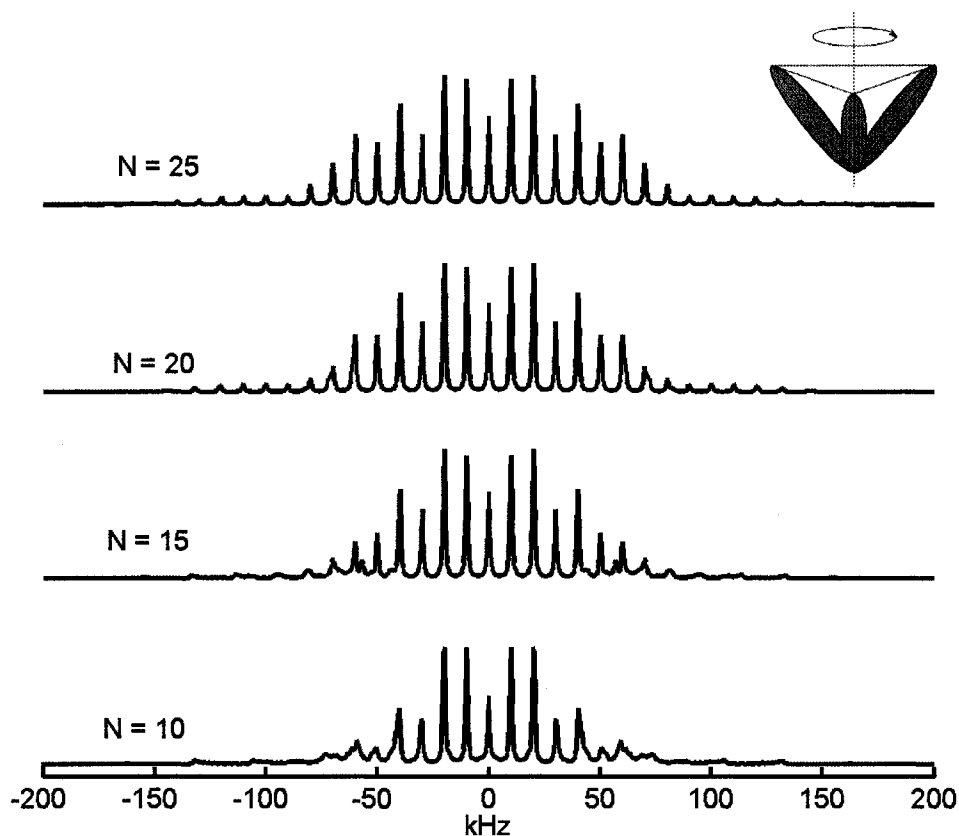


FIG. 3.9 Line shape and L_F matrix size

Here MAS simulations are shown with different number of sidebands pairs, N , that were shown in the figure. Other parameters are $C_Q = 180\text{kHz}$, $\eta_Q = 0$, three spins exchange with equivalent motion rate $k = 10^5\text{ s}^{-1}$ and their orientations are shown by the inset. N is the number of sideband pairs that are included in the simulation. It is obvious that when N increases to as twice as the number of experimental side bands, the truncation effect can be neglected.

3.4.4 Chemical shift effects

In general, deuterons in diamagnetic samples have small chemical shifts but this is not the case for paramagnetic solids, in which the chemical shift interaction can be large (20 ~ 100kHz) and comparable to the quadrupole coupling interaction (100~300kHz). Furthermore, the chemical shift increases linearly with field strength. Thus, deuteron chemical shift anisotropy on the order of 10-20 ppm is expected to produce easily observable distortions of deuteron quadrupole echo spectra at fields of ~11T or higher.^{35,}

86-89

The Hamiltonian of an isolated spin $I = 1$ can be written as the sum of the chemical shift and quadrupolar Hamiltonians:

$$\hat{H} = \hat{H}_{CS} + \hat{H}_Q \quad (3.71)$$

if Euler angles $(\alpha_{cs}, \beta_{cs}, \gamma_{cs})$ rotate the PAS of the chemical shielding tensor into the PAS of quadrupole interaction, then the chemical shift Hamiltonian under multiple frame rotation is given by

$$H_{CS} = \delta_{ISO}\omega_0 \cdot I_Z + \delta_{CSA}\omega_0 \cdot I_Z \cdot \left[\tilde{T}^{CS} D(\alpha_{cs}, \beta_{cs}, \gamma_{cs}) \overbrace{D(\alpha_1, \beta_1, \gamma_1) \cdots D(\phi, \theta, 0)}^{\text{Multiple rotation}} D(0, \beta_R, 2\pi\nu_R + \gamma) \right]_{2,0} \quad (3.72)$$

where the chemical shift tensor B^{CS} is

$$\begin{aligned} \tilde{T}^{CS} &= \begin{bmatrix} T_{2,2}^{CS} & T_{2,1}^{CS} & T_{2,0}^{CS} & T_{2,-1}^{CS} & T_{2,-2}^{CS} \end{bmatrix} \\ &= \left[\sqrt{\frac{1}{6}}\eta_{CS} \quad 0 \quad 1 \quad 0 \quad \sqrt{\frac{1}{6}}\eta_{CS} \right] \end{aligned} \quad (3.73)$$

and the secular part is given by

$$H = \delta_{ISO}\omega_0 I_Z + [\bar{\Lambda}^{CS} \cdot D(\alpha_{cs}, \beta_{cs}, \gamma_{cs}) \cdot \mathcal{D}]_{2,0} I_Z + [\bar{\Lambda}^Q \cdot \mathcal{D}]_{2,0} \hat{T}_{2,0} \quad (3.74)$$

where

$$\bar{\Lambda}^{CS} = \delta_{CSA} \omega_0 \left[\sqrt{\frac{1}{6}} \eta_{CS} \quad 0 \quad 1 \quad 0 \quad \sqrt{\frac{1}{6}} \eta_{CS} \right] \quad (3.75)$$

$$\bar{\Lambda}^Q = \frac{e^2 q_{ZZ} Q}{4I(2I-1)} \left[\sqrt{\frac{1}{6}} \eta_Q \quad 0 \quad 1 \quad 0 \quad \sqrt{\frac{1}{6}} \eta_Q \right] \quad (3.76)$$

$$\hat{T}_{2,0} = \sqrt{\frac{1}{6}} (3I_Z^2 - I \cdot I) \quad (3.77)$$

$$\bar{D} = \overbrace{D(\alpha_1, \beta_1, \gamma_1)}^{\text{Multiple Rotation}} \cdots D(\phi, \theta, 0) D(0, \beta_R, 2\pi\nu_R + \gamma) \quad (3.78)$$

Therefore, if the chemical shift and quadrupole interaction principal axis frames coincide, Eq. 3.74 can be simplified as Eq. 3.79 and 3.80 show, the two single-quantum coherences precess at frequencies given by

$$\omega_{\pm 1 \leftrightarrow 0} = [\bar{\Lambda}_{\pm} \bar{D}]_{2,0} \pm \delta_{ISO} \omega_0 \quad (3.79)$$

where

$$\bar{\Lambda}_{\pm} = \sqrt{\frac{1}{6}} \left(\frac{3e^2 q_{ZZ} Q}{4} \eta_Q \pm \delta_{CSA} \omega_0 \eta_{CS} \right) \quad 0 \quad \frac{3e^2 q_{ZZ} Q}{4} \pm \delta_{CSA} \omega_0 \quad 0 \quad \sqrt{\frac{1}{6}} \left(\frac{3e^2 q_{ZZ} Q}{4} \eta_Q \pm \delta_{CSA} \omega_0 \eta_{CS} \right) \quad (3.80)$$

Since the resulting NMR spectrum is asymmetric, the FID signals of the ± 1 coherences must be calculated separately. It is easy to code the precession frequency expressions needed either for direct integration or for Floquet simulations. The terms in Eq. 3.69 and 3.70 that only include quadrupole interaction are replaced by:

$$W_m(\beta_R) = d_{m0}^{(2)}(\beta_R) \cdot \frac{3e^2 q_{ZZ} Q}{4} \left[\bar{B} \cdot \overbrace{D(\alpha_1, \beta_1, \gamma_1) D(\alpha_2, \beta_2, \gamma_2) \cdots D(\phi, \theta, 0)}^{\text{multiple frame rotation}} \right]_{m,0} \quad (3.81)$$

and here, \bar{B} is mixed by CSA and quadrupole interactions.

$$\bar{B}_{\pm} = \left[\sqrt{\frac{1}{6}} \left(\frac{3e^2 q_{ZZ} Q}{4} \eta_Q \pm \delta_{CSA} \omega_0 \eta_{CS} \right), \quad 0, \quad \frac{3e^2 q_{ZZ} Q}{4} \pm \delta_{CSA} \omega_0, \quad 0, \quad \sqrt{\frac{1}{6}} \left(\frac{3e^2 q_{ZZ} Q}{4} \eta_Q \pm \delta_{CSA} \omega_0 \eta_{CS} \right) \right] \quad (3.82)$$

Now the FID under the effects from CSA is the sum of two different FIDs ($-1 \Leftrightarrow 0$ and $0 \Leftrightarrow +1$), since the energy levels of the quadrupole interaction are unequally distorted by CSA interaction and the line shape is no longer symmetric. In practice, On/Off MAS FIDs are calculated with B_+ and B_- (Eq. 3.82) separately, and the final FID is the sum of these two individual FIDs.

In order to study small chemical shift anisotropy, slow spinning MAS ($\nu_R = 1\sim 5$ kHz) is generally used to avoid the complete suppression of the interaction. The information about chemical shift anisotropy is then revealed by the asymmetry of sideband intensities on opposite sides of the center band. Direct integration is certainly more efficient than the Floquet method for such simulations. However, it is shown below in fig. 3.10, fig. 3.11 that the line shapes of On/OFF MAS side bands retain significant asymmetry even at high spin rates when CSA is sufficiently large. In fig. 3.12, CSA orientation effects on MAS spectra are shown. Thus, fast spinning On/OFF MAS can probably be used to investigate the intensity and orientations of chemical shift anisotropy, and Floquet methods could be used to simulate effects of motion on these spectra. Perhaps fortunately, deuteron CSA interactions in diamagnetic samples are often smaller than 5 ppm, and rarely exceed 20 ppm. As fig. 3.10 shows, the effects on MAS line shapes can be ignored when the CSA interaction is smaller than ~ 20 ppm. Therefore, in most deuteron NMR experiments and calculations, CSA effects can be ignored.

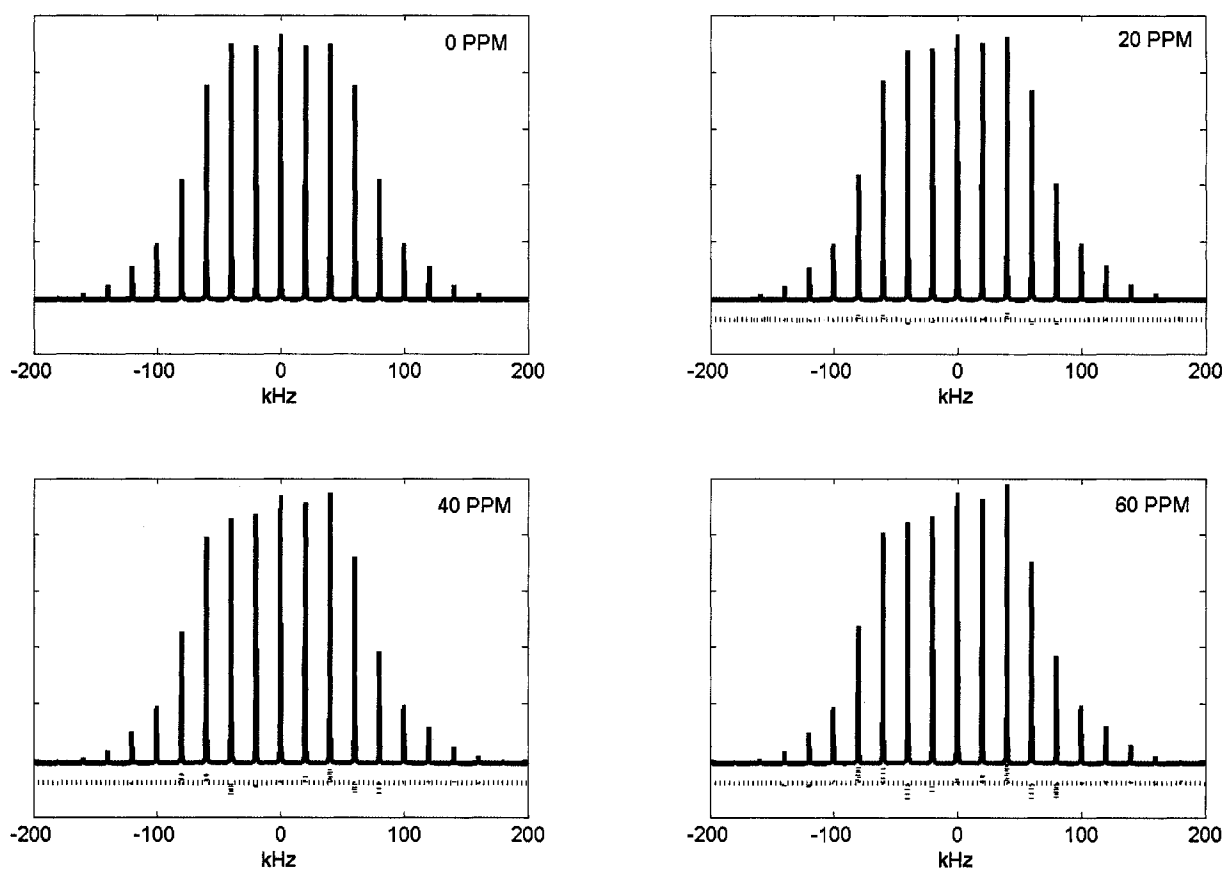


FIG. 3.10 Simulations of MAS spectra with co-axial CSA and quadrupolar interactions. Simulation parameters: 2-site jumps appropriate for phenyl ring π -flips, with $C_Q = 180$ kHz, $\eta_Q = 0$ and CSA increasing from 0 to 60 ppm. The differences between CSA-free and CSA distorted MAS line shapes are shown by dashed lines. The rotor spins at 20 kHz and the carrier frequency is 115.1 MHz. Jump rate is 10^3 s^{-1} and the CSA tensor shares the same orientations as EFG tensor and has $\eta_{\text{CSA}} = 0$.

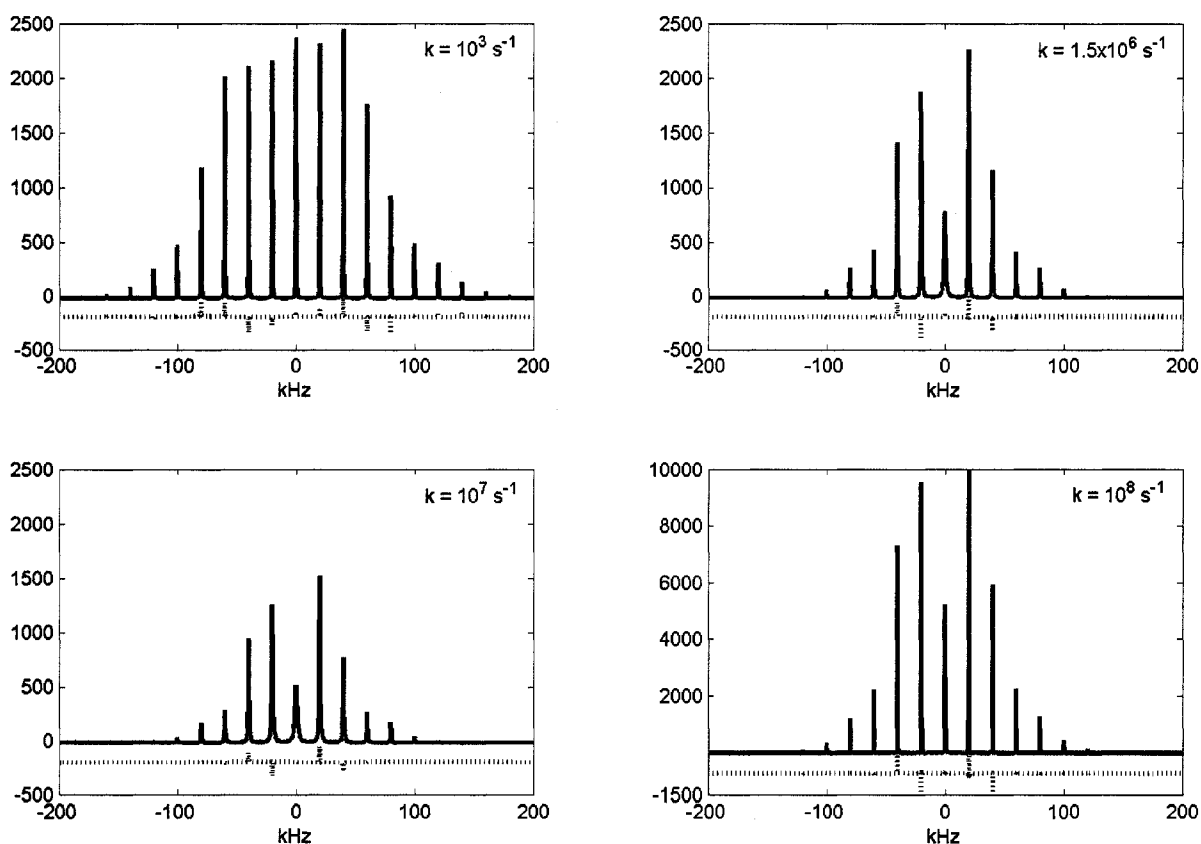


FIG. 3.11 Simulations of the effects motion on MAS spectra with of co-axial CSA and quadrupole coupling tensors

Jump rates are indicated in each panel, and other simulation parameters are the same as fig. 3.10 with CSA fixed at 60 ppm. As the motion rate becomes fast, the MAS spectrum changes its shape in a characteristic manner.

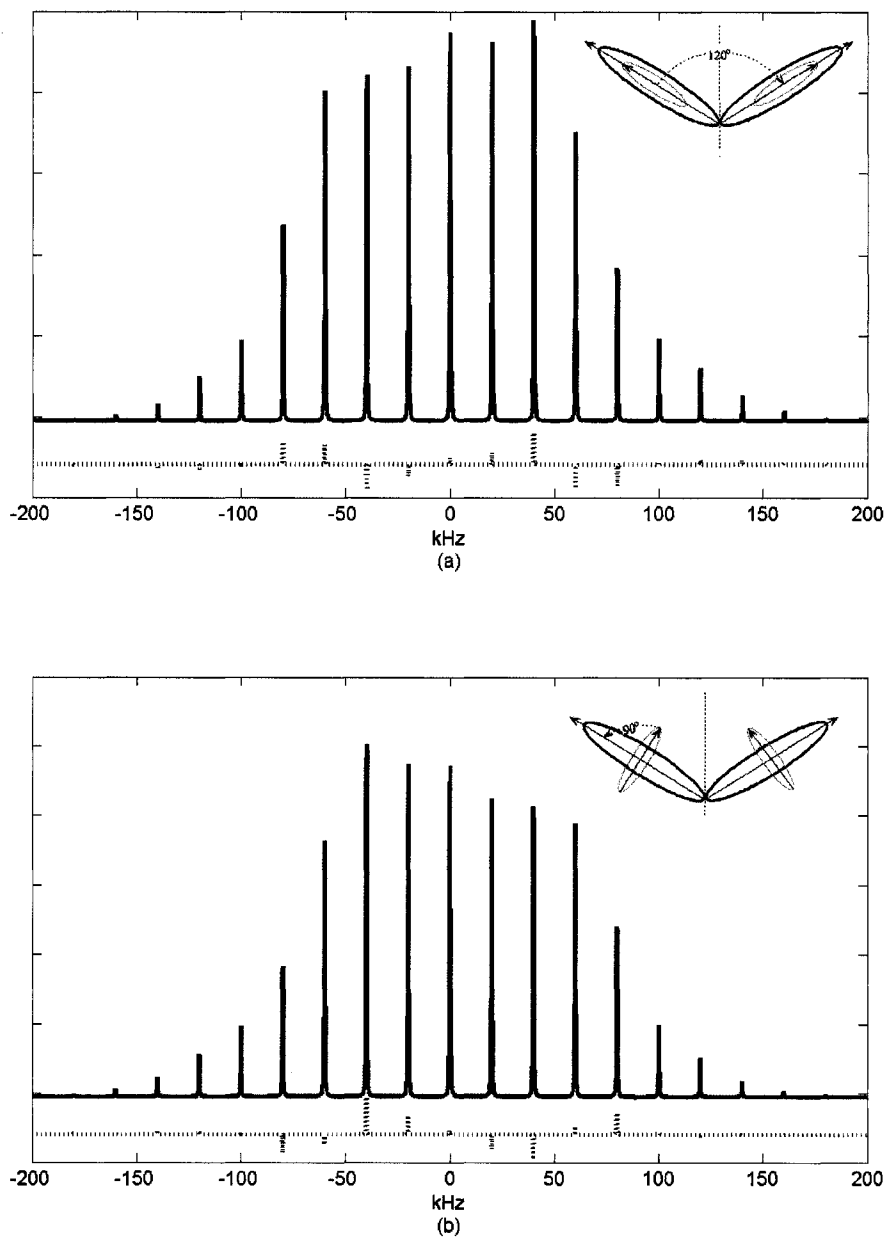


FIG. 3.12 Simulations of the effects of non-coaxial interactions

Here, the effects of CSA interactions whose PAS is not coincident with the EFG PAS are considered. (a) The CSA orientation is co-axial with EFG tensor and (b) the CSA orientation is defined by an extra group of Euler angles $(0, 90^\circ, 0)$, which transforms the CSA PAS into the PAS of the EFG tensor. The insets show the relationship between CSA and EFG PAS systems. The dashed lines show the difference between 60ppm and 0ppm MAS spectra for both cases. The motion rate is 10^3 s^{-1} , and other parameters are the same as fig. 3.10 and 3.11.

3.5 Conclusion

The development of new MAS line shape simulation procedures is a frustrating and difficult task, especially when effects of molecular motion must be included. Numerical methods used to simulate quadrupole echo spectra of stationary samples are well known and widely used. However, prior to the present work only a few simulations of MAS line shapes for simple cases of molecular motion had been described in the literature. The time consuming simulation for ON/Off MAS now can be finished in minutes though it still requires significantly longer computation time than simulations for non-rotating samples. Our procedures are coded in MATLAB, where operations with vectors and matrices are especially well optimized. In future investigations, the powder average is an idea target for parallel computation to achieve dramatic reduction in computation time. Complete MATLAB programs, including the user-friendly GUI, are available at <http://nmr.physics.wm.edu>

Chapter 4

Dynamics of Urea and its Inclusion Compound

4.1 Introduction

The primary goal of this chapter is to demonstrate the superiority of deuteron OMAS experiments in analyse multi-axis dynamical motion. Here two distinct molecular rotations occur around different axes on different time scales. Numerical simulations of OMAS spectra for urea and its inclusion compound will be presented and discussed in detail. OMAS experiments were carried out on a urea-d₄/octanoic acid inclusion compound (C₈A/UIC). Urea inclusion compounds (UIC) are typical host-guest materials⁹⁰. The host urea molecules are arranged around long hexagonal channels that are stabilized by inclusion of suitable guests. Long rod like guest molecules, such as n-alkanes, n-alkanoic acids, under go a variety of dynamical processes, for example, rapid rotation around the long molecular axis ($k > 10^8 \text{ s}^{-1}$), fast libration at the chain ends ($k > 10^{10} \text{ s}^{-1}$) and rapid methyl group rotation ($k > 10^{11} \text{ s}^{-1}$). These motions are generally much faster than and uncorrelated with motion of the host. It is well known that host molecular motions occur around two different bonds (CN and CO). Both motional rates have been measured as functions of temperature in C₈A/UIC, using quadrupole echo (QE) and selective inversion methods⁹¹. Because motion around the CN bond is slow on the QE time scale, it is difficult to determine this rate accurately in the presence of the much faster CO motion. Deuteron OMAS experimental spectra show a high sensitivity to both

motional time scales. A comparison between simulated and experimental OMAS spectra will be shown to yield high accuracy in measuring both motion rates simultaneously.

4.2 Structure and dynamics of urea and its inclusion compound (UIC)

4.2.1 Structure of urea and UIC

Urea, $(\text{NH}_2)_2\text{CO}$, is chosen as the first molecule to be studied since its structure is well known and its dynamics properties have been studied via various NMR experiments. In deuterium labeled urea, $(\text{ND}_2)_2\text{CO}$, four protons are replaced by deuterons and the structure is shown in fig. 4.1.

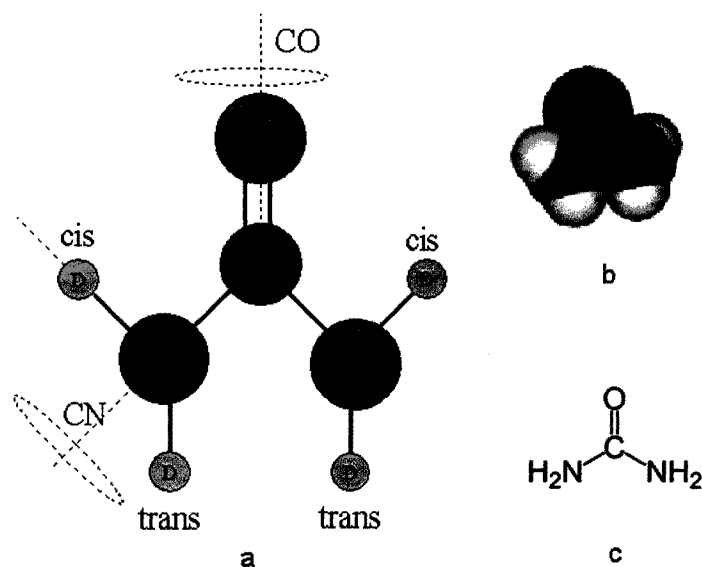


FIG. 4.1 Structure of urea

(a) The planer molecule has a symmetry axis parallel CO bond. (b) 3-D view of urea molecule. (c) The chemical formula of urea.

The molecule is planer with its symmetry axis along CO bond. Four deuterons split into two amide groups, each group has a symmetry axis along CN bonds. Two ND bonds are oriented almost anti-parallel to CO bond. These anti-parallel deuterons are called as

trans deuteron. The other two are oriented with approximately 60° respect to CO bond and defined as *cis* deuteron.

In pure urea, two urea molecules are contained in one tetragonal crystal lattice via hydrogen bonds. But in urea inclusion compounds (UIC), in which urea acts as host molecules, the urea molecules forms narrow channels with variety of long unbranched chain organic guest molecules, such as n-alkanes, n-alkanoic acids and alkandioic acids etc., packed into the channels^{92, 93}. Urea molecules in UIC are also held together by a network of hydrogen bonds between individual urea molecules to form the hexagonal cell unit. The carbonyl oxygen is interacted with the neighboring urea molecules via four hydrogen bonds. The length and orientation of these hydrogen bonds are listed in table 4.1.^{92, 94-96}

Table 4.1 Hydrogen Bond Parameters for pure urea and Hexadecane-UIC

	Urea / UIC (<i>cis</i>)	Urea / UIC (<i>trans</i>)
$d(\text{N}-\text{H})^\circ \text{\AA}$	1.064 / 0.996	1.042 / 0.990
$d(\text{N}-\text{H})^\circ \text{\AA}$	2.992 / 3.033	2.957 / 2.984
$d(\text{O}-\text{H})^\circ \text{\AA}$	1.948 / 1.976	1.976 / 2.034
$\angle(\text{C}=\text{O}\cdots\text{H})^\circ$	105.7 / 149.0	149.0 / 118.6
$\angle(\text{C}=\text{O}\cdots\text{N})^\circ$	110.6 / 157.3	157.3 / 119.3
$\angle(\text{N}-\text{H}\cdots\text{O})^\circ$	166.0 / 155.9	155.9 / 160.3

It is clear that the hydrogen bond length changes slightly for urea and UICs, but their orientations change dramatically. Thus, the local environment of each deuteron changes and their dynamical properties is not identical. In addition, UIC channels are held together by Van del Waals forces. X-ray studies of several UICs show that a few of the urea molecules could rotate into the channel and form hydrogen bonds with the guest molecules.^{69, 97} The structure of UIC is shown in fig. 4.2, which illustrates two anti-

parallel helical ribbons of ureas forms the walls of the channels. The diameter of the channel is between 5.1-5.9 Å and the length of the channel depends on the guest molecule length. In order to form a stable inclusion compounds, the channel length is slightly longer than the guest molecule. In addition, the stability of the compounds increases as the chain and channel becomes longer

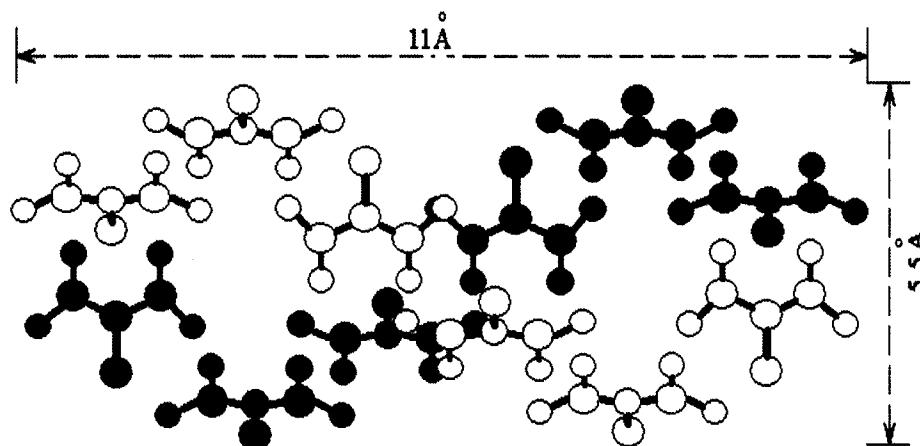


FIG. 4.2 One unit cell for octanoic acid / urea inclusion compound (C_8A -UIC) The channel is formed by two right-handed helices (black and gray) pointing in opposite directions. The screw direction points to the left for the gray helix and to the right for the black helix. The guest molecules that are packed inside the channel are not shown here. The length of the channel depends on the chain length of guest molecules.

Octanoic acid-UIC (C_8A -UIC) crystals are made by mixing warm saturated solutions of urea and the guest molecule in D_2O solution with mass ratio (urea to octanoic acid) 3: 1. The resulting precipitate is filtered, dried, and kept in a container under saturated by D_2O vapor in order to prevent the loss of deuterium by exchange with water vapor. About 6mg of small, needlelike C_8A -UIC crystals were finely ground and tightly packed into 2.5mm High-MAS NMR tubes.

4.2.2 Guest molecular motion

Various motions can occur in the guest molecules. Typically, straight chain hydrocarbon guests rotate rapidly about their long axis inside the one-dimensional urea channel. Some studies show⁹⁸⁻¹⁰⁰ that cooling of these inclusion compounds results in a phase transition involving anisotropic contraction of the hexagonal lattice into a orthorhombic lattice. Urea channel structure is conserved but the freedom of rotation of the guest molecules is severely reduced^{101, 102}. The phase transition temperature is dependent on the nature of guest molecules: the transition covers a 30 K temperature range centered at around 243K. It has been suggested that the driving force of the transition is an order-disorder transition of the guest molecules¹⁰³. Deuteron NMR has been widely used to study suitably labeled guest molecules. For alkane guests, the motions are rapid ($k \geq 10^8 \text{ s}^{-1}$).¹⁰⁴⁻¹⁰⁶ In addition to rotation about the long axis, rapid torsional libration ($k \geq 10^{10} \text{ s}^{-1}$) of the chain ends and rapid methyl group rotation ($k \geq 10^{12} \text{ s}^{-1}$) has been observed¹⁰⁷. Although not detectable by NMR, restricted (up and down) *translational* diffusion of the centers of mass of the guest molecules has been observed by X-ray and neutron scattering experiments and the diffusion coefficient is on the order of $10^{-6} \text{ cm}^2 \text{ s}^{-1}$, over a distance on the order of 2 \AA .

The guest molecular motions are considered to be independent of host molecular motions. Although hydrogen bonds can connect the host with alkanolic acid guest molecules, they are not strong enough to quench guest rotation at room temperature. The thesis focuses on the study of the host molecule, which is labeled with deuteron. Motions of the octanoic acid discussed with elsewhere^{27, 94}.

4.3 Host molecular motion

4.3.1 CO and CN motions

Two independent molecular motions occur in urea^{90, 108}. The first one is the flip of the whole molecule around its symmetry axis (CO bond). The 180° flip about the CO bond results a large change in the quadrupole coupling interaction tensor of cis deuterons since the EFG tensors of these deuterons orient at a large angle (~59°) with respect to the CO bond. On the other hand, this motion has almost no effect on the trans deuterons, whose largest EFG components are nearly co-linear with the CO bond.

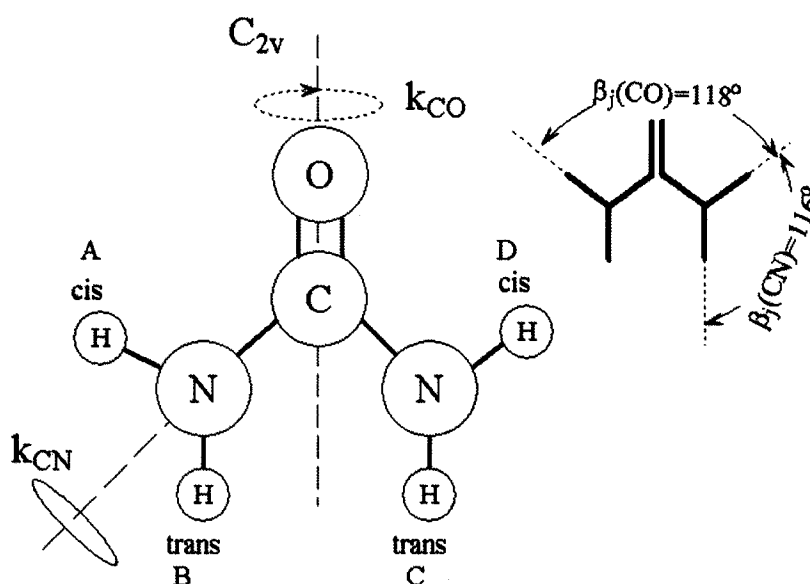


FIG. 4.3 Molecular motions in urea

The figure presents C_{2v} symmetry axes, rotation axes, rates k_{CO} and k_{CN} , the jump angles $\beta_j(CO)$ and $\beta_j(CN)$. CO motion leads the exchange between sites A and D (cis \leftrightarrow cis), or B and C (tran \leftrightarrow tran), but CN motion causes the exchange between sites A and B, or C and D, resulting the change of cis and trans deuteron.

Over the temperature range between 263K and 343K, the motion rate of whole body flips in pure urea varies between 10^5 and 10^7 s^{-1} ¹⁰⁹⁻¹¹². Therefore, quadrupole echo experiments can be employed to study this motion. Under different temperatures, the quadrupole echo spectrum from cis deuteron changes its line shape and corresponding

simulations can be carried on to simulate the motion effects. Since the flip of the whole molecule shows small effects on trans deuterium spectra, it is difficult to observe the CO flip effects on trans deuterium via quadrupole echo experiments.

The CN motion that occurs in urea is extremely slow π -flips ($k=1\sim 500\text{s}^{-1}$)¹¹³⁻¹¹⁵ around the CN bonds. When CN flips occur, cis and trans deuterons exchange their orientations within each amide group. Although QE experiments are able to distinguish cis from trans deuterons, showing two groups of doublets, they fail to detect the CN motion directly because it is too slow to broaden the line shape. However, this motion is revealed indirectly by the observation of an unusually short spin lattice relaxation time for the trans deuterons, resulting from slow exchange with fast relaxing cis deuterons.

In order to investigate both CO and CN motions in one experiment, On/Off MAS can be used⁶⁰. In On/Off MAS experiments, the signal to noise ratio is improved and the narrow sidebands (full width at half maximum intensity ~ 100 Hz) is sensitive to motion on the kHz time scale. In addition, the intensity profile of the sidebands retains sensitivity to faster motional rates.

4.3.2 Experimental procedures

On/Off MAS experiments were carried out at 46.07 MHz with Bruker AVANCE electronics, using an Oxford 89mm bore 7 Tesla superconducting magnet and a Bruker 2.5mm $^1\text{H}/\text{X}$ CPMAS probe, equipped with a backlash-free reducing gear assembly for accurate control of the magic angle. Experiments were repeated at several temperatures, set by a Bruker temperature controller within $\pm 0.1\text{K}$. In order to determine absolute sample temperatures, the system was calibrated using solid lead nitrate. A Bruker MAS

control unit was used to regulate the spinning speed within ± 2 Hz over the whole temperature range (243 K-343 K). Unless otherwise noted the spectral width was 400 kHz, 8192 points were collected, and the 90° -pulse width was $1.2 \mu\text{s}$ at 1.6 dB. The recycle delay was set to two seconds for $243 \text{ K} < T < 293 \text{ K}$ and one second for $294 \text{ K} < T < 393 \text{ K}$. Fourier transformation was started at the top of the first rotational echo to minimize first order phase corrections, and 50 Hz exponential apodization was applied prior to Fourier transformation.

After coarse adjustment of the magic angle using a KBr sample, fine adjustments were made while observing a spectrum of deuterium labeled polyethylene with $\nu_R = 20$ KHz. Subsequent spectral simulations verified that adjusting the angle to achieve minimum side band line width (< 100 Hz) corresponded to the exact MAS condition within about 0.01° . After calibration, On-Angle MAS experiments were carried on. Then the angle was offset by a fixed value representing a compromise between well-resolved sideband fine structure and lower signal to noise. Fig. 4.4 shows the relationship between OMAS sideband powder patterns and the value of offset angle. A 0.15° offset angle proved suitable for rotor speed 20 kHz while 0.21° was used for rotor speed 25 kHz. The resulting spectra from different temperatures will be shown in next section.

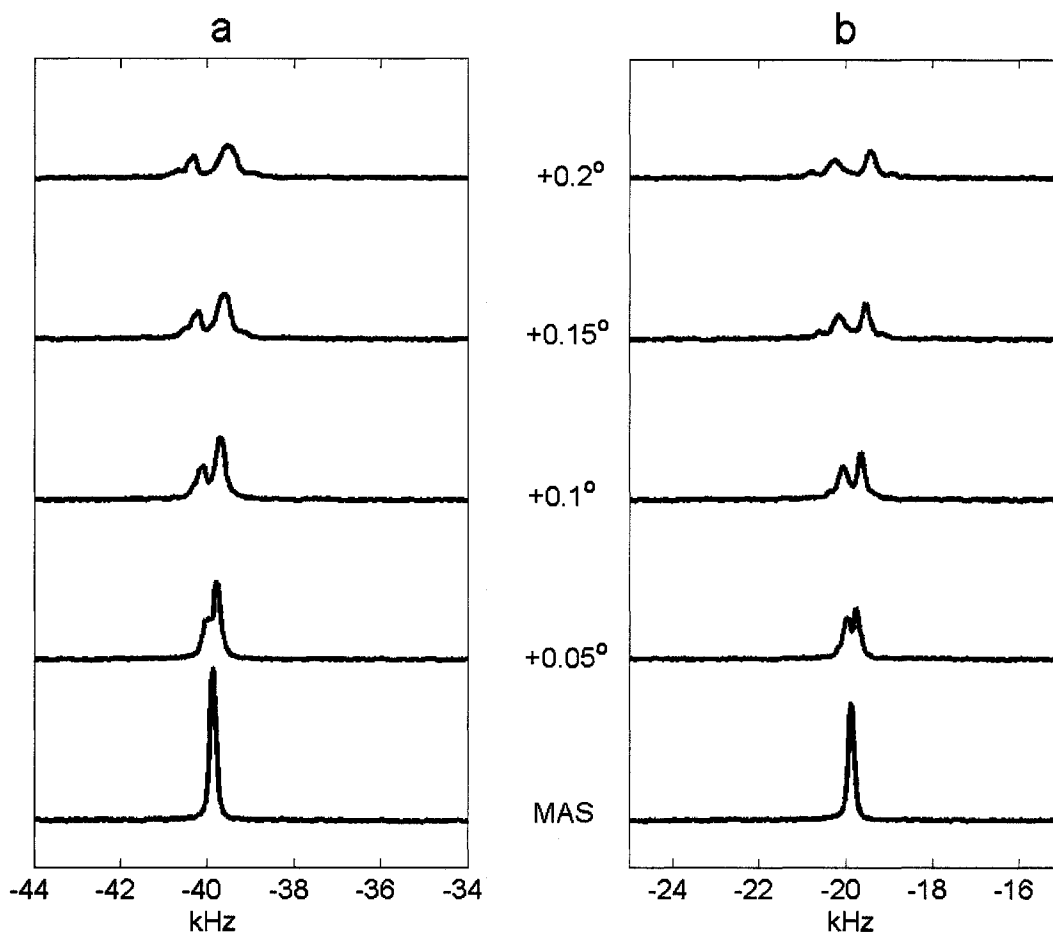


FIG. 4.4. The sensitivity of urea spectra to the offset angle. Expansions around (a) the second and (b) the first sidebands of spectra obtained at 303 K with $\nu_R = 20$ kHz. The indicated offsets were determined by comparison with spectra simulated for different offsets, matching the peak separation for major features without close attention to line shapes. In practice, deviations from exact MAS as small as $\sim 0.01^\circ$ can be detected by inspection of the experimental sideband line shapes.

4.3.3 Results

Variable temperature OMAS spectra ($\nu_R = 20$ kHz and 25 kHz) and the details of their first and second side bands are shown in Figures 4.5 – 4.8. At first glance, the spectra appear similar to ordinary MAS line shapes, but on closer inspection the fine structure introduced by OMAS differs from sideband to sideband to On angle MAS spectra. Because the offset angle, $\Delta = 0.21^\circ$, was larger at 25 kHz than that at 20 kHz ($\Delta = 0.15^\circ$), the intensities of OMAS side bands at 25 kHz are lower than those in the 20 kHz

spectrum. Fine structure is present in both spectra, shown on expanded scale in Fig. 4.6 and 4.8. Clearly, it is not even approximately correct to view these dynamic line shapes just as simple powder patterns defined by a scaled down quadrupole coupling.

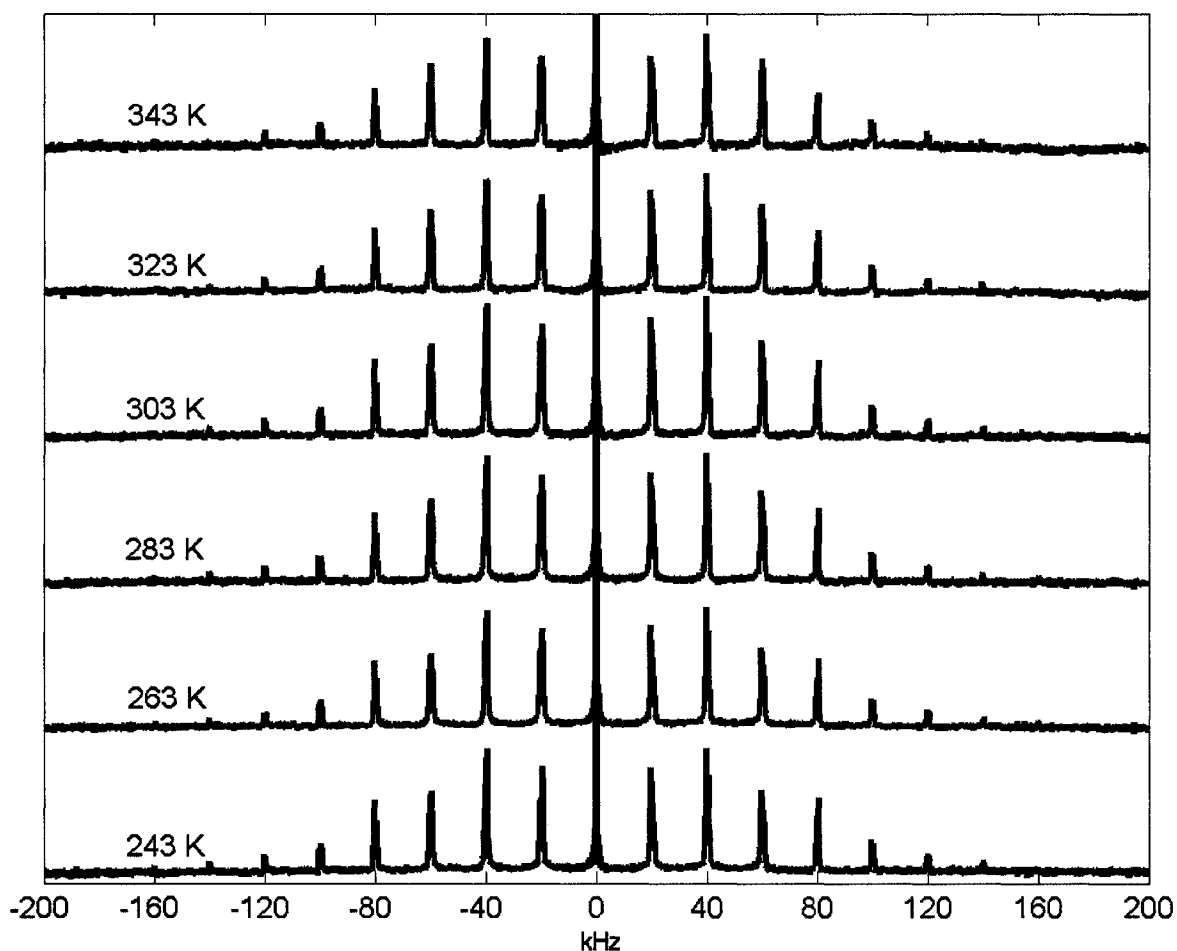


FIG 4.5. Deuteron OMAS spectra ($\nu_R = 20$ kHz) of C_8A -UIC at 46.05 MHz. Indicated temperatures have been corrected for frictional heating as described in the text. The spin rate is 20 kHz and offset $\Delta = 0.15^\circ$. The center band shows a prominent peak, possible arising from a small amount of highly mobile surface-absorbed D_2O . Single 90° pulse was used ($1.6 \mu s$ at 1.2 dB). For each temperature, 256 scans were acquired to obtain NMR FID with scan delay at 5 seconds. Dwell time is $2.5 \mu s$, which equivalent ± 200 kHz spectrum window. The spectra were obtained by FFD of the FID, which were modified by a necessary left shift that moves the first point to the top of the first rotation echo in order to reduce the first order phase correction.

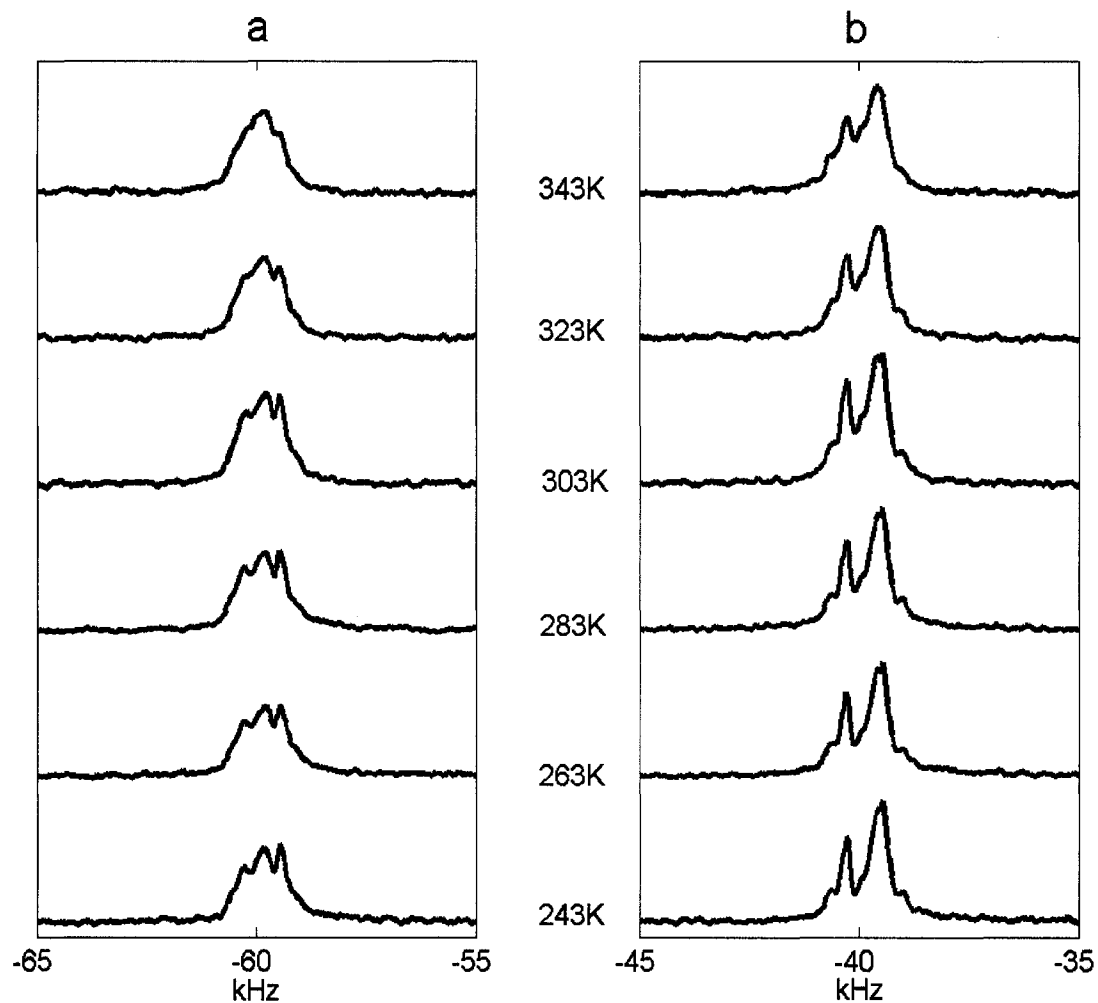


FIG 4.6. Expanded view of the third (a) and the second (b) side bands, $\nu_R = 20$ kHz
 The close inspection of each side bands shows that fine structures, which were caused by the reintroduced quadrupole interaction, differ with the single peaks in On-MAS spectrum side bands. The line shapes of these sub peaks also change with temperature. Different segments of these sub-peaks have different temperature dependence: some become narrow while others are broadening as the temperature rises from 243 K to 343 K.

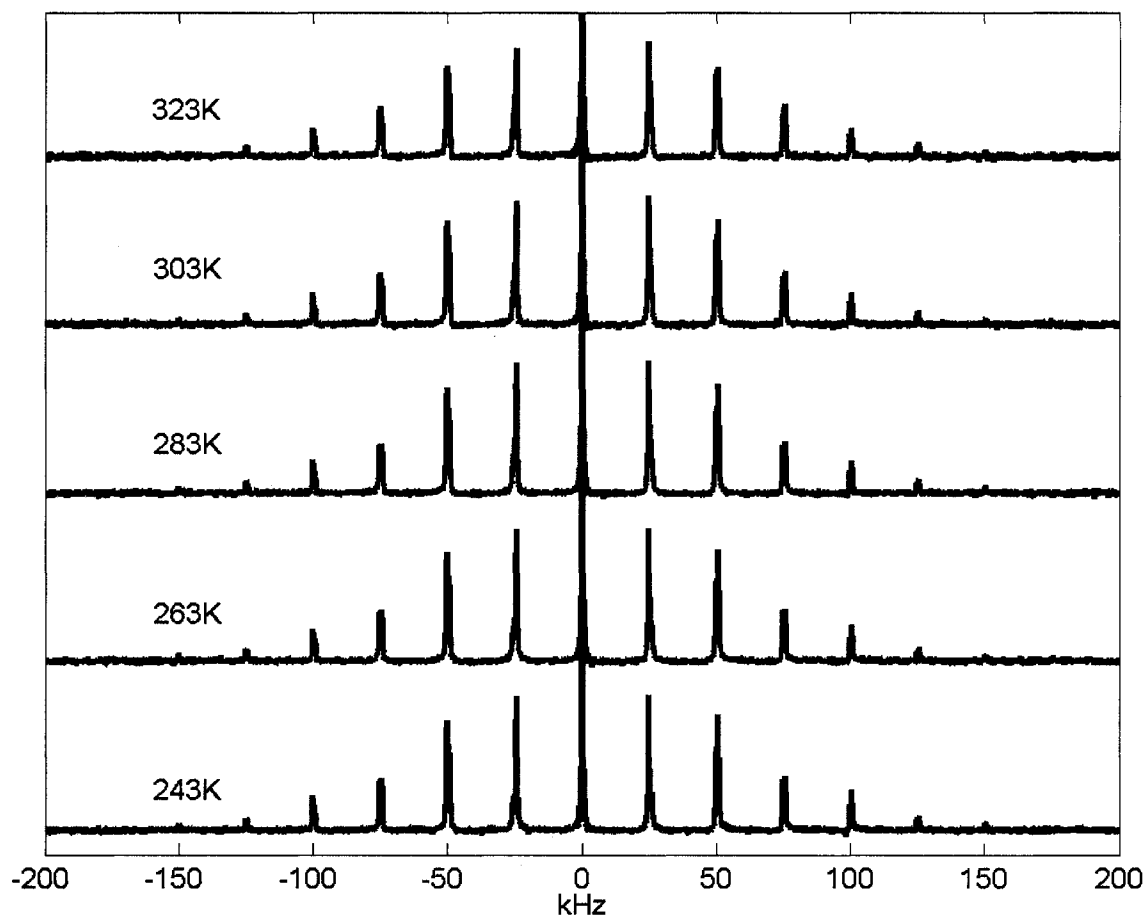


FIG 4.7. Deuteron OMAS spectra ($\nu_R = 25$ kHz) of C₈A-UIC at 46.05 MHz. The experimental parameters were the same as fig. 4.5, but the spinning speed was 25kHz and the offset angles Δ is 0.21° . Since the rotor speed increase from 20 kHz to 25 kHz, fewer side bands can be observed.

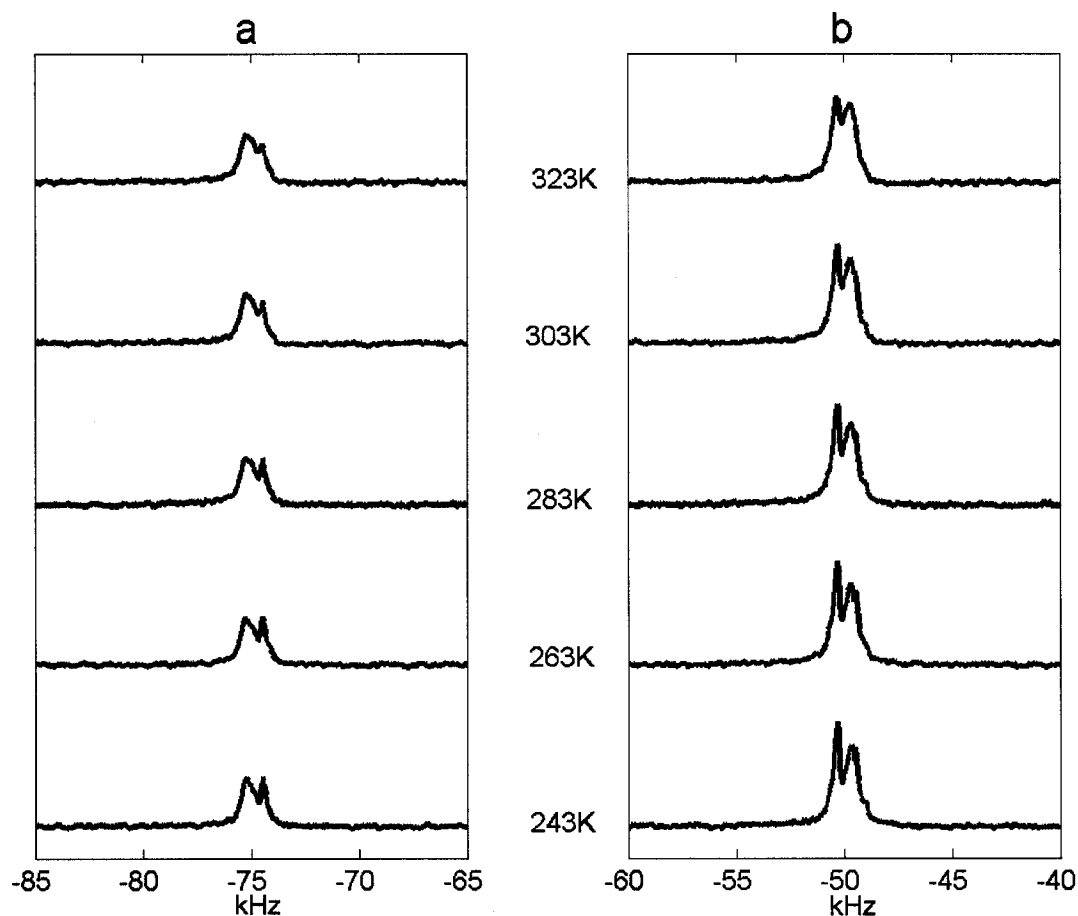


FIG. 4.8. Expanded view of (a) the third and (b) the second sidebands, $\nu_R = 25$ kHz. The experimental parameters were the same as fig. 4.5, but the spinning speed was 25kHz and the offset angles Δ is 0.21° . Here the fine structures of two side bands (-50 kHz and - 75 kHz) are shown. The temperature dependence of OMAS line shapes was used to compare with simulations in order to determine the motion rates.

The temperature dependences of the OMAS sideband envelopes for 20 kHz and 25 KHz spinning speeds are shown in Figures 4.6 and 4.8, respectively. There are small differences between side band intensities at different temperatures, but the determination of motional rates by analyzing these intensity distributions would not be very accurate. In fact, aside from increased signal to noise ratio there is little benefit to be gained by analyzing the integrated sideband intensities: quadrupole echo spectra provide better information and the simulations are much simpler. However, individual OMAS side band

fine structure exhibits far more sensitivity to temperature. For example, the two leftmost and two rightmost features in the -40 KHz side band (fig. 4.7), become narrower and more intense as the temperature increases from 243K to about 303K, and then broaden and start to coalesce with the rightmost features. The two central peaks also change line shape continuously; merging into one at high temperature. The third sidebands (centered at -60 kHz) exhibit similar splitting and merging phenomena. For individual MAS side bands, the line width is proportional to the motional rate in slow regime, but inversely proportional to the rate in the fast regime. Similar behavior may be expected for OMAS line shapes. Thus, the initial narrowing is due to increasingly fast CO rotation, while subsequent broadening is due to the onset of much slower CN motion.

The exquisite sensitivity of OMAS to motion on multiple time scales in Fig. 4.9. The fast CO and slow CN rotations have opposite contributions with increasing temperature, and their effects therefore tend to cancel so that MAS line widths are scarcely affected. However, the OMAS line shapes depend much more strongly on temperature because the CO and CN rotations have different effects on parts of the sideband line shape.

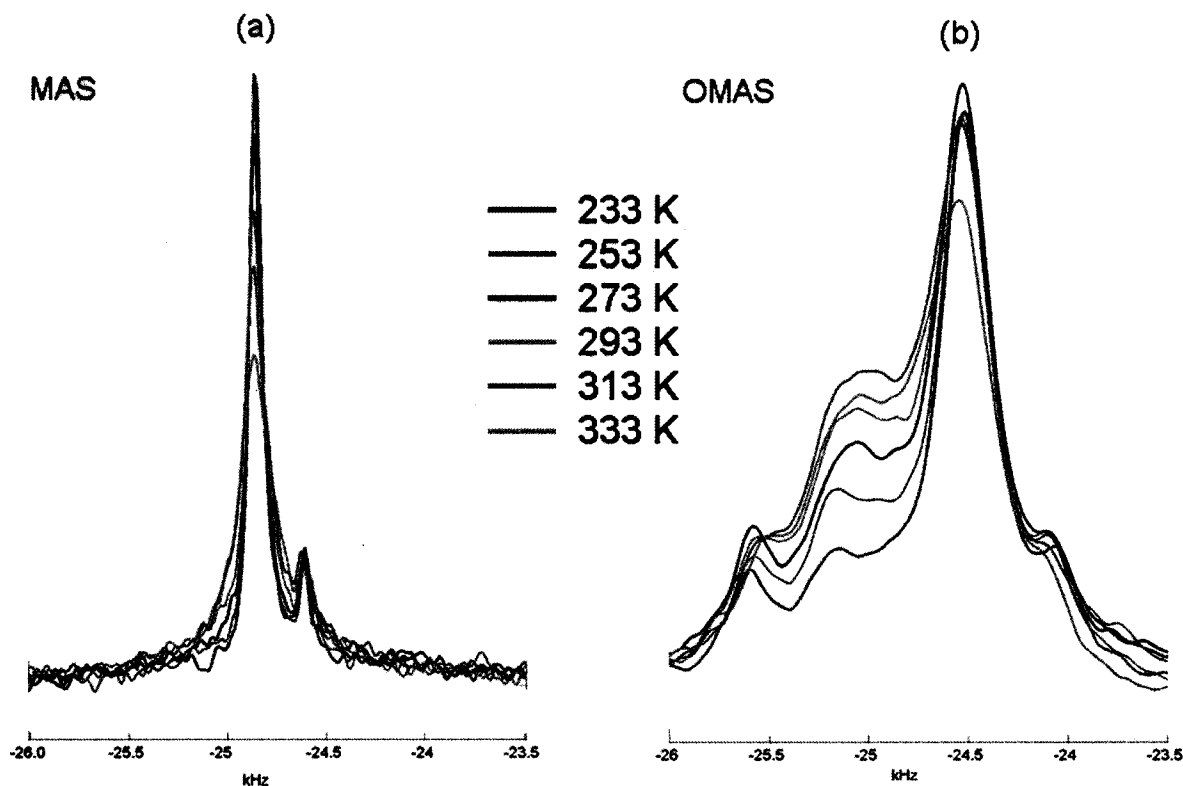


FIG. 4.9 Temperature dependence of the second sideband in MAS and OMAS (a) MAS and (b) OMAS spectra of C_8A -UIC, with spin rate $\nu_R = 25$ kHz and offset angle $\Delta = 0.21^\circ$. The small rightmost peak, which is most clearly resolved in the MAS spectra, is assigned to C_8A carboxyl deuterons. OMAS line shapes are far more sensitive to temperature: the sub set peaks of OMAS change both intensities and shapes. In MAS spectra, peaks at different temperatures heavily overlap on each other and obstruct the reliable quantitative simulations.

4.4 Simulation and motion rates

4.4.1 Simulation of UIC spectra

In order to simulate the dynamical OMAS spectra of UIC, Floquet method was employed. There are approximate 5~6 observed sideband pairs, as fig. 4.5 and 4.7 show. Thus the size of truncated Floquet matrix used in the calculation is less than 30×30 for each deuteron in urea. Two motion frames are defined as CO and CN frames. Assuming that principal z-axis of each deuteron EFG tensor lies along the relevant N-D bonds, Euler angles describing each of the two-site jump processes in each frame are listed in

Table 4.2. These angles are based on X-ray data for urea-alkane UICs^{103, 116, 117} refined for C₈A/UIC by fitting deuteron QE line shapes^{36, 118}

Table 4.2 Two frame representation of urea jump motions in C₈A-UIC

Motion ^(a)	Jump Rate	α	β ^(b)	γ
CO	k _{CO}	0	117°	0
CO	k _{CO}	0	117°	180°
CN	k _{CN}	0	58°	0
CN	k _{CN}	0	58°	180°

^(a) The CO and CN jump frames have their z-axes directed along the urea CO and CN bond directions, respectively.

^(b) In the CO frame, Euler angle $\beta = 117^\circ$ is the O-C-N bond angle, and 180° flips occur about the CO bond. In the CN frame, $2\beta = 118^\circ$ is the D-N-D bond angle. These values are consistent with X-ray and neutron diffraction data for other urea inclusion compounds.

For this type of multi-axis motion, the four possible orientations visited by each deuteron can equally well be defined in terms of a single, composite rotation. The results of automated calculation of the equivalent one-frame angles are listed in table 4.3.

Table 4.3 One-frame representation in urea/C₈A inclusion compound

Site ^(a)	α	β	γ
A	0°	59°	0°
B	0°	59°	180°
C	0°	175°	0°
D	0°	175°	180°

^(a) The site labels for each deuteron are shown in Figure 4.3. The Euler angles associated with each site may be derived as described in the text from the two-frame description in table 4.2. They rotate the principal axis frame for each deuteron into coincidence with the crystal fixed frame shown in Fig 4.3.

The equilibrium site populations are necessarily equal, so the corresponding 4×4 kinetic matrix is symmetric. Its diagonal elements determined by the principle of detailed balance:

$$K = \begin{bmatrix} -k_{CO} - k_{CN} & k_{CO} & k_{CN} & 0 \\ k_{CO} & -k_{CO} - k_{CN} & 0 & k_{CN} \\ k_{CN} & 0 & -k_{CO} - k_{CN} & k_{CO} \\ 0 & k_{CN} & k_{CO} & -k_{CO} - k_{CN} \end{bmatrix} \quad (4.1)$$

The diagonal frequency coefficient matrixes Ω_0 and two off-diagonal frequency coefficient matrixes $\Omega_{0\pm 1, \pm 2}$ in L_F are:

$$\Omega_i = \begin{bmatrix} W_i^A & 0 & 0 & 0 \\ 0 & W_i^B & 0 & 0 \\ 0 & 0 & W_i^C & 0 \\ 0 & 0 & 0 & W_i^D \end{bmatrix} \quad (4.2)$$

the calculation of W_i has been discussed in Chapter 3. In the end, the block 4×4 jump rate matrix and frequency coefficient matrices of each site compose the super operator L_F .

$$L_F = \begin{bmatrix} \Omega_0 - I \cdot 2\nu_R + iK & \Omega_1 & \Omega_2 & 0 & 0 \\ \Omega_{-1} & \Omega_0 - I \cdot \nu_R + iK & \Omega_1 & \Omega_2 & 0 \\ \Omega_{-2} & \Omega_{-1} & \Omega_0 + iK & \Omega_1 & 0 \\ 0 & \Omega_{-2} & \Omega_{-1} & \Omega_0 + I \cdot \nu_R + iK & \Omega_1 \\ 0 & 0 & \Omega_{-2} & \Omega_{-1} & \Omega_0 + I \cdot 2\nu_R + iK \end{bmatrix} \quad (4.3)$$

In previous studies of C₈A-UIC^{36, 118} it was found that the CO jump rate varied from $k_{CO} = 10^6 \sim 10^7 \text{ s}^{-1}$ in the temperature range 243 K to 343 K, while the CN jump rate, k_{CN} , changed from zero to 300 s^{-1} . However, it was noted that different rates were obtained from fitting quadrupole echo and Selective Inversion data: CO jump rates obtained from simple QE lines shape analyses were about three times faster than those determined from SI experiments. The difference was ascribed to systematic errors in analysis of the QE line shapes, arising from the presence of anisotropic contributions to

the underlying homogeneous dipolar line width. In view of these results, simulations of OMAS spectra are presented here for k_{CO} values between $0.4 \times 10^6 \text{ s}^{-1}$ and $10 \times 10^6 \text{ s}^{-1}$ and k_{CN} values between 0 s^{-1} and 500 s^{-1} .

In order to get artifact free spectral simulations, nearly one thousand crystallite orientations were included in each simulation, and the dimension of the Liouvillian matrix L_F was three times larger than the number of experimentally observed side bands. Computations were programmed in MATLAB. Each powder pattern required about ten minutes to simulate using an AMD64 3400+ workstation with 1G memory. Unless noted otherwise, all simulations were performed with $C_Q = 208 \text{ kHz}$, $\eta_Q = 0.14$, 8192 points in FID, and the dwell time is $2.5 \mu\text{s}$.

Simulated OMAS spectra, with k_{CN} fixed at the negligibly small value 50 s^{-1} , are shown in Fig. 4.10 as a function of k_{CO} . Although the overall OMAS spectral envelope changes only slightly for $6 \times 10^6 < k_{CO} < 12 \times 10^6$, the OMAS sub peaks (Fig. 4.10b) become significantly narrower and better resolved as k_{CO} increases. Evidently, this range of k_{CO} is a “fast” motional regime as defined with respect to the residual quadrupole coupling scaled down by OMAS. The ability to control this scaling by accurate adjustment of the rotor axis provides a unique way to tune the experimentally accessible kinetic window.

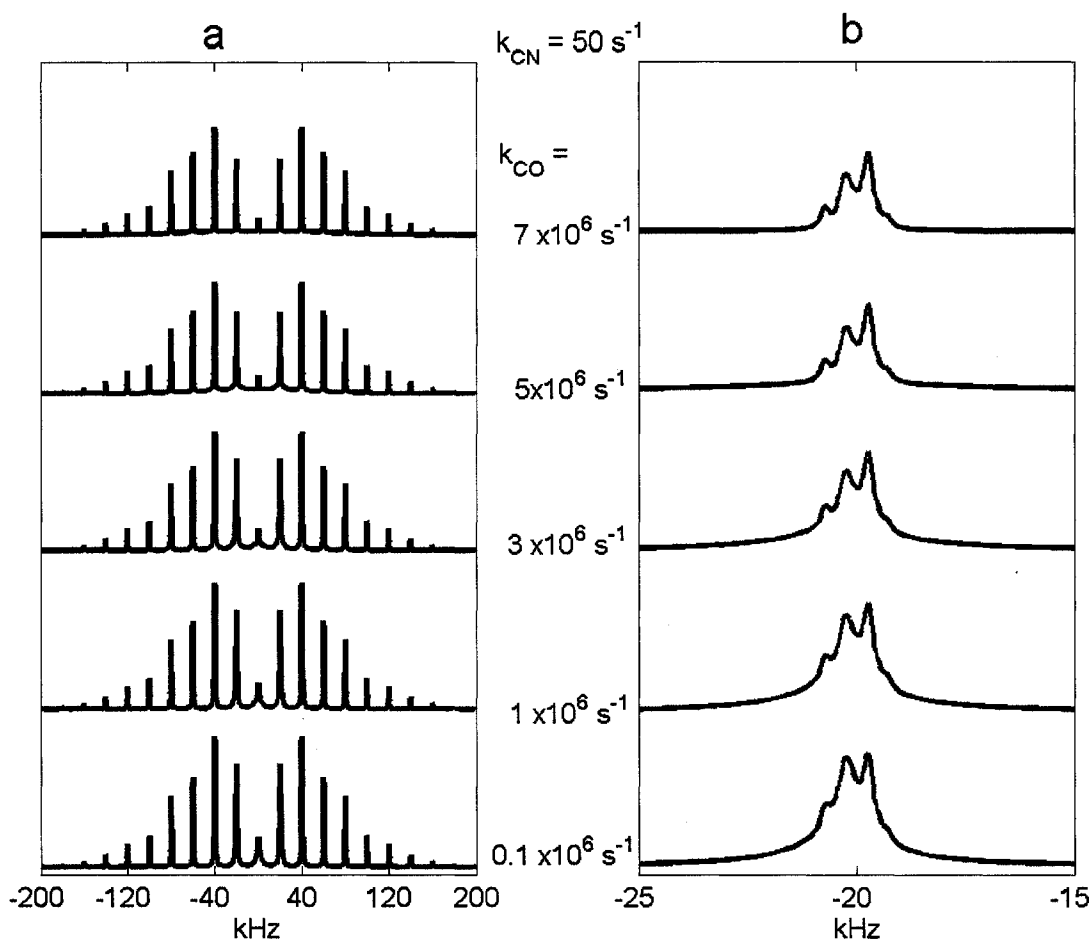


FIG 4.10. OMAS simulations showing the effects of changing k_{CO} (a) Full spectrum in a full 400 kHz spectrum window and (b) Expanded region around the first sideband. All spectra were simulated with the indicated values of k_{CO} and fixed values of the remaining parameters: $k_{CN}=50 \text{ s}^{-1}$ $C_Q=208 \text{ kHz}$ and $\eta_Q=0.14$ for all sites, offset $\Delta=0.1^\circ$ and spin rate $\nu_R = 20 \text{ kHz}$. The site orientations are defined in Table 4.3

Simulations shown in Fig. 4.11 illustrate effects of changing k_{CN} alone. Clearly, this is a “slow” motional regime in which peaks broaden with increasing rate. Although the dependence on k_{CN} is weaker than on k_{CO} , OMAS sideband line shapes are sensitive to both k_{CO} and k_{CN} in the experimentally accessible temperature range for $C_8A\text{-UIC}$.

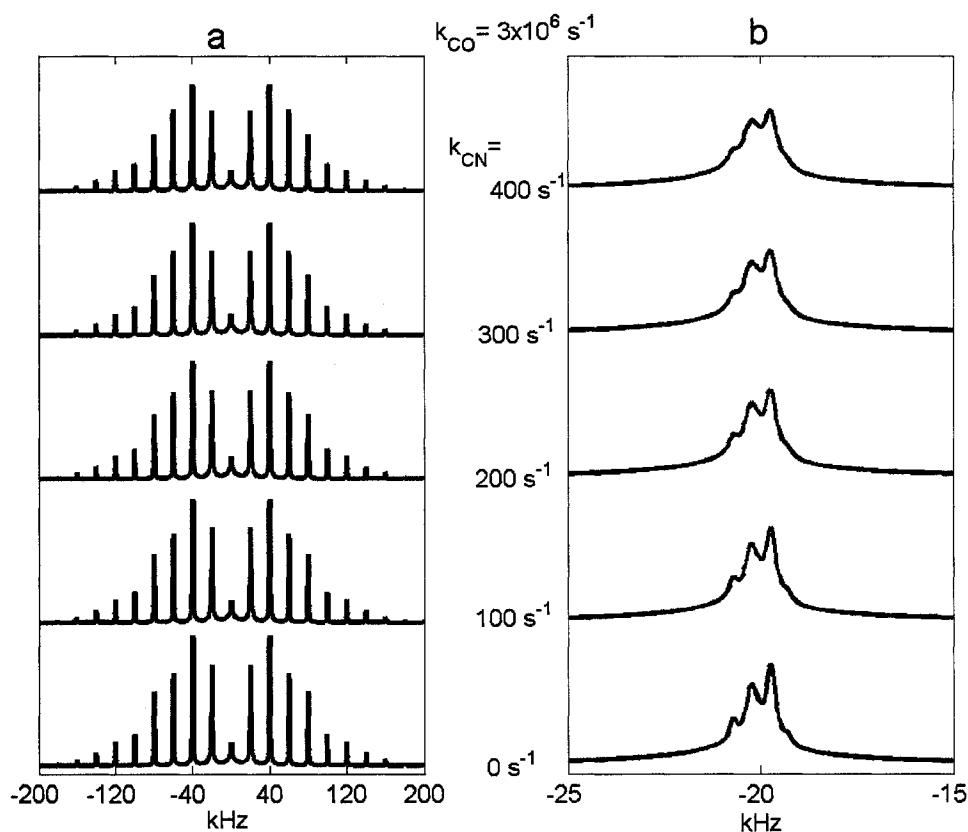


FIG. 4.11 OMAS simulation showing the effects of changing k_{CN} (a) Full spectrum in a 400 kHz spectrum window and (b) Expanded region around the first sideband. All spectra were simulated with the indicated values of k_{CO} and fixed values of the remaining parameters: $k_{\text{CO}}=3 \times 10^6 \text{ s}^{-1}$, $C_{\text{Q}}=208 \text{ kHz}$ and $\eta_{\text{Q}}=0.14$ for all sites, offset $\Delta=0.1^\circ$ and spin rate $\nu_{\text{R}}=20 \text{ kHz}$. The orientations are the same as fig 4.10

Dynamic consequences of different site orientation dependent quadrupole coupling constants are illustrated in Fig. 4.12. The solid line shows the line shape of the second OMAS sideband, simulated with $C_{\text{Q}} = 208 \text{ kHz}$ for all four sites. The dashed line shape was obtained with the same rate parameters, but with $C_{\text{Q}}(\text{trans})= 210 \text{ kHz}$, $C_{\text{Q}}(\text{cis})= 180 \text{ kHz}$. The dotted line shows the difference between two spectra.

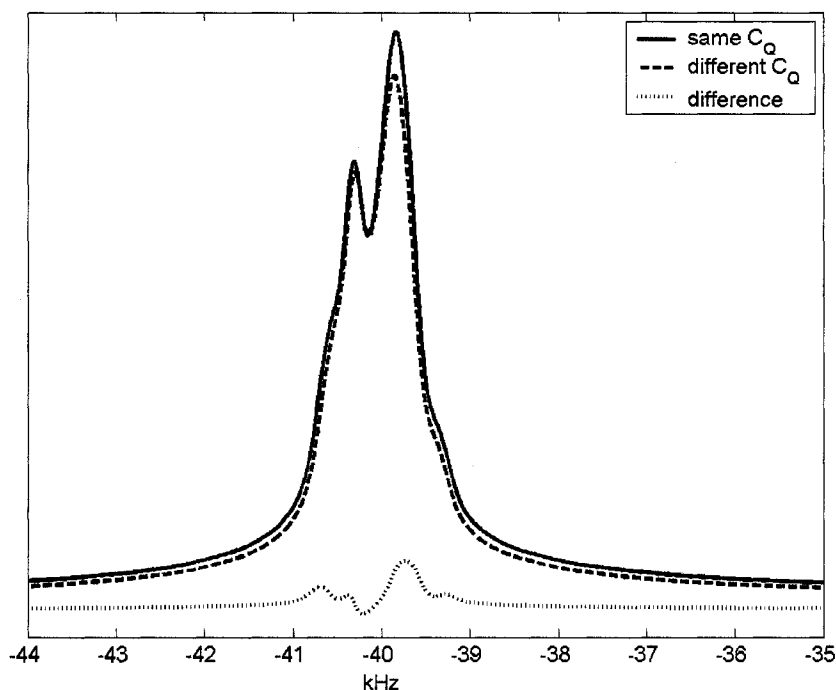


FIG. 4.12. The effects of the difference site-dependent quadrupole coupling constants. Solid line: $C_Q=208$ kHz for all four sites. Dashed line: $C_Q(cis)=180$ kHz and $C_Q(trans)=210$ kHz. For both spectra 50 Hz exponential apodization was applied. $k_{CO}=4 \times 10^6$ s⁻¹ and $k_{CN}=50$ s⁻¹. $\eta_Q=0.14$ and spin rate $\nu_R=20$ kHz. Dotted line: difference between two spectra.

The observed differences can be understood by comparing the CN jump rate with the scaled difference between the *cis* and *trans* quadrupole coupling constants:

$$\Delta C_Q(eff) = \frac{1}{2} \left| (C_Q(trans) - C_Q(cis)) \cdot (3 \cos^2(\beta_R - 0.15)) - 1 \right| \approx 120 \text{ Hz} \quad (4.4)$$

For some powder orientations, $\frac{2\pi}{k_{CN}} \cdot \Delta C_Q(eff)$ is greater than unity, resulting in motional broadening, which is apparent for the two central features, while for others it is less than unity, resulting in motional narrowing, which leads to coalescence of the outermost peaks. This sensitivity to small differences between the quadrupole coupling constants does not occur with exact ordinary MAS, for which ΔC_Q is exactly zero.

4.4.2 CO and CN motion rates

One advantage of OMAS experiments is that CO and CN motions can be studied simultaneously. Spectra calculations with Floquet method enable the motions rates analysis without the compromises that are necessary in quadrupole echo or 2D-exchange simulation: the slow CN motion is omitted in quadrupole echo study and the 2D-exchange fails to take the fast CO motion into account.

Extensive simulations were performed for spinning speed 20 kHz and grids of near 100 jumps rate pairs: $1 \times 10^4 < k_{\text{CO}} < 5 \times 10^6 \text{ s}^{-1}$ and $1 < k_{\text{CN}} < 500 \text{ s}^{-1}$. In addition to the virtual match of the line shapes at each temperature, the exponential χ^2 error surfaces for the second sidebands over the $k_{\text{CO}}-k_{\text{CN}}$ grid is also used to check the accuracy of the simulation. χ^2 is defined as:

$$\chi^2 = \sum_{j=1}^{100} \left\{ \frac{S_j^{\text{exp}} - S_j^{\text{sim}}}{\sigma^2} \right\}^2 \quad (4.5)$$

where the sum includes 100 data points covering just the left hand second sideband. The uncertainty of each point σ^2 is assumed to be a constant and is taken to be the base line noise. The exponential χ^2 error surface is shown in fig. 4.13.

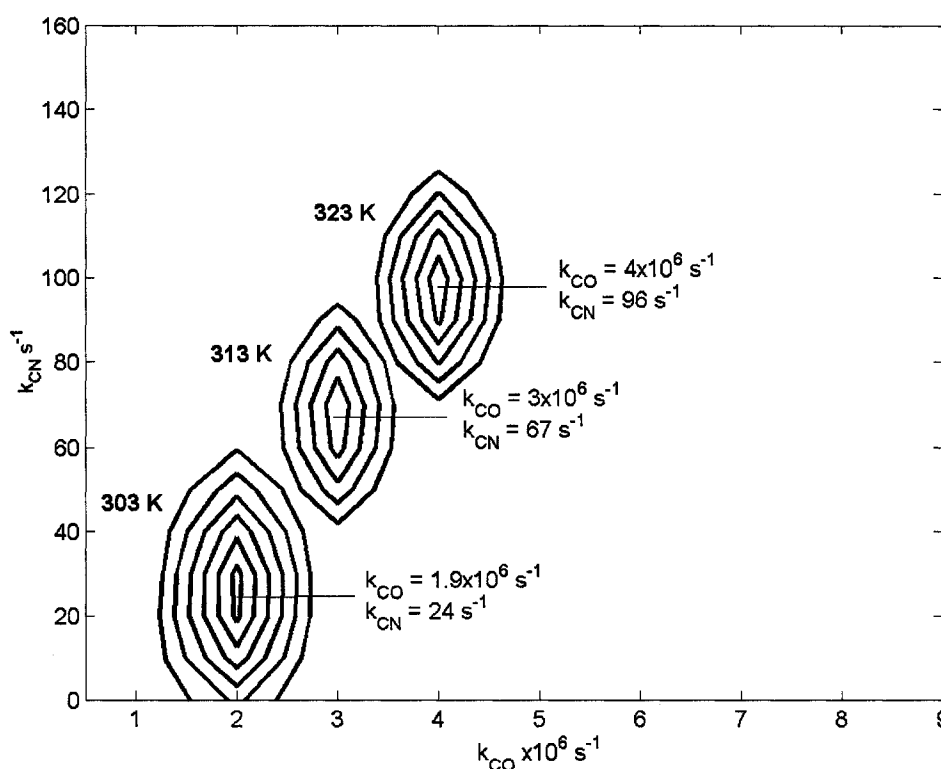


FIG. 4.13 Contour maps of $z = e^{-\chi^2}$ for 46.05 MHz OMAS spectra of C₈A-UIC.

The experimental data is obtained at temperature 303, 313, and 323 K. The best-fit values of motion rates k_{CO} and k_{CN} , determined from the coordinates of surface peaks, are listed in Table 4.4. The lowest z indicates the best fitting between experimental data and simulations. The maximum χ^2 is around 90.

The study of $z = e^{-\chi^2}$ surface reveals some interesting conclusions. At first, the maximum χ^2 for the simulation is around 90, indicating an acceptable model¹¹⁹. Secondly, the contour barely changes when the cis quadrupole constant and trans quadrupole constant were assigned different values. OMAS reintroduced a scaled down first order quadrupole interactions, thus the small quadrupole interaction difference (<30 kHz) between two types of deuterons now becomes neglected. In the simulation a fixed $C_Q = 208$ kHz is used for all sites. In end, the chemical shift anisotropy that distort selective inversion and quadrupole echo spectra is also scaled down, resulting more accurate measurement of motions rates. OMAS separates the dynamics effects from

other effects and greatly improves the sensitivity and degree of accuracy. Z surface are smooth and sharply peaked around the minimum χ^2 (maximum Z) at each temperature, which facilitates using Z surface in automated search procedures for finding motion rates in future researches.

The rate parameters listed in table 4.4 were obtained at each temperature simply by inspecting the location of Z_{\max} and the corresponding simulation spectra (fig. 4.14.) and their second side band (fig. 4.15) at several temperatures are shown.

Table 4.4 Temperature dependent jump rates of UIC-C₈A

Temperature (K)	$k_{\text{CO}} (10^6 \text{ s}^{-1})$	$k_{\text{CN}} (\text{s}^{-1})$
243	0.1*	0*
253	0.2*	0*
263	0.5±0.1	1*
273	0.6±0.1	2*
283	0.9±0.1	4*
293	1.1±0.2	11*
303	1.9±0.1	24±2
313	3.0±0.2	67±5
323	4.0±0.1	96±10
333	5.1±0.2	260±13
343	7.0±1.0	401±25

* The asterisk indicates values extrapolated from Arrhenius plots.

The uncertainties listed in table 4.4 are determined by visual comparison of simulations with experimental spectra, using the heuristic criterion that outside the quoted error limit, the simulated line shape begins to differ from the experimental one by more than approximately the width of the experimental noise band. Figure 4.16 show simulations, experimental line shape and residuals of the left six sidebands of the $\nu_{\text{R}} = 20$ kHz, $\Delta = 0.15^\circ$ OMAS spectra at 343K. It is clearly that the simulated spectra well fit the experimental spectra except the center and the first bands. This could be associated with

small amount of rapidly moving surface-adsorbed D_2O . By restricting the least squares fit to just the second sideband, we avoid biasing the fit by these artifacts, at the cost of throwing away potentially useful information coded in the relative sideband intensities. Since the portfolio of intensity is not used in the fitting procedure, the intensity artifacts arising from inadequate spectral coverage is avoided. It is gratifying that rate parameters determined by fitting only one sideband actually fit all the higher-order sideband line shapes equally well as fig 4.15 and 4.16 show.

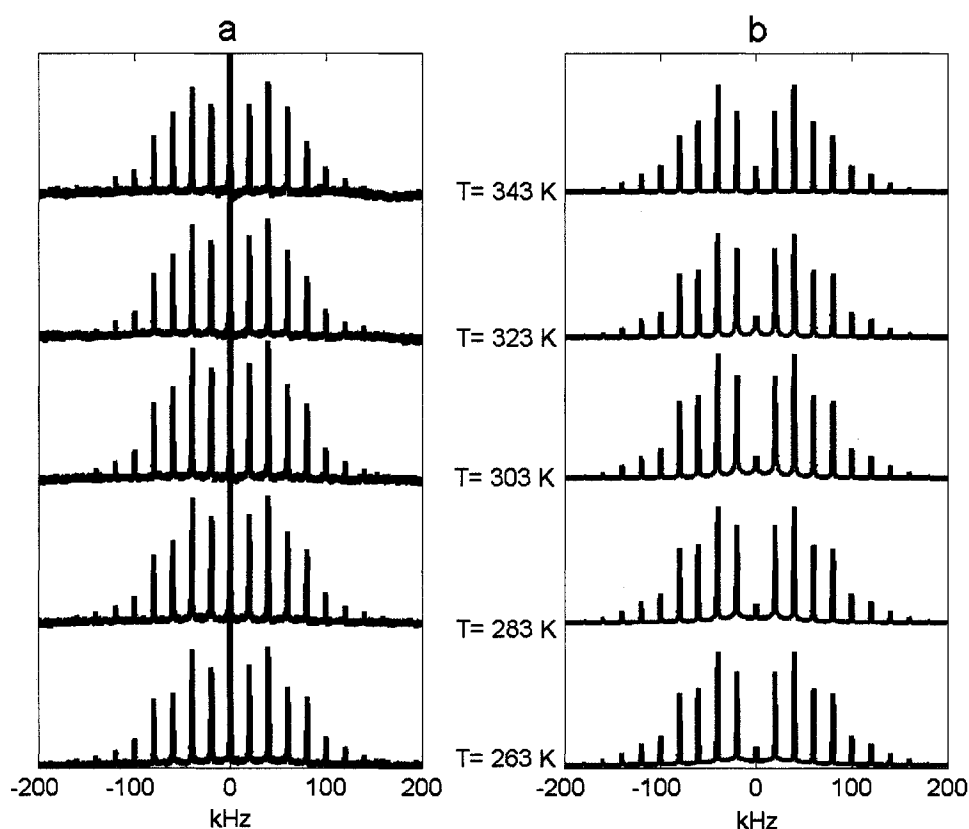


FIG. 4.14 Temperature-dependent experimental (a) and simulated (b) OMAS spectra. The OMAS experimental data was gained with $\nu_R = 20$ kHz and $\Delta = 0.15^\circ$. The simulations use values of k_{CO} and k_{CN} given in Table 4.4. $C_Q = 208$ kHz, $\eta_Q = 0.14$ and the sites orientations are given in Table 4.3. Each simulation contains 8192 data points and dwell time is $2.5 \mu s$.

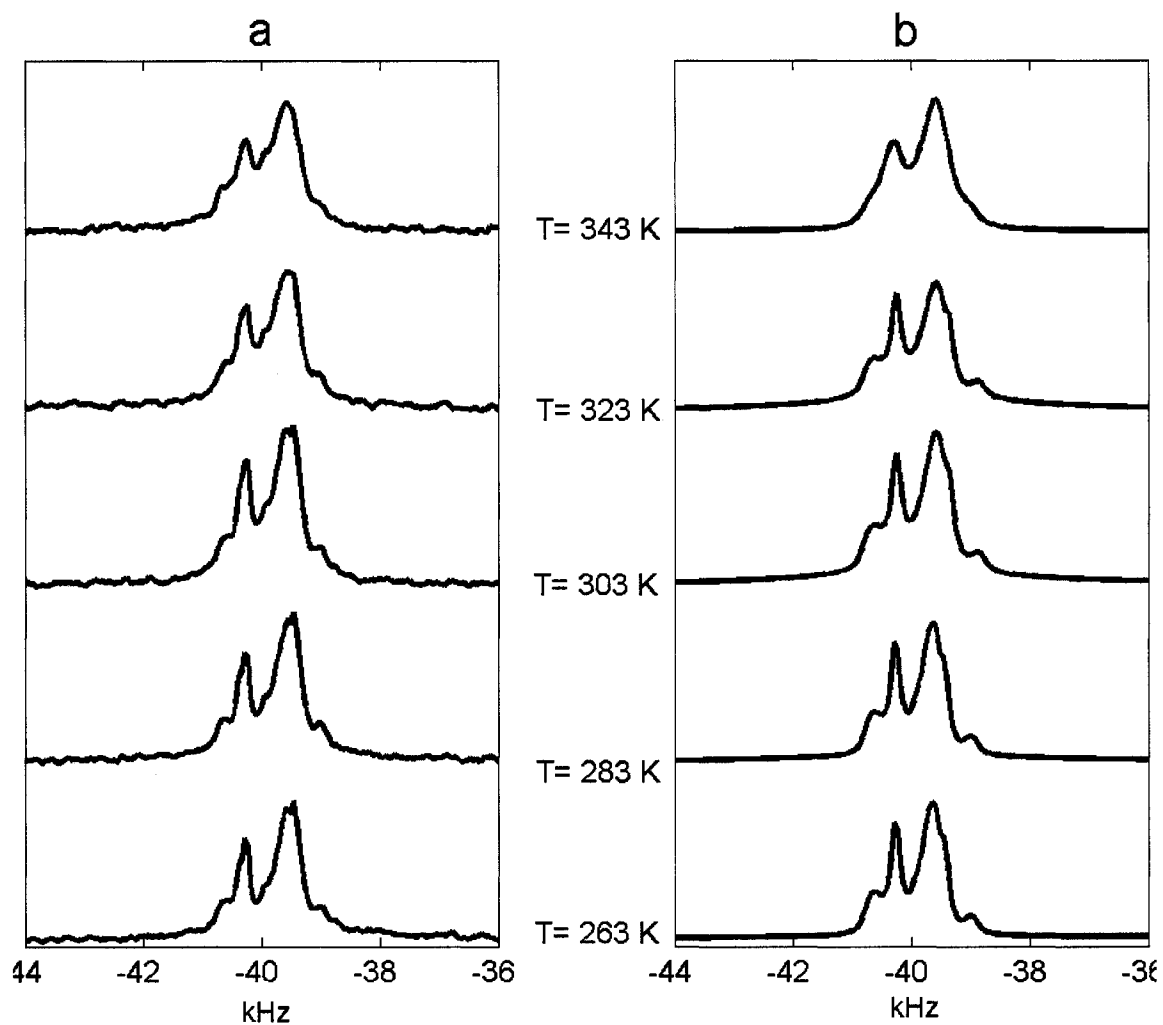


FIG. 4.15 The second sideband: (a) experimental spectra (b) simulated spectra
The parameters of experiment and simulation are the same as those in fig. 4.14.
Simulated spectra have the same fine details and identical temperature dependence as the experimental data.

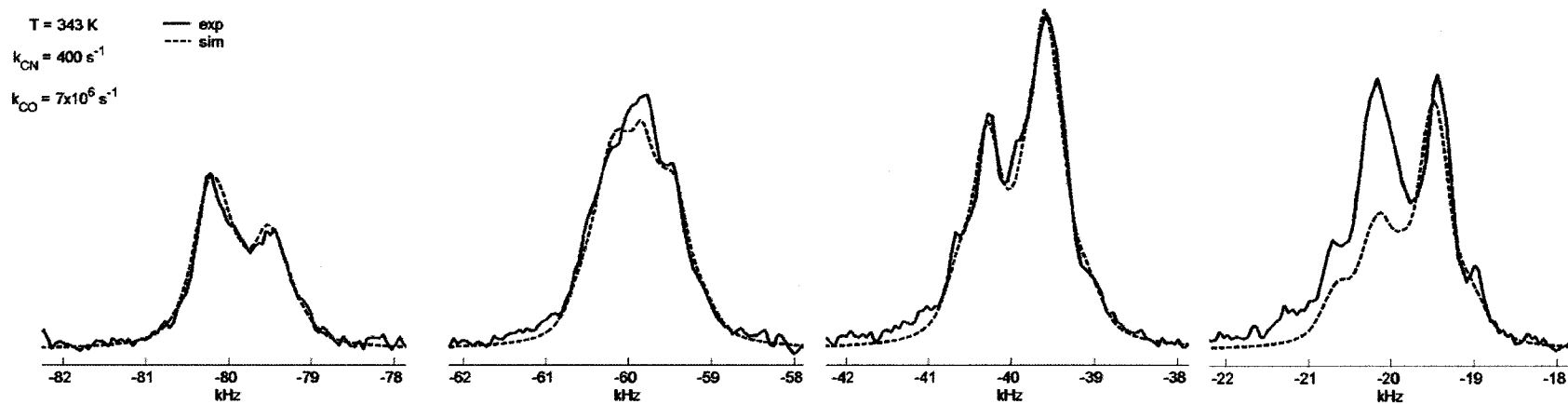


FIG 4.16 Simulated (dashed) and experimental (solid) OMAS spectra of $\text{C}_8\text{A-UIC}$. The spectrum is obtained at 343 K with spin rate of 20 kHz and offset $\Delta = 0.15^\circ$. The figure shows 100-point segments around each sideband. Motion rates are determined by least squares fitting of the second sideband, $k_{\text{CO}} = 7 \times 10^6 \text{ s}^{-1}$ and $k_{\text{CN}} = 401 \text{ s}^{-1}$. Simulation gives equally small residuals for all sidebands except the second side band, which is under the effect from D_2O .

4.5 Discussion

4.5.1 Arrhenius energy of CO and CN motions

Arrhenius plots for k_{CN} and k_{CO} are shown in Figures 4.17 and 4.18, respectively.

The activation parameters are compared in table 4.5 with those determined for C₈A-UIC and similar systems.

Table 4.5. UIC activation parameters

CO Rotation		
Sample	E_a [kJ/mole]	$\ln(A)$
UIC-C ₈ A (Off-MAS) ^(a)	26.3±0.4	24.9±0.3
UIC-C ₈ A (QE) ^(b)	22.3±0.3	24.8±0.6
UIC-C ₁₂ A) ^(b)	19.6±1.2	23.1±0.8
Urea-d ₄ ^(c)	62.0±0.6	34.3±0.2
CN Rotation		
	E_a [kJ mole ⁻¹]	$\ln(A)$
UIC-C ₈ A (Off-MAS) ^(a)	60.4±2.4	27.3±0.4
UIC-C ₈ A (SI) ^(b)	63.6±1.6	28.1±0.6

(a) This thesis

(b) M. J. Brown, Thesis for Doctor of Philosophy in *Dept. of Physics*, College of William and Mary, Williamsburg, 1996.

(c) J. C. Williams and A. E. McDermott, *J. Phys. Chem.* **97**, 12393 (1993).

Here, the quoted error limits are standard deviations (84% confidence limits) returned by the least squares fitting procedure. It is gratifying that for k_{CN} , OMAS line shapes and selective inversion experiments yield essentially identical results within experimental error. However, the activation energy for k_{CO} determined by OMAS differs from that determined by quadrupole echo line shapes by 4kJ/mole, about ten standard deviations. The discrepancy is most likely due to the difficulty of accurately accounting for a large, possibly temperature dependent homogeneous line width contribution to the quadrupole echo line shape. The activation energy for urea CO rotation, 26.3±0.4kJ/mole determined in the present work for C₈A-UIC, is significantly larger than the value 19.6±1 kJ/mole

reported previously for a C_{12} alkane guest. Presumably, this is a consequence of both increased hindrance and host-guest hydrogen bond interactions between urea and the alkanolic acid.

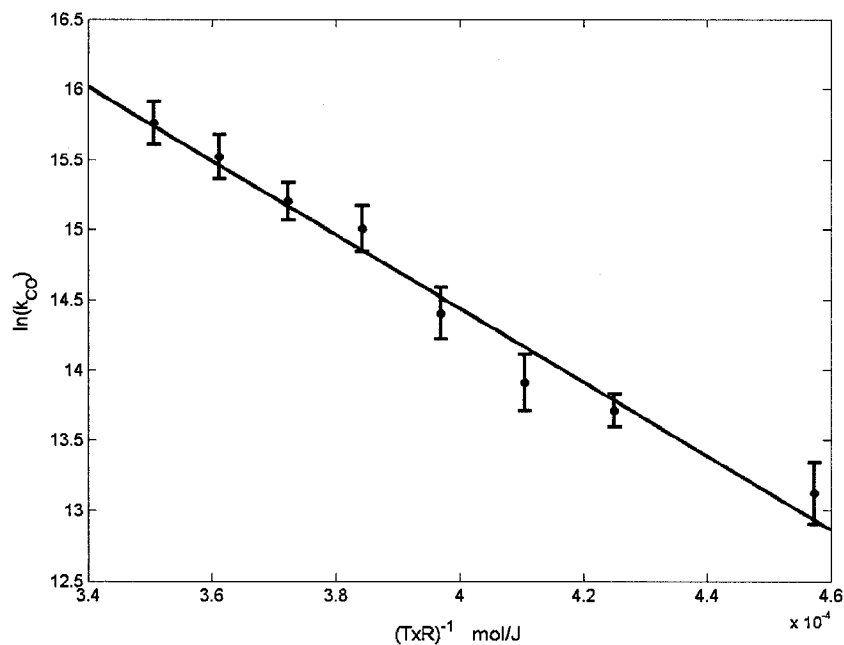


FIG. 4.17 The Arrhenius plot for rotation about the CO bond
Least squares fitting yields activation energy $E_a = 26.3 \pm 0.3 \text{ kJ/mol}$

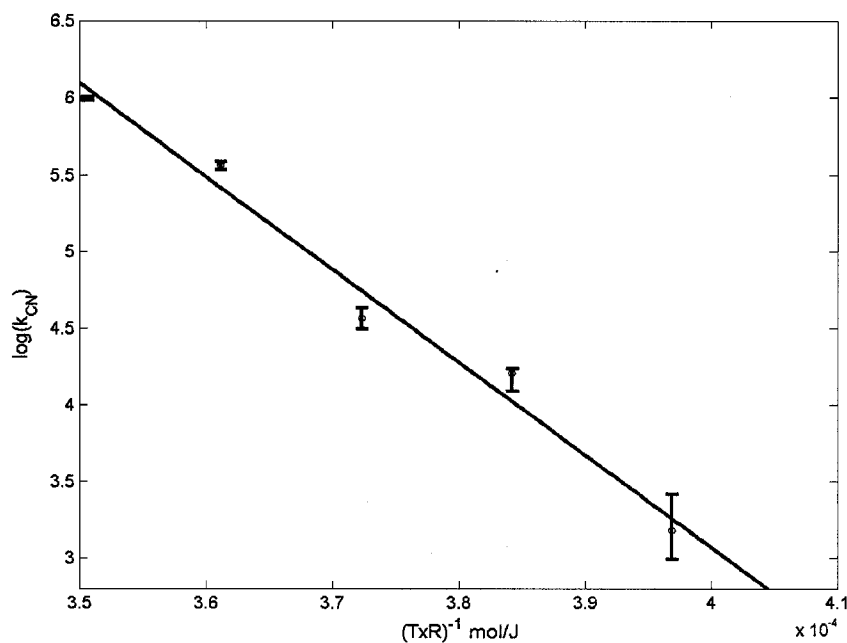


FIG. 4.18 The Arrhenius plot for rotation about the CN bond
Least squares fitting yields the activation energy $E_a = 60.4 \pm 2.4 \text{ kJ/mol}$.

4.5.2 Advantages of OMAS

Several advantages of OMAS are demonstrated by this study of multiple motions. In urea, the CO and CN motions belong to different motional regimes. Quadrupole echo experiments that are useful in the intermediate regime fails to detect the slow CN motion. Moreover, the CO motions obtained from quadrupole echo studies differ from those determined by selective inversion, due to uncertain contributions from anisotropic homogeneous broadening¹²⁰. In OMAS, anisotropic broadening effect is greatly reduced by rotating the sample rotation near the magic angle. It is gratifying that OMAS gives similar motional rates to those obtained by selective inversion.

The dynamical sensitivity of OMAS is also demonstrated. OMAS takes advantage of new, commercially available technology to set and maintain the angle between the static field and the rotor spinning axis reproducibly within a few hundredths of a degree. Compared with normal MAS experiments, OMAS sacrifices side band intensity but enhances motional sensitivity. In addition, OMAS expands the dynamic range of deuteron line shape measurements, especially for slow motion in the kilohertz regime.

It is shown that quantitative simulations that match experimental data can be achieved with the Floquet formalism described in Chapter 3. High spin rates help to reduce the size of the Floquet matrix representation, thereby improving the computational efficiency. It is shown that best fit rates determined from two-parameter least squares fitting of individual sidebands are significantly improved by simultaneous visual examination of residuals for several sidebands. Activation parameters for fast CO rotation and slower CN rotation in C₈A-UIC have been quantitatively characterized and briefly compared with results for similar compounds⁶⁰.

Chapter 5

Dynamics in Phenylalanine

5.1 Introduction

Phenylalanine is a common alpha-amino acid. It is contained in most protein rich foods such as milk, cottage cheese, fish and other seafood. Phenylalanine exists in two enantiomeric forms, D-phenylalanine (D-Phe or DPA) and L-phenylalanine (L-Phe), by virtue of the optically active α -carbon atom as shown in Figure 1. The chemical structure is that of alanine, with one of the methyl hydrogens replaced by a phenyl group.

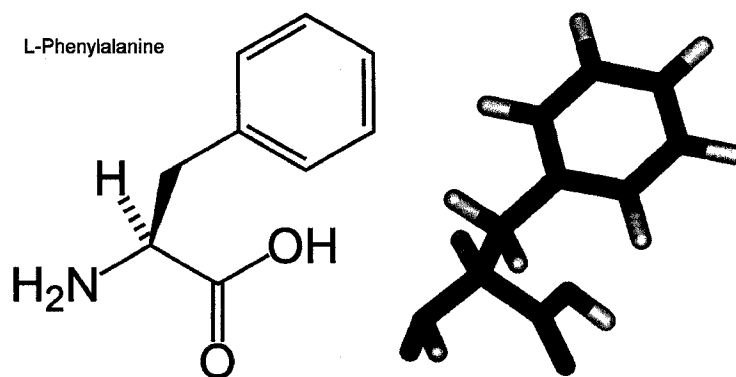


FIG. 5.1 Structure of L-Phenylalanine

Phenylalanine is a white powder at room temperature; it melts at 556K . D-Phenylalanine can only be synthesized artificially, but L-phenylalanine is a common component of proteins and is usually obtained from biological sources.

L-phenylalanine is one of the basic amino acids used to form proteins. In both L-phe and D-phe, the phenyl ring motion in protein side chains has received a great deal of attention

¹²¹ The ring motion involves rotation around the pseudo two-fold C_{2v} axis connecting the β and γ carbons, as shown in Figure 5.2

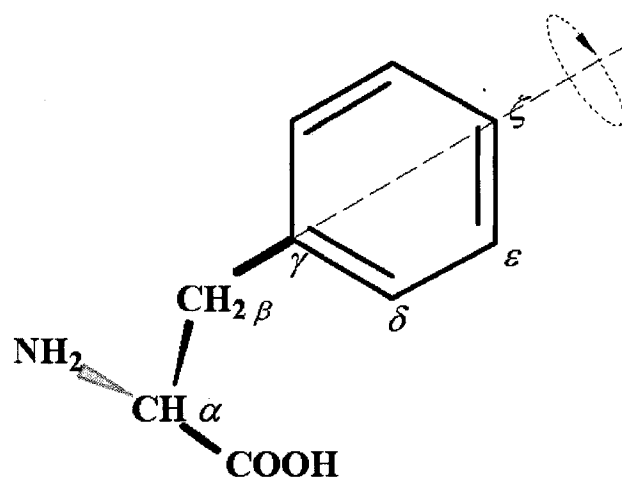


FIG. 5.2 Ring motion in phenylalanine

The aromatic ring rotates around the C_β - C_γ bond axis. Depending on the local potential energy function, the motion can vary from sudden, 180° jumps (" π -flips") to continuous rotational diffusion. The motional rates are strongly dependent on the local environment of the ring, varying from essentially zero to 10^8 s^{-1} .

The C_β - C_γ axis has approximately C_{2v} symmetry, which suggests that in highly restricted environments the rotational motion of the ring should be restricted to sudden, 180° jumps between symmetrically equivalent orientational "sites". Early relaxation NMR studies on natural abundance ^{13}C and ^{19}F labeled phenylalanine showed that the ring motions are faster than the overall rotation of host proteins in solution^{122, 123 124}. Analysis of high-field ^1H NMR spectra demonstrated motional averaging of chemical shift interactions: when phenylalanine is in an asymmetric protein environment, the phenyl ring proton spectrum has two triplets and one doublet, indicating that the chemical shift differences for opposite sides of the ring are averaged by motion about the C_β - C_γ axis. Previous studies of L-phe- d_5 ,^{72, 125} where only the phenyl rings are labeled by deuterons, concluded that only some of the phenyl rings flip rapidly ($k_{\text{Ring}} > 1 \times 10^8 \text{ s}^{-1}$) in phenylalanine itself, with the ratio of these two types of phenyl rings approximately 1:1 and apparently dependent upon conditions of crystallization⁷². Other studies suggested

that L-phe-d₅ can occur in at least two different crystalline forms. Although the crystal structures of some L-phe derivatives, such as L-phe-d₅.HCl, are known¹²⁶, the crystal structure of pure L-phenylalanine-d₅ has never been reported, because single crystals suitable for X-ray analysis are very hard to prepare.

Deuteron NMR provides an attractive alternative spectroscopic approach to ¹³C, ¹⁹F and ¹H NMR experiments for studying the motion of phenylalanine, because quadrupole echo and MAS spectra of the ring deuterons are affected by the phenyl ring motion in a manner that permits rigorous, quantitative simulation. Thus, the dynamical model and relevant rates can, in principle, be determined by comparing experimental and calculated spectra.

5.2 Experiments and simulations of L-phenylalanine-d₈

5.2.1 Quadrupole echo and MAS experiments

Deuteron labeled phenylalanine (L-phe-d₈), with the aromatic ring and aliphatic protons replaced by deuterons, was used as received from Sigma-Aldrich. Variable temperature quadrupole echo and MAS experiments were carried out on pure L-phe-d₈ at 115.16 MHz (17.6 T magnetic field) using a Bruker Avance® WB750 spectrometer. During the high speed MAS experiments, the powder sample was spun at 30 kHz \pm 2 Hz in a 2.5 mm rotor and the temperature was controlled by a Bruker temperature controller. The reported temperatures in this chapter include a correction for frictional heating, determined by calibration with lead nitrate. In quadrupole echo experiments, two high power 90° pulses (2.0 μ s) were used with a 30 μ s interpulse delay in order to move the spin echo outside the spectrometer dead time. Because of the poor signal/noise ratio of

quadrupole echo line shapes, 1024 scans were acquired to obtain one FID and the recycle delay was 6 seconds. As noted below, this short recycle delay selectively suppressed signal from non-flipping ring deuterons. In MAS experiments, a single 90° excitation pulse ($2.0 \mu\text{s}$) was used and only 64 scans were needed to obtain adequate signal to noise ratio. In dramatic contrast to the static QE experiments, a recycle delay of only 10 seconds was sufficient for full magnetization recovery of all sites. Presumably, this difference is due to rotor-induced cross relaxation: under MAS conditions, the time-dependent Zeeman eigenstates of deuterons on rigid and fast-flipping rings coincide twice per rotor cycle, permitting efficient energy exchange by otherwise non-secular dipolar coupling. This provides an efficient relaxation pathway for the deuterons on non-flipping rings, as well as nearby aliphatic CD and CD₂ deuterons (section 5.2.3). Each quadrupole echo FID contains 1024 points and each MAS FID contains 8192 data points. In all experiments, the dwell time between two data points was $2.5 \mu\text{s}$, corresponding to a ± 200 kHz spectral window after Fourier transformation. During the experiments, the probe was retuned at each temperature and the magic angle was adjusted to minimize the broadening effect that was introduced by any drift from magic angle, which might be introduced by the change of the differential thermal expansion. Quadrupole echo spectra at different temperatures are shown in Figure 5.3.

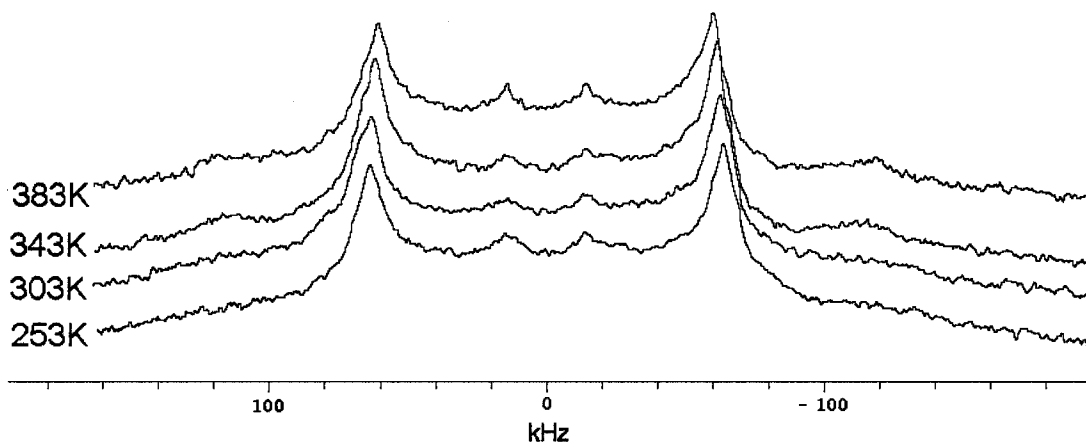


FIG. 5.3 Quadrupole echo spectra of L-phe-d₈. Overlapping powder patterns are observed in the QE spectra, that are difficult to analyze quantitatively because they represent a superposition of signals from all the deuterons. See text for details.

In these spectra the signals from all deuterons (side chain and aromatic ring) overlap. Previous QE experiments on selectively phenyl-labeled samples showed that the relaxation delay needed for full recovery of non-flipping ring deuterons is painfully long, in excess of 100 seconds.¹²⁶ It is therefore safe to assume that the "full width" powder patterns in Figure 5.3 arise primarily from side chain deuterons (with a small contribution from partially relaxed, non-flipping ring deuterons), while the narrower doublet feature in the middle of the spectrum is due to the rapidly flipping ring deuterons. The almost complete absence of temperature dependence in these spectra shows that all the phenyl flip rates are outside the kinetic window accessible to the QE lineshape technique: they are either slower than $\sim 100 \text{ s}^{-1}$ ("static") or faster than $\sim 10^8 \text{ s}^{-1}$ ("fast"). More complete analysis is precluded due to the limited resolution.

In contrast with quadrupole echo spectra, MAS spectra at high magnetic field only show a few narrow peaks at each sideband and have much better resolution. It is of interest historically that the $\sim 0.5 \text{ ppm}$ resolution attained in this deuteron MAS spectrum

at 17.6T (115 MHz) is comparable to state of the art high resolution, liquid state *proton* NMR spectroscopy at 2.4T (100 MHz) in 1960. The center band region of the MAS spectrum obtained at low temperature, 253K. Fig. 5.4 is shown

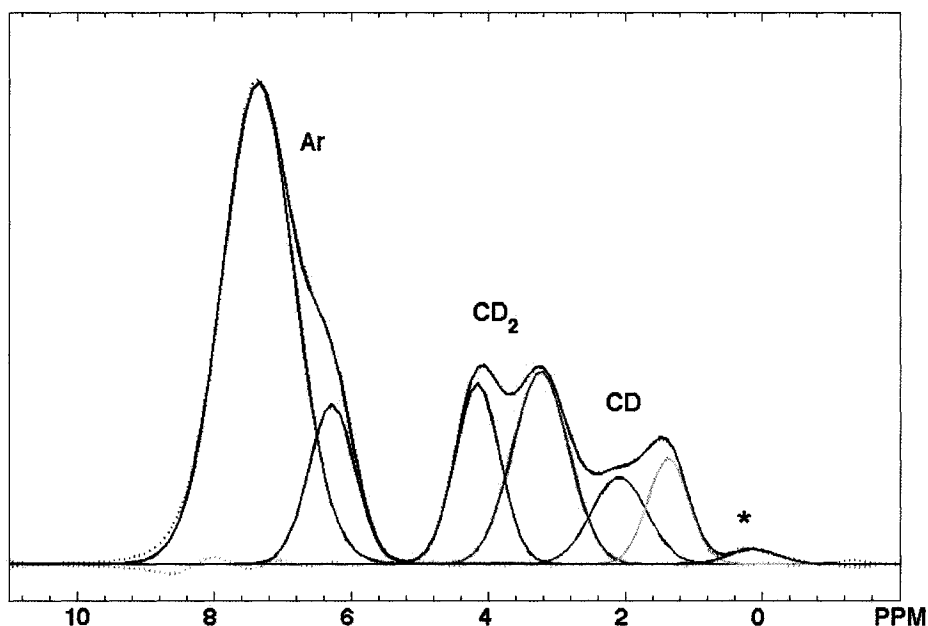


Figure 5.4: 17.6T MAS Spectrum of L-Phenylalanine- d_8 at 253K
Only the center band is shown; the sidebands at multiples of the 30 kHz spin rate all have similar structure.

This spectrum was decomposed into seven component lines by Levenburg-Marquardt procedures (using MATLAB nonlinear least squares procedures). Each component $P_j(\nu)$ consists of a weighted sum of Gaussian and Lorentzian line shape functions:

$$P_j(\nu) = I_j \left[g_j e^{-\left(\frac{\nu - \nu_j}{2\sigma_j}\right)^2} + (1 - g_j) \frac{R_j}{R_j^2 + 4\pi^2(\nu - \nu_j)^2} \right] \quad 5.2.1$$

Here, I_j is the integrated intensity of component j , centered at frequency ν_j , made up from a fraction g_j of Gaussian and $(1 - g_j)$ Lorentzian line shape functions. The width parameters σ_j (for Gaussian) and R_j (for Lorentzian) functions were fixed so that each has the same full width, W_j , at half maximum intensity. Thus, $W_j = \pi R_j$ for the Lorentzians and $W_j = 4(\ln 2)^{1/2} \sigma_j$ for the Gaussians. There are thus four independent parameters for each component: I_j , ν_j , g_j , and W_j . The best fit values that give the spectrum shown in Figure

5.4 are listed in Table 5.1. The error bars represent 67% (1 std dev) confidence limits returned by the fitting algorithm.

Table 5.1 Best fit parameters from the MAS spectrum

Peak	Intensity ¹	Frequency (ppm)	Width (Hz)	G/L Ratio ²	Assignment
1	4.7±0.1	7.362±0.002	142±0.3	0.89±0.03	Ar (o,m)
2	0.97±0.25	6.289±0.003	91±0.7	0.92±0.3	Ar(p)
3	1.0±0.3	4.170±0.016	88±2.5	1.0±0.3	CD ₂
4	1.3±1.5	3.246±0.013	111±12	1.0±1.2	CD ₂
5	0.5±1.4	2.102±0.026	109±28	1.0±2.4	CD
6	0.5±0.4	1.381±0.023	81±3	1.0±0.8	CD
*	0.1±0.1	0.140±0.030	97±8	0.8±1.3	Artifact ³

(1) Integrated relative intensity I_j of each component as defined in Eq. 5.2.1, scaled to give peak 3 unit intensity. (2) This is g_j as defined in Eq. 5.2.1. (3) The weak "peak" labeled with a * in Figure 5.4 is an artifact of data processing for reasons described in the text.

Not surprisingly, this 28-parameter fit is not unique and depends on the initial conditions of Gaussian/Lorentzian peaks, and several of the error bars are very large. In particular, the Gaussian/Lorentzian fraction of each component (column 5) could simply be fixed at 1.0 for all the peaks, reducing the number of independent fitting parameters from 28 to 21, and this does not significantly alter the other best-fit parameters. Since the time domain data was apodized with a judicious combination of Gaussian and Lorentzian functions designed to enhance resolution at the expense of introducing noise, the best fit G/L values are of little significance. This apodization, while useful for determining the most probable number of components, has the undesirable side effect of introducing baseline oscillations at the skirts of narrow peaks. This is the origin of the spurious small peak labeled with a star in Figure 5.4; it had to be included in the fit to prevent the automated fitting routine from trying to match it by putting a wide, weak Lorentzian line in the middle of the spectrum. It should be noted that while the fitting routine does have trouble determining proper widths and relative intensities of overlapping peaks 3,4, and

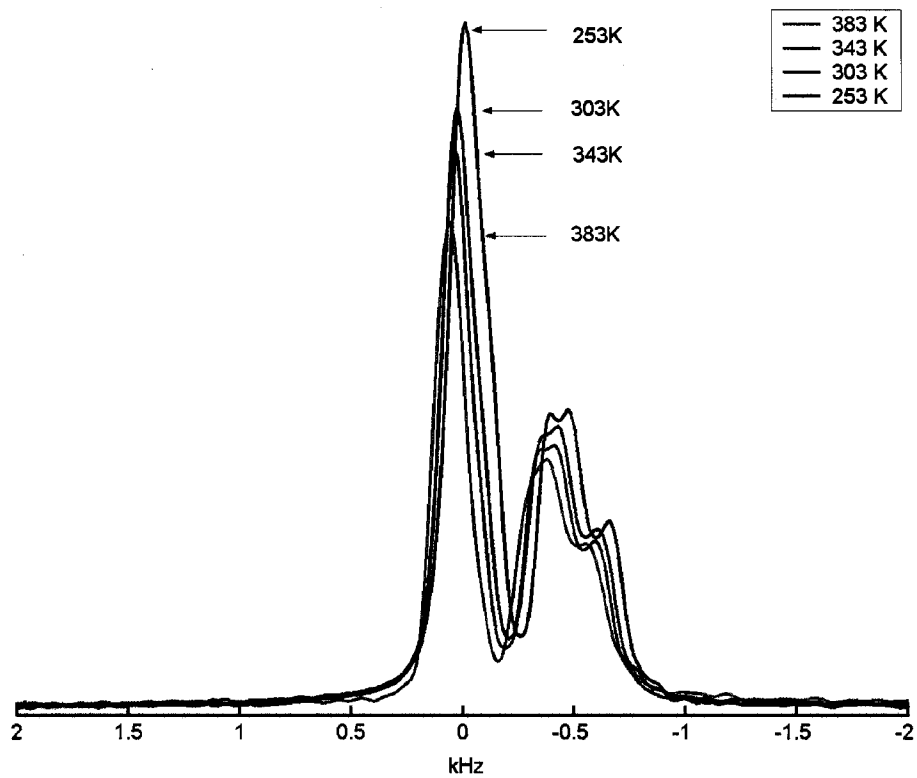
5, replacing these with only two peaks gives noticeably larger residuals and increases the minimum value of chi-squared by more than a factor of three. In summary, the frequencies, relative intensities, and line widths of peaks 1 through 6 can be determined with sufficient precision that detailed interpretation is warranted.

The high resolution (proton decoupled) solution state spectrum of L-phenylalanine consists, as expected, of a closely spaced set of three peaks between 7.3 and 7.4 ppm, (relative intensities 2:2:1); and single peaks at 3.97 and 3.27 ppm with relative intensities 1:2.¹²⁷ These are easy to assign unambiguously to aromatic, CH, and CH₂ protons, respectively: the two *ortho* protons and the two *meta* protons are rendered magnetically equivalent by virtue of rapid, unrestricted ring rotations in the liquid, and the two protons of the CH₂ group are also magnetically equivalent by virtue of fast internal rotation about the relevant C-C bonds. The 0.5 ppm down field shift of CH relative to CH₂ in solution state phenylalanine is normal for these functional groups, as is the large down field shift of aromatic protons due to ring current effects¹²⁸.

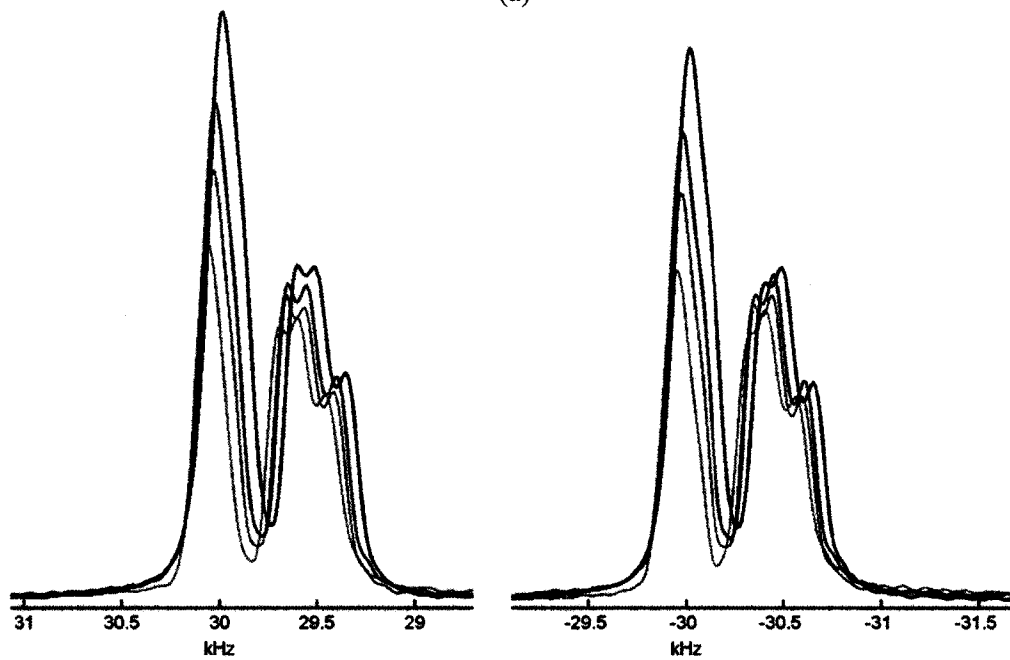
The solid state spectrum of L-phenylalanine is very different. Naively, one might expect the CD-CD₂ spectrum to consist of three peaks with equal relative intensity since the two CD₂ deuterons become magnetically inequivalent when crystal constraints quench the internal rotation about C-C bonds. Residual dipole-dipole coupling obscures small chemical shift differences among the aromatic deuterons, leading to the prediction of a simple, four line spectrum with relative intensities 5:1:1:1. Casual inspection of Figure 5.4 reveals that this is certainly not the case. If the CD and CD₂ peaks are assigned on the basis of their 1:2 relative intensities, then compared to the solution state, the CD deuterons have shifted *up field* with respect to the aromatic deuterons by more than 2

ppm, and now resonate at higher field than the CD₂ group. Moreover, the relative intensities of aromatic, CD₂, and CD deuterons appear in the ratio ~6:2:1 rather than 5:2:1, there are *two* CD peaks rather than one, and part of the aromatic peak (with relative intensity one) has shifted up field by almost 1 ppm with respect to its companions. All these observations are consistent with the idea that there are two distinct phenylalanine molecules in the unit cell, with different conformations about the C_α-C_β-C_γ chain. In both molecules, (denoted by A and B respectively), the CD deuterons are constrained to lie relatively close to and above the aromatic ring planes, producing large up field ring current shifts. A similar situation prevails for CD₂ deuterons in *one* of the two molecules (peak 4 in Table 5.1). The two CD₂ deuterons in each molecule will have the same chemical shift in the solid if the ring plane from the same molecule bisects the D-C-D bond angle, *and* both deuterons are equidistant from ring planes of neighboring molecules. It is indeed unfortunate that there is no crystal structure available to check this hypothesis.

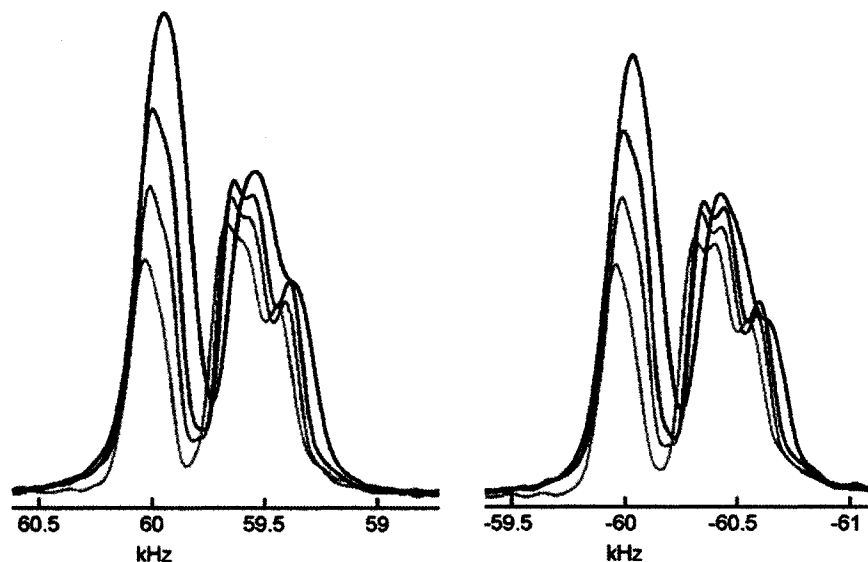
The temperature dependence of MAS center band and side band line shapes is shown in Figure 5.5. The positions, widths, and relative intensities of the CD-CD₂ peaks shift significantly with temperature. At 383K, for example, deconvolution of the CD-CD₂ region (not shown here) reveals three peaks instead of the four observed at lower temperatures. In general, this behavior can be ascribed to ring current shifts associated with conformational changes that accompany crystal lattice expansion at high temperature, but in absence of single crystal X-ray data a detailed interpretation is not possible.



(a)



(b)



(c)

FIG. 5.5 Temperature dependent MAS side band line shapes of L-phe- d_8 . The figure shows (a) the center band at 0 Hz, (b) the first sideband pair at -30 kHz and 30 kHz and (c) the second sideband pair at -60 kHz and 60 kHz at different temperatures. It is obvious that the aromatic peak, pointed out by the arrows in (a), shows stronger temperature dependent intensity than the others.

In contrast with the aliphatic deuterons, the integrated intensity and line width of the aromatic deuteron resonance is strongly temperature dependent. The T_{1Z} relaxation experiment described in Section 5.2.2 below confirms the hypothesis that this behavior is associated with rapid phenyl ring flips.

5.2.2 T_{1Z} relaxation study

The phenylalanine T_{1Z} relaxation times under MAS conditions were measured at 303 K. The pulse program consisted of a 180° -pulse train is used to generate uniform saturation of the entire spectrum, and after variable delay τ , a single 90° pulse followed by acquisition of the FID signal and subsequent Fourier transformation in the usual manner. The spin rate in this experiment was 30 kHz. The pulse sequence is shown in

Figure 5.6, and expanded regions showing the center and the first left side band are presented in Figure 5.7.

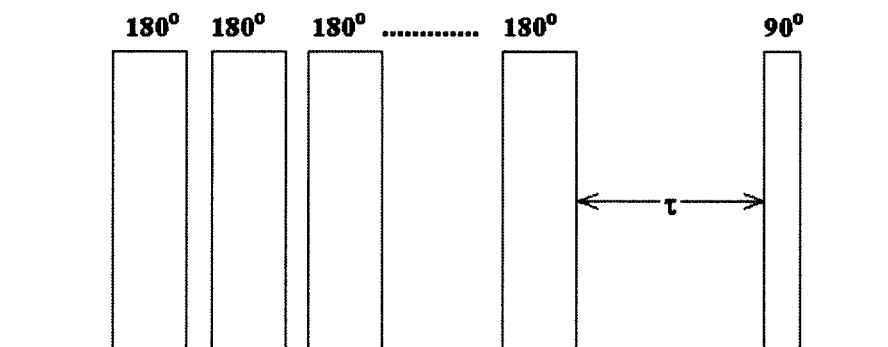
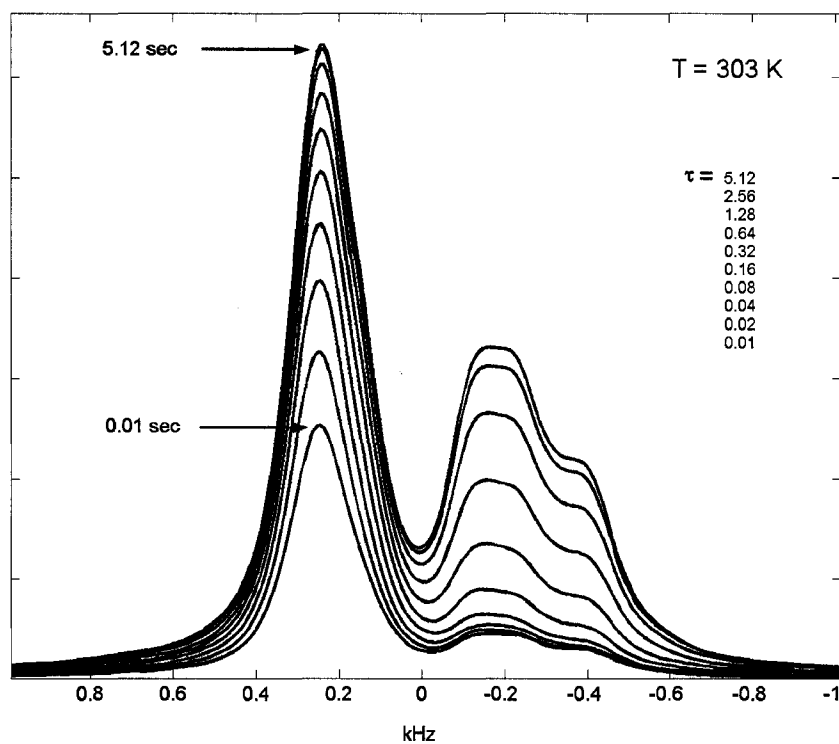
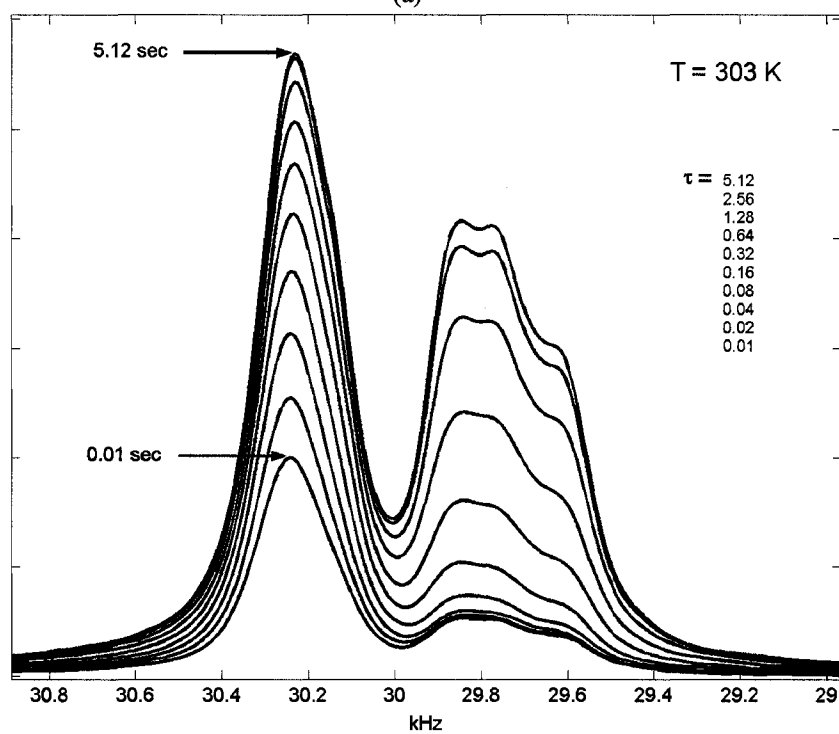


FIG. 5.6 Phenylalanine T_{1z} relaxation experiments

The 180° pulse train contains 120 pulses ($4 \mu\text{s}$) and ten τ values between .01 and 5.12 seconds were used. Right after the pulse train, the initial magnetization, $M(0)$, was assumed to be zero and used in T_{1z} fitting.



(a)



(b)

FIG. 5.7 The center and the left first sideband of the relaxation spectra (a) The center and (b) the left first sideband are shown. τ value increase from 10 μ s to 5.12 s. The intensities reflect the spin magnetization value after the relaxation period.

The relationship between T_{1Z} and τ can be described by following equation ¹²⁹

$$m(\tau) = m(\infty) + e^{-(\tau/T_{1Z})} (m(0) - m(\infty)) \quad (5.1)$$

The saturating pulses train is supposed to make $m(0)$ exactly zero, so that only a two-parameter fit: T_{1Z} and $m(\infty)$ need be done, but since this is never exact, we just keep $m(0)$ as a variable to be fit.

$$M(\infty) = M(0) \cdot \left(1 - 2 \exp\left(\frac{\tau}{T_{1Z}}\right) \right) \quad (5.2)$$

Therefore, T_{1Z} can be obtained by fitting the intensity profile with different relaxation periods. The double exponential fitting of the intensity profile is useful when the intensity profile is affected by two different dynamical processes.

$$M(\infty) = P \cdot M(0) \cdot \left(1 - 2 \exp\left(\frac{\tau}{T_{1Z}^A}\right) \right) + (1 - P) \cdot M(0) \cdot \left(1 - 2 \exp\left(\frac{\tau}{T_{1Z}^B}\right) \right) \quad (5.3)$$

The fitting routine used MATLAB software to select five representative points, whose positions are chosen according to the decomposition shown in fig 5.8, to match peaks already assigned to aromatic deuterons (D and E), CD₂ deuterons (A and B), and CD deuterons(C). The measured T_{1Z} values for each peak were determined for the center band and for all the side bands are shown in Figure 5.9.

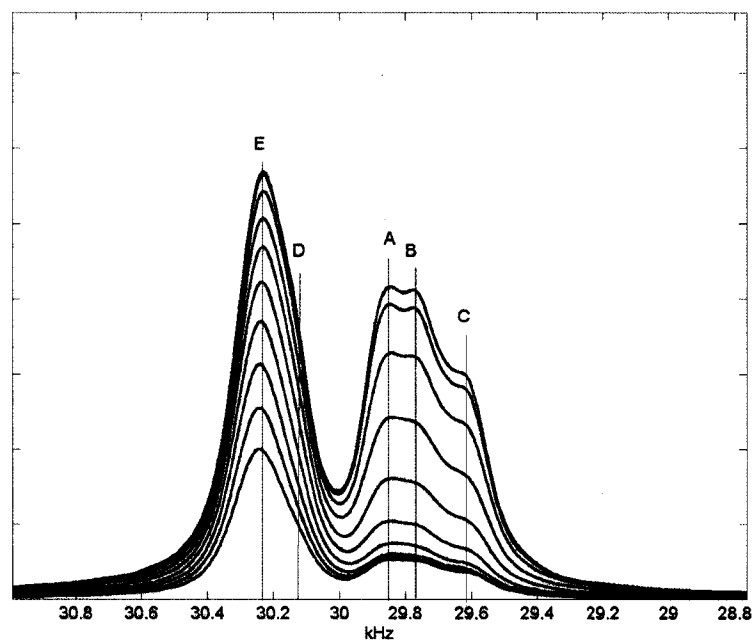


FIG. 5.8 Points chosen to measure site-selective relaxation times
Intensity at points D and E arises from aromatic deuterons, points A and B monitor CD_2 deuterons, and point C monitors CD deuterons. The region between points B and C includes overlapping signals from both types of aliphatic deuterons.

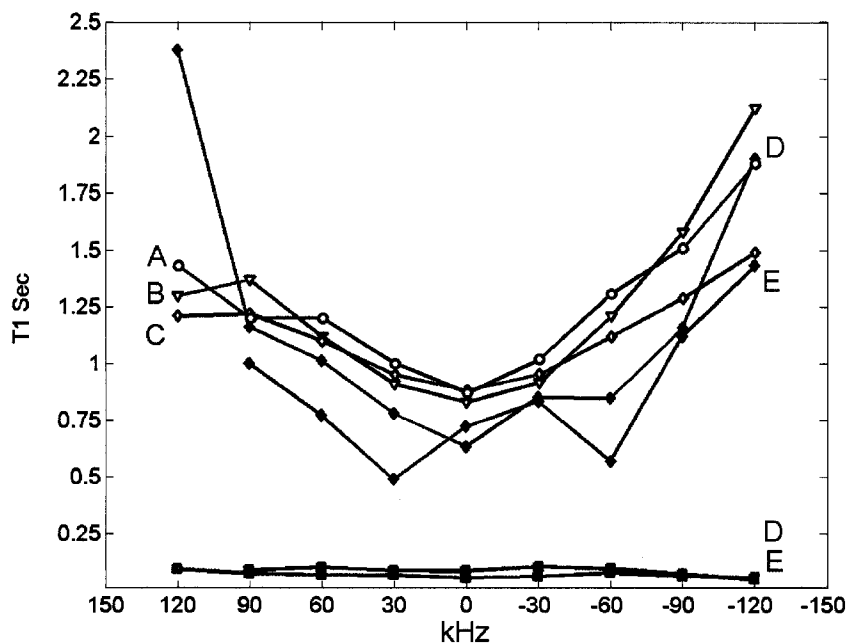


FIG. 5.9 T_{1Z} measurements of the intensity profile
The MAS peaks, D and C, consist both para-deuteron and mobile deuterons. Therefore, double exponential T_{1Z} fitting is used. The fast T_{1Z} component is much smaller than the slow T_{1Z} component (0.5-2.5 sec). The single T_{1Z} value of sub-peaks A, B, C and the slow T_{1Z} component of D and E depend upon their frequencies, but the fast T_{1Z} component of D, E do not change with their positions.

Semi-log recovery curves for peaks A, B and C are single exponentials, with T_{1Z} values increasing from 1 ± 0.2 sec for the center band to 1.5 ± 0.3 sec for the sidebands. The recovery curve for points D and E is double exponential. The fast component is smaller than 50 μ s, independent of sideband number. The slow component T_{1Z} values are the same within experimental error as those found for peaks A, B, and C. The fast component arises from flipping phenyl rings; this motion efficiently relaxes the *ortho* and *meta* ring deuterons (peak D in fig. 5.8) because their electric field gradient tensors experience large angle reorientation with each jump. Measurements of this type of motion under MAS conditions have not previously been reported, but the lack of dependence on sideband number is expected since the fast ring flips tend to average relaxation time anisotropy^{130, 131}. The longer, anisotropic T_{1Z} values observed for all other deuterons are considered arising from small angle librational motion¹³⁰.

When analyzing relaxation data, the dominant nuclear spin interaction effecting relaxation must be known and it must exceed the effects of other interactions by at least an order of magnitude, otherwise the data become extremely complex to interpret. In deuteron MAS relaxation experiments, where the dominant spin interaction is quadrupole coupling, the relationship between motion rate and relaxation time is still molecule orientation dependent. In addition, rotor-induced cross relaxation permits MAS spectra to be obtained with shorter recycle delays than the delays that is required for static quadrupole echo spectra, and this cross relaxation effect must be included in quantitative interpretation of MAS T_{1Z} . These two properties of MAS relaxation experiments preclude a quantitative T_{1Z} simulation of phenylalanine. However, the MAS relaxation experiments confirm that the signals from different segments of phenylalanine could be

distinguished, and the peak D, E can be compared with MAS spectrum simulations based on the π -flip motion model to calculate the motion rates since the peak D, E come from phenyl ring deuterons.^{132, 133}

5.2.3 Simulation of phenylalanine MAS spectra

The calculation of phenylalanine molecular motion is based on the π -flip motion model. The model consists four deuterons that are included in the aromatic ring flip. Their orientations are listed in table 5.2.

Table 5.2 The Euler angles of aromatic ring deuteron

Site	α	β	γ
ortho-1	0	120°	0
ortho-2	0	120°	180°
meta-1	0	60°	0
meta-2	0	60°	180°

In order to improve the computation efficiency, the symmetric four sites model can be reduced to two sites model containing only δ -1 and δ -2 deuterons. Since the immobile phenyl rings exist in the sample, the simulation basing on the flip motion is not accurate as fig. 5.10 shows. The center band in fig 5.10 is shown in fig 5.11. The simulation demonstrated that when the motion is in the fast motion regime ($k > 10^6 \text{ s}^{-1}$), the peak width depends inversely on temperature. Further more, when the motion is close to the fast limitation ($k > 10^8 \text{ s}^{-1}$), MAS peak width becomes insensitive to the flip rate.

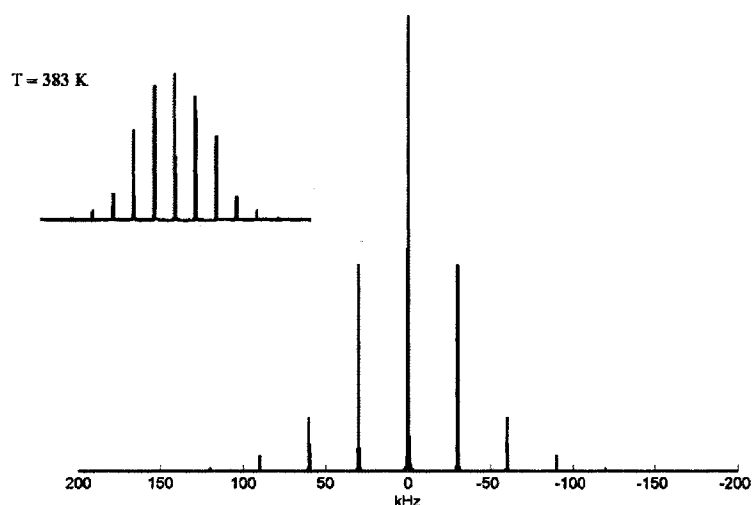


FIG. 5.10 The calculated MAS spectra

The motion model is two site π -flip motion model with $C_Q=160\text{kHz}$, $\eta_Q=0.05$. The calculated FID contains 8192 data points and the dwell time is $2.5\ \mu\text{s}$. Since the signals of immobile and flip phenyl rings are mixed in the experimental spectrum, the intensity profile doesn't match the experimental data well as is shown in the insert. However, the effects of the flip motion on the intensity and peak width can be separated as fig. 5.14 shows.

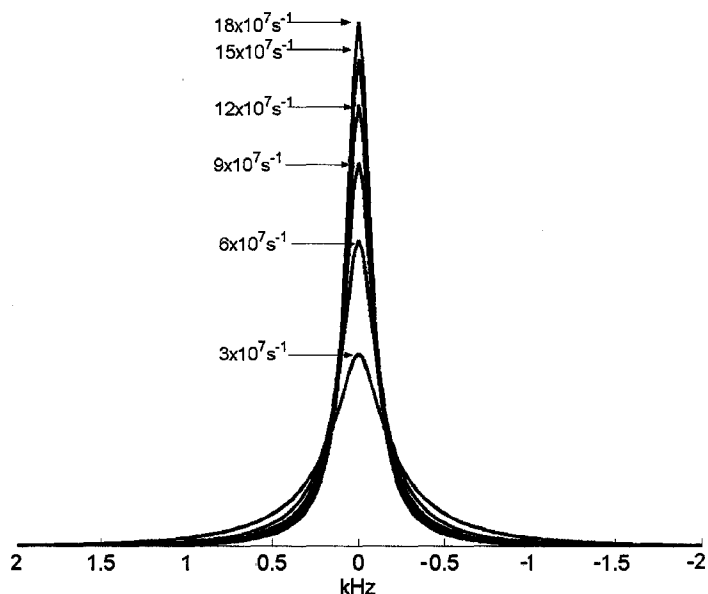


FIG. 5.11 The center band of calculated MAS

The calculated center bands are shown here. The motion rate increases from 3×10^7 to $1.8 \times 10^8\ \text{s}^{-1}$. We can observe that the line width decrease when the motion rate increases from 3×10^7 to $1.8 \times 10^8\ \text{s}^{-1}$. The simulation demonstrated that when the motion is fast ($k > 10^6\ \text{s}^{-1}$), the peak width depends inversely on temperature. Furthermore, when the motion is close to the fast limitation, the relationship between peak width and flip rate is weakening.

In order to match the experiment spectrum that contains both flip and immobile phenyl rings, the FID of static phenyl ring and FID of para-deuteron were also calculated. If the percentage of the flipping phenyl ring is $m\%$, the mixed FID is

$$FID = 2 \cdot (m\% \cdot FID_{flip} + (1 - m\%) \cdot FID_{immobile}) + FID_{para} \quad (5.3)$$

Where $FID_{immobile}$ uses the same orientation as the two sites π -flip motion model but the jump rate is zero, FID_{para} includes only one deuteron and simulates the para-deuteron in phenylalanine. In fig. 5.12, these three calculated spectra are shown individually. The full spectrum and its three frequency bands are shown in fig 5.13 and 5.14. The simulation takes the fast limitation assumption, in which the flip rate is fixed at $5 \times 10^8 \text{ s}^{-1}$. The percentage of the flipping phenyl ring could vary in a small range (45~65%) in order to get the best visual fit. For the MAS spectrum at 383 K, this percentage is around 60%, and consistent with other studies.⁷²

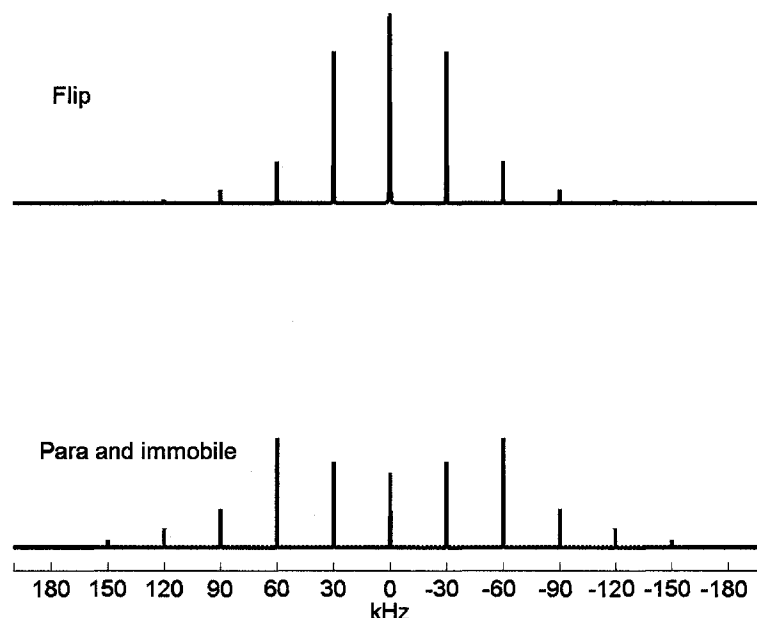


Fig. 5.12 Simulations of flip, immobile and para-deuteron

The calculations of the π -flip phenyl ring and the para-deuteron are shown here. The spectra from static deuterons including immobile and para-deuterons are assumed to be same within simulation round error. This artificial is introduced by FID-truncation effects and distorted the center and the first pair of side bands. The motion rate of fast flipping phenyl ring is $5 \times 10^8 \text{ s}^{-1}$.

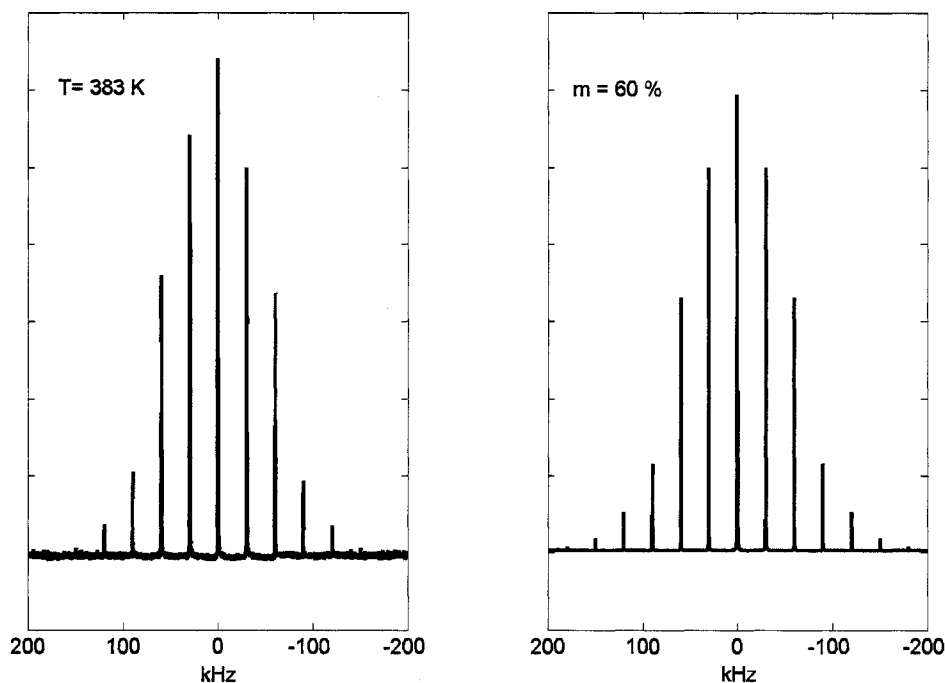


FIG. 5.13 The simulation of phenylalanine MAS spectrum

Here the contributions from about 45% immobile phenyl ring and the para-deuteron are also included. The FID is the sum of three separate simulations: one with $k = 5 \times 10^8 \text{ s}^{-1}$ (fast π -flip) and one with $k = 0$ (immobile), the para-deuteron FID included only one deuteron. Compared with fig. 5.13, the mixed simulation matches the experimental spectrum better. The percentage of fast flipping phenyl ring is 60% because at high temperature, part of immobile phenyl rings might be untied from their crystal lattices and flip.

It should be notified that the total integrated intensity drops at the highest temperature. This phenomenon cannot be explained when the motion rate is in the fast motion regime ($k > 10^6 \text{ s}^{-1}$), where the intensity always increase as the motion becomes fast when the temperatures higher. The possible reason for this intensity drop is that when the immobile phenyl rings begin to flip, part of them can only rotate with an ultra-slow motion rate ($k < 150 \text{ s}^{-1}$) that causes the drop of MAS peak intensities. However, the simulations demonstrate that the dominant motion is still fast π -flip motion and the insensitivity of D, E peaks to the temperature (253~343 K) indicates that the underlying motion belongs to the fast limitation ($k > 10^8 \text{ s}^{-1}$).

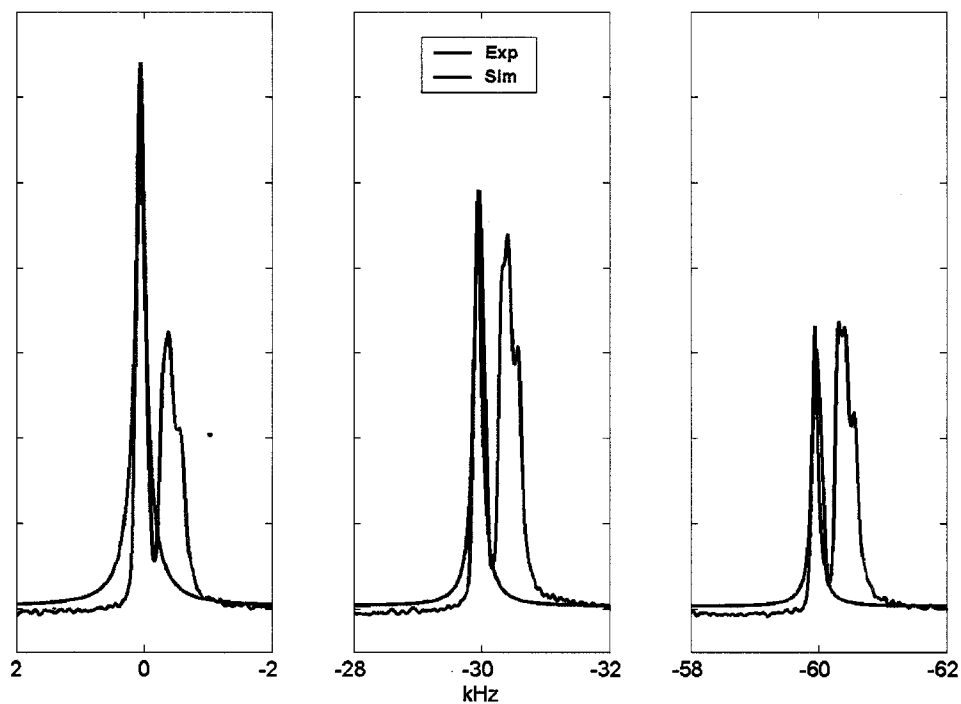


FIG. 5.14 Comparison between simulation and experiment

The center, first, second side bands are shown in three insets. Blue line is the simulation MAS spectrum and solid line is the experimental spectrum at 383 K. It is clear that when the FID contains 60% flip and 40% immobile phenyl deuterons, the simulation well matches the experimental data. In this simulation, chemical shift anisotropies that contributed to the asymmetry of the experimental spectrum were not considered.

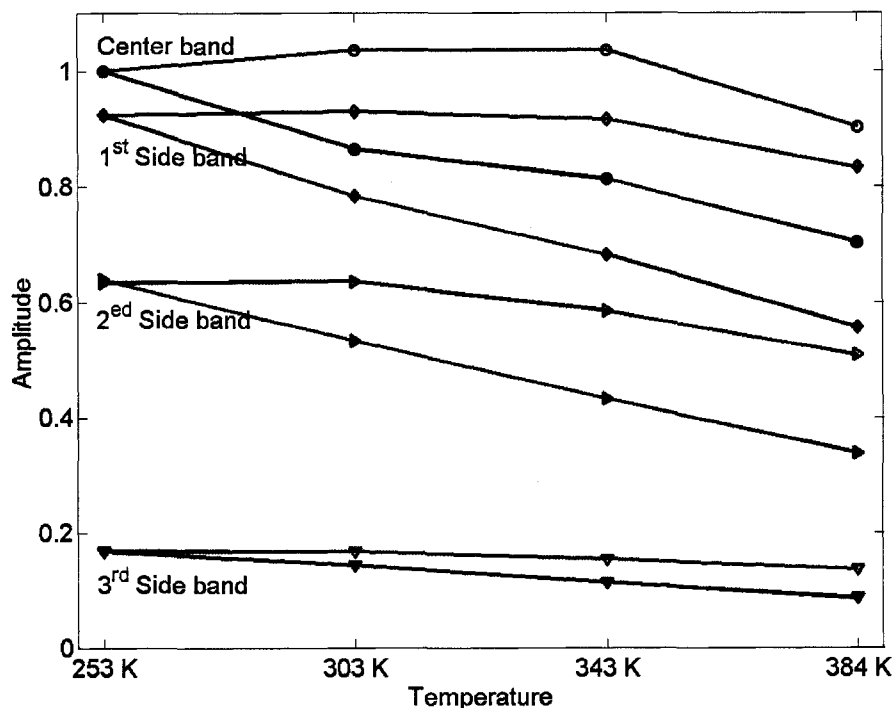


FIG. 5.15 Amplitude profiles of L-phen-d₈

The amplitudes of overlapping peak D and E in the center and side bands under different temperatures are shown here. Peak amplitudes are measured respect to the highest peak, the center band of 253 K. The red lines are adjusted by a temperature parameter (T/T_{respect}) and the black lines are the original amplitude values. In experimental error range, the amplitudes of center and all side bands can be considered as independent to temperature, demonstrating that the flipping motion approaches the fast limitation ($k > 10^8 \text{ s}^{-1}$). At highest temperature, the amplitude drops at around 10%, this sudden intensity change indicates that some immobile phenyl rings now able to flip at an ultra-slow motion rate ($k < 150 \text{ s}^{-1}$). But the simulation shows that the dominant motion is still fast π -flip motion (60%) and the immobile phenyl rings (40%).

5.3 NAPME/ β -cyclodextrin inclusion compound

5.3.1 MAS experiments

In addition to the study of pure phenylalanine, measurements were also carried out on N-acetyl-L-phenylalanine-methyl-ester (NAPME) trapped in cavities of a solid inclusion compound with β -cyclodextrin. Cyclodextrins are cyclic oligosaccharides, consisting of 6 (α), 7(β) or 8(γ) glycosyl-unites.^{134 135} These compounds have unique structures that can be described as toroidal, hollow, truncated cones with a hydrophilic exterior and a hydrophobic interior. This unique arrangement allows guest molecules with hydrophobic groups to enter the cavity and be bound by non-covalent forces. In this study, NAPME molecules act as guest molecules while β -cyclodextrin is the host molecules.

Motivation for this study is provided by the possibility that the cyclodextrin cavity could be a model for the environment of phenylalanine in the active site of proteins, where the intermolecular potentials are certainly different than those imposed by the crystal lattice of pure phenylalanine.^{136 124, 137} In the inclusion compound, two limiting cases for rotational motion of phenylalanine molecules can be envisioned : (1) Discrete jumps among a small number of orientation sites, with residence times that are much longer than the transit times; and (2) restricted continuous diffusion, where jumps occur only between neighboring sites within a fixed domain, and the Euler rotation that connects each site to the next is infinitesimal.

In ^1H -NMR studies of phenylalanine side chains in proteins³⁸, discrete jump motion was assumed on the grounds that within the closely packed protein interior, the bulk of the aromatic rings should be severely hindered. However, ^{13}C and ^{19}F relaxation

data for similar systems ⁷² are consistent with both discrete jumps and continuous diffusion. Solid-state ²H-MAS NMR provides an unambiguous way to characterize the difference between these two models. In particular, it will be shown in this section that the spin-rate dependent loss of spectral intensity that occurs at intermediate motional rates is much larger for large angle jumps.

Inclusion compound samples were prepared by Joanna L. Clark and Prof. John J. Stezowski at the Department of Chemistry, University of Nebraska-Lincoln. Deuteron labeled L-phenylalanine-d₈ was used to produce NAPME, β-cyclodextrin was mixed with NAPME in 1:1 mole ratio, and polycrystalline inclusion compound was obtained by precipitation. Previous, extensive variable temperature X-ray investigations of (unlabeled) single crystals of this material ¹³⁸ reveal that ~25 water molecules are left per unit cell.

Deuteron MAS experiments were performed at the College of William and Mary using the Bruker 750WB spectrometer described elsewhere in this thesis. Single pulse excitation (1.5μs) was used and the rotation speed was 15kHz. At each temperature, 8192 scans were acquired with a 0.5 s recycle delay, that was adequate for full recovery between scans. Temperature was controlled by the Bruker temperature controller to within ±0.1 K. Reported temperatures have been corrected for frictional heating due to sample rotation. Fig. 5.16 shows the central band of the deuteron spectrum at 340 K. Three well resolved peaks are observed, with integrated relative intensities 5:1:2, as expected for the aromatic, CD, and CD₂ deuterons. At this temperature, the narrow lines widths (<0.5 ppm), strong central band, and near absence of sidebands are characteristic of rapid, liquid-like isotropic motion. The spectrum is in all respects similar to a low

resolution version of the proton spectrum of phenylalanine in aqueous solution. Not surprisingly, detailed analysis of single crystal X-ray data¹³⁸ reveals extensive guest disorder at this temperature, such that phenylalanine molecules can migrate into interstices between the cyclodextrin cavities.

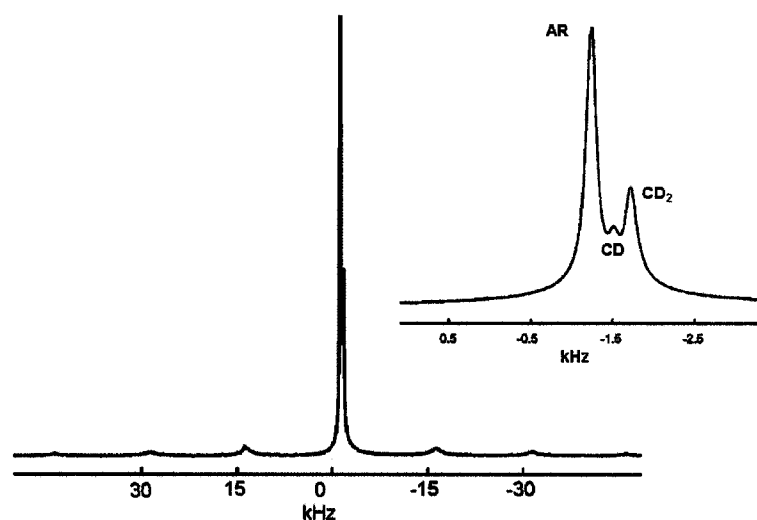


FIG. 5.16 The MAS Spectrum of NAPME/ β -CD inclusion compound at 340 K. The inset shows a 2000 Hz window expanded about the center band. The spectrum is characteristic of almost guest isotropic motion. Three peaks marked as AR, CD and CD₂ are similar to those observed in L-phe solution.

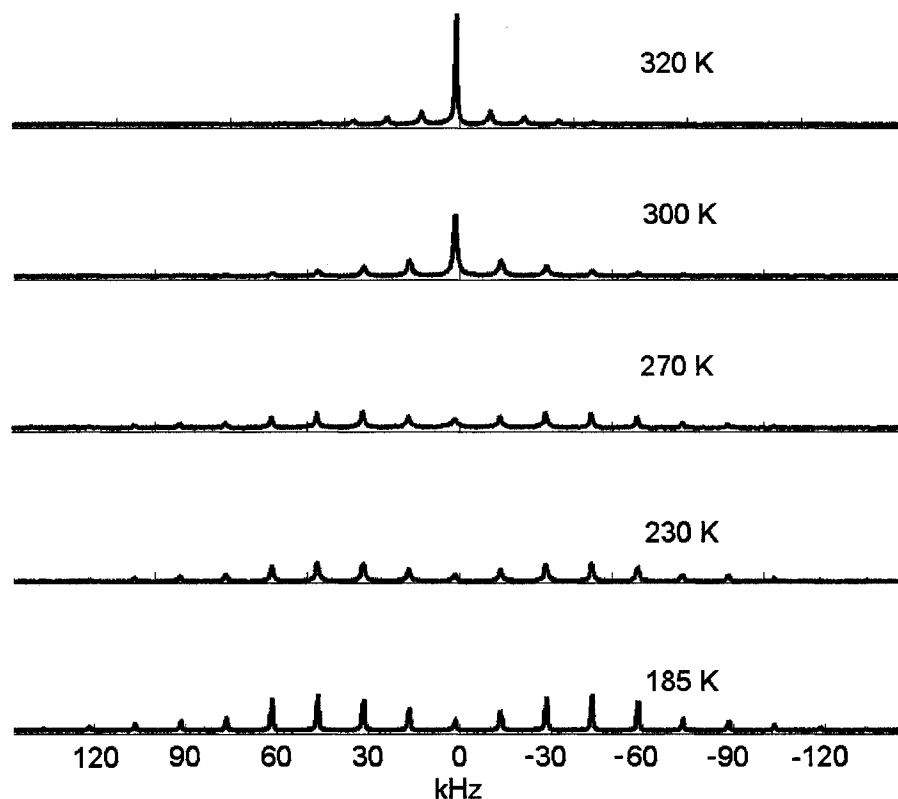


FIG. 5.17 VT-MAS Spectra of NAPME/ β -CD inclusion compound
 ^2H -MAS spectra are shown at different temperatures. At 185 K, the guest motion is slow ($k < 10^4 \text{ s}^{-1}$). The side bands and center band broadening as the temperature rises to ~ 270 K, and narrow again at higher temperature as the center band grows at expense of the side bands. This behavior is characteristic of continuous rotational diffusion, over an angular region that becomes larger with increasing temperature.

Fig. 5.17 shows MAS spectra at different temperatures. At room temperature (300 K), molecular motion is not quite fast and the quadrupole tensors are not fully averaged. Multiple side bands appear at multiples of the rotation speed (15 kHz). However, the intensity profile is different from those computed by any simulation based on discrete sites jump models. For example, simulations based on aromatic ring flips predicts a very significant loss of overall intensity in the intermediate rate regime due to the correlation between MAS rotation and molecular motion, and collapse to a motion narrowed intensity profile characteristic of a reduced quadrupole coupling tensor with asymmetry parameter ~ 0.6 . The observed collapse to zero quadrupole coupling tensor rules out the

discrete model unambiguously. Instead, we attempt in the next section to mimic the onset of continuous diffusion model.

5.4.2 Simulation and Discussion

In order to simulate diffusional dynamics via routines based on discrete jumps, a large number of orientational sites are defined on a geodesic lattice, shown in fig. 5.18, and jumps are allowed to occur only between nearest neighbor sites.

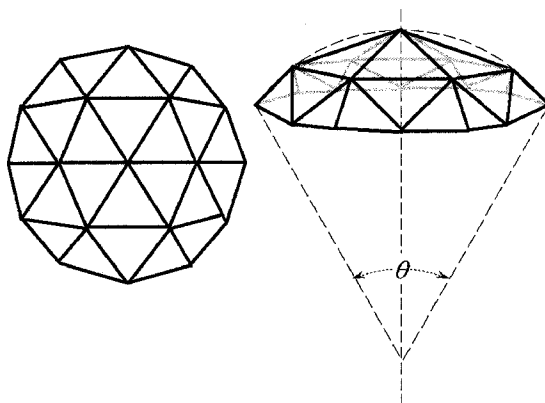


FIG. 5.18 19-Site system

Left: the top view. Right: the horizontal view. There are 19 sites distributing on triangular lattices. Jumps are allowed only between nearest neighbor sites. As the number of sites increasing, this discrete system approaches continuous diffusion in a restricted cone.

The cone angle, θ , is an additional parameter in this model in fig.5.18. It can be shown that in the fast motion limit, the motionally narrowed quadrupole coupling constant is zero for $\theta = 90^\circ$. However, for such large cone angles (that would be needed to simulate the experimental MAS line shapes), the number of sites becomes impractically large if the solid angle subtended by the geodesic triangles is kept small. In our simulations, two cone half-angles, 15° and 60° , were used, partitioned into systems containing 7, 19 or 43

sites to mimic increasingly smaller and smaller jump angles. In these MAS simulations, C_Q is 200 kHz and dwell time is 2.5 μ s.

With 25 kHz spinning rate, 10 pairs of sidebands were included the computation, and the Floquet matrix dimension was fixed at $20 \times N_{\text{sites}}$, i.e., 140 for seven sites and 860 for the 43 site simulations. The simulations were carried on an AMD64 workstation. The computation time per line shape varied between 5 minutes for 7 sites to 4 hours for 43 sites. Two different cone angles were used, 15° and 60° . Simulated MAS spectra with different jump rates are shown in fig. 5.19 and 5.20.

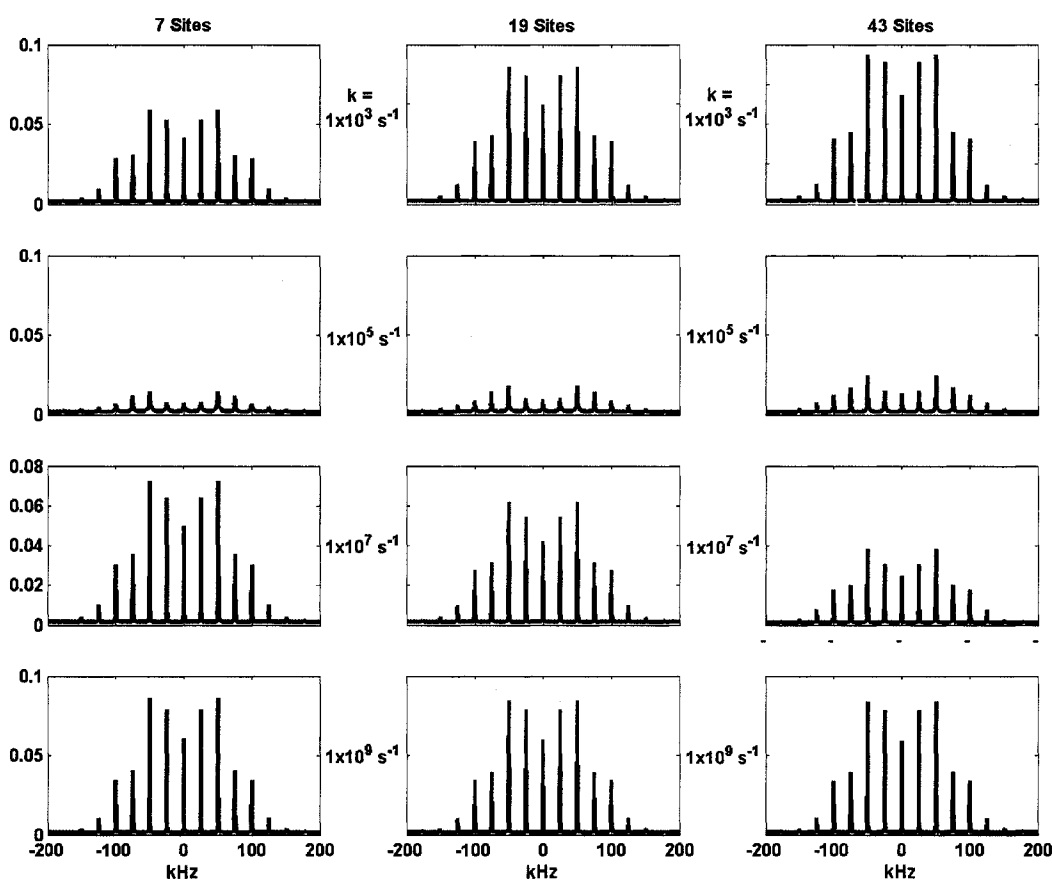


FIG. 5.19 Multi-site simulation of diffusion in a 15° cone.

MAS spectra are simulated with different numbers of sites (7, 19 and 43). Four motional rates are used to cover the slow, intermediate and fast motional regimes. Loss of spectral intensity occurs when the jump rate matches the sample spinning rate; this effect is noticeably *reduced* as the angular size of inter-site jumps is reduced.

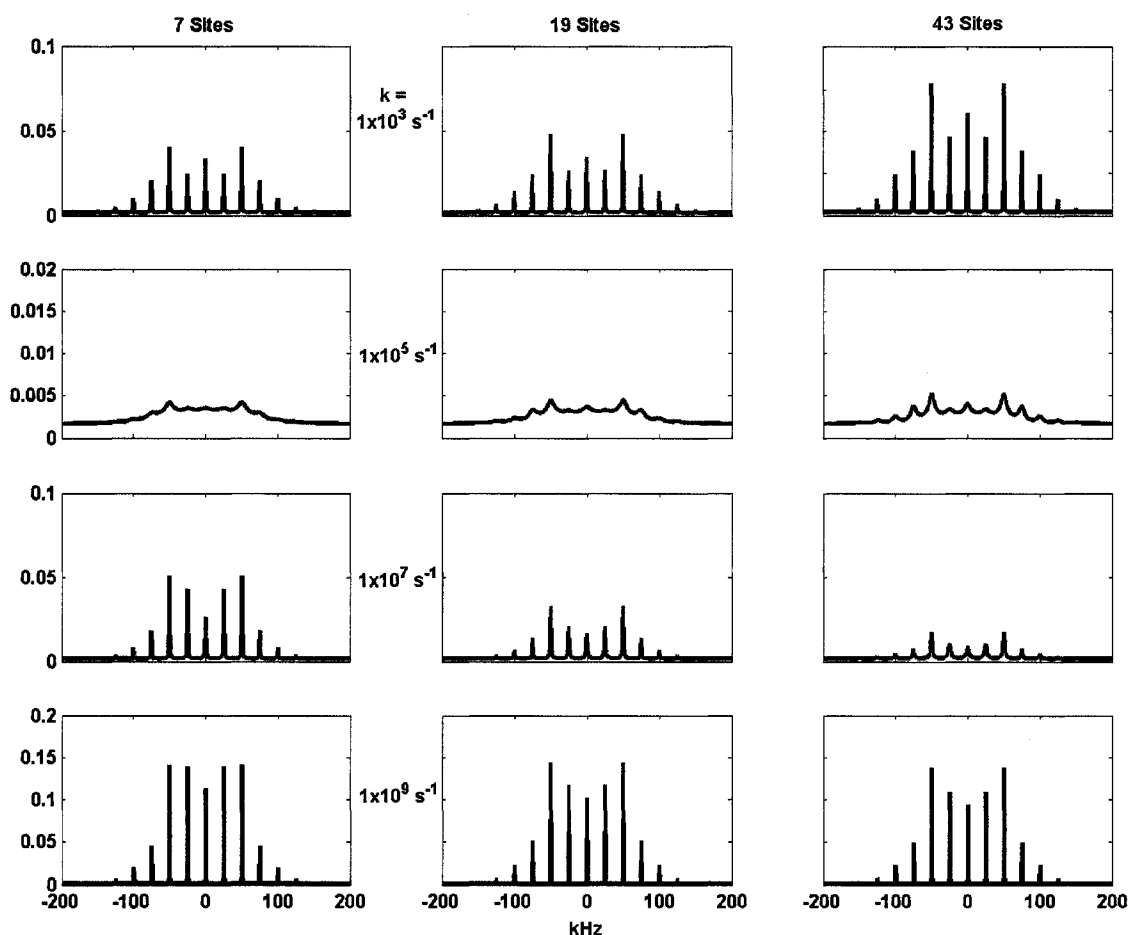


FIG. 5.20 Multi-site simulation of diffusion in a 60° cone.

Compared to 15° cone angle, these simulations show more pronounced loss of intensity in the intermediate motional regime, and much stronger dependence of the number of sites used to model the diffusive motion. Only the 43-site model has small enough inter-site jump angles to be considered truly diffusive.

The intermediate side band ($k = 10^5 \text{ s}^{-1}$) intensities increase as the number of sites increasing as Fig 5.19 and 5.20 reveal. However, a more quantitative analysis of motional rates and especially trajectories would require an impractically large number of sites. A more promising approach would be to extend the Smoluchowski model developed by Kristensen, et al.¹³⁹⁻¹⁴¹

Simulations of a 15kHz MAS spectra is compared with experiments performed at 185 K, 270 K, and 320 K in Fig. 5.21. The cone angle of 60° was chosen to achieve complete

collapse of the spectrum for fast motion, and 43 sites were used in an attempt to approximate continuous diffusion. However, eight sideband pairs were observed in the experiments but considerations of computational efficiency limited the number of sideband pairs included in the simulation to ten. This is not enough for convergence, and quantitative agreement with experiment is not to be expected.

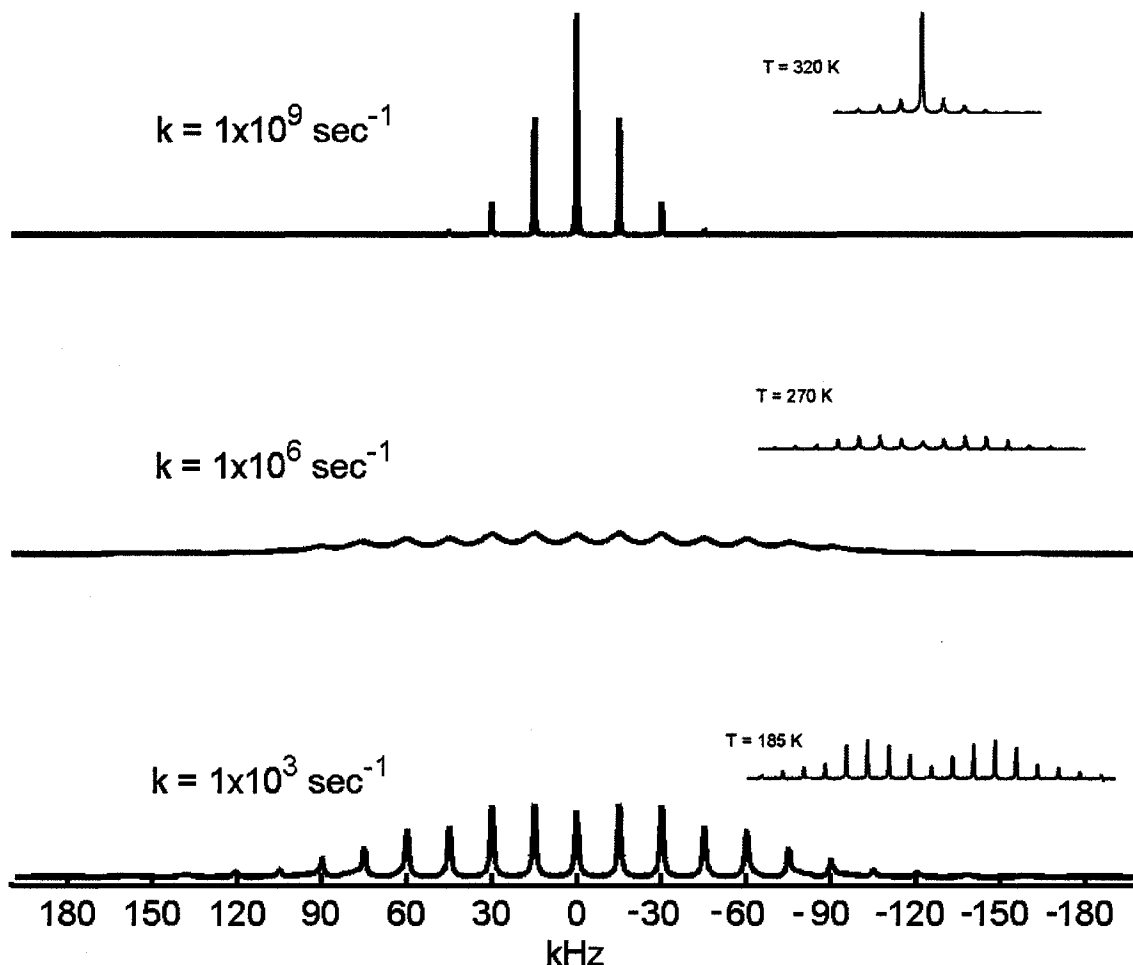


FIG. 5.21 Simulation at 15kHz with 60° cone-angle
43 sites distribute on the lattices of a 60° cone. $C_Q = 200 \text{ kHz}$, $\eta_Q = 0$, dwell time is $2.5 \times 10^{-6} \text{ s}$ ($\text{SW} = \pm 200 \text{ kHz}$). Different motion rates are used in order to simulate the diffusion effects that were observed in experimental spectra.

However, despite these difficulties, the simulations do show how the MAS line shape evolves with temperature, and the discussion based on small cone angle simulations indicates that if more sites are could be included in the computation, the sideband intensities in the intermediate regime ($k = 1 \times 10^5 \sim 1 \times 10^6 \text{ sec}^{-1}$) would better match the experimental data. It is clear that fast sample spinning is advantageous for such comparisons since fewer side bands would appear in the spectrum window.

5.5 Conclusions

The NMR experimental data for labeled L-phenylalanine demonstrate that high speed MAS experiments in 17.6 T field can distinguish the signals from aromatic ring and side chain deuterons. Compared with static quadrupole echo powder patterns, the signal to noise ratio the spectral resolution have been dramatically improved by MAS. The analysis of temperature dependent side band fine structure, supported by relaxation time measurements, reveals that the motion of about half of the aromatic rings is in the fast motional regime and consists of sudden 180° jumps. Even at 383 K, $\sim 40\%$ of the phenyl rings do not undergo large amplitude motion.

The motion of N-methyl-L-phenylalanine-methyl-ester in a β -cyclodextrin inclusion compound is very different from that in crystalline phenylalanine itself. Multi-site jump approximations to restricted, continuous rotational diffusion is a better approximation than large site jumps.

Appendix

Wigner Rotation Matrices

The Wigner rotation matrix, D that was used in this thesis is defined by the Euler angles (α, β, γ) , which specify the coordinate transformation. The coefficients of $D_{m',m}^L(\alpha, \beta, \gamma)$ is

$$D_{m',m}^L(\alpha, \beta, \gamma) = d_{m,m'}^L(\beta) \cdot \exp(-im'\alpha) \cdot \exp(-im\gamma)$$

where the second rank Wigner coefficient $d_{m',m}^L(\alpha, \beta, \gamma)$ is

$d_{m',m}$	$m = 2$	$m = 1$	$m = 0$	$m = -1$	$m = -2$
$m' = 2$	A	-B	C	-D	E
$m' = 1$	B	F	-G	H	-D
$m' = 0$	C	G	I	-G	C
$m' = -1$	D	H	H	F	-B
$m' = -2$	E	D	C	B	A

where

$$A = \frac{1}{4} \cdot (1 + \cos \beta)^2$$

$$B = \frac{1}{2} \cdot (1 + \cos \beta) \cdot \sin \beta$$

$$C = \sqrt{\frac{3}{8}} \cdot \sin^2 \beta$$

$$D = \frac{1}{2} \cdot (1 - \cos \beta) \cdot \sin \beta$$

$$E = \frac{1}{4} \cdot (1 - \cos \beta)^2$$

$$F = \frac{1}{2} (\cos \beta - 1) + \cos^2 \beta$$

$$G = \sqrt{\frac{3}{8}} \cdot \sin 2\beta$$

$$H = \frac{1}{2} \cdot (1 + \cos \beta) - \cos^2 \beta$$

$$I = \frac{1}{2} \cdot (3 \cos^2 \beta - 1)$$

Bibliography

1. Spiess, H. W. *Encyclopedia of Nuclear Magnetic Resonance* (Wiley, Chichester, 1996).
2. Griffin, R. G. et al. Deuterium NMR studies of dynamics in solids. NATO ASI C228, 81-105 (1988).
3. Spiess, H. W. Pulsed deuteron NMR investigations of structure and dynamics of solid polymers *Journal of Molecular Structure* 111, 119-133 (1983).
4. Hoatson, G. L., Tse, T. Y. & Vold, R. L. Deuterium Spin Relaxation and Molecular Motion in a Binary Liquid Crystal Mixture. *Journal of Magnetic Resonance* 98, 342-361 (1992).
5. Vold, R. R. & Vold, R. L. Nuclear spin relaxation and molecular dynamics in ordered systems: models for molecular reorientation in thermotropic liquid crystals. *Journal of Chemical Physics* 88, 1443-1457 (1988).
6. Spiess, H. W. Molecular dynamics of solid polymers as revealed by deuteron NMR. *Colloid and Polymer Science* 261, 193-209 (1983).
7. Davis, J. H., Jeffrey, K. R., Bloom, M., Valic, M. I. & Higgs, T. P. Quadrupole Echo Sequence for $2H$. *Chemical Physics Letters* 42, 390-392 (1976).
8. Bloom, M., Davis, J. H. & Valic, M. I. Exact Calculation of $I=1$ QE spin response. *Canadian Journal of Chemistry* 58, 1510-1520 (1980).
9. Levitt, M. H. *Spin Dynamics: Basics of Nuclear Magnetic Resonance* (Wiley, New York, 2001).
10. Jackson, J. D. *Classical Electrodynamics* (Wiley, New York, 1975).
11. Bleaney, B. I. & Bleaney, B. *Electricity and Magnetism* (Oxford University Press, Oxford, 1976).
12. Abragam, A. *The Principles of Nuclear Magnetism* (Clarendon Press, Oxford, 1961).
13. Duer, M. J. *Introduction to Solid-State NMR Spectroscopy* (Blackwell Publishing, 2004).
14. Ernst, R. R., Bodenhausen, G. & Wokaun, A. *Principles of Nuclear Magnetic Resonance in One and Two Dimensions* (Clarendon Press, Oxford, 1987).
15. Sakurai, J. J. *Modern Quantum Mechanics* (Addison-Wesley, Reading, MA, USA, 1994).
16. Schmidt-Rohr, K. & Spiess, H. W. *Multidimensional Solid-State NMR and Polymers* (Academic Press, London, 1994).
17. Mehring, M. *High Resolution NMR in Solids* (Springer, Berlin 1982).
18. Goldman, M. *Quantum Description of High-Resolution NMR in Liquids* (Clarendon, Oxford, 1988).
19. Dyson, F. J. The Radiation theories of Tomonaga, Schwinger, and Feynman. *Phys. Rev.* 75, 486 (1949).
20. Tycko, R. Broadband Population Inversion. *Phys. Rev. Lett.* 51, 775-779 (1983).

21. Brink, D. M. & Satchler, G. R. *Angular Momentum* (Clarendon Press, Oxford, 1993).
22. Varshalovich, D. A., Moskalev, A. N. & Kheronskii, V. K. *Quantum Theory of Angular Momentum* (World Scientific, Singapore, 1988).
23. Stejskal, E. O. & Memory, J. D. *High Resolution NMR in the Solid State* (Oxford, 1994).
24. Sanders, J. K. & Hunter, B. K. *Modern NMR Spectroscopy. A Guide for Chemist* (Oxford University, Oxford, 1993).
25. Derome, A. E. *Modern NMR Techniques in Chemistry Research* (Pergamon Press, Oxford, 1990).
26. Cohen, M. H. & Reif, F. NQR Spectroscopy. *Solid State Physics* 5, 321-421 (1957).
27. Vold, R. L., Hoatson, G. L. & Subramanian, R. Deuteron NMR studies of guest motion in alkanolic acid urea inclusion compounds. *J. Chem. Phys* 108, 7305-7316 (1998).
28. Vogel, M. & Rossler, E. Effects of Various Types of Molecular Dynamics on 1D and 2D ^2H NMR Studied by Random Walk Simulations. *J. Magn. Reson.* 147, 43-58 (2000).
29. Levitt, M. H. Demagnetization field effects in two-dimensional solution NMR. *Concepts Magn. Reson.* 8, 77 (1996).
30. Greenfield, M. S., Vold, R. L., Vold, R. R., Ellis, P. D. & Raidy, T. E. Deuterium quadrupole echo NMR spectroscopy III practical aspects of lineshape calculations for multiaxis rotational processes. *J. Magn. Reson.* 72, 89-197 (1987).
31. Fukushima, E. & Roeder, S. B. W. *Experimental Pulse NMR. A nuts and Bolt Approach* (Perseus Press, Cambridge, Massachusetts, USA, 1986).
32. Marshall, A. G. & Verdun, F. R. *Fourier Transforms in NMR, Optical and Mass Spectrometry* (Elsevier, Amsterdam, 1990).
33. Hoch, J. C. & Stern, A. S. *NMR Data Processing* (Wiley, New York, 1996).
34. Freeman, R. *Spin Choreography. Basic Steps in High Resolution NMR* (Spektrum, Oxford, 1997).
35. Antonijevic, S. & Wimperis, S. Separation of quadrupolar and chemical/paramagnetic shift interactions in two-dimensional ^2H ($I = 1$) nuclear magnetic resonance spectroscopy. *J. Chem. Phys* 122, 44312 (2005).
36. Brown, M. J., Hoatson, G. L. & Vold, R. L. Shaped Pulses for Selective Inversion in Solid-State Deuteron NMR Spectroscopy. *J. Magn. Reson.* 122, 165-178 (1996).
37. Heaton, N. J., Vold, R. L. & Vold, R. R. Deuterium quadrupole echo study of urea motion in urea/n-alkane inclusion compounds. *J. Am. Chem. Soc.* 111, 3211-3217 (1989).
38. Kinsey, R. A., Kintanar, A. & Oldfield, E. Dynamics of Amino Acid Side Chains in Membrane Proteins by High Field Solid State Deuterium NMR Spectroscopy. *J. Bio. Chem.* 256, 9028-9036 (1981).
39. Larsen, F. H., Jakobsen, H. J., Ellis, P. D. & Nielsen, N. C. Molecular dynamics from ^2H Quadrupolar Carr–Purcell–Meiboom–Gill solid-state NMR spectroscopy. *Chem. Phys. Lett.* 292, 467-473 (1998).

40. Bain, A. D. Chemical exchange in NMR. *Prog. NMR Spectrosc.* 43, 63-103 (2003).
41. Eden, M. & Levitt, M. H. Computation of Orientational Averages in Solid-State NMR by Gaussian spherical quadrature. *J. Magn. Reson.* 132, 220-239 (1998).
42. Hodykinson, P. & Emsley, L. Numerical simulation of solid-state NMR experiments. *Prog. NMR Spectrosc.* 36, 201-239 (2000).
43. Andrew, E. R. The narrowing of NMR spectra of solids by high-speed specimen rotation and the resolution of chemical shift and spin multiplet structures for solids *Prog. NMR Spectrosc.* 8 (1971).
44. Andrew, E. R. & Eades, R. G. Possibilities for high-resolution nuclear magnetic resonance spectra of crystals. *Discuss Faraday Soc* 34, 38 (1962).
45. Herzfeld, J. & Berger, A. E. Sideband intensities in NMR spectra of samples spinning at the magic angle *J. Chem. Phys* 73, 6021-6030 (1980).
46. Maricq, M. M. & Waugh, J. S. NMR in rotating solids. *J. Chem. Phys.* 70, 3300-3316 (1978).
47. Sinnig, G., Mehring, M. & Pines, A. Dynamics of spin decoupling in carbon-13—proton NMR. *Chemical Physics Letters* 13, 382-386 (1976).
48. Farjon, J., Bermel, W. & Griesinger, C. Resolution enhancement in spectra of natural products dissolved in weakly orienting media with the help of ^1H homonuclear dipolar decoupling during acquisition: Application to ^1H – ^{13}C dipolar couplings measurements. *J. Magn. Reson.* 180, 72-82 (2006).
49. Gan, Z. & Grandinetti, P. Rotary resonance in multiple-quantum magic-angle spinning. *Chem. Phys. Lett.* 352, 252-261 (2002).
50. Antzutkin. Sideband manipulation in magic-angle-spinning nuclear magnetic resonance. *Prog. NMR Spectrosc.* 35, 203-266 (1999).
51. Frydman, L. et al. Variable-angle correlation spectroscopy in solid-state nuclear magnetic resonance. *J. Chem. Phys* 97, 4800-4808 (1992).
52. Sethi, N. K., Alderman, D. W. & Grant, D. M. NMR spectra from powdered solids spinning at any angle and speed. *Mol. Phys.* 71, 217-238 (1990).
53. Bell, K. A., Hoatson, G. L. & Vold, R. L. Relaxation, Selective-Inversion, and Two-Dimensional Deuteron NMR Measurements of Slow Motion in a Single Crystal Urea/Alkane Inclusion Compound *J. Magn. Reson.* 108 (1994).
54. Isfort, O., Geil, B. & Fujara, F. 2D Deuteron Exchange NMR and Stimulated Echoes: Molecular Dynamics of the Vacancy Diffusion in Polycrystalline Benzene *J. Magn. Reson.* 130, 45-50 (1998).
55. Rosenke, K., Sillescu, H. & Spiess, H. W. Chain motion in amorphous regions of polyethylene: interpretation of deuteron n.m.r. line shapes. *polymer* 21, 757-763 (1980).
56. Kulik, A. S. & Prins, K. O. Deuteron nuclear magnetic resonance study of high-pressure effects on the molecular dynamics in amorphous polyethylene. *polymer* 35, 2307-2314 (1994).
57. Kang, H.-J., Meesiri, W. & Blum, F. D. Nuclear magnetic resonance studies of the hydrolysis and molecular motion of aminopropylsilane. *Materials Science and Engineering A* 126, 265-270 (1990).

58. Hoatson, G. L., Vold, R. L. & Tse, T. Y. Individual spectral densities and molecular motion in polycrystalline hexamethylbenzene-d₁₈. *J. Chem. Phys.* 100, 4756-4765 (1993).
59. Oldfield, E., Chapman, D. & Derbyshire, W. Lipid mobility in Acholeplasma membranes using deuterium magnetic resonance. *Chemistry and Physics of Lipids* 9, 69-81 (1972).
60. Huang, Y., Vold, R. L. & Hoatson, G. L. Investigation of multiaxis molecular motion by off-magic angle spinning deuterium NMR. *J. Chem. Phys.* 124 (2006).
61. Kristensen, J. H., Hoatson, G. L. & Vold, R. L. Investigation of multiaxial molecular dynamics by ²H MAS NMR spectroscopy. *Solid State NMR* 13, 1-37 (1998).
62. Vega, S., Olejniczak, E. T. & Griffin, R. G. Rotor frequency lines in the nuclear magnetic resonance spectra of rotating solids. *J. Chem. Phys.* 80, 4832-4840 (1984).
63. Schmidt, A. & Vega, S. The Floquet theory of nuclear magnetic resonance spectroscopy of single spins and dipolar coupled spin pairs in rotating solids. *J. Chem. Phys.* 96, 2655-2680 (1991).
64. Schmidt, A. et al. Chemical exchange effects in the NMR spectra of rotating solids. *J. Chem. Phys.* 85, 4249-4253 (1986).
65. Bracewell, R. N. *The Fourier Transform and its Applications* (McGraw-Hill, New York, 1986).
66. Brigham, E. O. *The Fast Fourier Transform and its Applications* (Prentice Hall, Upper Saddle River, NJ, USA, 1988).
67. Ernst, R. R. Numerical Hilbert Transform and automatic phase correction. *J. Magn. Reson.* 1, 7 (1969).
68. Slichter, C. P. *Principles of Magnetic Resonance* (Springer, New York, 1990).
69. Brown, M. E. & Hollingsworth, M. D. Stress-induced domain reorientation in urea inclusion compounds. *Nature* 376, 323 (1995).
70. Hoatson, G. L., Tse, T. Y. & Vold, R. L. Deuterium spin relaxation and molecular motion in a binary liquid-crystal mixture. *J. Magn. Reson.* 98, 342-361 (1992).
71. Vold, R. R. & Vold, R. L. Deuterium relaxation in molecular solids. *Advances in Magnetic and Optical Resonance* 16, 85-171 (1991).
72. Torchia, D. A. Solid State NMR studies of Protein Internal Dynamics. *Annual review of biophysics and bioengineering* 13, 125-144 (1984).
73. Schraml, J. & Bellama, J. M. *Two-Dimensional NMR Spectroscopy* (Wiley, New York, 1988).
74. Wittebort, R. J., Olejniczak, E. T. & Griffin, R. G. Analysis of deuterium nuclear magnetic resonance line shapes in anisotropic media. *Journal of Chemical Physics* 86, 5411-5420 (1987).
75. Gutowsky, H. S. & Holm, C. H. Rate Processes and Nuclear Magnetic Resonance Spectra. II. Hindered Internal Rotation of Amides. *J. Chem. Phys.* 25, 1228 (1956).
76. McConnell, H. M. Reaction Rates by Nuclear Magnetic Resonance. *J. Chem. Phys.* 28, 430-431 (1957).
77. Kaplan, J. I. Generalized Bloch-Type Equations for Chemical Exchange. *J. Chem. Phys.* 29, 462 (1958).

78. Bloch, F., Hansen, W. W. & Packard, M. Nuclear Induction. *Physics review* 69, 127.
79. Redfield, A. G. Theory of nuclear relaxation processes. *Adv. Magn. Reson.* 1, 1 (1965).
80. Varner, S. J., Vold, R. L. & Hoatson, G. L. An efficient Method for calculating powder patterns. *J. Magn. Reson. A* 123, 72-80 (1996).
81. Kristensen, J. H., Hoatson, G. L. & Vold, R. L. Effects of restricted rotational diffusion on ^2H magic angle spinning nuclear magnetic resonance spectra. *J. Chem. Phys* 110, 4533-4553 (1999).
82. Hazendonk, P., Bain, A. D., Grondey, H., Harrisona, P. H. M. & Dumonta, R. S. Simulations of Chemical Exchange Lineshapes in CP/MAS Spectra Using Floquet Theory and Sparse Matrix Methods. *J. Magn. Reson.* 146, 33-42 (2000).
83. Dembiski, S. T. On the Dyson method in the theory of magnetism. *physica* 30, 1217-1224 (1963).
84. Duer, M. J. & Levitt, M. H. Time-domain calculation of chemical exchange effects in the NMR spectra of rotating solids. *Solid State Nucl. Magn. Reson.* 1, 211 (1992).
85. Zheng, Z., Gan, Z., Sethi, N. K., Alderman, D. W. & Grant, D. M. An efficient simulation of variable-angle spinning lineshapes for the quadrupolar nuclei with half-integer spin. *J. Magn. Reson.* 95, 509-522 (1991).
86. Lin, T.-H., DiNatale, J. A. & Vold, R. R. Determination of Molecular Reorientation Rates and Electron-Nuclear Coupling in Paramagnetic Materials by Deuterium Solid Echo NMR Spectroscopy. *J. Am. Chem. Soc.* 116, 2133 - 2134 (1994).
87. Spaniol, T. P., Kubo, A. & Terao, T. Two-dimensional deuterium magic-angle-spinning nuclear magnetic resonance of paramagnetic compounds: Separation of paramagnetic and quadrupole interactions. *J. Chem. Phys* 106, 5393-5405 (1997).
88. Lee, H., Polenova, T., Beer, R. H. & McDermott, A. E. Lineshape Fitting of Deuterium Magic Angle Spinning Spectra of Paramagnetic Compounds in Slow and Fast Limit Motion Regimes. *J. Am. Chem. Soc.* 121, 6884 - 6894 (1999).
89. Paik, Y., Osegovic, J. P., Wang, F., Bowden, W. & Grey, C. P. ^2H MAS NMR Studies of the Manganese Dioxide Tunnel Structures and Hydroxides Used as Cathode Materials in Primary Batteries. *J. Am. Chem. Soc.* 123, 9367 - 9377 (2001).
90. Brown, M. J., Hoatson, G. L. & Vold, R. L. in 37th Experimental NMR Conference (Asilomar, CA., 1996).
91. Brown, M. J. in *Physics* (College of William and Mary, Williamsburg, 1997).
92. Vaughan, P. & Donohue, J. The structure of urea. Interatomic distances and resonance in urea and related compounds. *Acta. Cryst* 5, 530-535 (1952).
93. Sklar, N., Senko, M. E. & Post, B. Thermal effects in urea: the crystal structure at -140°C and at room temperature. *Acta. Cryst.* 14, 716-720 (1961).
94. Brown, M. J. in *Dept. of Physics* (College of William and Mary, Williamsburg, 1996).
95. Mullen, D. & Hellner, E. A simple refinement of density distributions of bonding electrons. V. Bond electron density distribution in urea, $\text{CO}(\text{NH}_2)_2$, at 123 K. *Acta. Cryst B* 34, 1624-1627 (1978).

96. Harris, K. D. M. & Thomas, J. M. Structural aspects of urea inclusion compounds and their investigation by X-ray diffraction: a general discussion. *Trans. Faraday Soc.* 86, 2985 - 2996 (1990).
97. Brown, M. E., Hollingsworth, M. D. & Santarsiero, B. D. Small Molecule Diffraction Studies with the R-AXIS Area Detector -Structural Aspects of a Class of Urea Inclusion Compounds. *The Rigaku Journal* 11, 4 (1994).
98. Casal, H. L., Cameron, D. G., Kelusky, E. C. & Tulloch, A. P. A spectroscopic study of the structure and dynamics of the urea inclusion adduct of stearic acid. *J. Chem. Phys* 81, 4322-4327 (1984).
99. Guillaume, F., Smark, S. P., Harries, K. D. M. & Dianoux, A. J. Neutron scattering investigations of guest molecular dynamics in alpha , omega -dibromoalkane-urea inclusion compounds. *J. Phys: Cond. Mat.* 6, 2169 (1994).
100. Chatani, Y., Taji, Y. & Tadokoro, H. Low-temperature form of urea adducts with n-paraffins. *Acta. Cryst. Sect. B* 33, 309-311 (1977).
101. Gilson, D. F. R. & McDowell, C. A. Nuclear magnetic resonance studies of urea and thiourea adducts. *Mol. Phys.* 4, 125-134 (1961).
102. Meakins, R. J. The dielectric properties of urea occlusion compounds. *Trans. Faraday Soc.* 51, 953 - 961 (1955).
103. Chatani, Y., Anraku, H. & Taki, Y. Phase transition and structure change of urea adducts with n-paraffins and paraffin-type compounds. *Mol. Cryst. Liq. Cryst* 48, 219 (1978).
104. Casal, H. L. Conformations of n-alkanes in urea inclusion adducts. *J. Phys. Chem.* 94, 2232 (1990).
105. Casal, H. L., Cameron, D. G. & Kelusky, E. C. A ^2H NMR study of molecular motions of nonadecane- d_{40} in a urea inclusion adduct. *J. Chem. Phys* 80, 1407-1410 (1984).
106. Greenfield, M. S., Vold, R. L. & Vold, R. R. Deuterium spin relaxation and guest motion in the n-nonadecane/urea clathrate. *Mol. Phys.* 66, 269-298 (1989).
107. Greenfield, M. S., Vold, R. L. & Vold, R. R. Deuterium relaxation and vibrationally averaged quadrupole coupling in an alkane/urea clathrate. *J. Chem. Phys* 83, 1440 (1985).
108. Williams, J. C. & McDermott, A. E. Cis-Trans energetics in Urea and Acetamide studied by deuterium NMR. *J. Phys. Chem.* 97, 12393-12398 (1993).
109. Emsley, J. W. & Smith, J. A. S. Proton magnetic resonance studies of amides. Part 2.—Molecular motion in thiourea and urea. *Trans. Faraday Soc.* 57, 1233 (1961).
110. Zussman, A. Effect of molecular reorientation in urea on the ^{14}N PNQR linewidth and relaxation time. *J. Chem. Phys* 58, 1514-1522 (1973).
111. Mantsch, H. H., Saitô, H. & Smith, I. C. P. Deuterium magnetic resonance, applications in chemistry, physics and biology. *prog. NMR Spectrosc.* 11, 211-272 (1977).
112. Aliev, A. E., Smart, S. P. & Harris, K. D. M. Dynamic properties of the urea molecules in alpha, omega-dibromoalkane/urea inclusion compounds investigated by ^2H NMR spectroscopy. *J. Mater. Chem* 4, 35 (1994).
113. Das, T. P. Tunneling through High Periodic Barriers. II. Application to Nuclear Magnetic Resonance in Solids. *J. Chem. Phys* 27, 763-781 (1957).

114. Das, T. P. Erratum: Tunneling through High Periodic Barriers. II. Application to Nuclear Magnetic Resonance on Solids. *J. Chem. Phys* 35, 1897-1898 (1961).
115. Williams, J. C. & McDermott, A. E. Cis-trans energetics in urea and acetamide studied by deuterium NMR. *J. Phys. Chem.* 97, 12393 - 12398 (1993).
116. Harris, K. D. M., Smart, S. P. & Hollingsworth, M. D. Structural properties of alpha, omega-dibromoalkane/urea inclusion compounds: a new type of interchannel guest molecule ordering. *Trans. Faraday Soc.* 87, 3423 - 3429 (1991).
117. Smith, A. E. The crystal structure of the urea-hydrocarbon complexes. *Acta. Cryst* 5, 224-235 (1952).
118. Brown, M. J., Vold, R. L. & Hoatson, G. L. Selective inversion investigations of slow molecular motion in solid state deuterium NMR spectroscopy. *Solid State Nucl. Magn. Reson.* 6, 167-185 (1996).
119. Flannery, B. P., Teukolsky, S. A. & Vetterling, W. T. *Numerical Recipes* (Cambridge Univ. Press., Cambridge, 1986).
120. Brown, M. J., Hoatson, G. L. & Vold, R. L. Selective Inversion Spectroscopy for Studies of Slow Motion in Solids. Poster presented at 34 th ENC, St. Louis MO (1993).
121. Gurd, F. R. & Rothgeb, T. M. Motions in proteins. *Advances in protein chemistry* 33, 73-165 (1979).
122. Opella, S. J., Nelson, D. J. & Jardetzky, O. Carbon magnetic resonance study of the conformational changes in carp muscle calcium binding parvalbumin. *J. Am. Chem. Soc* 96, 7157-7159 (1974;).
123. Hull, W. E. & Sykes, B. D. Fluorotyrosine alkaline phosphatase: Internal mobility of individual tyrosines and the role of chemical shift anisotropy as a ^{19}F nuclear spin relaxation mechanism in proteins. *Journal of Molecular Biology* 98, 121-153 (1975).
124. Campbell, I. D., Dobson, C. M. & Williams, R. J. P. Proton Magnetic Resonance Studies of the Tyrosine Residues of Hen Lysozyme-Assignment and Detection of Conformational Mobility. *Proceedings of the Royal Society of London. Series B, Biological Sciences* 189, 503-509 (1975).
125. Gall, C. M., DiVerdi, J. A. & Opella, S. J. Phenylalanine ring dynamics by solid-state deuterium NMR. *J. Am. Chem. Soc* 103, 5039 (1981).
126. Rice, D. M., Gingrich, P., Herzfeld, J. & Griffin, R. G. Interfacial Free Energies and the Control of the Positioning and Aggregation of Membrane Protein. *Biophysical Journal* 37 145 (1982).
127. Govindaraju, V., Young, K. & Maudsley, A. A. Proton NMR chemical shifts and coupling constants for brain metabolites. *NMR in Biomedicine* 13, 129-153 (2000).
128. Becker, E. D. *High Resolution NMR: Theory and Applications* (Academic Press, New York, 1969).
129. Muhandiram, D. R., Yamazaki, T., Sykes, B. D. & L. E. Kay Measurement of 2H T_1 and T_1 Relaxation Times in Uniformly ^{13}C -Labeled and Fractionally 2H -Labeled Proteins in Solution. *J. Am. Chem. Soc.* 117,, 11536 (1995).

130. Vold, R. L. & Hoatson, G. L. Deuteron Spin Relaxation and Molecular Dynamic Simulations of Urea/Alkane Inclusion Compounds. Paper presented at the 38th ACS Symposium on Solid State NMR, Denver, CO (1996).
131. Hoatson, G. L. & Vold, R. L. in Encyclopedia of Nuclear Magnetic Resonance (eds. Grant, D. M. & Harris, R. K.) 1582 (Wiley & Sons Scientific, 1995).
132. Vold, R. L., Hoatson, G. L. & Tse, T. Y. Effects of Slow Motion on the Interpretation of Deuteron Relaxation Times. Chem. Phys. Lett. 263, 271-273 (1996).
133. Hoatson, G. L., Vold, R. L. & Tse, T. Y. Individual Spectral Densities and Molecular Motion in Polycrystalline Hexamethylbenzene-d₁₈. J. Chem. Phys. 100, 4756-4760 (1994).
134. Szejtli, J. Cyclodextrin Technology (Kluwer Academic, Dordrecht, 1988).
135. Steed, J. W. & Atwood, J. L. Supramolecular Chemistry (Wiley-VCH, Weinheim, 200).
136. Gall, C. M., DiVerdi, J. A. & Opella, S. J. Phenylalanine Ring Dynamics by Solid-State ²H NMR. J. AM. Chem. Soc. 103, 5039-5043 (1981).
137. Snyder, G. H., Rowan, R., Karplus, S. & Sykes, B. D. Complete tyrosine assignments in the high field proton nuclear magnetic resonance spectrum of the bovine pancreatic trypsin inhibitor. Biochemistry 14, 3765-3777 (1975).
138. Clark, J. L. et al. Molecular Recognition in Cyclodextrin Complexes of Amino Acid Derivatives: The Effects of Kinetic Energy on the Molecular Recognition of a Pseudopeptide in a Nonconstraining Host Environment as Revealed by a Temperature-Dependent Crystallographic Study. Journal of Physical Chemistry 110, 26375 - 26387 (2006).
139. Kristensen, J. H., Bildsoe, H., Jakobsen, H. J. & Nielsen, N. C. Theory and simulations of molecular dynamics in 2H MAS NMR. Journal of Magnetic Resonance 100, 437-443 (1992).
140. Kristensen, J. H., Hoatson, G. L. & Vold, R. L. Investigation of Multiaxis Molecular Motion by ²H MAS Spectroscopy. Solid State NMR 13, 1 (1998).
141. Kristensen, J. H., Hoatson, G. L. & Vold, R. L. Effect of Restricted Rotational Diffusion on 2H MAS NMR Spectra. J. Chem. Phys. 110, 4533 (1999).

Vita

The author was born in Hubei, China on Nov. 27 1979. After graduated from his high school, the author went to Wuhan University in 1997. In 2001, the author finished his undergraduate study with a Bachelor of Science degree, came to the United States on Aug. 14 2001 and began his graduate study in Department of Physics at the college of William and Mary. After six years study and research, he finished his Doctorate in Physics specializing in Solid State NMR.